Quantifying co-seismic and post-seismic slip on fault scarps and their erosional modification using high-resolution Pleiades optical satellite data and repeat Terrestrial Laser Scanning: the 2016 Mw 6.6 Norcia earthquake (Central Italy)

ROBERT GILES ELLIOTT

Department of Earth Sciences, University of Durham

Quantifying co-seismic and post-seismic slip on fault scarps and their erosional modification using high-resolution Pleiades optical satellite data and repeat Terrestrial Laser Scanning: the 2016 M_w 6.6 Norcia earthquake (Central Italy)

A thesis submitted to the University of Durham for the degree of Doctor of Philosophy (PhD)

Robert Giles Elliott

June 2022

Declaration

No part of this thesis has previously been submitted for a degree at this or any other university. The work described in this thesis is entirely that of the author. Where appropriate, work in this thesis which has already been published is clearly indicated. In my work for this thesis I have used previously unpublished datasets collected by my supervisors and data provided by researchers from COMET (the Centre for Observation and Modelling of Earthquakes, Volcanoes and Tectonics). Work for this thesis was conducted from October 2018 to June 2022 under the primary supervision of Prof Kenneth McCaffrey (University of Durham) and secondary supervision of initially Richard Walters (also at the University of Durham) and (since January 2022) Laura Gregory of the University of Leeds.

Funding

The work contained in this thesis contains work carried out during a PhD study undertaken as part of a Natural Environment Research Council (NERC) Iapetus Doctoral Training Partnership (DTP) grant, whose support is gratefully acknowledged.

Copyright

Abstract

Fault scarps are a topographical expression of sharp gradients in ground movements in an active tectonic region. However, inferences of slip history and causative earthquake sizes may be biased by co-seismic slip gradients, near-fault deformation, afterslip and erosional processes.

To address these biases, I investigate co-seismic and continuing post-seismic deformation of near-fault areas and degradation of fault scarps, using high resolution Pleiades optical satellite images and repeat Terrestrial Laser Scans (TLS). The study area is Monte Vettore in the Apennines, Cental Italy, which has extensive surface ruptures associated with the M_w 6.6 30th October 2016 Norcia earthquake, part of the Central Italy Earthquake Sequence.

I combine image correlation techniques with novel median-based filtering to effectively de-noise the Pleiades data, creating Digital Elevation Models (DEMs) from before and after the Norcia earthquake. Those DEMs are then differenced horizontally and vertically. The results identify detail of near-fault co-seismic surface deformation. I jointly invert those data with far-field InSAR (Interferometric Synthetic Aperture Radar) and GNSS (Global Navigation Satellite System) datasets to model co-seismic slip at depth. My model reveals detail of slip transfer from the Monte Vettore fault at shallow depth. This provides insights into the distribution of near-fault co-seismic slip in an area of complex faulting by slip being partitioned onto minor near-surface hanging wall structures, with slip vectors diverging from those at greater depth.

The causes of post-seismic alteration or degradation of fault scarps are expected to be tectonic-related after-slip and/or erosion. Combining careful alignment of repeat TLS, use of an ICP (Iterative Closest Point) algorithm, filtering and detrending techniques, I characterise post-seismic deformation at 6 individual sites at ~centimetre scale. This provides insights into how individual factors (e.g. underlying geology, topography, and co-seismic slip gradients and distribution) influence which causes dominate and how degradation develops spatially and temporally. I show that fault scarps are highly

variable records of a fault's slip history. Any assessment of previous slip history using fault scarps as evidence needs to have regard to all those factors.

Acknowledgements

First and foremost, I would like to thank my supervisors for their invaluable support. Ken McCaffrey has undoubtedly borne the brunt of this by being thoroughly involved from beginning to end, and has done so with great patience, good humour and wise guidance. Until he left Academia to pursue an alternative career in November 2021 Rich Walters was an indispensable source of encouragement and guidance as to the many geophysical areas of my thesis for which my Geology undergraduate studies had not begun to prepare me. This included throwing me in at the deep end by encouraging me to teach geophysical subjects to undergraduates (as a demonstrator) when I had only just begun to get a grip with them myself. Finally, Laura Gregory stepped into the frame when Rich moved on. Despite having only just returned from maternity leave, she managed in a very short time period to assimilate what I was doing, and to make valuable suggestions which have helped significantly to improve the overall result. Also, although not a "supervisor" as such, thanks to Luke Wedmore for his helpful contributions at various stages.

The period when Covid-19 restrictions were in place amounted to nearly half the time spent working on my thesis. I am grateful to NERC for an extension of funding of 3 months to compensate for time lost as a consequence. Covid restrictions also made it difficult at times to maintain a collegiate environment within the Earth Sciences Department. Nevertheless, I am grateful for the companionship and friendship of many of my fellow students. Foremost among those have been Emma Ownsworth and Katharine Groves, both of whom have helped to make the process much more enjoyable than it would otherwise have been. Others I'd like to thank specifically are Madeleine, Eloise, Jack, Tim, Annabelle, Bex, Miles and Sarah. Thanks also to Tom Phillips for being my field assistant and helping with scanning in Italy in August 2019.

My family have put up with me and my studies throughout this period, for which I'm grateful. At times they've even shown some interest in what I've been doing! I was also allowed to use our home dining room as an office for over 2 years during the worst of the Covid-19 pandemic, which I've now been able to hand back for its intended use.

Figures

The majority of the figures I have produced for this thesis have been made using the open source collection of command-line tools Generic Mapping Tools (GMT), version 5.4, Wessel et al., 2013.

Table of Contents

Table of Contents

Table of Contents

Table of Contents

Table of Contents

Table of Contents

CHAPTER 1. Introduction

1.1 Overview of the study

A typical active tectonic region in continental crust is likely to have a history of seismic activity on millenial timescales, but earthquake recurrence times can be hundreds or thousands of years. The most recent event or events may well pre-date modern remote sensing methods. Fault scarps may be the topographic expression of the tectonic history of a region where other instrumental or historical records are too limited in scope. Thus the most readily accessible evidence of a region's tectonic history may be fault scarps preserved in the landscape. However, fault scarps may exhibit bias due to co-seismic slip gradients, fault geometry and ongoing processes of deformation through afterslip and erosion. Therefore information on slip rates and recurrence intervals derived from fault scarps contains uncertainties that mean they may need to be used with caution. The resolution and extent of available data means that it is now possible to investigate these processes in detail by using high resolution satellite imagery and laser-based surveying methods, that allow us to investigate how such processes have operated in the case of a modern fault scarp.

I use a combination of high resolution optical satellite images and repeat TLS scans of near-fault areas to investigate both co-seismic and continuing post-seismic deformation of near-fault areas and degradation of fault scarps, in the context of co-seismic shallow slip deficit models. I do so in relation to an active tectonic region, the Monte Vettore/Monte Bove area in the Apennines, Cental Italy that was the site of the well-documented 2016 Central Italy Earthquake Sequence ("CIES"). The area contains extensive surface ruptures associated with the M_w 6.6 30th October 2016 Norcia earthquake that was part of the CIES. The area is readily accessible, making it feasible to undertake repeat Terrestrial Laser Scanning (TLS).

1.2 Scientific questions to be addressed

I aim to characterise co-seismic near-fault deformation and scarp formation, and continuing deformation over the immediate post-seismic period, covering a time span of ~3 years.

The overall hypothesis that I will test is that bedrock fault scarps preserved in the landscape are highly variable records of a fault's slip history, its degradation and preservation.

My aim is to provide spatial and temporal insights into how reliable fault scarps are as evidence of previous seismic activity. This question is of wider importance in the context of how seismic hazard analysts interpret field data from faults (e.g. the work of the FAULT2SHA ESC working group), in seeking to improve the reliability of seismic hazard assessments.

1.3 How this thesis addresses the issues.

I aim:

(a) to develop existing models of near-fault co-seismic deformation by the addition of high-resolution optical satellite data to complement existing InSAR and GPS datasets, to provide near-fault detail previously lacking;

(b) to characterise near-fault post-seismic deformation in a number of fault scarp locations using repeat TLS, using the results to model localised post-seismic shallow slip; and

(c) to analyse the post-seismic deformation in the context of the co-seismic deformation established using shallow slip distribution models and field observations. This is in order to help improve understanding of how co-seismic and post-seismic deformation interrelate, the extent to which the co-seismic record in the form of the fault scarp varies spatially and over time, and the causes of such variation.

1.4 Study Area: The Monte Vettore-Monte Bove region, central Italy

1.4.1 Geological Background

The Monte Vettore study area is part of an active extensional region in the Apennines, Central Italy. The current extensional regime derives from the evolution of a thrust front associated with subduction of the Eurasian plate beneath the African plate. During the Eocene, westward subduction led to the creation of an accretionary complex. As the thrust front migrated eastwards towards the Adriatic, extension developed in the Tyrrhenian Basin back arc region (e.g. Jolivet et al., 1998) and migrated eastwards to the

Apennines. Extensional faulting in the form of westerly dipping normal faults in the Apennines initiated ~2-3 Ma as the thrusting in the Adriatic slowed. It has been suggested that a slab window opened allowing mantle upwelling that created a topographic bulge in the Apennine region (D'Agostino et al., 2001a, Faure Walker et al., 2012). The current extensional regime in the Apennines has overprinted earlier structures associated with the thrust regime (Pizzi and Galadini, 2009).

More recently, the dominant control on the morphology of the Apennines region has been glaciation and subsequent tectonic activity. Glacial evidence from the Gran Sasso Massif area suggests that the last glacial maximum in central Italy was ~22,600 years ago (the Campo Imperiale Stadial), and the glacial retreat started ~21,000 years ago. The interstadial was followed in turn by a stadial at ~16,000 years b.p., further retreat at ~ 15,000 years b.p., and most recently the Monte Aquila Stadial of ~11,000 years b.p. (Giraudi and Frezzotti, 1997).

The long-term regional extensional faulting has led to a complex array of predominantly northwest-southeast trending and southwest dipping normal faults in the central Apennines region. Typically, those fault systems are in the range of ~20-40 km in length (Galadini and Galli, 2000, Roberts and Michetti, 2004). The faulting shows complex relationships of cross-cutting or reactivation of older structures from previous compressional tectonic phases (e.g. Pizzi and Scisciani, 2000, Pizzi and Galadini, 2009).

The initiation of the extensional faulting in the Apennines is estimated to have been ~2.5-3.3 Ma (Cavinato and De Celles, 1999, Roberts and Michetti, 2004). During the glacial maximum, rates of repeat surface fault slip were matched or exceeded by footwall erosion, leading to fault scarp degradation, or burial with sediment (Roberts and Michetti, 2004). Smooth hillsides formed by periglacial processes are now offset by bedrock fault scarps, which evidence slip over the intervening period of up to ~14-18 ka. The footwalls are formed predominantly from Mesozoic and Tertiary carbonate rocks. Regional slip rates on those faults have been measured at in the region of ~3 mm per year since the last glacial maximum (D'Agostino et al., 2001b, Faure Walker et al., 2010), with higher slip rates towards the centre of the array (Roberts and Michetti, 2004).

The Monte Vettore-Monte Bove Fault System ("VBFS") is a complicated fault system towards the northeast flank of the extensional region, in an area of elevated and steep

topography, dominated by Monte Vettore, a Mesozoic carbonate ridge. **Figure 1** is a simplified geological map of the area (from Scognamiglio et al., 2018).

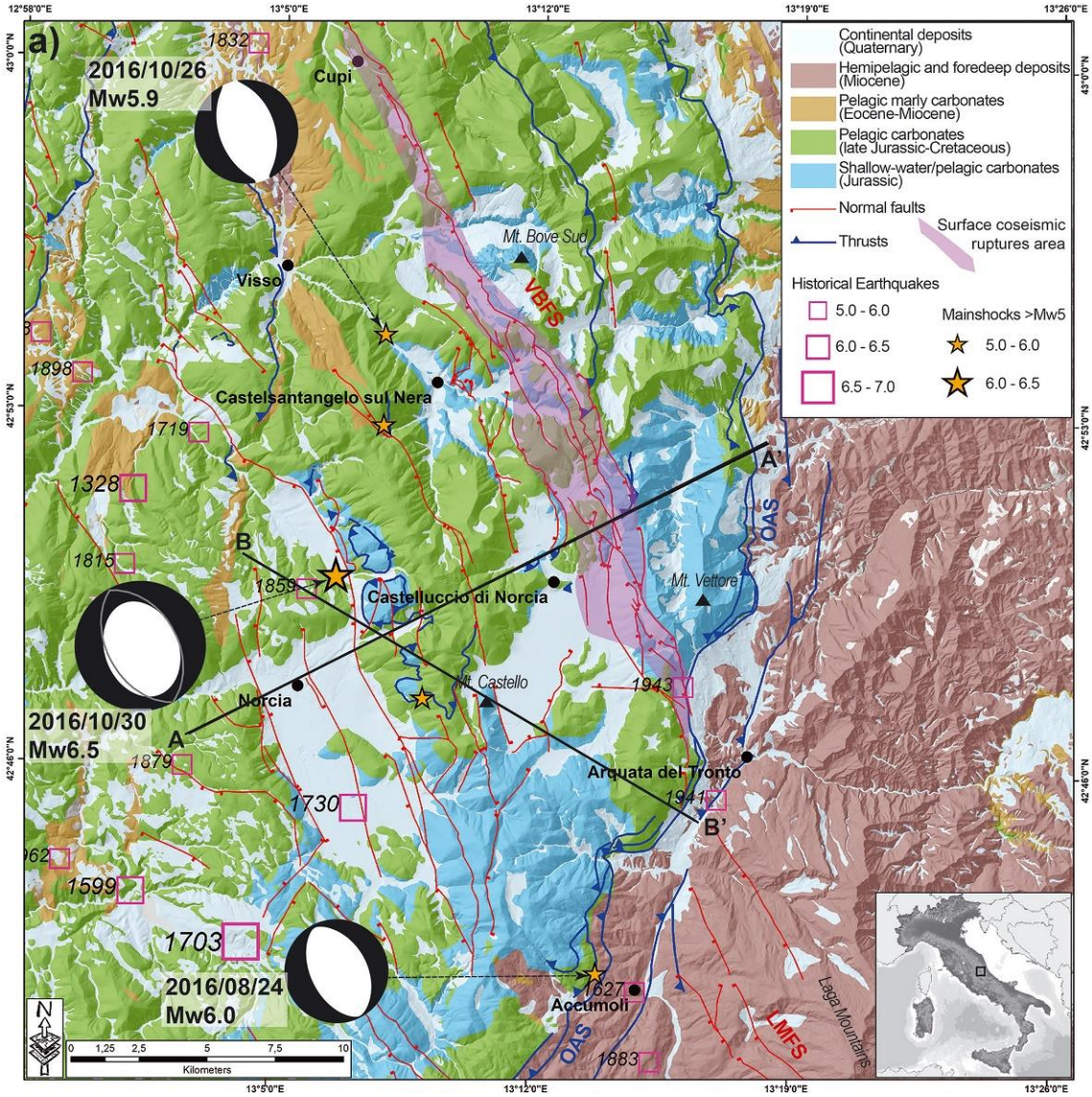

Figure 1: *From Scognamiglio et al., 2018, simplified geological map of the study area, (compiled from 1:10,000-scale cartography of Regione Umbria and Marche; Centamore et al., 1992; Pierantoni et al., 2013) showing epicentres of the Amatrice, Visso and Norcia earthquakes within the CIES, and approximate locations of historical earthquakes (magnitude indicated by box sizes). VBFS = Mte Vettore-Mte Bove Fault System, LMFS = Laga Mts Fault System, OAS = Olevano-Antrodoco-Sibillini thrust. Shaded pink polygon encloses area with co-seismic surface ruptures following the 2016 CIES main shocks. For sections AA' and BB' see Scognamiglio et al., 2018.*

Together with the Laga Mountains Fault System ("LMFS") to the southeast, the VBFS forms the most important extensional fault system in the area. It is ~25 km in length. As such, and as a fault system which initiated less than 5 Ma years ago, with a maximum long-term slip rate of < 1 cm/year and likely total maximum displacement of < 10 km it is classified as an "immature" system (Manighetti et al., 2007).

The system trends NNW-SSE. The VBFS and LMFS are separated by the line of a major regional structure from the previous compressional phase, the Olevano-Antrodoco-Sibillini Thrust ("OAST") (Pierantoni et al., 2013), which trends SSW-NNE in the southern part of the area. The OAST juxtaposes Triassic-Miocene (Umbria-Marche) carbonates onto Messinian siliciclastic turbidites of the Laga Formation (ibid).

1.4.2 Earthquake recurrence times - Trenching results in the Monte Vettore area from previous studies

Pre-instrument normal faulting earthquakes in this area include two shocks of M_w 6.8 and M_w 6.7 in 1703, near the town of Norcia (Galli et al., 2005, Galli et al., 2018) (location shown on **Figure 1**). There was no known earthquake of similar magnitude in the historical record (since 1349) on the Monte Vettore Fault. However, it was considered to be an active "silent fault" from palaeoseismic investigations (Galadini and Galli, 2003, Galli et al., 2019). Palaeoseismological analysis from trenching at three locations on a synthetic splay across an alluvial fan in the Pian Grande to the west of Monte Vettore has suggested a recurrence interval of not more than 4690 years (Galadini and Galli, 2003), with the previous event having occurred no later than the 6^{th}-7^{th} century. The expected magnitude of a recurrence event was M_w 6.5. The available data suggested 3 Holocene displacement events, although with uncertainty as to whether one apparent event might have been multiple events. Those estimates were updated following the CIES. New palaeoseismic trenching work at three sites in the Colle Infante and San Lorenzo basin areas (along the antithetic San Lorenzo fault) in conjunction with previous work (Galadini and Galli, 2003) has revealed 6 surface faulting events (including the CIES) in the past 9 kyr, with average return periods of 1.8 ± 0.3 kyr for $M_w \geq 6.6$ earthquakes (Galli et al., 2019). The previous event was dated at ~1573 years before the CIES (ibid). The recurrence time found was very similar to that found by trenching work in connection with the neighbouring Norcia fault (~1.8 kyr) (Galli et al., 2018).

1.4.3 Geomorphology of the Monte Vettore area

The study area includes a mixture of steep topography in the area of Monte Vettore and Monte Bove, and more planar topography, particularly in the agricultural (lentil growing) region of the Pian Grande to the southwest of Monte Vettore (**Figure 2)**. The area is forested to the south and southeast of Monte Vettore.

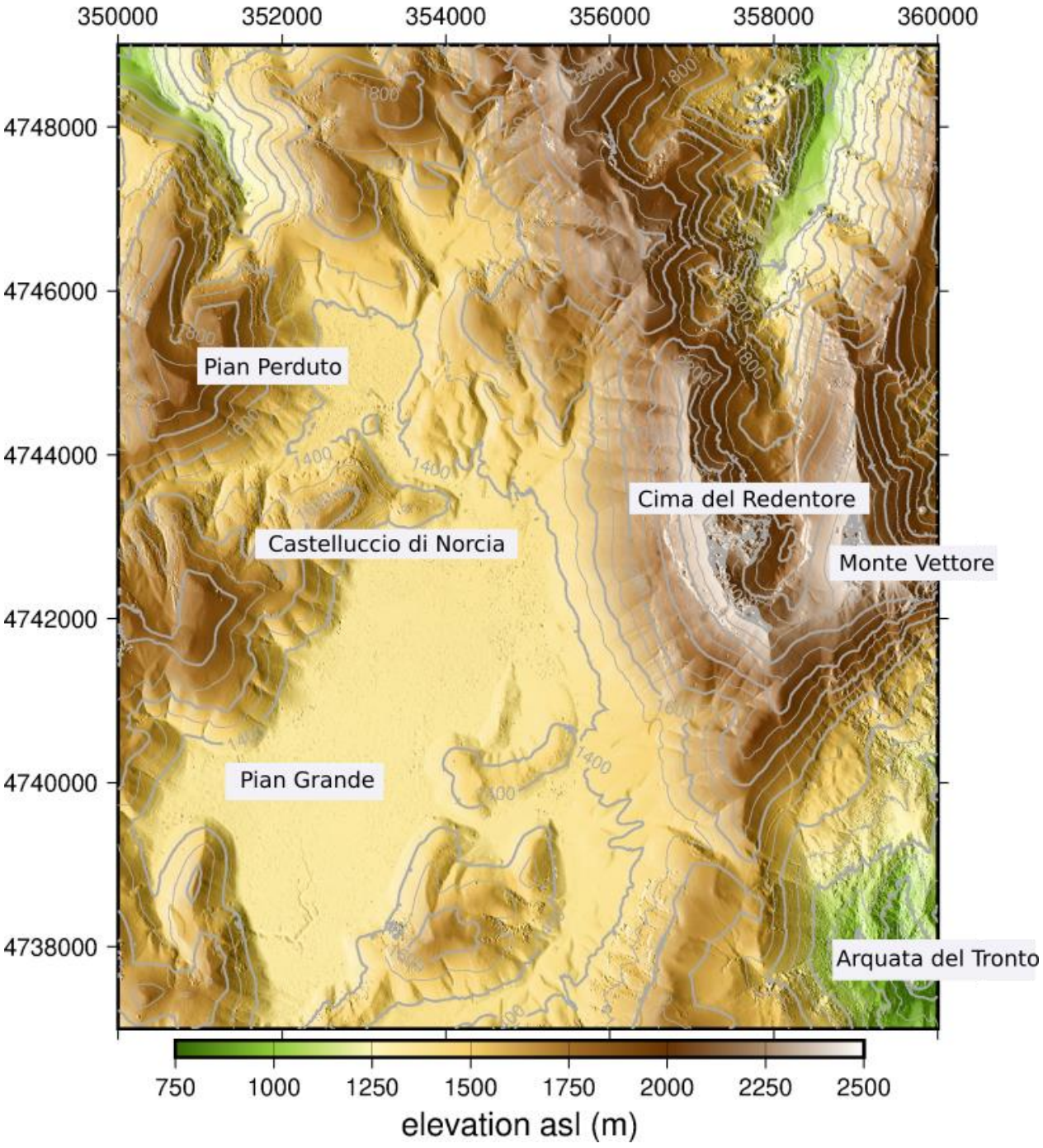

***Figure 2**: Area surrounding Monte Vettore, DEM from Pleiades optical satellite data, 1st December 2016. Coordinates are in UTM 33T. Contours at 100 m intervals.*

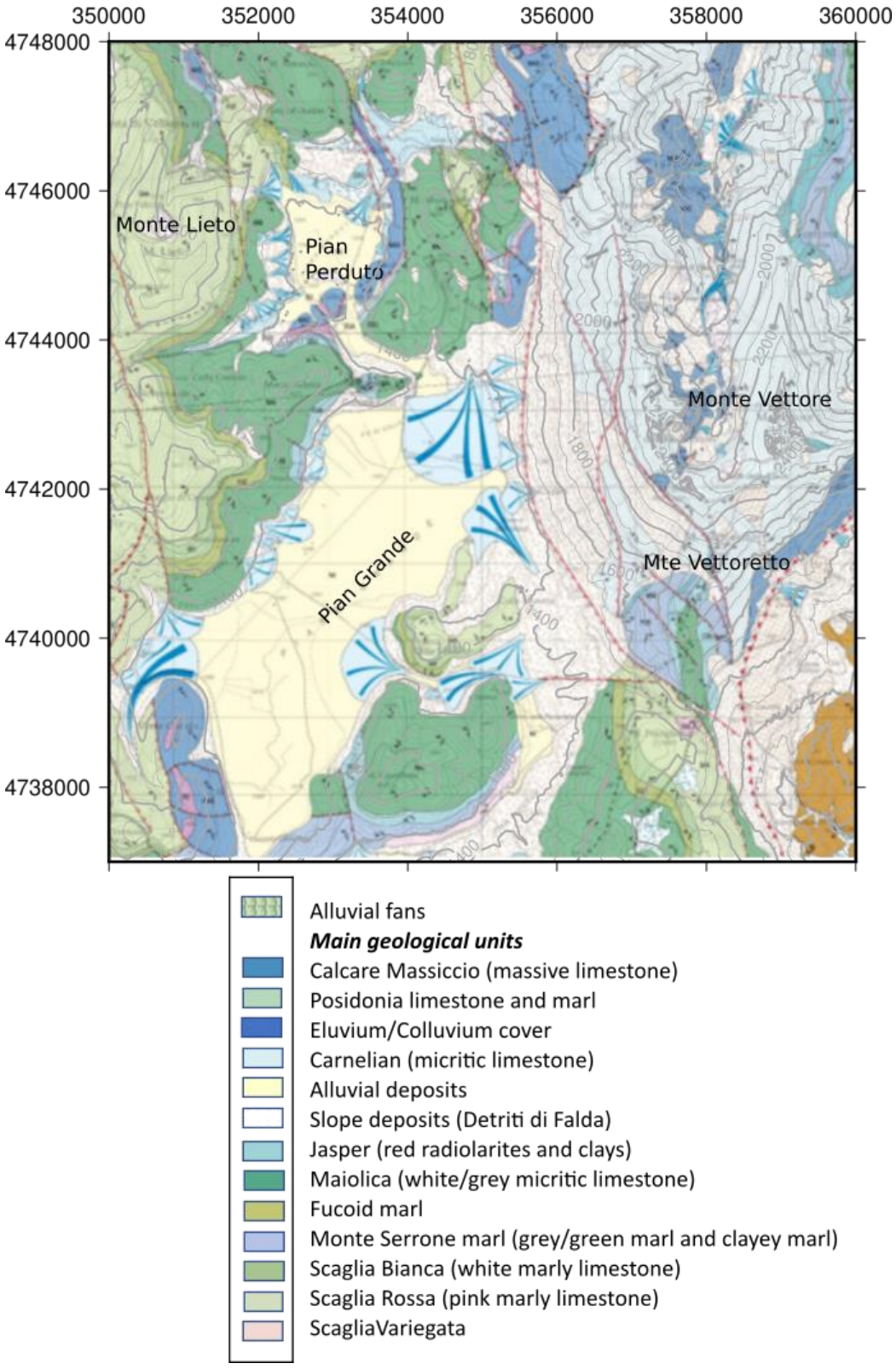

Figure 3: *Geological map of main Monte Vettore area, adapted from Pierantoni et al., 2013 overlain with contours at 100 m intervals, with description of main geological units translated from Italian. Coordinates are in UTM 33T.*

Due to the high mountainous terrain, and relatively rapid tectonic uplift, erosion in the area is heavily affected by gravitational factors.

Slope deposits and landslide accumulations in the form of scree and loose boulders are present in the hanging wall on most of the west-facing slopes below the main Monte Vettore ridge (below the Cima del Redentore mountain) (Coltorti and Farabollini, 1995), with extensive alluvial deposits and landforms at the base of the mountainside in the Pian Grande area (ibid), which forms a small intra-montane basin. These main areas of alluvial and gravitational deposits can be seen from a geological map of the area, **Figure 3** (adapted from Pierantoni et al., 2013).

The bedrock in the Monte Vettore area is almost exclusively Jurassic and Cretaceous limestones and marls (ibid), heavily distorted by tectonic activity since the previous glacial maximum (see above).

1.5 The Central Italy Earthquake Sequence, 2016/17

1.5.1 The sequence

The VBFS was the source of the CIES in 2016/17 between August 2016 and January 2017 (**Figure 4**). The first earthquake in the sequence (Amatrice, M_w 6.0 on 24 August 2016) caused widespread loss of life and nucleated at a relay between the VBFS and LMFS (Pizzi et al., 2017). The second, Visso, M_w 5.9, on 26 October 2016, nucleated at a minor relay zone within the north section of the VBFS (ibid). The largest magnitude (Norcia, M_w 6.6 on 30 October 2016) caused widespread property damage and involved almost the entire length of the VBFS (ibid). The final main shocks (Laga, M_w 5.0-5.5, on 18 January 2017), nucleated within the LMFS. Cross-cutting structures trending SSW-NNE (including the OAST) are thought to have controlled lateral propagation of the ruptures (e.g. Chiaraluce et al., 2017, Pizzi et al., 2017, Walters et al., 2018).

In total, the CIES ruptured ~60 km of normal fault systems. The CIES ruptured both the VBFS (Pizzi et al., 2017, Villani et al., 2018) and (in the case of the Amatrice and Laga earthquakes) the LMFS. Its location falls between two previous sequences involving similarly oriented (~NNW-SSE) normal fault systems, the 1997 M_w 6.0 Colfiorito earthquake sequence (further to the northwest) (also known as the Umbria-Marche

sequence) (e.g. Vittori et al., 2000, Chiaraluce et al., 2005), and the 2009 M_w 6.1 L'Aquila sequence (to the southeast) (e.g. Chiarabba et al., 2009, Cheloni et al., 2010).

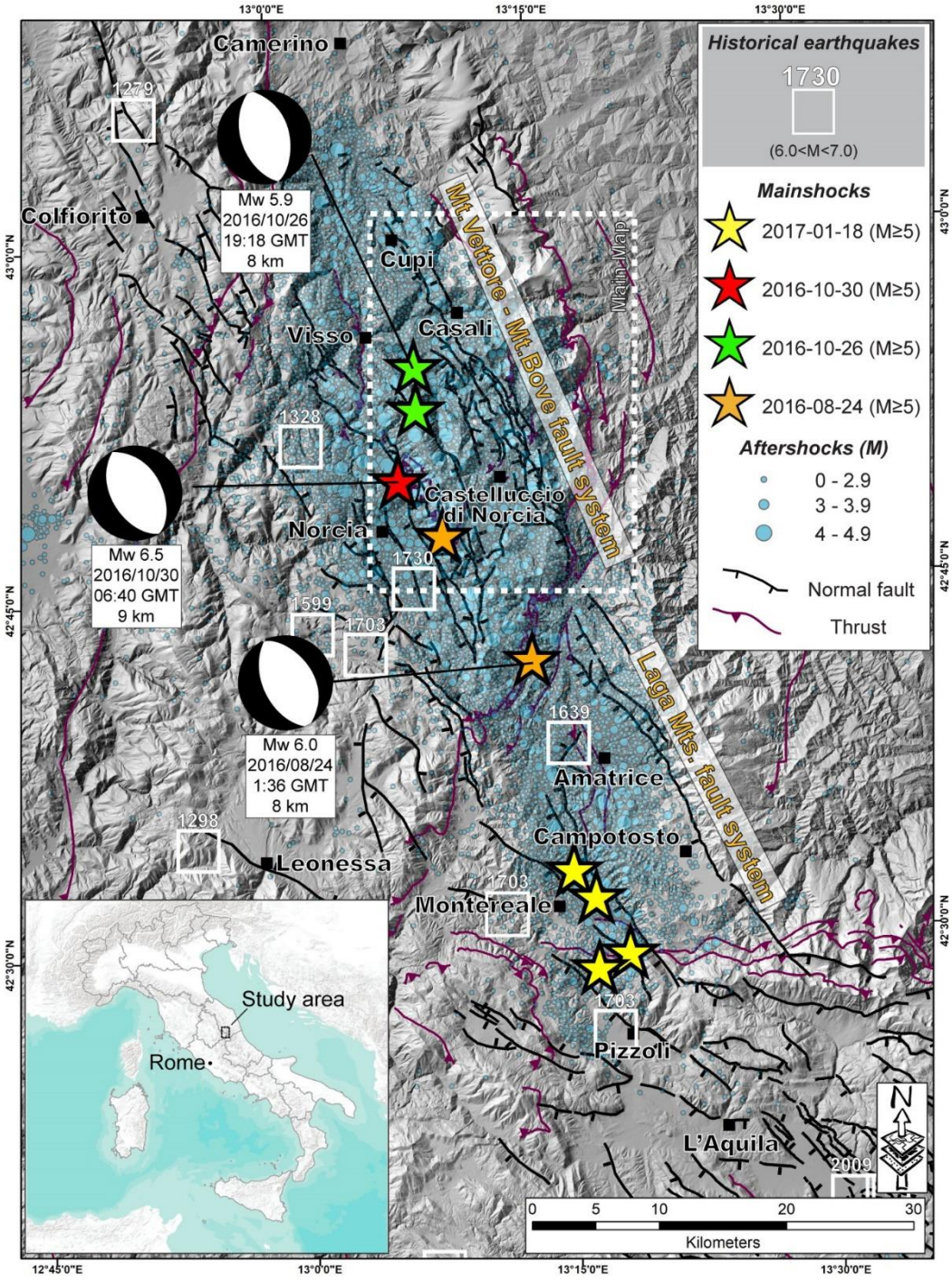

Figure 4: *Location of Central Italy 2016–17 earthquake sequence (including the Laga earthquake in January 2017), aftershocks and historical earthquakes, figure from Civico et al., 2018, based on work by the Open EMERGEO Working Group.*

1.5.2 The structures affected by the Norcia earthquake

The structures affected by the Norcia earthquake were the main Monte Vettore Fault System ("MVFS") (including synthetic and minor antithetic structures in the hanging wall), and a further structure on the east side of the Pian Grande basin reaching the surface in the Norcia area. This latter structure is generally assumed to be antithetic to the MVFS, dipping to the northeast, in order to fit geodetic (e.g. Walters et al., 2018, Cheloni et al., 2019) and seismological data (from alignment of aftershocks) (Chiaraluce et al., 2017). However, Delorme et al., 2020 postulate a synthetic structure in the same location. It is also thought that a further structure trending WSW-ENE was involved. It has been suggested that the OAST was reactivated as a high-angle normal fault near Arquata del Tronto (Cheloni et al., 2017, Scognamiglio et al., 2018, Walters et al., 2018). Although some feel that this is not clearly shown or that its role was merely passive (e.g. Cheloni et al., 2019), a structure with that trend towards the south of the Castelluccio basin seems to have played a role in the distribution of aftershocks (Chiaraluce et al., 2017, Pizzi et al., 2017).

1.5.3 Co-seismic field measurements

An extensive database of co-seismic surface measurements was compiled following the Norcia earthquake, from a collaboration of some 130 researchers from several teams (the Open EMERGEO Working Group), coordinated by INGV (Villani et al., 2018). A summary of the statistics collected from the field data shows a dominant strike for the faulting of 135°-160°, with southwest-dipping faults, maximum throw of between 2 m and 2.5 m, maximum opening 1 m-1.5 m, and slip vector trend from ~northeast-southwest (~60°-~240°) (**Figure 5**, from Villani et al., 2018).

The collated co-seismic ruptures showed a complex faulting pattern of parallel or sub-parallel synthetic and antithetic fault splays. These were presented in map form in Civico et al., 2018 . The map can be accessed here: Surface ruptures following the 30 October 2016 Mw 6.5 Norcia earthquake, central Italy: Journal of Maps: Vol 14, No 2 (tandfonline.com).

Within the central area, the locations and identification of results as measuring either synthetic or antithetic dip direction are shown in **Figure 6**.

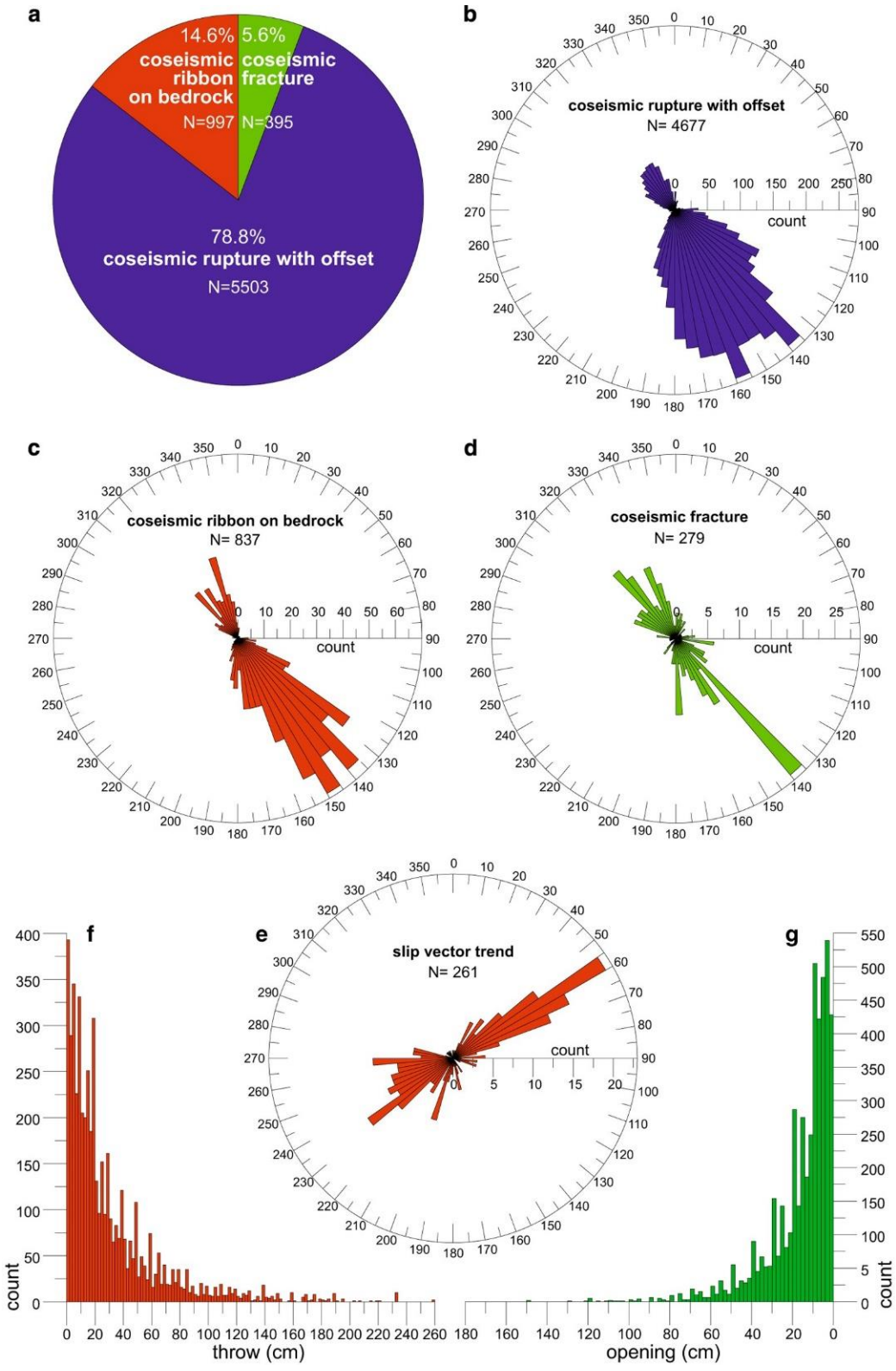

Figure 5: *From [Villani et al., 2018](). Statistical properties of the Norcia earthquake co-seismic ruptures.*

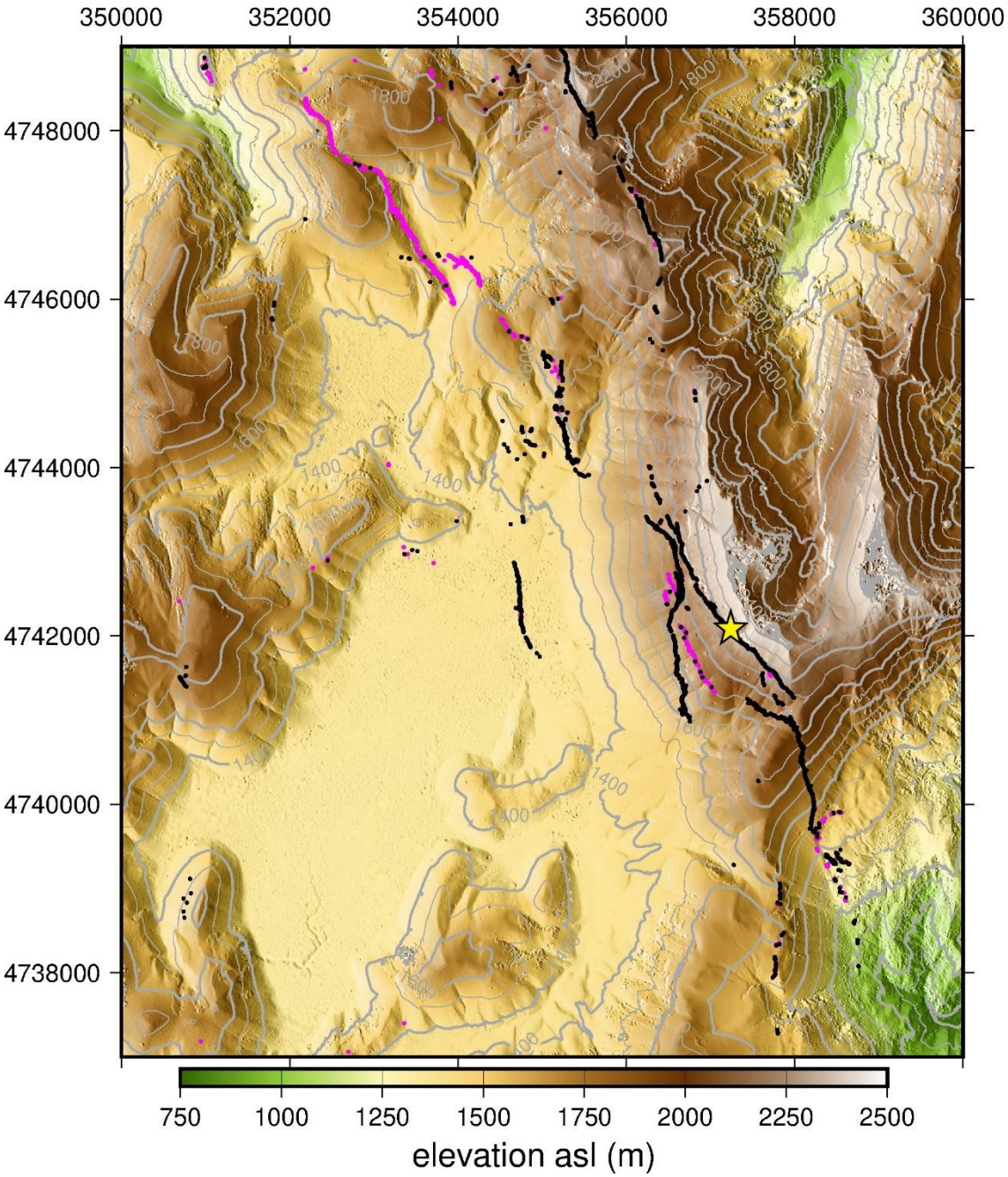

Figure 6: *Area surrounding Monte Vettore, DEM from Pleiades optical satellite data, 1st December 2016. Coordinates are in UTM 33T. Contours at 100 m intervals. Locations of co-seismic field measurements (from Villani et al., 2018) are shown with either synthetic dip direction (black) or antithetic dip direction (magenta). Yellow star marks the approximate location of the Scoglia dell'Aquila outcrop.*

The highest values for co-seismic slip were recorded on the Monte Vettore fault itself, in an area either side of the Scoglia dell'Aquila outcrop below the Cima del Redentore (marked with a yellow star in **Figure 6**). This is an area where the fault trace appears to

bend, that has been identified as a fault section with abnormally steep near-surface dips compared to neighbouring fault sections, and long-term throw greater than elsewhere on the fault (Iezzi et al., 2018).

1.5.4. Norcia earthquake post-seismic deformation

Localised deformation connected to the Norcia earthquake in the 10 weeks following the earthquake has been identified using InSAR in two regions: in the west side of the Pian Grande basin (up to ~1.5 cm - likely to be due to afterslip), and in a smaller region in the vicinity of the postulated reactivation of the OAST near Arquata del Tronto (up to ~5 cm – unlikely to be solely due to afterslip) (Pousse-Beltran et al., 2020). Over a longer timescale (~28 months) and a wider area, using ground displacement time series from GNSS regional data, vertical post-seismic movement of up to ~4-5 cm has been observed, with a horizontal component of up to ~2 cm towards ~250^{o} (Mandler et al., 2021). In this wider context, the probable mechanism for the deformation is believed to be a combination of afterslip and viscoelastic relaxation of the lower crust, with afterslip being the more important process (ibid).

1.6 General considerations affecting evolution of landforms associated with earthquakes

In addition to the site-specific background to the Monte Vettore area and the CIES, I set out here some of the main general considerations applicable to post-seismic landform evolution. These include both co-seismic considerations such as the extent to which faulting is distributed in the near fault region, and post-seismic processes associated with tectonic activity and erosion.

1.6.1 Off Fault Deformation ("OFD")

Simple models of fault growth over time envisage a number of possible ways in which elongate faults might develop at depth over time. Those include radial propagation, where the fault lengthens over time and accumulates more displacement; linkage of smaller fault segments which increase the fault length, but do not increase the total displacement; and rapid lengthening in the early history of a fault but which then accumulates displacement without any corresponding increase in length (Cartwright et al., 1995 and Walsh et al., 2002).

The possible linkage between fault segments may over time also give rise to complex structures and/or transfer of extension between adjacent faults, such as by transfer faults oblique to the main fault traces, or relay ramps (Gawthorpe and Hurst, 1993).

Normal faults form in settings where the maximum compressive stress is vertical, with a deviatoric tensile stress in a horizontal direction, and typically rupture the surface at high angles (~50-70^{o}) (Burbank and Anderson, 2012). Looking at the surface evidence of the faulting in cross-section, there is commonly an asymmetric division of co-seismic displacement between hanging wall and footwall, set against a horizontal datum. The subsidence in the hanging wall is typically several times greater than the uplift in the footwall. Over time, with repeated faulting, the hanging wall of a normal fault generally accumulates sediment in a basin and is relatively gently sloping, whereas the footwall is uplifted, steeper in profile and in a continental setting becomes eroded (ibid).

Half graben structures may form, with secondary synthetic and antithetic structures within the hanging wall block (**Figure 7**).

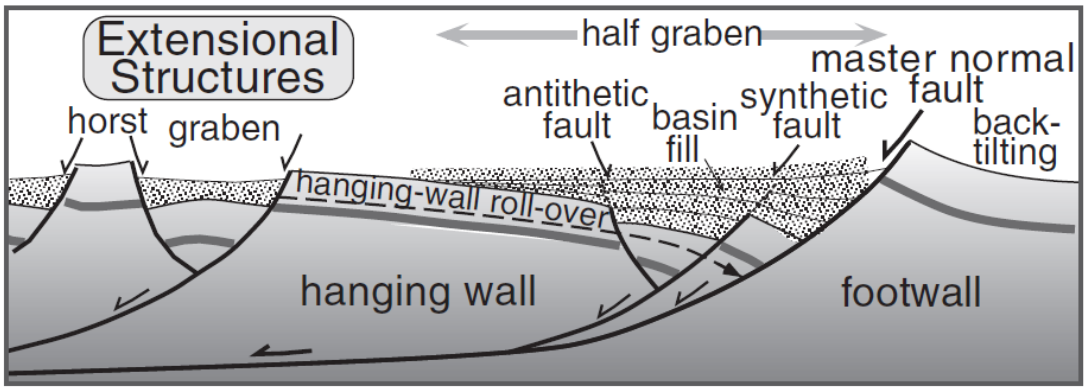

Figure 7: *Schematic representation of cross-section of normal faults in an extensional region. From Burbank and Anderson, 2012.*

The extent and nature of secondary structures will be important factors in how co-seismic slip is distributed as the earthquake ruptures the surface. Due to the heterogeneous nature of materials in the Earth's crust, and the fact that hundreds of small rupture surfaces actually accommodate the total co-seismic displacement,

surface deformation is expected to result in complex deformation patterns over time (ibid).

Co-seismic deformation seen at the surface following an individual earthquake will be split between deformation on the fault plane itself and associated distributed deformation in the surrounding area, or Off Fault Deformation ("OFD"). As an example, 46% of the total surface displacement associated with the Landers, California earthquake of 1992 occurred in the form of OFD (Milliner et al., 2015). Field measurements on their own may significantly underestimate the amount of net slip due to the difficulties of measuring OFD in the field (Gold et al., 2021). Failure to characterize the full extent and nature of near-fault distributed surface deformation may result in slip inversions failing reliably to constrain spatial patterns of slip (Xu et al., 2016).

The size and width of the OFD may be controlled by the geometrical structural complexity of the fault system, and secondary controls in the form of the type of near-surface materials involved (e.g. Xu et al., 2016, Zinke et al., 2014 and Teran et al., 2015). Structural immaturity of the fault system may also be a controlling factor (e.g. Milliner et al., 2016, Teran et al., 2015, Gold et al., 2021). The complexity of fault systems tends to simplify with fault maturity (Wesnousky, 1988). Fault bends and stepovers tend to produce the most complex rupture zones (e.g. Johnson et al., 1998, Teran et al, 2015). Surface deformation tends to be more localised at the fault trace in the case of relatively mature systems (Dolan and Haravitch, 2014). Distance from the primary structure, fault geometry and lithology have been found to be key factors controlling the extent to which distributed faulting occurred in relation to the Norcia earthquake (Ferrario and Livio, 2018).

The concentration of maximum fault slip distribution at shallow depths may give rise to surface features which disappear more easily over a relatively short time period of as little as 10^1- 10^3 years (Quigley et al., 2012).

1.6.2 Post-seismic tectonic-related deformation

Time and velocity of slip both have an effect upon friction. Laboratory-observed effects of time and velocity of slip on friction have been formulated in rate and state variable

friction laws (e.g. Dieterich, 1979 and Ruina, 1983). In experiments measuring the variation in static friction with hold time, and responses to sudden increases in sliding velocity, a pattern of stick-slip is demonstrated in unstable regions, such as the Apennines. In such circumstances slip commences once a static friction coefficient is exceeded, slip is then resisted by dynamic friction, and over time the static value is regained following what is essentially a "healing" process. Dynamic friction decreases with log of velocity, through what is termed "velocity-weakening" behaviour (**Figure 8**).

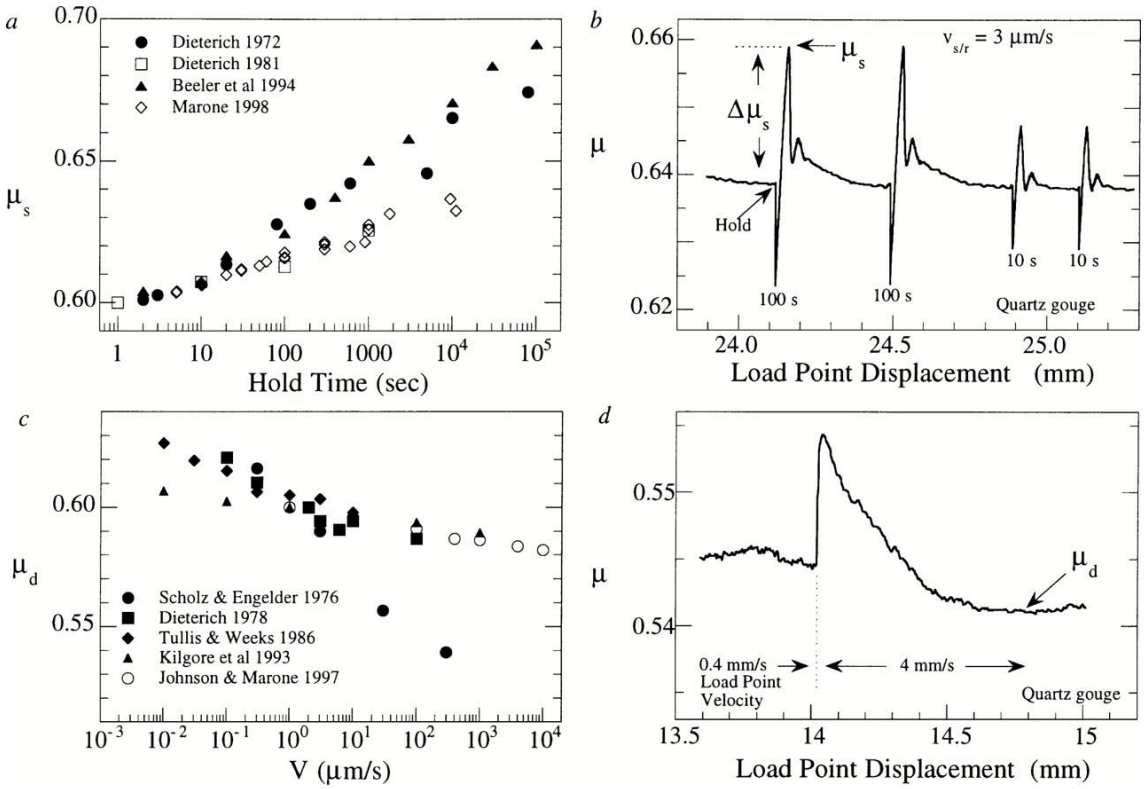

Figure 8: *(a) Measurements of the relative variation in the static coefficient of friction (μ_s) with hold time for initially bare rock surfaces (solid symbols) and granular fault gouge (open symbols). (b) Friction data versus displacement, showing measurements of the static coefficient of friction and the change in static friction in slide-hold-slide experiments. Hold times indicated in seconds, loading velocity before and after holding is 3 µm/s. (c) The relative dynamic coefficient of friction (μ_d) is shown versus slip velocity, same symbols as (a). (d) Data showing the transient and steady-state effect on friction of a change in loading velocity for a 3-mm–thick layer of quartz gouge sheared under nominally dry conditions at 25-MPa normal stress. From Marone, 1998b.*

Post-seismic slip therefore occurs as part of the velocity-weakening behaviour seen in relation to unstable, stick-slip faults evolving towards regaining a steady-state value.

The mechanisms involved in post-seismic deformation linked to tectonic activity can vary, such as afterslip (e.g. Freed et al., 2007a), a combination of afterslip and pore fluid flow (poroelastic rebound, e.g. Peltzer et al., 1998), or upper mantle flow (viscoelastic response, e.g. Pollitz et al., 2001). In the near-field afterslip dominates the response beneath the earthquake rupture and at shallow depths together with poroelastic rebound. Bulk viscoelastic relaxation tends to dominate deformation over longer timescales and distances from the fault zone (Scholz, 2019). It is often difficult to distinguish clearly between the different relaxation mechanisms (ibid). As an example, in relation to the M_w 7.9 Denali, Alaska earthquake (2002) all three mechanisms were observed, with initial near field deformation dominated by afterslip on a deep shear zone and poroelastic relaxation, but with far field deformation resulting from mantle relaxation (Freed et al., 2006). In this study, afterslip is the most relevant process to near-fault deformation over a limited time period.

1.6.2.1 Afterslip

Afterslip is post-seismic relaxation by means of sliding on the fault beyond the extent of the co-seismic rupture. The form of afterslip depends upon the nature of the fault's seismic coupling configuration (Scholz, 2019).

Models of afterslip (e.g. Marone et al., 1991), assume interaction of a velocity-weakening region at depth with a velocity-strengthening region nearer the surface during the earthquake as the earthquake propagates upwards. Post-earthquake the stress perturbation is relaxed, leading to afterslip as the stress perturbation decays. Decay is derived from a friction constitutive law which uses an approximation based upon thickness-averaged displacements and slip velocities within the upper region, applying a thickness-averaged stiffness of that region. The stiffness of the upper region is assumed to be inversely proportional to the thickness of the region. The models expect proportionately more afterslip for earthquakes where co-seismic surface slip is small compared to co-seismic slip at depth. In Marone et al., 1991, the equation proposed is:

$$U_p = (A-B)/k \ln[(kV_{CS}^s/(A-B))t+1)] + V_o\, t$$

$$(or\ U_p = \alpha\, ln[(\beta/\alpha)t+1]\ where\ \alpha = (A-B)/k\ and\ \beta = V_{CS}^s)$$

where U_p is post-seismic slip, $A-B$ is the friction rate parameter, k is the stiffness, V_{CS}^s is the thickness-averaged co-seismic slip velocity within the upper, velocity-strengthening region, V_o is long-term creep rate (or pre-seismic slip rate), and t is time after mainshock.

In a rate-strengthening area this equation can be simplified to:

$$U_t \approx \alpha \ln[(ct)+1]$$

$$c = (\beta V_i)/\alpha$$

where U_t is afterslip at time t, α = characteristic length scale over which the elastic stress changes by order of the frictional stress, and (βV_i) = the initial rate at the beginning of the post-seismic period, with β a scaling vector by which the sliding rate evolves in response to stress, and V_i the pre-seismic slip rate (as reformulated in Zhou et al., 2018).

1.6.2.2 Poroelastic relaxation

Poroelastic relaxation mechanisms driven by fluid flow tend to operate within the high-porosity fault zone. The material in that zone is likely to undergo either compression or extension during the earthquake, which is then followed by recovery: e.g. if the earthquake produces local dilatancy, that is then followed by dilatancy recovery, as in the 2003 M_w 6.6 Bam earthquake (Fielding et al., 2009). However, poroelastic recovery may also occur in the far field (cases reviewed in Muir-Wood and King, 1993), particularly in the case of normal faulting (ibid).

1.6.2.3 Bulk viscoelastic response

Viscoelastic response involves a bulk relaxation of the lower crust and/or upper mantle, such as observed in broad flow of the upper mantle beneath a strong lower crust in connection with the Hector Mine earthquake (Freed et al., 2007b) and in connection with the Norcia earthquake (Mandler et al., 2021).

1.6.2.4 Magnitude of tectonic-related post-seismic deformation

A typical rate of tectonic-related post--seismic deformation after a medium-sized earthquake is in the order of a few millimetres per year. Rates of up to ~ 6 mm p.a. long term viscoelastic relaxation and afterslip were found following the M_w 6.5 1997 Norcia earthquake (Riva et al., 2007). Although the central Apennines is known to be an area of heterogeneous crust thicknesses, with the brittle-ductile transition deepening from west to east (e.g. Di Stefano et al., 2009) similar rates should be expected nearby. Continuing deformation in the near-fault region after a medium- to large-sized earthquake might, in unusual cases, exceed the co-seismic deformation (Freed et al., 2007a). However, the more normal position is that the post-seismic deformation is orders of magnitude smaller than the co-seismic deformation (e.g. Freed et al., 2006). In general, longer term post-seismic velocity patterns consistently show velocity as inversely proportional to the time since an earthquake (Ingelby and Wright, 2017) although signals from fault zone processes in near-field sites are likely initially to dominate (ibid).

The use of remote sensing methods such as InSAR, aerial photography or GPS has enabled scientists to investigate continuing time-dependent decaying post-seismic slip over periods of over 20 years (e.g. Copley et al., 2014, Zhou et al., 2016, Zhou et al., 2018). However, time periods vary considerably – afterslip has been found to decay to zero after less than 10 years (Segall et al., 2000, Wimpenny et al., 2017). Long term studies of post-seismic viscoelastic relaxation in the lower crust and/or upper mantle suggest time periods of between a few months and a few hundred years (see e.g. Wright et al., 2013 reviewing studies up to 2013).

1.6.2.5 Local factors influencing location of tectonic-related post-seismic deformation

At smaller spatial and temporal scales local variations in subsurface lithology over distances of a few kilometres can play important roles in determining post-seismic slip pattern and locations (Floyd et al., 2016). Post-seismic slip in the 60 days following the 2009 L'Aquila earthquake was probably concentrated in specific areas due to afterslip controlled by high gradients in co-seismic slip leading to increased shear stress (and possibly where fluid diffusion played an important part in the first few hours after the earthquake) (Cheloni et al., 2010). Afterslip otherwise broadly consistent with models

may result in variations due to locally high gradients in co-seismic slip (Wilkinson et al., 2012), but also vary between hanging wall and footwall due to the development of a syncline and/or changes in the competency of the hanging wall rock due to the earthquake (Wilkinson et al., 2010). The afterslip seen in the Arquata del Tronto area in the 10 weeks after the Norcia earthquake may have been due to heterogeneities of pore fluid pressure, perhaps facilitated by structural complexity (Pousse-Beltran et al., 2020, using InSAR time series). Afterslip may also be accommodated through post-seismic relaxation up to 90 km from the epicentral area (Mandler et al., 2021, relating to the CIES).

1.6.3 Post-seismic effects of erosion and gravity

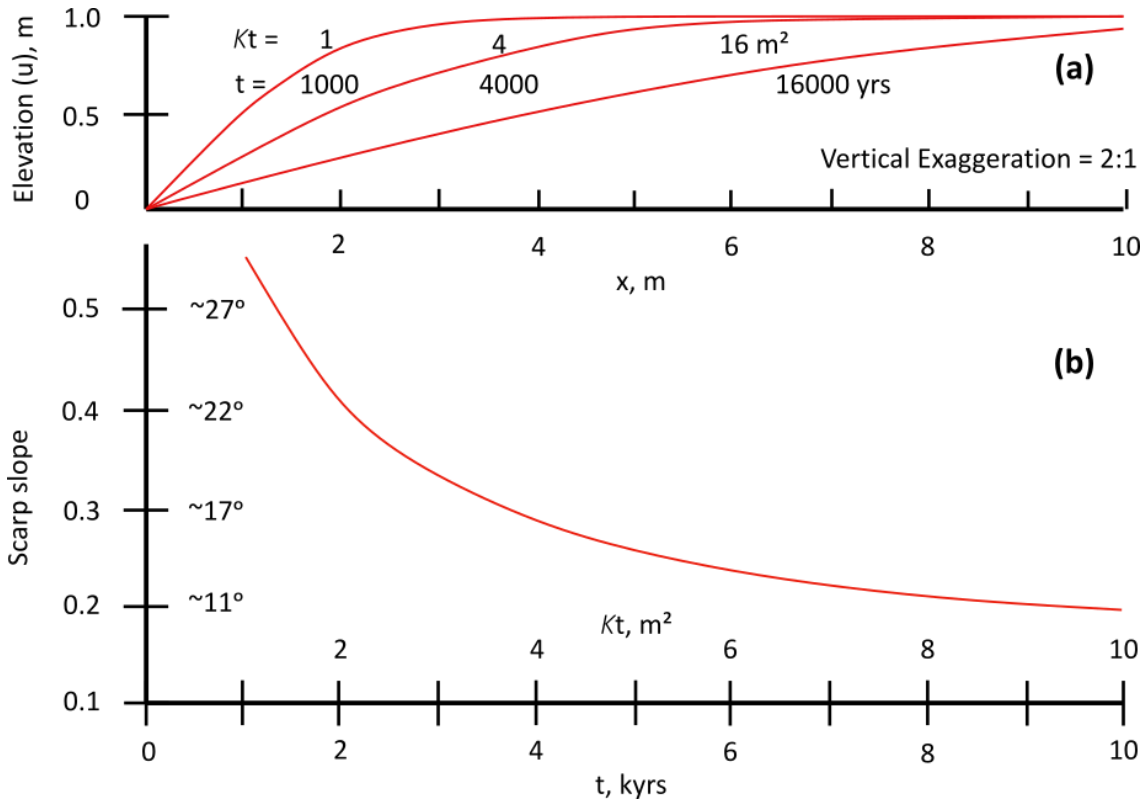

Figure 9: *Adapted from Hanks et al. 1984 - (a) Evolution of a 2m-high scarp in the spatial dimension x at several times after initial vertical offset (b) Evolution of the scarp slope by decay from 1 to 10 kyr. κ = constant of proportionality/mass density, or diffusivity, in this example κ = 1 m^2/kyr.*

It is known that degradation of the fault scarp due to weathering and erosion will begin immediately following its formation (Wallace, 1977). Gravitational erosional processes are expected initially to dominate when the scarp slope angle is at its steepest (Hanks et al., 1984). In simplified form using a basic diffusion equation, this is shown in **Figure 9**.

After time, the angle of the slope declines (Bucknam and Anderson, 1979), and water erosion becomes the dominant erosional process (ibid). In practice, a simplified model along these lines is unlikely to deal with the complexities caused by the many variations in local conditions which can affect the diffusion of material. For example, gravitational erosion will be greater in areas of steep topography (e.g. Kokkalas and Koukouvelas, 2005). Multiscarps or composite scarps from repeated events will also complicate the geomorphology (e.g. Hodge et al., 2020).

More extreme weather conditions in areas of elevated topography (such as freeze-thaw) can be expected to contribute to the erosional degradation (Wallace, 1977). Failure of the scarp by gravitational slumping will significantly alter the profile, and lead to talus formation (Pierce and Colman, 1986). The degree of vegetation may also be relevant (north-facing slopes may be more vegetated than south-facing slopes, and therefore less degraded by erosion) (ibid). Competent lithologies are expected to be comparatively resilient to both weathering and gravitational erosion (Bucknam and Anderson, 1979, and Wallace, 1980). The effect of erosional processes is likely to vary along strike due to differences in topography (e.g. due to the presence of gullies, Bubeck et al., 2015). Erosion of the footwall will provide colluvial debris which accumulates on the hanging wall, and in some cases can become cemented due to meteoric fluid flow (e.g. Mason et al., 2017).

1.7 Contents of this thesis

I have set out above the geological background to the study area, and the general considerations which apply in post-seismic landform evolution. In the following chapters, I will:

- provide an overview of the types of data involved, and the techniques commonly used to derive deformation from repeated data captures at different times using differencing techniques (Chapter 2);
- present the results of a joint inversion in respect of the Norcia earthquake using differencing results from high-resolution Pleiades optical satellite data to complement existing datasets (Chapter 3). I also present a workflow for processing optical satellite data which successfully removes noise and artefacts from the data. The addition of such detail to the inversion enables the model to characterise detail of co-seismic near-surface distributed deformation not previously available, giving insights into how reliable the fault scarps were as co-seismic evidence of the earthquake;
- investigate the post-seismic evolution of a fault scarp using one particular case study from the Norcia earthquake (Meterff) (Chapter 4) to analyse the processes which have resulted in continuing deformation over time, and how those relate to co-seismic slip distribution. In this particular case, post-seismic processes appear limited in time, and primarily relate initially to afterslip rather than erosion. They also reveal the possible presence of a second structure adjacent to the main fault scarp which did not rupture co-seismically, but which has subsequently seen displacement;
- use a comparative study of the evolution of several fault scarps to identify the particular characteristics of those sites which lead to differences in their evolution over time after the Norcia earthquake (Chapter 5). Those characteristics include topography, underlying geology, and the size, distribution and nature of co-seismic slip. The results show that afterslip had largely ceased at all the sites within a 3 year period, and the effects of the earthquake on erosion have been largely limited to the immediate vicinity of the fault scarps. Erosion due to factors not related to tectonics now dominates the continuing degradation of the scarps; and
- conclude by summarising how co-seismic and post-seismic processes interrelate, how those processes combine to show the variable unreliability of fault scarps as evidence of previous seismic activity, and what lessons can be

learned from this study in assessing the extent and nature of degradation of fault scarps over time (Chapter 6).

1.8 Disruption due to Covid-19

The SARS-CoV-2 (Covid-19) virus pandemic during 2020 and 2021 caused widespread disruption to society, and to academic life. Working from home was encouraged by the University of Durham on 12th March 2020, even before the UK Government restrictions were imposed later that month. Initial phased relaxation of rules was followed by further lockdowns during 2020 and 2021 severely restricting overseas travel during much of this period, making planning of fieldwork outside the United Kingdom especially difficult. This has impacted my preparation of this thesis primarily in two ways:

1. The initial plan for fieldwork supporting this thesis included a return to sites in Italy to undertake further repeat TLS in Spring/Summer 2021, which would have enabled me to have included data covering a longer study period for post-seismic deformation effects. I concluded with my supervisors in early 2021 that it was not going to be practical to accomplish that work in the light of constantly changing travel restrictions in both the United Kingdom and Italy and the need to factor in advance customs clearance for scanning equipment, after the United Kingdom's departure from the European Union;
2. Various difficulties were encountered in establishing a home working environment which would successfully replicate the set-up at the University of Durham, allowing me to use a number of licensed software programmes. Initial problems with establishing reliable remote working also proved time-consuming to resolve. Although ultimately overcome, those problems led to what was effectively a time delay of several months, which was balanced by a welcome extension of 3 months in my completion date and funding for that period.

CHAPTER 2. Methodology

In this chapter, I provide an overview of the theory and methodology of how 3D displacements can be extracted from point cloud data, by creating multiple digital terrain models ("DTMs") at differing points in time, then differencing those DTMs to derive deformation between those time points. In particular, I describe techniques to derive DTMs from (a) optical satellite data, and (b) terrestrial laser scans, and how to difference those multiple DTMs.

2.1 Source and format of data

2.1.1 Optical satellite data.

2.1.1.1 Advantages of stereo and tri-stereo images

Optical satellites provide a way of taking very high-resolution images of the same object from multiple locations in a fixed trajectory at the same height above sea level, with known angles of sight. Unlike satellite systems which actively illuminate the Earth's surface with electro-magnetic waves (e.g. InSAR), optical satellite systems passively record energy from the sun that is reflected off the Earth's surface.

3D imaging from stereo satellite images involves taking optical images of an object from two or more different angles to derive 3-dimensional structure which is not possible from a single image. The stereo images are combined into a single digital elevation model ("DEM"), which shows height above sea level as well as latitude and longitude.

As illustrated in simplified form by **Figure 10** (assuming a spherical earth), the use of two or more images allows calculation of a height above sea level (h) for any one point on the Earth's surface (A). This is done by relatively simple geometry using the known height above sea level of the satellite when the respective images are taken (H1 and H2), the distance between the satellite locations (L), and the angles from which the images are taken relative to the ground (θ1 and θ2 respectively).

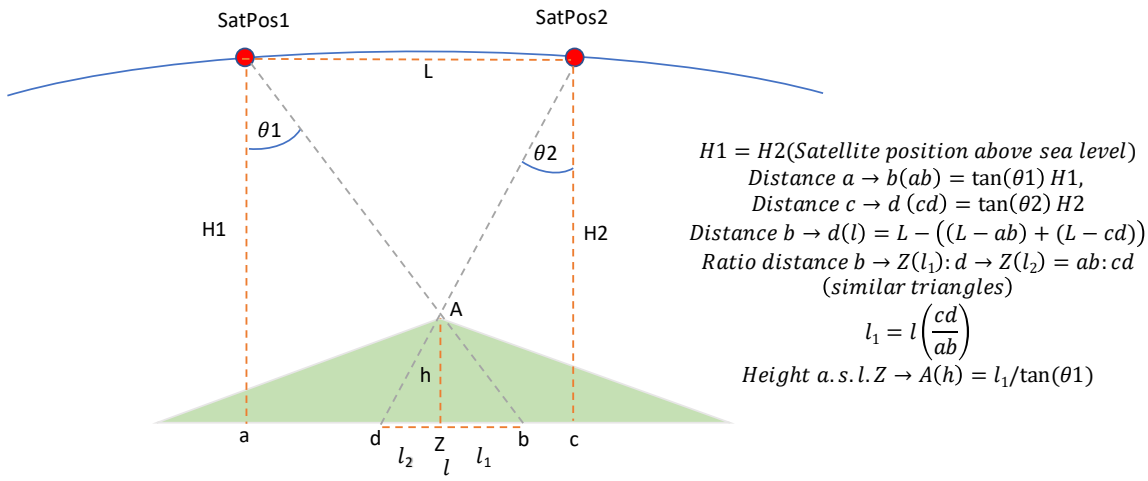

Figure 10: *Calculating height above sea level from 2 satellite images, calculating the height (h) of a point A using stereo images taken from two satellite positions (SatPos1 and SatPos2) at a known height above sea level (H1/H2), at a known distance from each other (L), and taken at known angles to the vertical (θ1 and θ2 respectively).*

The first optical satellite capable of providing stereo images, SPOT-1, was launched by the French CNES in 1986, with a panchromatic sampling distance of 10 m (Elliott et al., 2016), with subsequent SPOT satellites in the series achieving higher resolution (1.5 m, SPOT 6/7). The IKONOS commercial satellite system was the first to achieve a resolution of less than 1 m (defined as "very high resolution") in 1999 (NASA Space Science Data Coordinated Archive, 2021). KOMPSAT-3 is capable of 70 cm resolution (ESA eoPortal Directory, 2021). Currently, military satellites are understood to be capable of at least 10 cm resolution (following a tweet of an image released by President Trump – e.g. O'Callaghan, 2019). Commercially available data is generally restricted by national satellite licensing regimes to resolutions in excess of ~30 cm. The imagery and data used in this study is from the first generation of Pleiades satellites, 1A and 1B, with a resolution of 50 cm. The first generation Pleiades satellites are in the process of being supplemented by 4 more advanced Pleiades Neo satellites with a resolution of 30 cm (Pleiades Neo 3-6).

However, in areas of rough or steep topography, or where the area is itself in shadow, the use of only two images (typically a pair of images respectively taken forward-looking and backward-looking relative to the satellite's flight path) may lead to areas

where part of the target area is not covered by either image. The advantages of tri-stereo satellite images in such regions are illustrated in **Figure 11** (from www.satimagingcorp.com). In this set-up, the three images are respectively one forward-looking, one backward-looking and a third near-nadir image. Areas which would otherwise not be seen with only two images are reduced by having a third image, in the illustration providing coverage of the valley between two peaks which would otherwise be partly obscured.

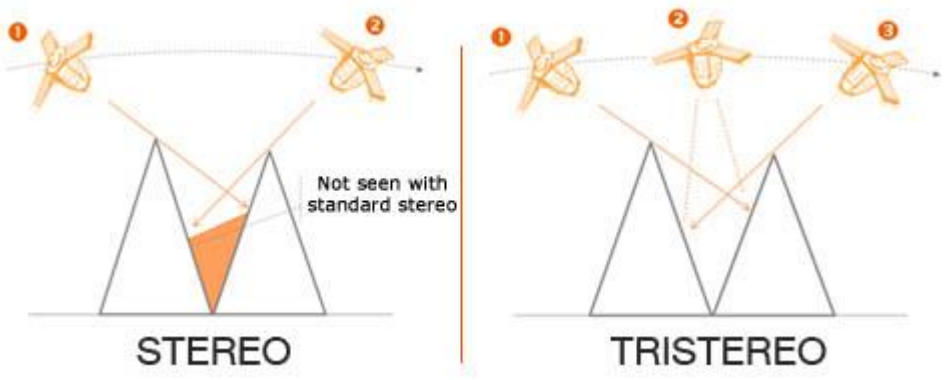

Figure 11: *From Satellite Imaging Corporation, www.satimagingcorp.com website, adapted from Pleiades Imagery User Guide, 2012, advantages of tri-stereo imagery in areas of steep topography.*

The extent of improvements in data coverage from the use of tri-stereo images compared to stereo images is illustrated in **Figure 12** (from Zhou et al., 2015), with the tri-stereo result significantly bettering any combination of stereo images in point density per m^2.

Tri-stereo images have proved suitable for measuring a variety of 3D displacements, such as changes in glacier height (Bertier et al., 2014), co-seismic offsets along faults (Zhou et al., 2015), and lava flow volume estimates (Bagnardi et al., 2016). In the last of these examples, the authors found that by merging the datasets (forward-near-nadir pair, backward-near-nadir pair, forward-backward pair, and tri-stereo triplet), the data density achieved was ~6.5 times greater than the classic forward-backward stereo pair. Although varying in density according to the terrain, this significantly reduced the number of 1 m^2 pixels with no data coverage.

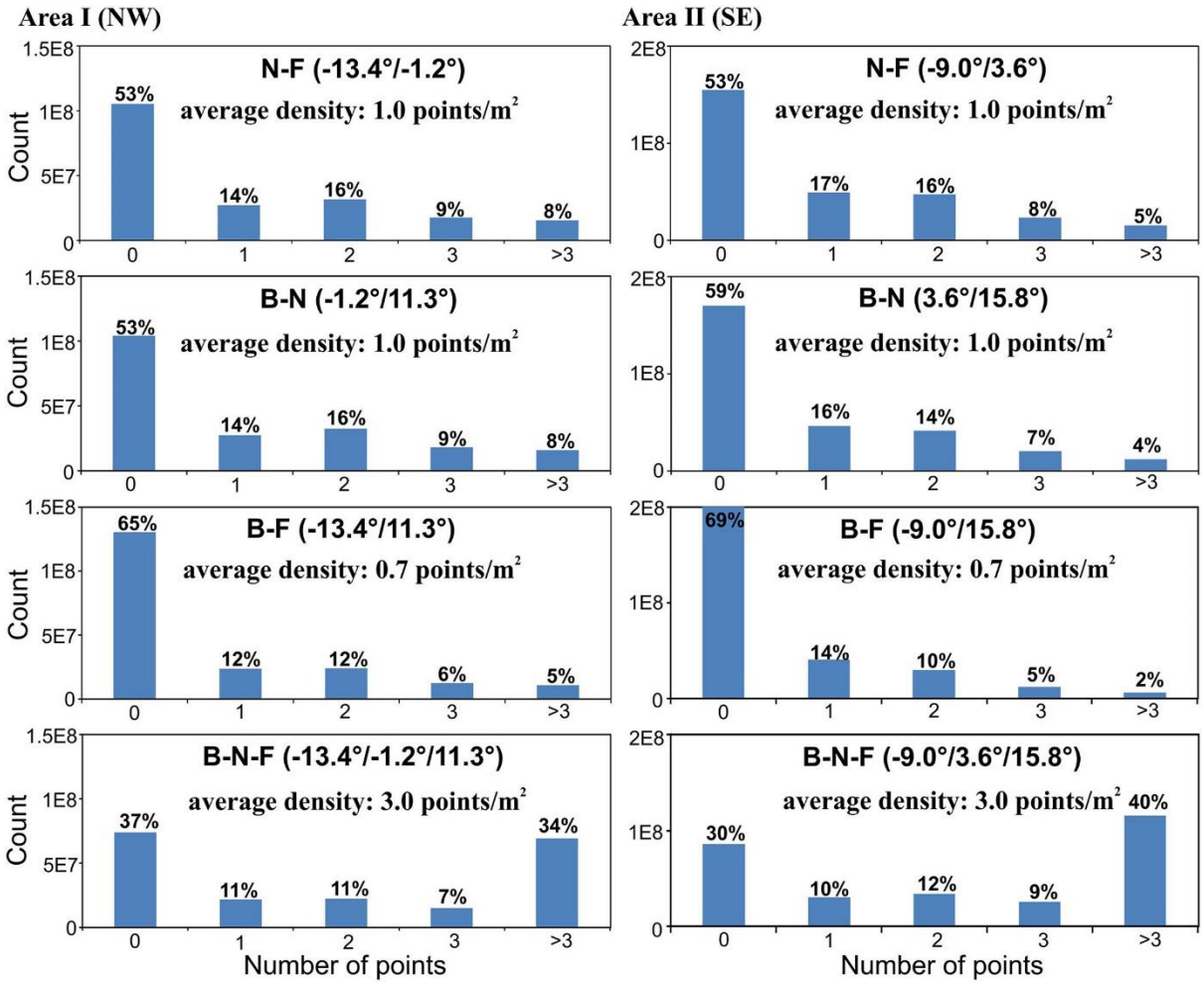

Figure 12: *Statistics of the number of points within a grid cell for a grid spacing of 1m for Nadir-Forward (N-F), Backward-Nadir (B-N), Backward-Forward (B-F), and Backward-Nadir-Forward (B-N-F) combinations for two tri-stereo Pleiades datasets. The B-N-F data provide significant data density. From Zhou et al., 2015.*

Since the 1980's, many satellites with stereo capabilities have been launched, some with very high resolution, but to date relatively few are capable of producing near-simultaneous tri-stereo images. Examples of freely available data derived from stereo pairs are ASTER GDEM, which now covers 99 per cent of the Earth's landmass (Nasa Earthdata, 2019), and SPOT 6/7 which allow daily revisits and a daily acquisition capacity of 3 million km^2 per satellite (ESA eoPortal Directory, 2021b). The satellites which have tri-stereo capability are, in general, commercial satellites, and the data from those satellites are not normally readily freely available. Examples of tri-stereo

systems are WorldView-3 (0.31 m resolution) and the Pleiades constellation (0.5 m resolution).

When originally launched in December 2011 and December 2012 respectively the Pleiades 1A and 1B satellites formed the first system of its kind capable of acquiring three or more near-synchronous images of an area with a stereo angle of between ~6° and ~28° (Gleyzes et al., 2012). The Pleiades 1A and IB optical satellites provide images with a ground sampling distance of 50 cm for the panchromatic band (and 2 m multispectral), covering a swath width of 20 km at nadir. The satellites are in sun synchronous phased orbits (at 180° phasing) with an inclination of 98.2° (ESA eoPortal Directory, 2021a). Those satellites are in the process of being supplemented by 4 more advanced Pleiades Neo satellites providing panchromatic images with a resolution of 30 cm covering a swath width of 14 km, with a twice-daily revisit. Pleiades Neo 3 and 4 were launched in 2021, and Pleiades Neo 5 and 6 are scheduled for launch in 2022 (ESA eoPortal Directory, 2021c).

2.1.1.2 Orthorectification of optical satellite images

The multiple view geometry tri-stereo data sets from the Pleiades constellation are provided in a sensor model as a rational polynomial coefficient (RPC) model, which describes the relationship between each image's (x,y) coordinate system and the ground (X,Y,Z) coordinates. The geolocation accuracy of that model is reported to be in the region of 8.5 m CE 90 (the 90th percentile of circular error distribution) (Pleiades User Guide, 2012). The geolocation accuracy of each image therefore needs refining (or optimising) using the RPCs. This initial step needs to be done using Ground Control Points (GCPs) (or tie points) and the image coordinates, typically using least squares adjustment. Those adjusted images and sensor models are used to generate an intermediate DSM (Digital Surface Model) for each stereo pair of images. Those intermediate DSMs are then fused and post-processed to produce a final DSM. The process of deriving a DEM (Digital Elevation Model) (or DTM, Digital Terrain Model) from the DSM involves ground point filtering to interpolate non-ground information and post-processing removal of outliers, with the aim of removing man-made structures and vegetation to achieve a "bare earth" result. This processing is typically done using proprietary software such as the ERDAS IMAGINE Photogrammetry toolbox

or Orthoengine which apply an algorithm to extract point clouds for each image pair, for the tri-stereo triplet, and from the merging of the four data sets. The final orthorectified image can then be filtered using a median filter, and gridded to a set resolution using a continuous curvature spline (e.g. Bagnardi et al., 2016, Zhou et al., 2015). **Figure 13** is an outline proposed model workflow for the extended process (without specific use of proprietary software).

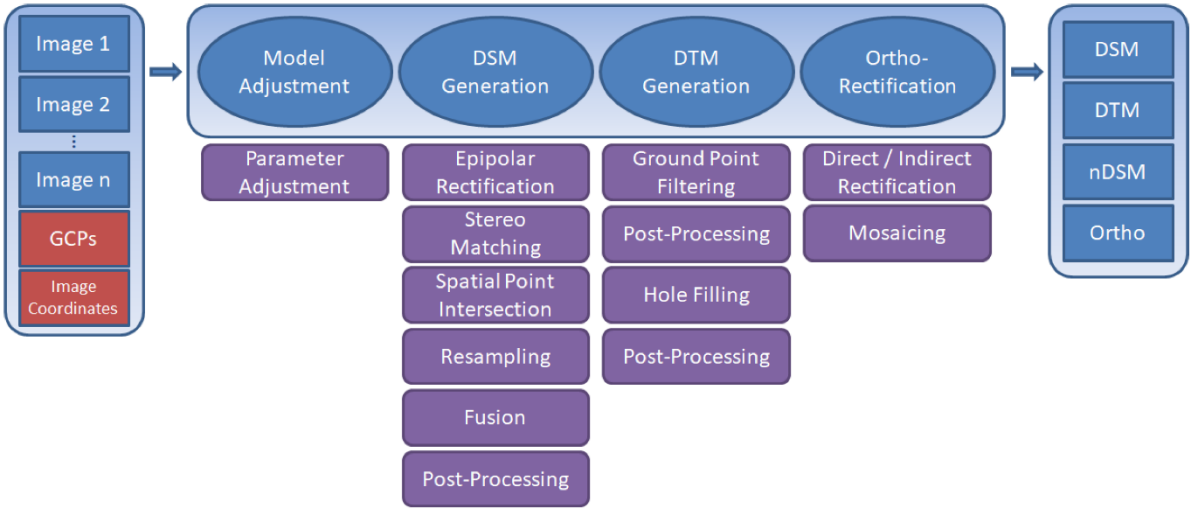

Figure 13: *From Perko et al. (2019), their proposed end-to-end mapping workflow for multi-view stereo Pleiades images. DSM = Digital Surface Model, DTM = Digital Terrain Model, nDSM = normalised Digital Surface Model, GCPs = Ground Control Points.*

2.1.1.3 Coverage limitations of optical satellite images

Pleiades tri-stereo images have been used successfully to derive sub-metre 3D displacements in DEMs in each of the examples given above. In the case Berthier et al., 2014 the subject was glaciers, Zhou et al., 2015 dealt with the Mayor-Cucapah earthquake in 2010, and Bagnardi et al., 2016 the Fogo Volcano. Pleiades images have also been used for co-seismic deformation in Delorme et al., 2020 (the Norcia earthquake in 2016).

The potential disadvantages of the coverage provided by optical satellite data, particularly compared to radar satellite images, concern its limitations in areas of cloud cover or where there is poor visibility or atmospheric interference, possible distortions due to the nature of ground cover (such as extensive vegetation where there is little

reflected light), and areas with relatively featureless regions, perhaps with granular deposits (Bagnardi et al., 2016).

It is expected, however, that the results from optical satellite data should provide clearer and more complete data coverage in near-fault regions than InSAR. InSAR techniques which involve ascertaining phase differences between repeat images using interferometry typically find it hard to capture detail in those areas. The deformation gradients close to surface ruptures of medium or large scale earthquakes, where there may be > 10s of cm of vertical deformation in a comparable horizontal distance, lead to steep fringe patterns which are difficult to unwrap.

Using optical satellite images enables the capture of fine detail away from the fault scarp itself which should significantly widen the extent of coverage available compared to data from field mapping and from individual GNSS sources. In the case of field data those are inherently limited by mapping ground features visible to the eye (such as the surface rupture itself). In the case of GNSS the results are limited by the position of the individual locations chosen.

2.1.2 Terrestrial Laser Scanning (TLS).

LiDAR (light detection and ranging) is an active remote sensing method, using laser scanners to collect large 3-D point clouds over areas that in terrestrial mode cover typically tens to many hundreds of metres in width. LiDAR has been used extensively to investigate outcrops since the early 2000's (e.g. McCaffrey et al., 2004, Buckley et al., 2008). A typical high-resolution scan of an outcrop area of ~5,000 m^2 may contain upwards of 20 million data points (> 4,000 points per square metre). The electro-magnetic waves used are confined to the near-infrared to ultraviolet spectrum. They do not travel through solid objects, so the scanner needs to have a clear sight of the object being scanned, which may involve using multiple scan positions.

The main methods of using LiDAR for geological purposes involve either airborne laser scanning (ALS) (taken with scanners mounted on aircraft or unmanned airborne vehicles (UAVs, or "drones")), or terrestrial laser scanning (TLS) with scanners mounted either statically on tripods, or on moving vehicles. In practice, although ALS can be used to scan outcrops it is a very expensive application and TLS is more commonly

used. The choice of which method to use will depend upon how fine a resolution is required for the scan (or how dense the point cloud needs to be to identify clearly the features which are being investigated). That will in turn depend upon the size of the area to be surveyed and the scale of the features being investigated (e.g Perroy et al., 2010, Haddad et al., 2012). In general, with a smaller area where finer resolution is required (such as identifying co-seismic movement at centimetre to millimetre scale) the choice will be of a static terrestrial scanner, or possibly a combination of that and a mobile method of scanning if wider context is needed (such as meter-scale topographical features) (Haddad et al., 2012). Other factors determining the choice might include topography where TLS's side-looking orientation may not be suitable, such as where there are deeply incised gullies (e.g. Perroy et al., 2010), although those issues may be mitigated by using multiple view angles (ibid).

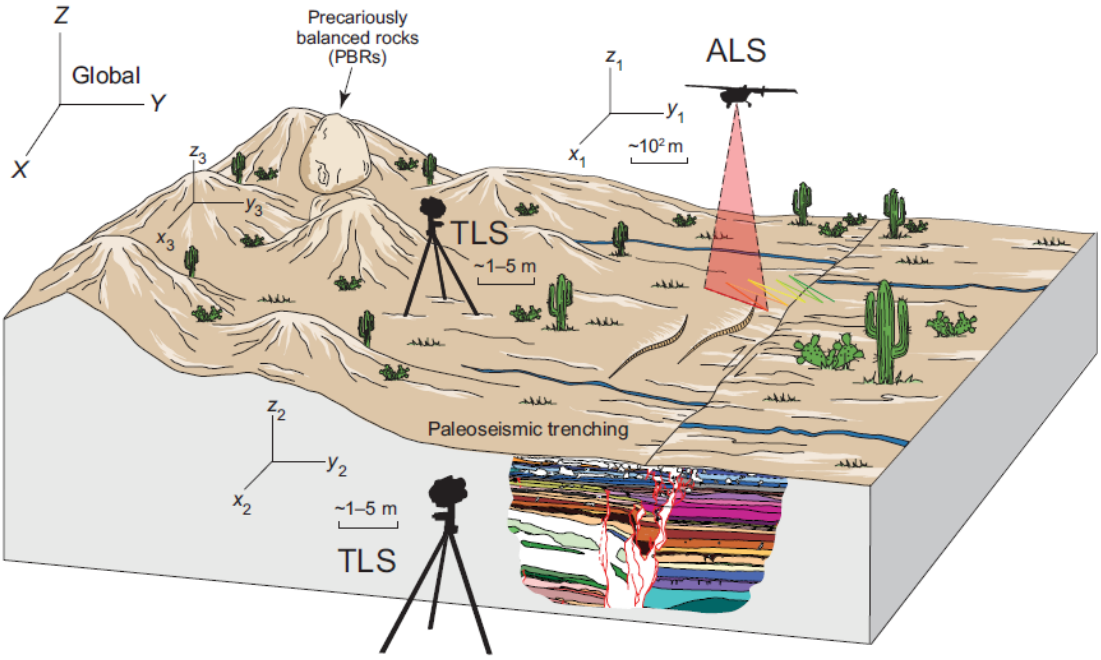

Figure 14: *Illustration of lidar platforms as used in palaeoseismology, from Haddad et al., 2012, ALS = airborne terrestrial laser scanning, TLS = terrestrial laser scanning.*

In either case (ALS or TLS) the scan will provide detailed extended coverage of areas, compared to the selective datapoints involved in either traditional fieldwork, surveying (e.g. levelling on transects) or GNSS stations. The density of the point cloud will vary according to the angle and distance from the scanner to the target area. **Figure 14**

illustrates the respective uses of ALS and TLS in the context of palaeoseismic research (trenching) (from Haddad et al., 2012). The point cloud data are acquired in their local coordinate system (e.g. in **Figure 14** x_2, y_2, z_2, for TLS), which is then transformed to a global coordinate system (X, Y, Z), to georeference the local scan. For TLS this is typically done by placing three or four reflective targets with known geographic coordinates (acquired using survey-grade GNSS units) around the feature being scanned, and using those positions to align the point cloud within a global reference frame.

Figure 15 is an example of a terrestrial laser scanning site from Italy, showing one of the three reflectors used in that case.

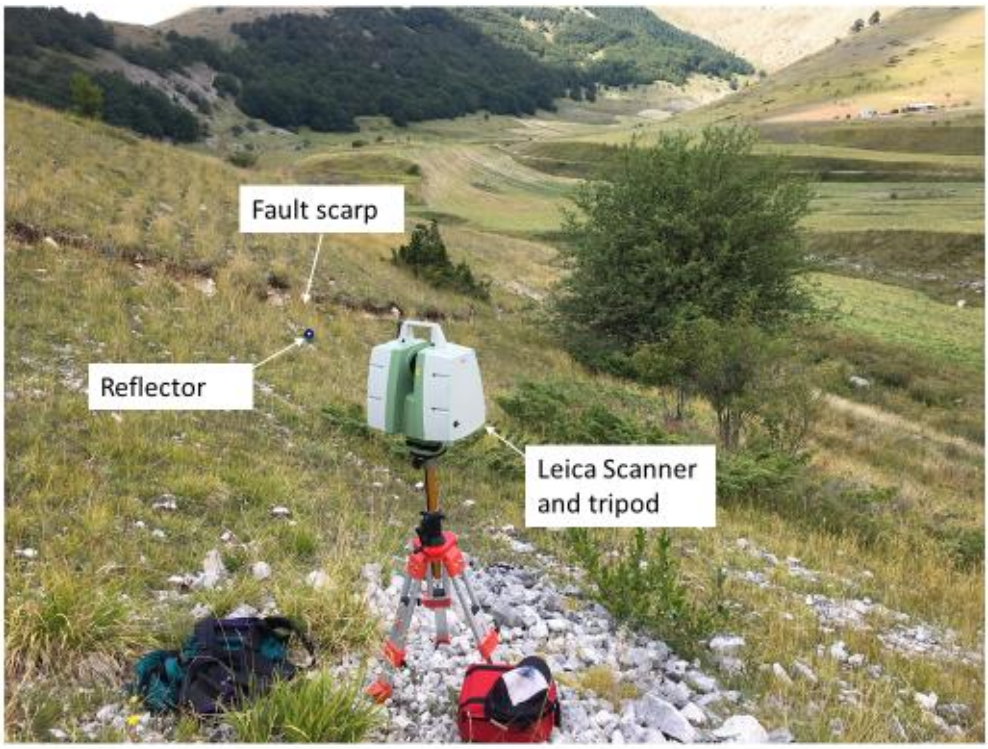

Figure 15: *Field example of terrestrial laser scanning site, from Central Italy, 2019. Reflectors are used to tie multiple scans together and their GPS locations enable georeferencing to global coordinate systems.*

Manual cleaning of point clouds is normally required to remove points which are clearly erroneous (such as dust specks which are picked up by fine resolution scans).

With any TLS scan, downsampling of the point cloud may be required to reduce the size of the cloud to more manageable levels on the basis of a spatial parameter, creating a new subsampled cloud as a subset of the original where points within the subset are no closer to another point than a specified distance (Buckley et al., 2008, Jones et al., 2009).

In cases of multiple scans of the same area taken on the same occasion at differing resolutions or from different viewpoints (to improve coverage of areas which might be less visible to the scanner from particular viewpoints), co-registration of the scans using tie points (usually the common reflector positions) results in a composite point cloud.

2.2 The use of two or more DEMs to characterise 3D deformation over a period of time by differencing

In order to derive 3D deformation using point clouds from different points in time there are essentially two main steps, whether the scale is over many km^2 or limited to tens of metres. The first step is to correlate the point clouds in 3D space relative to each other. The second is to recover accurately the 3D displacement between those point clouds over time avoiding any biases inherent within the data.

2.2.1 Outline of differencing methods using multiple DEMs

There are three main possible approaches to deriving differences between two images of the same area taken at different points in time. Each method assumes an initial step of bulk alignment of the images due to global referencing differences on the assumption that large areas of the data have not moved between the images.

The first differencing method is vertical differencing with an assumption of no horizontal movement of the images, where the vertical coordinates of pixels in one image are deducted from the vertical coordinates of pixels at the same horizontal location (e.g. Oskin et al., 2012). This could be termed a “1D” approach and, as is explained further at paragraph **2.2.3** below, is likely to lead to significant biases due to the effect of horizontal movement in all but the most straightforward of cases. It precludes recovering the horizontal displacement field, and is restricted to recovering the vertical displacement field.

A second, "2.5D" approach, involves an initial correlation to solve for 2D (east-west and north-south) deformation in sliding windows. The correlation results are then applied to one of the images, removing the distortion, before the vertical coordinates are deducted from each other (e.g. LePrince et al., 2008 and LePrince et al., 2011).

The third, "3D" approach, involves the use of an iterative closest point ("ICP") algorithm, to characterise the east-west, north-south and vertical constituent parts of deformation between point clouds. This involves picking the closest point in a target cloud to a post-event cloud, calculating the rotation and transformation required to move the post-event cloud towards the target cloud by minimising the sum of the squared differences, then repeating the exercise over a set number of iterations (e.g. Bouaziz et al., 2013, Chen and Medioni, 1992, Nissen et al., 2017).

Each of these methods is considered in more detail below.

2.2.2 Initial global referencing

2.2.2.1 Initial global referencing – optical satellite data

Before differencing using any of the above methods, it is necessary to consider whether the reported coordinates of images coincide with each other. Even in areas where there has been no apparent movement, the reported locations of pixels may differ between satellite images because of issues with image referencing (primarily related to sensor geometry and topography). The claimed image 2D location accuracy at nadir for Pleiades imagery is 6.5 m (CE90 - Circular (horizontal) error at 90th percentile, October 2017 figure) (Pleiades Imagery User Guide, 2012). By comparing the reported locations of identifiable pixels in the 2D pre- and post-seismic images (such as at the corner of a building), in areas where no significant co-seismic movement is expected, it is possible to estimate the extent to which the coordinates of the images do not coincide. By applying east-west and north-south offsets to the post-seismic image to correct for that effect, the post-seismic image can be translated to the correct horizontal location.

The vertical coordinates of optical satellite data also may not coincide between images (with apparent spurious displacement) and need a further vertical offset to the post-seismic data.

2.2.2.2 Initial global referencing – TLS data

Images and point clouds produced from repeat TLS also face potential problems of correlation at a smaller scale. The scope and scale of repeat scans is derived from field settings, including point cloud density, scanner and reflector positions, which are likely to differ between scans taken on different occasions. The global scanner and reflector positions are themselves derived from GPS (Global Positioning System) units mounted on the reflector locations, which may have a margin of error ranging from centimetre scale up to several metres depending upon the extent of satellite coverage when the scans were obtained and GPS locations noted, and the grade of GPS receiver used (including whether real-time kinematic positioning ("RTK") is used). The accuracy of GPS-derived locations in mountainous areas may often be affected by blockage of signals due to the surrounding topography.

After initial translation of a selected point cloud relative to another one to roughly align the clouds, point picking of 3 or more point pairs from the respective point clouds allows a cloud to be aligned more precisely to the coordinates of a reference cloud by a rigid transformation (producing a combined matrix showing the rotation about 3 axes, X, Y and Z, and a 3D translation vector (e.g. using Open Source CloudCompare software: CloudCompare Online User Guide).

Fine registration of the pair of clouds is then achieved using an ICP (Iterative Closest Point)-based tool (ibid). A "data" cloud (usually the later one) will be registered to the "model" cloud using an ICP algorithm, allowing adjustment according to the degree of overlap between the point clouds. The computation of the distance between finely registered point clouds by default uses a nearest neighbour comparison within the respective octree structures (recursively partitioning a cubical volume of space to a maximum depth of 10). The result is a rigid transformation matrix, combining rotation and translation. The adjustment is ideally calculated by registering an area (or reference patch) which is unlikely to have moved significantly during the period in question in the data cloud (such as the footwall of the fault) to the same area in the "model" cloud, then applying that transformation matrix to the whole post-event image. Fine registration using ICP may not work properly if there are extensive differences between the two point clouds, in which case this final step in alignment

may not be appropriate (ibid). Fine registration will also be difficult to achieve satisfactorily by using the "reference patch" method when there is little terrain which has not been subject to change during the period in question (for example, where gravitational erosion is widespread). In such cases fine registration may need to be by reference to the whole of the respective clouds.

2.2.3 Vertical "1D" differencing without correction for horizontal movement

2.2.3.1 "1D" differencing

The differencing stage of the "1D" process is relatively simple: after any initial bulk alignment, the "before" and "after" point clouds or DEMs are sampled to the same grid (typically using a median filter), giving coordinates for X,Y positions which match between the two clouds (e.g. Oskin et al., 2012). The "before" cloud elevation data is then subtracted from the "after" cloud elevation data, to give a vertical difference between the two. This approach is shown in cartoon form in **Figure 16**.

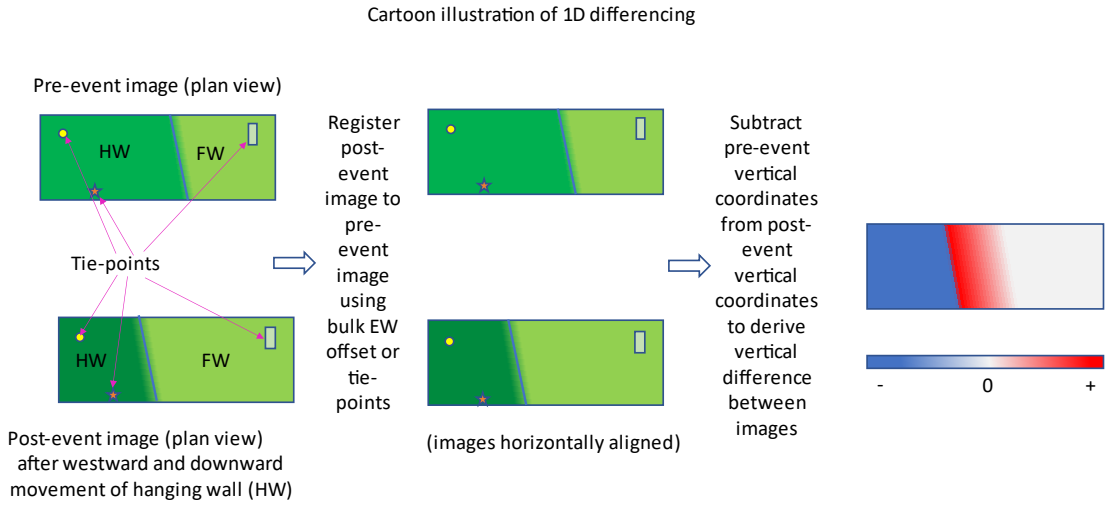

Figure 16: *Cartoon illustration of processing multiple images through "1D" differencing – assumes westward and downward movement of hanging wall during seismic event, correction of post-seismic image to align images horizontally, then subtraction of elevation of pre-seismic image from elevation of post-seismic image.*

2.2.3.2 The distorting effect of horizontal movement

Although the simplest of differencing techniques, 1D differencing by this subtraction of vertical coordinates between 2 point clouds is likely to produce biases or artefacts

when estimating co-seismic deformation. In nature, it is extremely unlikely that any movement associated with seismic deformation will be exclusively two-dimensional. Movement is likely to be a combination of dip-slip and strike-slip. The terrain is very unlikely to be flat.

Images taken from differing time points either side of a seismic event will not align exactly with each other in 2D space where there has been horizontal as well as vertical co-seismic movement.

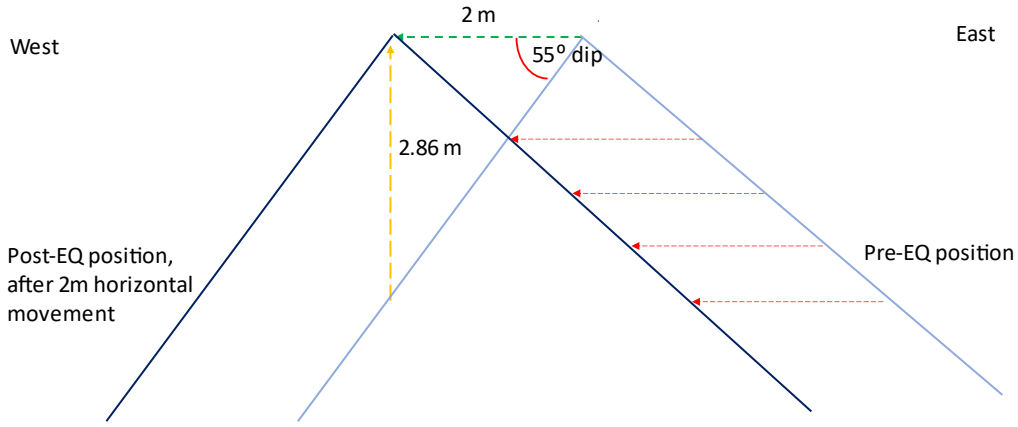

Figure 17: *Cartoon illustration of effect of solely strike-slip horizontal movement in creating apparent vertical movement in an area of steep topography.*

In **Figure 17** it is assumed that there is no actual vertical movement, but only horizontal movement of 2m towards the west perpendicular to the strike of the slopes. The effect of the west-facing slope (at 55° from vertical) is to introduce an apparent (but false) upwards vertical displacement of ~2.86m.

An illustration of this effect for a small area using Pleiades optical satellite data is shown in **Figure 18.** The apparent vertical displacement seen where an east-west purely horizontal movement of 2 m is introduced across an area of differing dips and aspects shows the correlation between the landform geometry, and the extent of the distortion. Where the slope aspect is closest to east-west, and the dip is highest (at ~45°), the apparent vertical movement approaches 2 m. Where the aspect is nearer northwest-southeast and the dip is nearer to 0-10°, very little vertical movement is apparent.

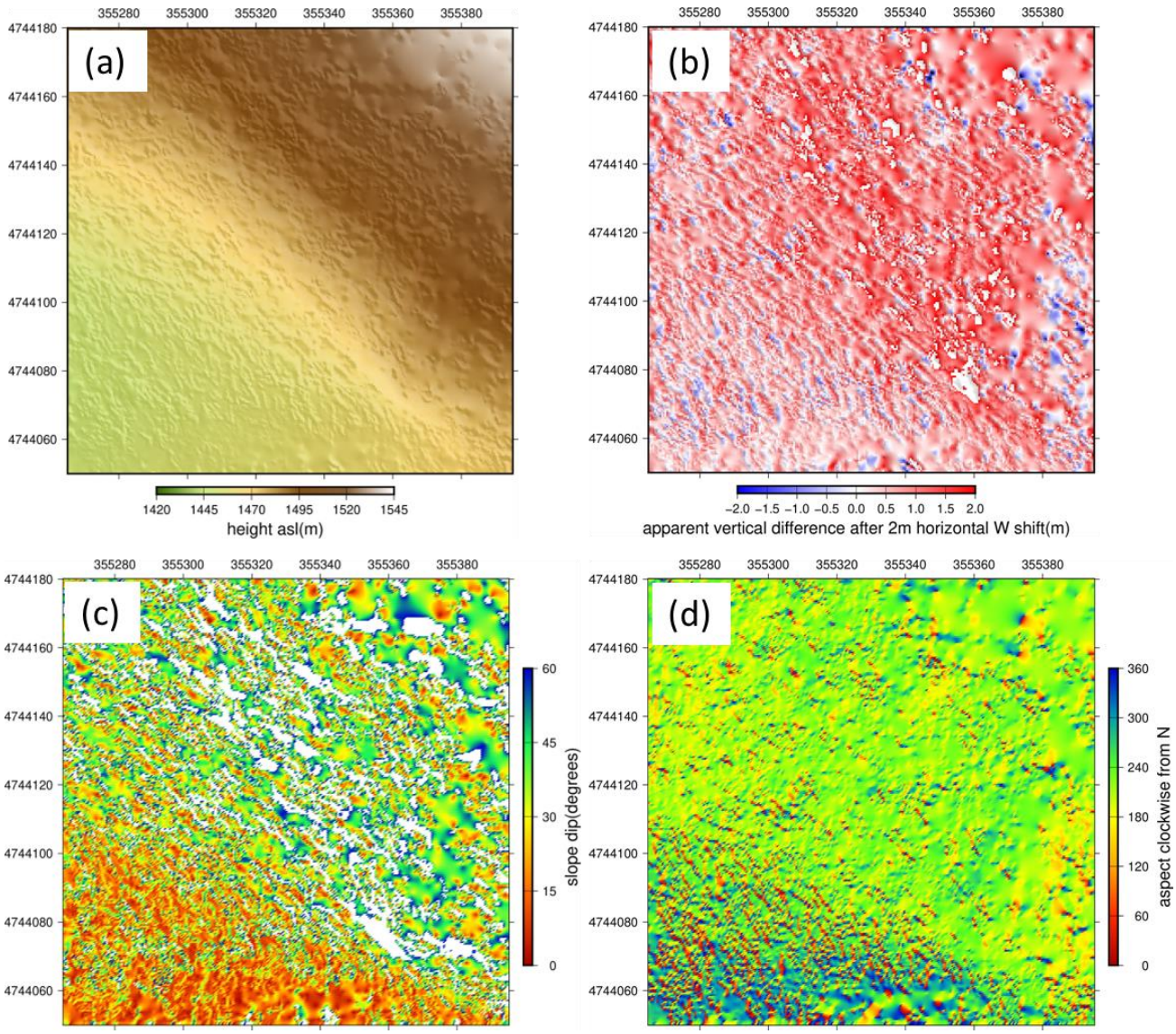

Figure 18: *Illustration of apparent vertical displacement created by horizontal movement. (a) DEM from Pleiades data showing southwest-facing slope, dipping at ~40^{o} to vertical, with relatively flat alluvial channel at base, (b) apparent vertical effect over the same area created by horizontal movement of 2 m towards west, (c) slope dip and (d) slope aspect (0-360 degrees clockwise from north) of the pre-movement DEM.*

In a more typical situation untangling tectonic slip from landform geometry will be more problematic (Mackenzie and Elliott, 2017).

For these reasons, and because it will only produce a “vertical” result, the “1D” approach is very unlikely to be suitable for investigating co-seismic and post-seismic slip associated with a major earthquake, in an area of elevated topography.

2.2.4 "2.5D" differencing after correction for horizontal movement

2.2.4.1 2D Image Correlation – use of correlation tools to derive east-west and north-south vectors of horizontal displacement from Pleiades optical satellite images

As noted above, unless the east-west and north-south components of co-seismic movement are applied to one of the datasets involved the estimated vertical movement is likely to be biased.

After any bulk offset to deal with issues arising from global referencing, deriving the east-west and north-south vectors of horizontal displacement requires the application of a correlation tool. This runs as a two step process. Its aim is to correlate two images by finding the respective east-west and north-south displacements between those images over the elapsed time period (e.g. LePrince et al., 2008 and LePrince et al., 2011). The first step involves a rough estimation of the displacement involved (pixel-wise) before setting the size of an initial sliding window that is then used to calculate a series of pairwise correlation matrices, where the sliding widow is moved by a pre-set step in X and Y directions. Where noisy images are involved, the initial sliding window is typically set to a large size, with a recommended window (in pixels) of at least twice the expected displacement and preferably greater multiples. This gives an estimate for the displacement between the pixels. The second step operates after the initial displacement estimate to retrieve sub-pixel displacement. This second sliding window should be set at the smallest size that still allows for a reasonable amount of noise (in the order of a minimum of 32 x 32 pixels), and operates in the same way to calculate a series of pairwise correlation matrices for windows which are moved in X and Y directions by the same pre-set step.

The result is essentially two maps – an east-west displacement map and a north-south displacement map, in each case showing the extent to which the later image has moved compared to the earlier image.

An example of such a tool (used in this study) is the COSI-Corr correlation sub-pixel tool which is a plug-in to the ENVI software package (ENVI version 5.6 from L3Harris Geospatial) (LePrince et al., 2007 and Ayoub et al., 2008).

2.2.4.2 "2.5D" differencing of Pleiades DEMs/point clouds after use of a correlation tool

The use of a correlation tool returns values for deformation in 2D, with values for east-west and north-south movement between the respective images. By using those values, the coordinates of the post-event cloud can be adjusted to effectively transform the pixel X and Y locations of the post-event dataset into the same pre-event reference frame.

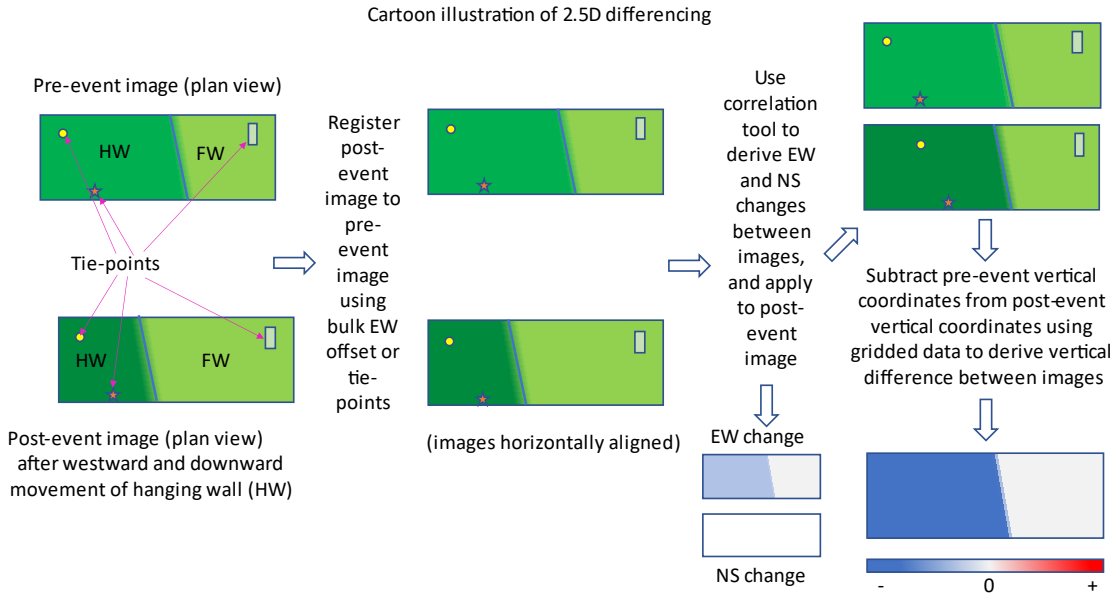

Figure 19: *Cartoon diagram of processing multiple images using 2.5D method of differencing. The initial stage of image co-registration is followed by the use of a correlation tool to produce maps of east-west and north-south deformation between the images, which are then applied to the post-event image to transform the pixel locations of that image into the pre-event image reference frame. Once transformed and gridded to the same resolution, the vertical coordinates can be used to derive vertical difference between the images.*

Once adjusted in that way, the vertical coordinates for the pre-event cloud and the post-event cloud can be gridded to the same resolution and the vertical coordinates of the former subtracted from the latter to obtain a value for vertical difference between the two clouds over the intervening time period. The process is shown in cartoon form in **Figure 19**.

2.2.5 "3D" differencing using iterative closest point ("ICP") algorithm

2.2.5.1 Introduction to 3D differencing

Although 2.5D differencing produces 3 outputs, east-west, north-south and vertical, the 2.5D approach involves gridding of the datasets to produce the vertical difference at a resolution which exceeds the resolution of the underlying datasets (e.g. Nissen et al., 2012). This smooths the data and potentially introduces biases or artefacts in the resulting displacements. The use of an iterative closest point algorithm as the final step in the differencing process allows for comparison of the raw datasets (with any east-west and north-south offset derived from the correlation process first applied to the horizontal location of the pixels) and aims to avoid this problem. The results from the ICP process should be a more reliable vertical displacement field, together with refinement of the previously calculated horizontal offsets.

3D differencing using ICP can be used for either large-scale point clouds, such as those from optical satellite data, or smaller, denser point clouds from TLS (e.g. Bouaziz et al., 2013, Chen and Medioni, 1992, Nissen et al., 2012, Nissen et al., 2017).

2.2.5.2 Iterative Closest Point ("ICP") algorithms.

Once finely registered (in the case of the TLS data), or adjusted by horizontal shifts from correlation tools (in the case of the optical satellite data) an alternative approach to differencing using an ICP algorithm may yield all three components of deformation through a single process. In the case of the optical satellite data the ICP algorithm is applied to each pixel of the post-seismic image by interpolating the gridded results from the calculated offset. In the case of the TLS data, the fine registration process has applied a rigid transformation, usually based upon a sample area of the footwall. The ICP algorithm then calculates the horizontal deformation of the raw datasets after applying the offset or transformation. In the case of the optical satellite date, this is the residual horizontal deformation (which then needs to be added to the previously calculated horizontal offset to derive a final total for horizontal displacement). The vertical deformation is calculated by the ICP algorithm without any prior vertical offset of either dataset (except for a potential bulk shift where there are georeferencing issues).

A windowed point-to-plane ICP algorithm developed within Matlab calculates the rigid body transformation (a translation and a rotation) that iteratively minimises the difference between windows of, respectively, the (fixed) target cloud and the post-event (source) cloud (Bouaziz et al., 2013, Chen and Medioni, 1992, Nissen et al., 2012, Nissen et al., 2017). Pairs of the closest points in each respective cloud are identified. The algorithm calculates the rotation and transformation required to move the post-event cloud towards the target cloud by minimising the sum of the squared differences of the paired points, and applies that transformation to the points in the source cloud. The exercise is then repeated over a set number of iterations until a threshold of a local minimum closest point distance is reached. The totals of such transformations (t_x, t_y and t_z) and rotations about the x, y and z axes for each pair of cells map the surface displacement field (**Figure 20**).

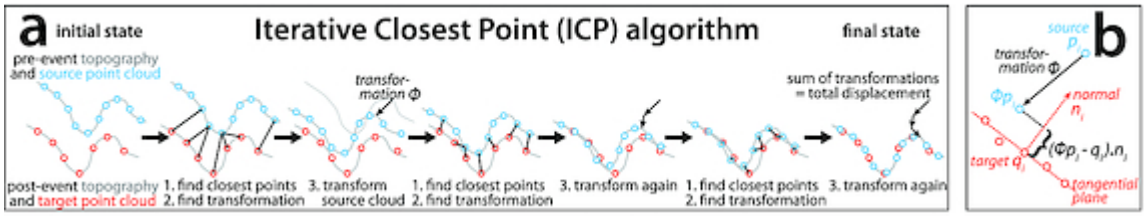

Figure 20: *Illustration of operation of ICP algorithm, from Nissen et al., 2012.*

In order to avoid differences from co-seismic surface displacements varying spatially, the operation of the ICP algorithm splits the point clouds into set window sizes, with a "fringe" or buffer zone around the windows to account for horizontal displacement between datasets, and a sliding window approach which leads to an overlap between adjacent cells. The algorithm then runs on each window separately and calculates the summed total of translations t_x, t_y, and t_z for each window, which correspond to displacement east-west, north-south and vertically respectively.

The combination of translation and rotation is explained further in **Figure 21**.

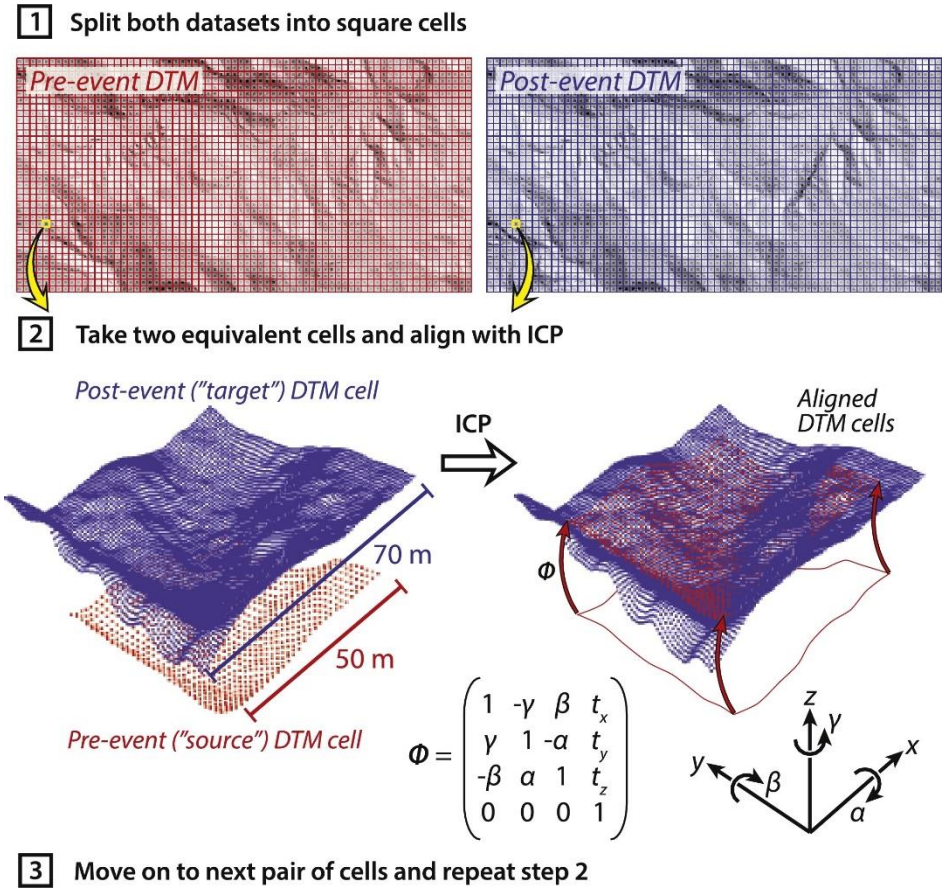

Figure 21: *Illustration of operation of ICP using pre- and post-event Digital Terrain Models ("DTMs"), from Nissen et al., 2014. In step 2, the rigid body transformation* ϕ *that minimizes closest point distances between the pre- and post-event DTM nodes comprises translations tx, ty and tz in the* x, y *and* z *directions, and rotations* α, β *and* γ *about the* x, y *and* z *axes*

A cartoon illustration of the "3D" ICP-based differencing processing steps is at **Figure 22**.

Although developed for use in connection with airborne LiDAR (e.g. Nissen et al., 2012, Nissen et al., 2017), this version of the ICP algorithm has been used successfully in connection with TLS (e.g. Wedmore et al., 2019) and differencing Pleiades post-earthquake optical satellite data with lower resolution pre-earthquake LiDAR data (Zhou et al., 2015). It is not thought to have been used previously in connection with differencing only optical satellite data.

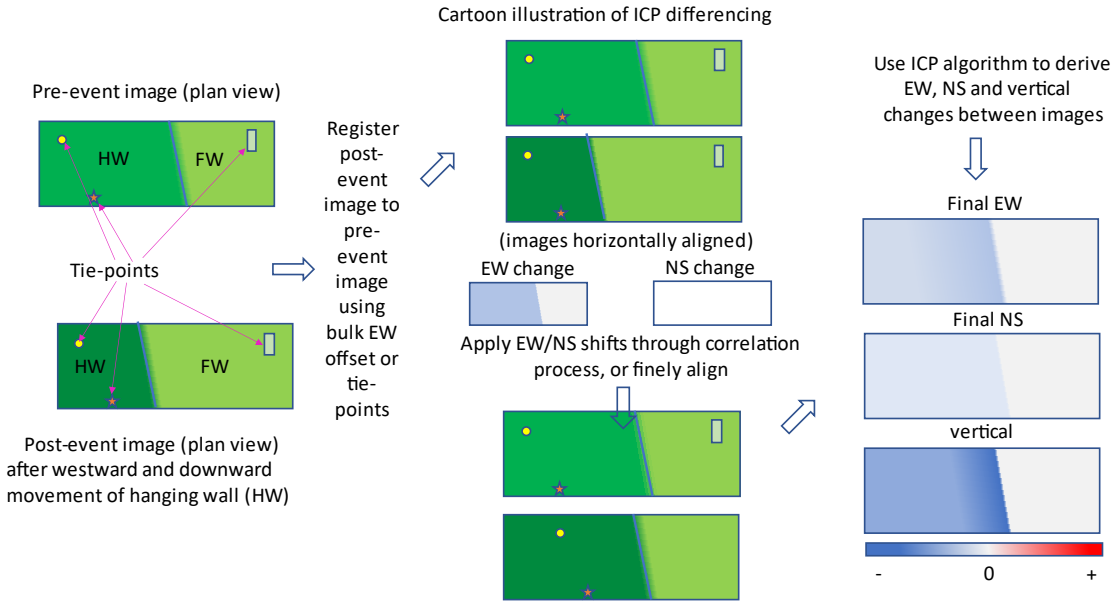

Figure 22: *Cartoon diagram of processing multiple images using ICP method of differencing.*

2.3 Pre-processing and post-processing data or results to remove biases - the use of filters to reduce noise and to remove seasonal differences between images

Optical satellite data may contain a number of biases from the relationship between the orbit of the satellite and the viewing angle and surface features such as aspect or dip, which make it necessary to consider either filtering data before differencing, or filtering of the results post-differencing where the results are too noisy to derive a clear deformation signal. Optical satellite data is known also to suffer from geometrical distortions arising from the modelling inaccuracy of CCDs (Charge-Coupled Devices, or photon detectors) and unrecorded satellite jitter during image acquisition arising from platform instability (Ayoub et al., 2008). Temporal changes between images such as the addition of snow covering, and changes in shadow due to differing seasonal sun angles can also introduce artefacts. The same sort of biases may arise from TLS data, where (for example) seasonal changes in vegetation or anthropogenic intervention between the dates of the respective scans may mean that differencing results are unreliable. Variations in point cloud density (both internally, and between TLS scans) and scan angles may also distort the results from differencing.

The following are examples of two techniques which can be employed to reduce noise and improve the clarity of results without losing the underlying signal.

2.3.1 Filtering noisy results using recursive filtering

The east-west and north-south offsets derived from the pre-differencing correlation process are expected to be noisy, in the light of the variation in coherence in results depending upon, inter alia, steepness or aspect of slope and data density, producing outliers. A typical decision filter applied to remove outliers is a median filter which replaces a value within a moving set data window with the median of the values within that window (first introduced by Tukey, 1974). A Hampel filter adds a further requirement for replacement that the value is only replaced if the outlier is far enough away from the median to match a set threshold (e.g. Pearson et al., 2016). Variations on the median and Hampel filters include recursive median filters and recursive Hampel filters (ibid) which use a median value from the prior median filter output. With datasets which vary considerably in data density, where denser point clouds are likely to represent more reliable values, a refinement of that recursive filtering process may look to replace outlying pixel results with median values, whilst retaining values which are more likely to be accurate in areas of high pixel density (such as in near-fault areas) and substituting median values for outliers particularly in areas of lower pixel density. This may be achieved by recursively increasing the size of the moving window through a series of iterations, continuing to replace outlying values which repeatedly fail to meet the set threshold during the series of iterations. A similar filtering process may also be required to reduce noise from differencing results from the TLS datasets.

As example of the operation of this filtering approach is shown at **Figure 23**. In this case, the sample data being filtered are the east-west offset results derived from the correlation process between two sets of optical satellite data which are then to be applied to the post event image.

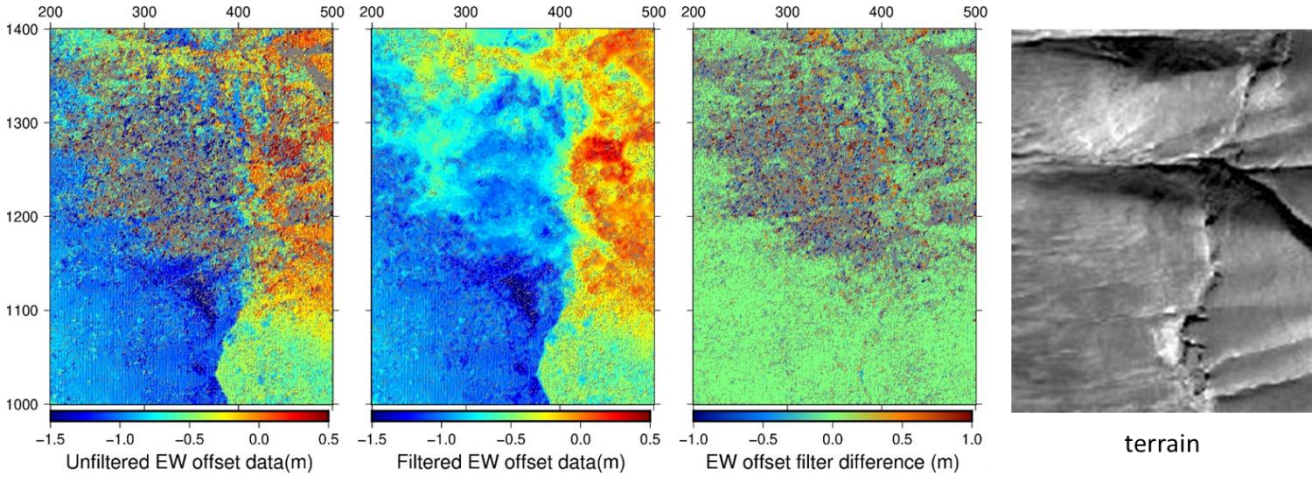

Figure 23: *Example of operation of an iterative median filter using a threshold set at deviation of points from median values within a window applied at increasing window sizes combined with minimum non-NaN percentage, with values being substituted by the median until the threshold value is no longer met or the iterations have completed, whichever is the earlier. Figures are respectively the unfiltered data (LH), filtered data (LH centre), difference between the two (RH centre) and satellite image of terrain (RH).*

The unfiltered data is a mixture of very noisy (upper part) and very coherent (lower half) stretched across a north-south trending fault scarp, where co-seismic movement has been towards the west in the hanging wall (left side of figures) and towards the east in the footwall side (right side). In this case the aim is to reduce the level of noise in the upper part, whilst keeping the detail in the lower half. The threshold applied is a mixture of differences between successive pairs of median values and a minimum required level of non-NaN values in the datasets involved.

As an example, three of the initial iterations here involve respective median tile widths of 3, 5, and 7 points applied to a gridded dataset. For any one point within the grid its Z value is part of the calculation of a median value together with the Z values of (respectively) 8, 24, and 48 neighbours (m_3, m_5, and m_7). If the difference between the point's initial value m_0 and the subsequent median value m_3 is less than 0.1 (10%), the original value is not replaced. If it is more than 0.1, the value is replaced with m_3, and the same calculation is then done in respect of the difference between m_3 and m_5. A difference of more than 0.1 means the value is replaced. If less, the value is kept. The same process then applies in respect of the next iteration comparing m_5, and m_7. In

this particular set-up of the filter, a further condition (that is optional) is applied at each stage, which is that the threshold of 0.1 is multiplied by the percentage of non-Nan points within the window. If the percentage of "real" (non-Nan) points within the window is high and approaching 100%, the threshold stays largely unaltered. If low, the threshold reduces, meaning that points in areas of low pixel density are more likely to be replaced by the median (which will result in some smoothing of the data).

2.3.2 Image filtering of TLS point clouds using lowest points filter

Prior to differencing, where vegetation appears to be a likely source of distortion of TLS results due to seasonal changes in growth (or where human intervention introduces height differences), an option is to filter the point cloud data by selecting the lowest points within set window sizes which then vary iteratively (e.g. Whitman et al., 2003) (a neighbourhood-based approach). This aims to identify and retain what are "ground" returns, rather than the vegetation above the ground. One variation on this approach is to use decreasing area window sizes containing increasing point densities to select the lowest points in each window, removing points above the lowest point elevation (retaining the ground surface detail in areas of high point density).

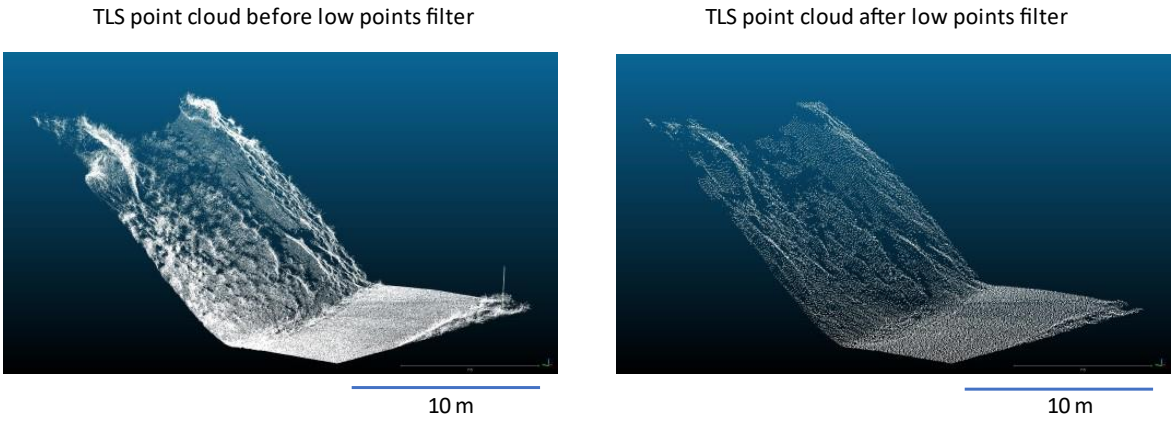

Figure 24: *Comparison of TLS point cloud with vegetation, road and man-made object (snow pole) before (LH) and after (RH) application of a lowest points filter.*

An example of the results obtained from the application of this type of filter is shown in **Figure 24**. In this example, a section of a TLS point cloud has been used which shows a vegetated slope adjoining a road, on the other side of which is a snow pole and more

vegetation. Neither of these features may necessarily appear in the same place in another TLS scan of the same site taken on another occasion. Here, the lowest points filter has effectively removed both vegetation and snow pole, leaving the essentials of the slope and road. The filter does, however, lead to loss of definition, with fewer than a tenth of the points in the original cloud (~520,000 points) retained in the filtered cloud (~34,800 points) using these particular settings.

2.4 Conclusion

These methodologies allow potentially noisy remote datasets acquired on different occasions to be differenced in ways that yield results showing both horizontal and vertical deformation over time at different scales. In the following chapters I use the methodologies and resources described here to derive displacements from sets of remote data which differ significantly in scale. Firstly, I use two sets of optical satellite data, one from the day before the 30th October 2016 Norcia earthquake, the other from a month after the earthquake, to derive co-seismic horizontal and vertical displacements in the near-fault area within ~1 km of fault traces. In that case, the scale of displacement seen is from centimetres up to ~2 metres. Secondly, at a significantly smaller scale I use pairs of TLS data taken at a number of dates post-earthquake to derive post-seismic horizontal and vertical displacements within up to ~100 m from fault scarps from the Norcia earthquake over varying time periods of up to ~3 years. In that case, the scale of displacement seen is of the order of millimetres up to tens of millimetres. This illustrates the flexibility of these differencing techniques in dealing with varied remote datasets.

CHAPTER 3. Refining shallow slip distribution models of the M_w 6.6 Norcia earthquake using Pleiades optical satellite data

3.1 Introduction

The overall aim of this study is to investigate how reliable fault scarps are as evidence of previous seismic activity. An important part of that investigation is to gain spatial insights into the extent of near-fault co-seismic deformation (and in particular the effect of distributed faulting close to the surface), which is not necessarily fully represented by the evidence in the form of a surface rupture (e.g. Milliner et al., 2015, Teran et al., 2015, Quigley et al., 2011). Evidence preserved in the landscape by way of fault scarps may, in active tectonic regions, be one of the few available resources to those endeavouring to assess future seismic hazard (e.g. Wallace et al., 1977, Bucknam and Anderson, 1979, Papanikolaou et al., 2005). Such scarps will probably degrade to some extent over time due to erosional (e.g. Wallace, 1977, Hanks et al., 1984) and ongoing post-seismic processes (e.g. Marone et al., 1991, Freed et al., 2007, Peltzer et al., 1998, Pollitz et al., 2001). However, how reliable are they as evidence of an earthquake even shortly after it occurred?

There is a wealth of geodetic and field data available in relation to the 2016 Central Italy earthquake sequence (CIES) (e.g. Falcucci et al., 2016, Civico et al., 2018, Villani et al., 2018, Chiaraluce et al., 2017, Wilkinson et al., 2017, De Guidi et al., 2017). This has enabled a number of studies to use geodetic measurements at the surface, applying inversion techniques, to model slip below the surface from the individual earthquakes within the sequence (including the largest earthquake in the sequence, the Norcia M_w 6.6 earthquake of 30th October 2016), in order to try to obtain a better understanding of the fault geometry involved in near-fault areas (e.g. Cheloni et al., 2017, Xu et al., 2017, Walters et al., 2018, Cheloni et al., 2019, Xu et al., 2020, Delorme et al., 2020). However, the level of detail in these models is insufficient to enable us to untangle the intricacies of distributed faulting and strain partitioning in an area where field data of

ruptures at surface and previous fault mapping show that there is considerable complexity involved.

I aim to improve upon the level of near-fault detail provided in existing models by supplementing the datasets that have been used to date. InSAR techniques on their own, while providing an invaluable way of characterising deformation on a regional scale, typically fail to capture near-fault resolution due to unwrapping difficulties. The deformation gradients close to surface ruptures of medium scale earthquakes, where there may be > 10s of cm of vertical deformation in a comparable horizontal distance, lead to steep fringe patterns in interferograms that are difficult to unwrap, and loss of coherence due to near fault rupture shaking. An example of this effect is shown in **Figure 25**, which shows the observed line-of-sight displacements for a combination of the Visso and Norcia earthquakes, from Sentinel-1 data (from Walters et al., 2018), with large data gaps in the hanging wall below the main Monte Vettore fault.

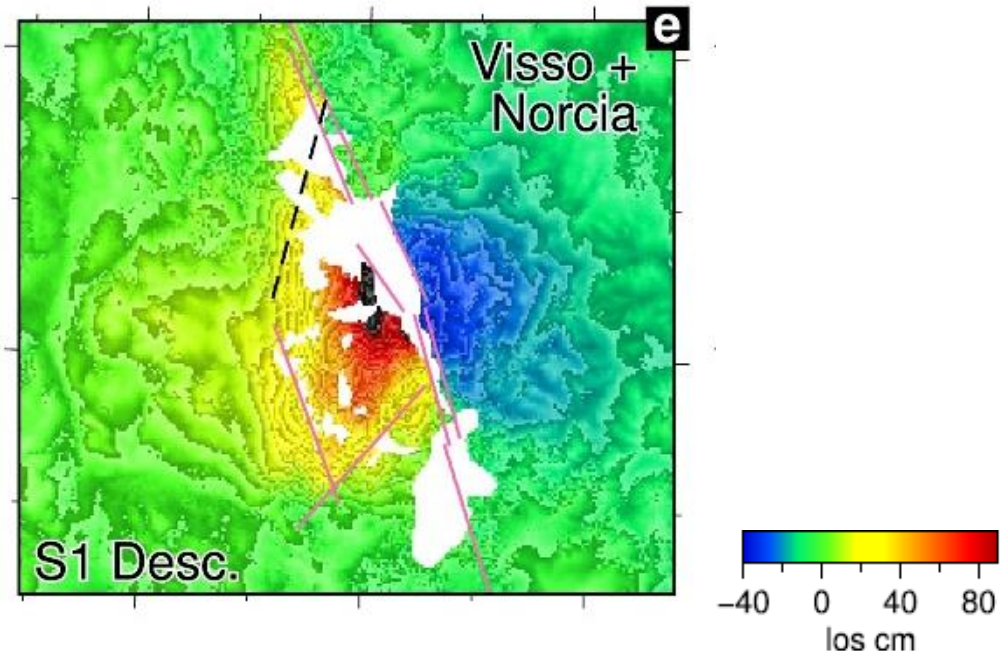

Figure 25: *Observed InSAR line-of-sight displacements for the combined Visso and Norcia earthquakes from Sentinel-1 satellite, warm colours show motion away from the satellite, fringes show 2.8 cm contours, solid pink lines show surface projection of modelled faults, from Walters et al., 2018.*

Field data and GNSS are by their localised and selective nature incapable of providing a coherent and complete picture of detailed near-fault deformation over a continuous area.

My aim is to combine existing geodetic data with near-fault detail of deformation obtained from very high resolution optical satellite data. I will jointly invert a variety of geodetic datasets covering both regional and more localised deformation, based upon a more detailed fault geometry than has been used in other studies to date (in turn informed in part by the results from the optical satellite data). By doing so, I aim to obtain better insights into the nature of distributed faulting and strain partitioning, and to use that to put into context and assess the spatial reliability of evidence of the earthquake in the form of fault scarps.

I will start by reviewing the existing shallow slip distribution models of the Norcia earthquake, the data relied upon in those studies, and the (generally) relatively simplistic fault geometry adopted in those modelling processes. I will then explain my alternative approach, and its results.

3.2 Existing shallow slip distribution models of the Norcia earthquake

There are a number of significant differences in the existing shallow slip distribution models of the deformation associated with the Norcia earthquake, possibly reflecting the complexity of the underlying geology, and the difficulties in finding models which fit the various available datasets.

3.2.1 Datasets used in the inversions

The data relied upon in the inversions includes a combination of interferograms from ALOS-2 InSAR and continuous and survey mode GNSS data (Cheloni et al., 2017), to which have been added interferograms from Sentinel-1 (Xu et al., 2017, Xu et al., 2020), and field data (Walters et al., 2018, Cheloni et al., 2019). In one case (Delorme et al., 2020), optical satellite data from the Pleiades constellation has also been added to the datasets. Seismograms and continuous and survey mode GNSS data have also been used without data from InSAR (Scognamiglio et al., 2018).

3.2.2 Fault geometry models

The fault geometry models used in the joint inversions vary considerably, with differences as to the existence, placing and form of various structures, particularly away from the main Monte Vettore Fault. Geometries proposed include:

- a relatively simple split of the Bove and Monte Vettore fault systems into two fault planes, each striking at 160°, with dimensions of 20 km x 4 km, making a composite 40 km long tectonic structure (Cheloni et al., 2017);
- an even simpler model of one fault of 30/35 km length dipping at ~40° and striking at 160° (Xu et al., 2017, Xu et al., 2020);
- a modelled main fault of 34 km length, strike of 155° and dip of 47°, plus a 10 km long blind transverse structure striking 210° and dipping 36° corresponding to the deep portion of the OAST (Scognamiglio et al., 2018);
- a "three fault" half-graben structure involving a single main (Monte Vettore) fault of ~30 km length striking at 159° and dipping at 38° plus two more steeply dipping antithetic structures both parallel to the main structure - one blind structure of ~14 km length at ~8km from the main structure, and another structure of ~10 km length at ~6 km from the main structure (Cheloni et al., 2019, in preference to other more complicated geometries);
- 4 faults, with a main Monte Vettore Fault of 21 km length, divided into two sub-faults with a 40° dip at surface and 35° dip at depth, an antithetic fault in the hanging wall of the main fault, with a mean strike of 300° with variable dip, a normal (synthetic) fault in the hanging wall of the main fault intersecting the antithetic fault, and a normal (synthetic) fault ~8 km to the west of the main fault (Delorme et al., 2020);
- a more complicated geometry of 9 fault segments combining the main (segmented) Monte Vettore Fault plus a transverse structure, antithetic and minor synthetic structures combining elements of the previous geometries (Walters et al., 2018) – see **Figure 26**.

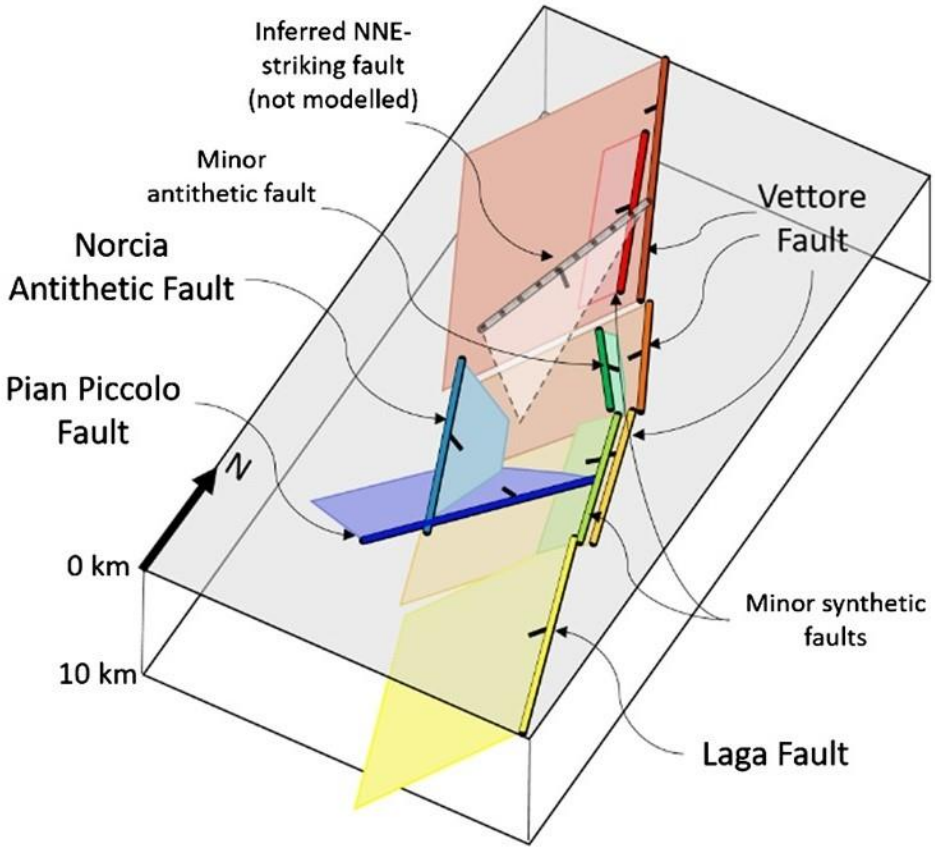

Figure 26: *Geometry of faults modelled in Walters et al., 2018, from figure 1c of that paper.*

3.2.3 Inversion results

The results of the joint inversions also disagree on some fundamental points (discussed below).

(a) Did the deformation involve a structure ~8 km west of the main Monte Vettore fault, and if so, what was that structure?

A hypothetical blind antithetic northeast-dipping structure with slip of ~0.7-0.8 m mainly at 2-4 km depth was proposed as an alternative to a pre-existing low-angle WNW dipping thrust segment below the Castelluccio plain (possibly related to a segment of the OAST) to accommodate residuals in the interferograms after accounting for slip on the main Monte Vettore fault (Cheloni et al., 2017) (**Figure 27**). Although this found favour with some (Walters et al., 2018 - their Norcia Antithetic Fault in **Figure 26** - and Scognamiglio et al., 2018), others thought it either was not

necessary to fit the data (Xu et al., 2017, Cheloni et al., 2019, Xu et al., 2020), or should instead be a synthetic structure (Delorme et al., 2020).

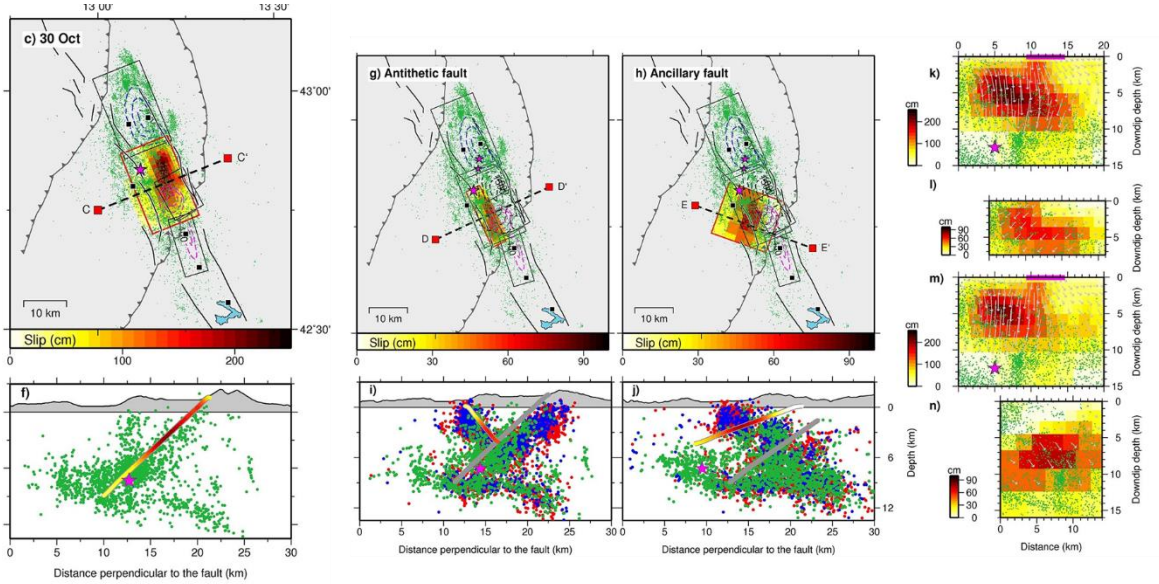

Figure 27: *From Cheloni et al., 2017, LH panel geodetic model of Norcia earthquake co-seismic slip distributions, central panels ancillary slip distributions assuming normal slip occurred on either an antithetic fault (LH centre) or pre-existing compressional structure (RH centre) (green dots show relocated aftershocks between 26th October and 30th November 2016), RH panels show slip distributions on the fault plane and ancillary structures on alternative hypotheses, with antithetic fault (upper panels) or compressional structure (lower panels).*

(b) Did the surface deformation observed reflect deformation on a transverse structure striking at ~210° near the south side of the Castelluccio plain?

This proposed hypothetical alternative to the structure discussed above (Cheloni et al., 2017 and **Figure 27**) also found favour with some either as an additional structure (Walters et al., 2018 – their Pian Piccolo Fault in **Figure 26**) or in its place (Scognamiglio et al., 2018 (**Figure 28**), Delorme et al., 2020). Others found it not necessary to fit the data (Xu et al., 2017, Cheloni et al., 2019 (who thought it was unjustified by field data and cross-cut other structures)), or considered it as just a possibility (Xu et al., 2020).

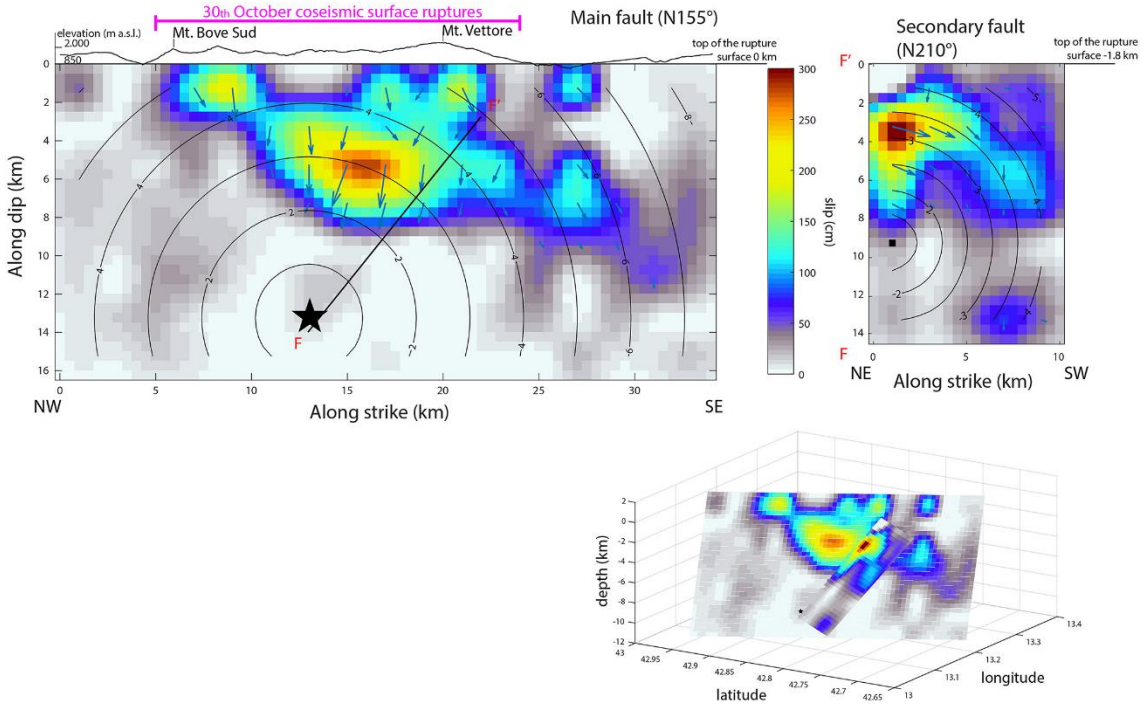

Figure 28: *From Scognamiglio, 2018 rupture model from inversion of ground velocity time histories and GPS displacements. Blue arrows show slip direction. F-F[1] on main fault shows intersection with second, transverse structure.*

(c) Where and at what depth did slip occur on the main Monte Vettore fault?

There is some level of consensus that most of the co-seismic slip (> 2 m) occurred in one main area concentrated up-dip of the hypocentre, between 2 km and 7 km depth (e.g. Cheloni et al., 2017 **Figure 27**). The residuals in that study also required some slip (up to ~1 m) in the shallower portion of the fault plane, and in the deeper southeast part of the fault (the latter of which gave rise to the alternative hypothetical suggestions discussed above). Broadly, the results agree with those found by Scognamiglio et al., 2018 (**Figure 28)**, Xu et al., 2017 (who also suggested slip of > 60 cm in the southern-most part of the fault, at depths of 6-10 km, without explaining why there should be such apparent partitioning of slip), and Xu et al., 2020. Models that included a transverse fault showed slip on the main Monte Vettore Fault restricted to a depth of < 6 km (Walters et al., 2018), with slip distributed onto other modelled fault segments, a result that was similar to the "4 fault" solution (Delorme et al., 2020). The addition of ancillary antithetic faults produced a narrower distribution

of slip between 3-9 km depth on the main fault with less slip shown along strike towards the southeast (Cheloni et al., 2019).

3.2.4 The effect of adding near-fault datasets in the form of optical satellite data

The results of most of these inversions suggest that the extent of near-fault distributed faulting is a critical factor in trying to characterise co-seismic subsurface slip. A common feature of all the inversions which rely upon InSAR data is that the InSAR interferograms produced lack detailed near-fault data. In the area of the epicentre of the Norcia earthquake, and up-dip for several kilometres from the focal point there appears to be little data available to the authors from InSAR (see for example Walters et al., 2018, Figure 5 and Xu et al., 2017, Figure 6). The fixed location GNSS regional data used also appear to be from stations that fall well outside the immediate near-fault region.

Optical satellite data offers a possible additional geodetic resource that can be used to add data for relatively large areas of off-fault deformation. Combined with other available geodetic datasets, it can be used to improve models of near-fault co-seismic deformation by pairing high-resolution data at local scale with lower resolution regional geodetic data.

The only study to use this data so far in connection with the Norcia earthquake (Delorme et al., 2020) combined the use of InSAR (interferograms from ALOS-2), regional and campaign GNSS with data derived from images from the Pleiades 1-A and 1-B optical satellites.

Using these datasets, Delorme et al.'s preferred "4 fault" model shows release of most of the seismic moment on the Monte Vettore Fault, with slip reaching a maximum of 3 m at depth (mainly concentrated in a depth range of 2-6 km, with a maximum at ~4 km depth), decreasing to ~1.5 m at the surface. Smaller amounts of slip (< 1m) are also recovered on the minor faults. The authors go on to model a number of non-unique possible fault geometries based on a 3-km long profile crossing the western slope of Monte Vettore (**Figure 29**), with a view to determining which geometry and slip distribution at shallow depth would best reproduce their model observations.

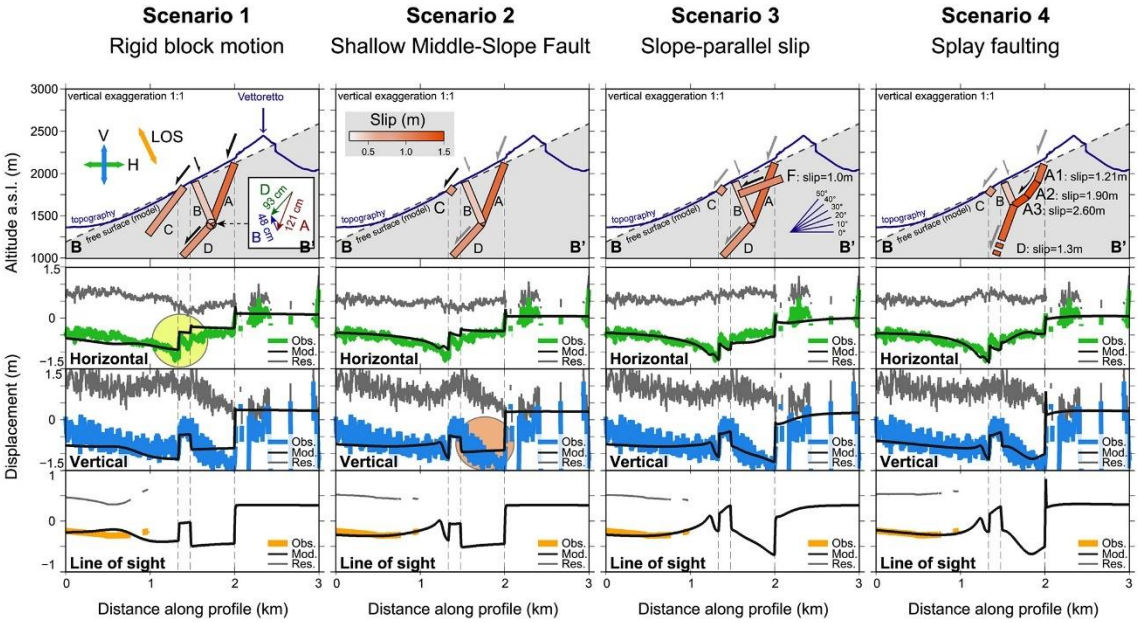

Figure 29: *From Delorme et al., 2020. Near-fault simulations of surface displacement using 4 scenarios of fault geometry and slip at depth, based upon a profile across the main areas of faulting. Lower panels show observed (coloured), modelled (black) and residual (grey) surface displacements. See Delorme et al., 2020 for detailed explanation of scenarios and profile location.*

In seeking to recover near-fault distributed faulting through inverse modelling, Delorme et al., 2020 represents an improvement in their addition of optical satellite data to other geodetical datasets. However, their results in terms of shallow slip distribution do not enable detail to be recovered over a wide area. In concentrating on a 3 km long profile where the deformation is clearest (and seen in the form of ruptures visible at the surface), the authors do not address in detail the complexities seen elsewhere, including potential "blind" faulting. The geometry used remains relatively simplistic compared to the known field ruptures and residuals seen in the interferograms. No allowance is made for a possible blind fault trending towards ENE bounding the southern part of the Castelluccio basin, and the authors' choice of a dip towards the west for a fault ~8 km west of the main Monte Vettore Fault appears at odds with the aftershocks shown in Chiaraluce et al., 2017. Although the authors identify a previously unreported level of complexity in co-seismic deformation at shallow depth, they acknowledge that the short spatial wavelength involved is too short for their large-scale inversion to capture it.

My aim is to eliminate or reduce significantly biases in the Pleiades data through an alternative approach to pre-differencing image alignment and use of filtering techniques. Using that data in conjunction with other available datasets I aim to recover detailed shallow, distributed slip over a wider area (not just in the areas of greatest deformation seen in the form of surface ruptures) by further constraining near-fault geometry to provide a better fit between the model and the Pleiades data, whilst maintaining a good fit with other datasets.

3.3 Data collection and coverage.

3.3.1 Source and time coverage of Pleiades data

In order to estimate high-resolution, near-fault co-seismic displacements, I processed point clouds in the form of .las files produced from orthorectification of six sets of tri-stereo optical satellite imagery acquired by the Pleiades 1A and 1B satellites between September 2016 and July 2017. The Pleiades constellation optical satellite data have a pixel resolution of 50 cm.

Table 3.3 Pleiades tri-stereo imagery

Pleiades 1B 26th September 2016

Pleiades 1B 29th October 2016

Pleiades 1B 12th December 2016

Pleiades 1B 13th June 2017

Pleiades 1A 20th June 2017

Pleiades 1A 7th July 2017

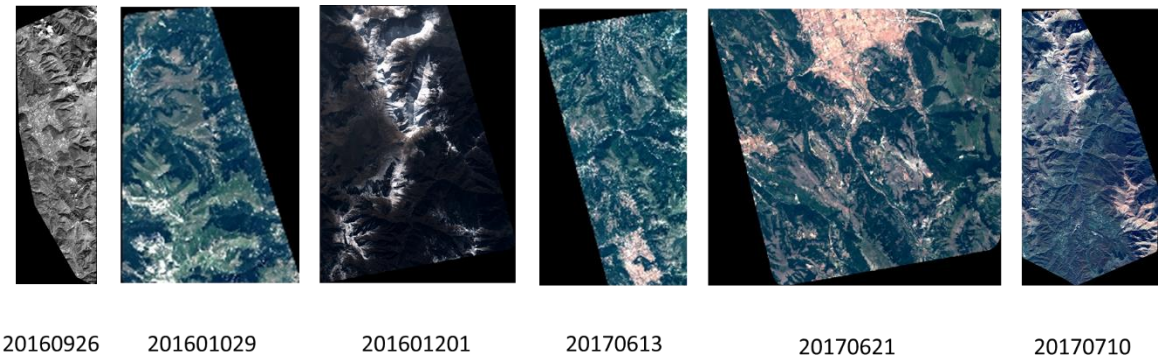

Figure 30: *Thumbnail views of the Pleiades imagery, not to scale.*

The images give coverage from two pre-Norcia earthquake tracks, and four post-earthquake tracks.

The Pleiades data are in the form of DEMs (Digital Elevation Models) and supporting .las files images from orthorectification of pan-chromatic tri-stereo acquisitions by Dave Mackenzie (then of Oxford University) and made available through the CEOS (Committee on Earth Observation Satellites) seismic hazards project. I have not been able to confirm with him his detailed method of processing, but a Readme provided with one of the datasets (for 29th September 2016) includes the following (which I have assumed would describe the method used throughout):

"Processing:

Data processed using the Leica Photogrammetry Suite (LPS) under ERDAS Imagine by David Mackenzie.

The RPC model was refined with tie points but no ground control. Matching was performed using a 9x9 pixel window at the full resolution of 0.5m. The resultant pointcloud was filtered with a mean filter and gridded at 2m."

Each dataset includes DEMs at 2 m resolution. In some cases, the DEMs have also been gridded at resolutions of 1 m, 5 m and 10 m. I have used the 2 m resolution point cloud data throughout.

3.3.2 Spatial extent of Pleiades data

The spatial extent of the each of the Pleiades datasets is shown in **Figure 31**. There is only one spatial overlap covering the area of principal interest. This is between 29 October 2016 and 1 December 2016, and therefore straddles the Norcia earthquake with relatively little time delay (the same datasets as were used by Delorme et al., 2020). The datasets from those dates are therefore the primary resource I have used in seeking to refine previous models of shallow slip distribution in relation to the Norcia earthquake.

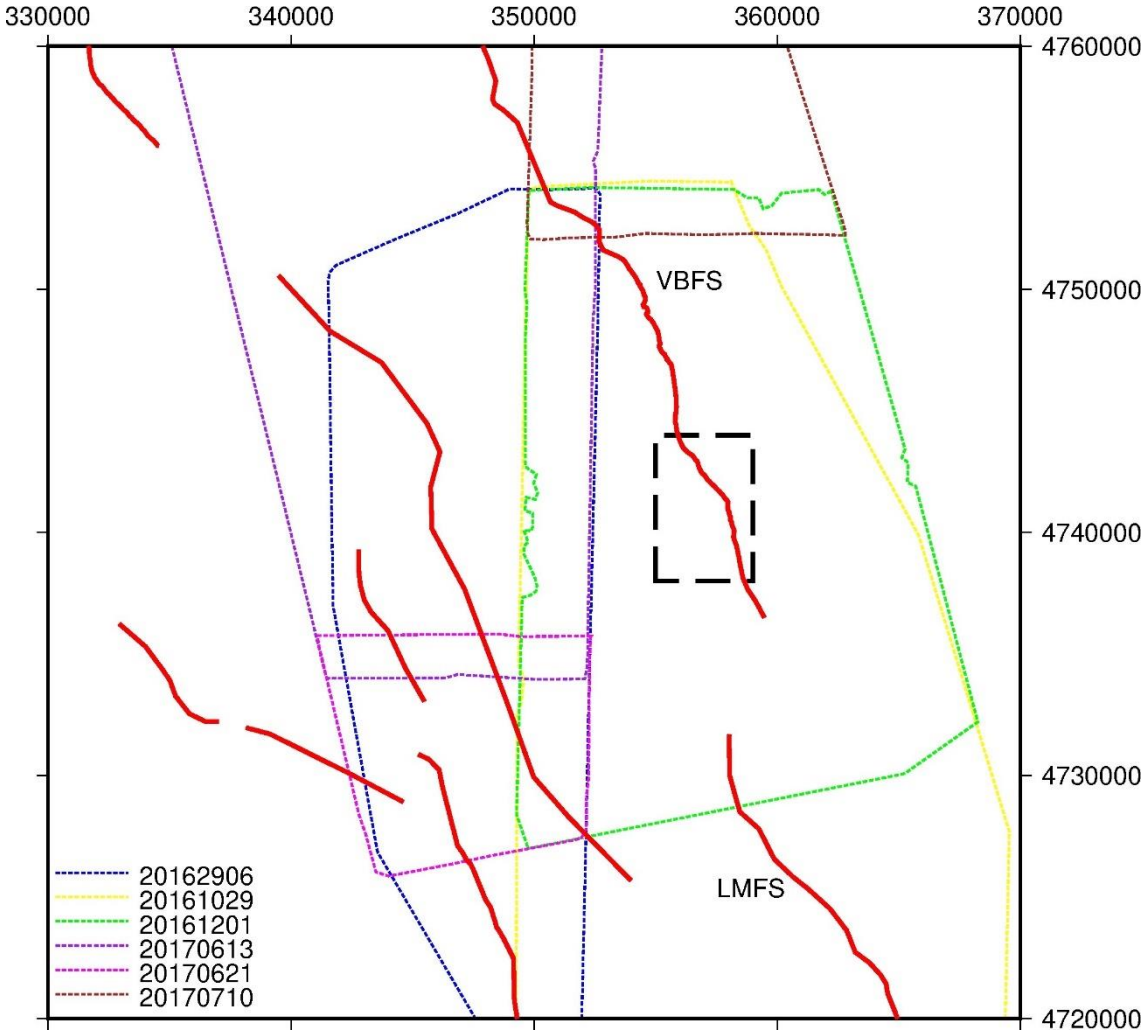

Figure 31: *Extent of coverage of Pleiades satellite datasets, red solid lines simplified fault traces from Roberts, 2008. VBFS = Mte Vettore-Mte Bove Fault System, LMFS = Laga Mountains Fault System. Dashed black line area = area covered by DEMs (**Figure 32** below).*

The full extent of the data covered by the two Pleiades datasets from 29 October and 1 December 2016 is as shown in the overlap between the yellow and green boxes in **Figure 31**).

In order to show a smoothed representation of the near-fault terrain in the area of greatest co-seismic displacement I created my DEMs from the Pleiades datasets using initial mean gridding of the data at 5 m intervals (to avoid aliasing short wavelengths), followed by interpolation using the Generic Mapping Tools ("GMT") Surface utility to

produce continuous curvature splines at a tension factor of 0.35, at intervals of 8 m (**Figure 32)**.

The area covered in these DEMs is a sample area of 355000-359000 UTM 33T, 4738000-4744000 UTM 33T, which includes the areas where greatest co-seismic deformation was recorded by the Open EMERGEO joint working party (Villani et al., 2018) (shown in the black box area in **Figure 31**). See also the equivalent sections of images from the 2 m resolution orthorectified DEMs (**Figure 33**).

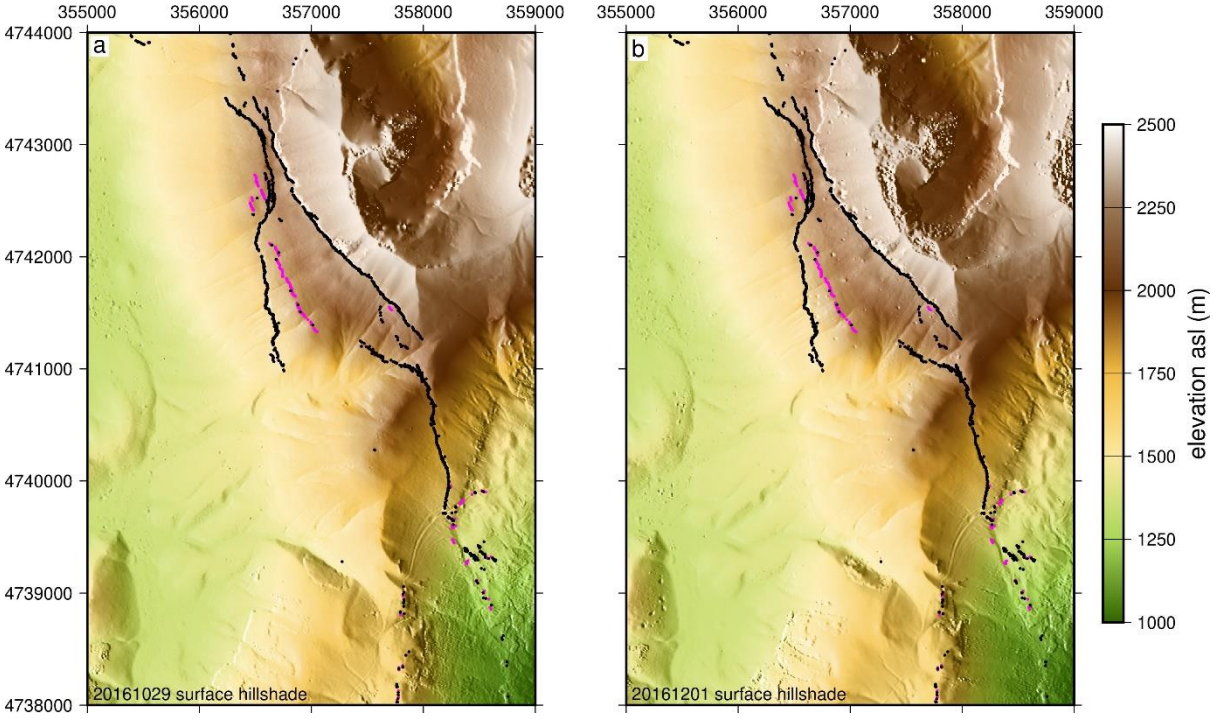

Figure 32: *Hill-shaded interpolated Surface DEMs for (a) pre-EQ (29th October 2016) and (b) post-EQ (1st December 2016) Pleiades data. Black and magenta points show the locations of Open EMERGEO Working Party data recording synthetic and antithetic dips respectively (Villani et al., 2018).*

In terms of the quality of data coverage, areas neighbouring fault scarps on relatively steep hill sides (particularly in the hanging wall of the main Monte Vettore fault) are relatively well constrained. However, areas further afield such as on the east-facing slope of Monte Vettore in the footwall, on relatively flat areas or in areas with extensive vegetation (such as from forestry and agriculture) lack detail where the satellites have not been to record a reflection from the Earth's surface.

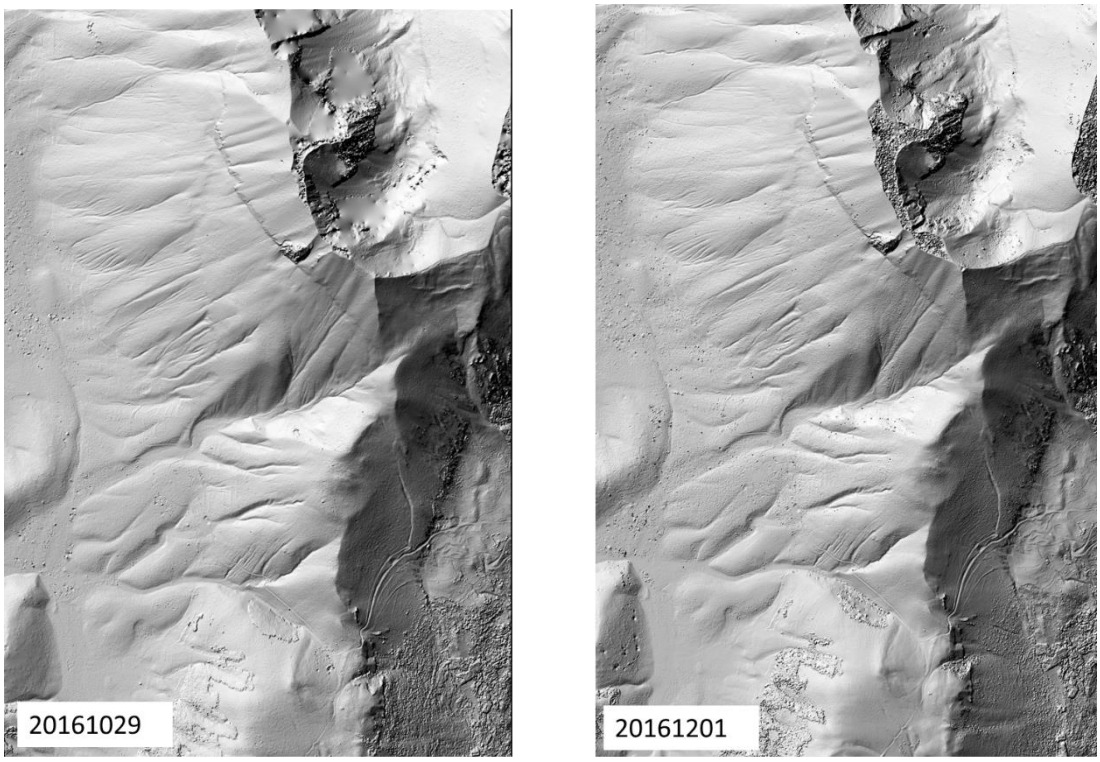

Figure 33: *Extracts from orthorectified DEM images at 2 m resolution.*

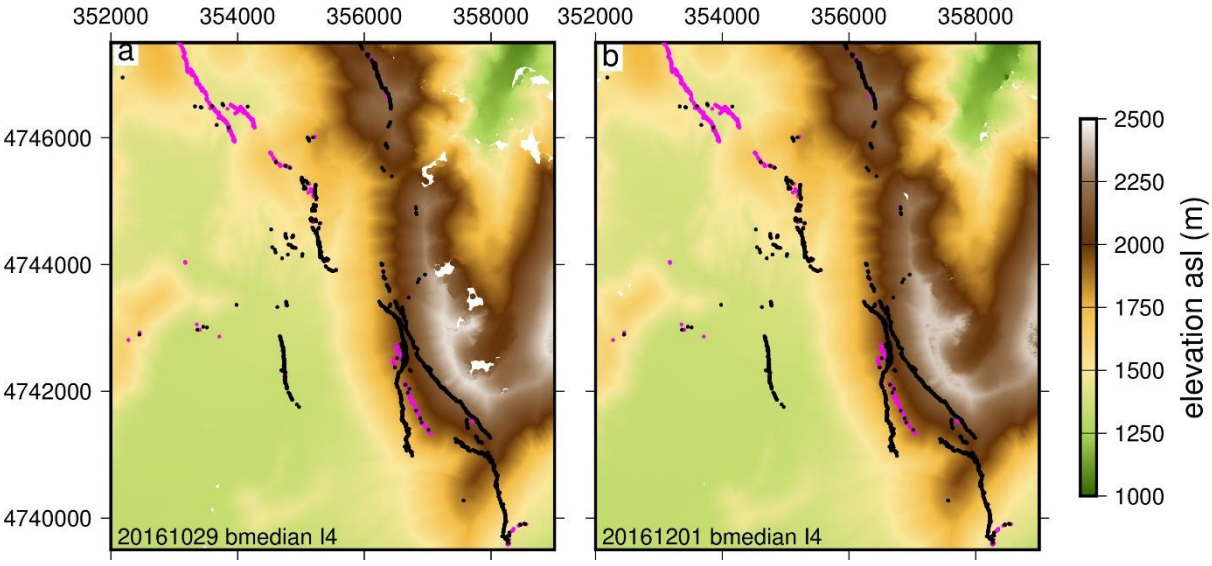

Figure 34: *4 m median gridded DEMs Surface DEMs for (a) pre-EQ (29th October 2016) and (b) post-EQ (1st December 2016) Pleiades data. Black and magenta points show locations of Open EMERGEO Working Party data recording synthetic and antithetic movement dips (Villani et al., 2018).*

Figure 34 shows the coverage over an expanded area without interpolation or hill-shading, using a 4 m median filter grid. This demonstrates in more detail the patchy

nature of some of the data, and lack of detail in the east-facing slope areas behind the main Monte Vettore ridge (particularly in the pre-earthquake image).

3.4 Pre-processing Pleiades data using ENVI (COSI-Corr) and recursive outlier filtering techniques

3.4.1 Correction for referencing misalignments between Pleiades images.

Due to issues with image referencing (primarily related to sensor geometry and topography), as a precursor to the use of a correlation tool I investigated possible misalignment between the Pleiades datasets with a view to solving for any apparent offsets.

I chose 20 pairs of pixels from both 29 October 2016 and 1 December 2016 images as tie points with locations away from any known areas of significant surface deformation. The average returns from those tie points showed recorded position differences between the earlier and later images of 4.087 m (east-west) and -0.0155 m (north-south) respectively (meaning that on average the pixel showing an object in the later image was located 4.087 m west and 0.0155 m south of the same pixel in the earlier image). Given the pixel resolution of 50 cm, I disregarded the north-south difference, and applied only a 4.1 m bulk adjustment by deduction of that value from the east-west coordinates of the later image to correct this misalignment.

Although I aim to recover relative (rather than absolute) values for vertical co-seismic displacement from the Pleiades datasets, comparison of vertical alignments based upon median values for early vertical displacement results from differencing, set against field measurements of co-seismic deformation (from Villani et al., 2018) suggested that referencing issues had also resulted in exaggerated values for vertical co-seismic deformation which were ~2.25 m greater than expected values. I therefore applied a further bulk shift by the addition of 2.25 m to all of the post-earthquake elevation figures to limit relative co-seismic displacements to more realistic levels.

3.4.2 Use of COSI-Corr correlation tool to correct horizontal offsets between the 29th October and 1st December 2016 orthorectified 2 m resolution Pleiades images.

I used the COSI-Corr software plug-in (Leprince et al., 2007) to ENVI (ENVI version 5.6 from L3Harris Geospatial) to try to reduce any topographic biases in vertical displacement using the correlation function within the COSI-Corr module. I used this tool to estimate the extent to which the pixels in the post-earthquake image had moved horizontally relative to the equivalent pixels in the pre-earthquake image, with a view to applying that estimated horizontal movement by offsets to the later image.

I ran the correlation tool over a total area of 56 km^2 (bounded by 352000/4739500 UTM33T and 359000/4747500 UTM33T). The region chosen is a sub-set of the wider area where the two Pleiades images overlapped. It comprises the area where, in general, there appeared to be less distortion within the images, and includes the majority of the co-seismic deformation recorded in field work (e.g. from Villani et al., 2018). I divided this region into two equal-sized halves of 28 km^2 for computational reasons, split horizontally along 4743500 33T UTM. For each half I used an initial window size of 64 x 64 pixels (32m x 32m), and a final window size (to derive sub-pixel displacement) of 16 x 16 pixels (8m x 8m). The step in X and Y directions between sliding windows was 8 pixels (4 m). The correlation engine used was the frequency correlator (Fourier-based). I chose a Robustness Iteration of 4, adaptively recomputing the frequency mask 4 times per measurement, to reduce noise. The Mask Threshold (which allows masking of frequencies according to the amplitude of the log-cross-spectrum of the image signals) was set at 0.9 (close to unity).

I applied a NLMF filter (Non-Local Means Filter) algorithm to both east-west and north-south components, using a search area of 21 x 21 pixels, and a patch area of 7 x 7 pixels (to characterise the area surrounding each data point). I applied a Noise Parameter of 0.22 within the filter (approximately 1 x the Standard Deviation of the noise, which I calculated as 0.23 in respect of the east-west shift and 0.205 in respect of the north-south shift). I chose a simple weighted average as the weighting method.

The results from the use of the correlation tool are shown in **Figures 35 and 36**.

Figures 35 and 36 are gridded at intervals of 4 m and illustrate the gaps in coverage of the datasets, as well as the noisiness of the data away from the areas of highest density data coverage. The north-south data seems to have a possible sinusoidal effect with a wavelength of ~2.5 km to the west of a line at about 355600 33T UTM.

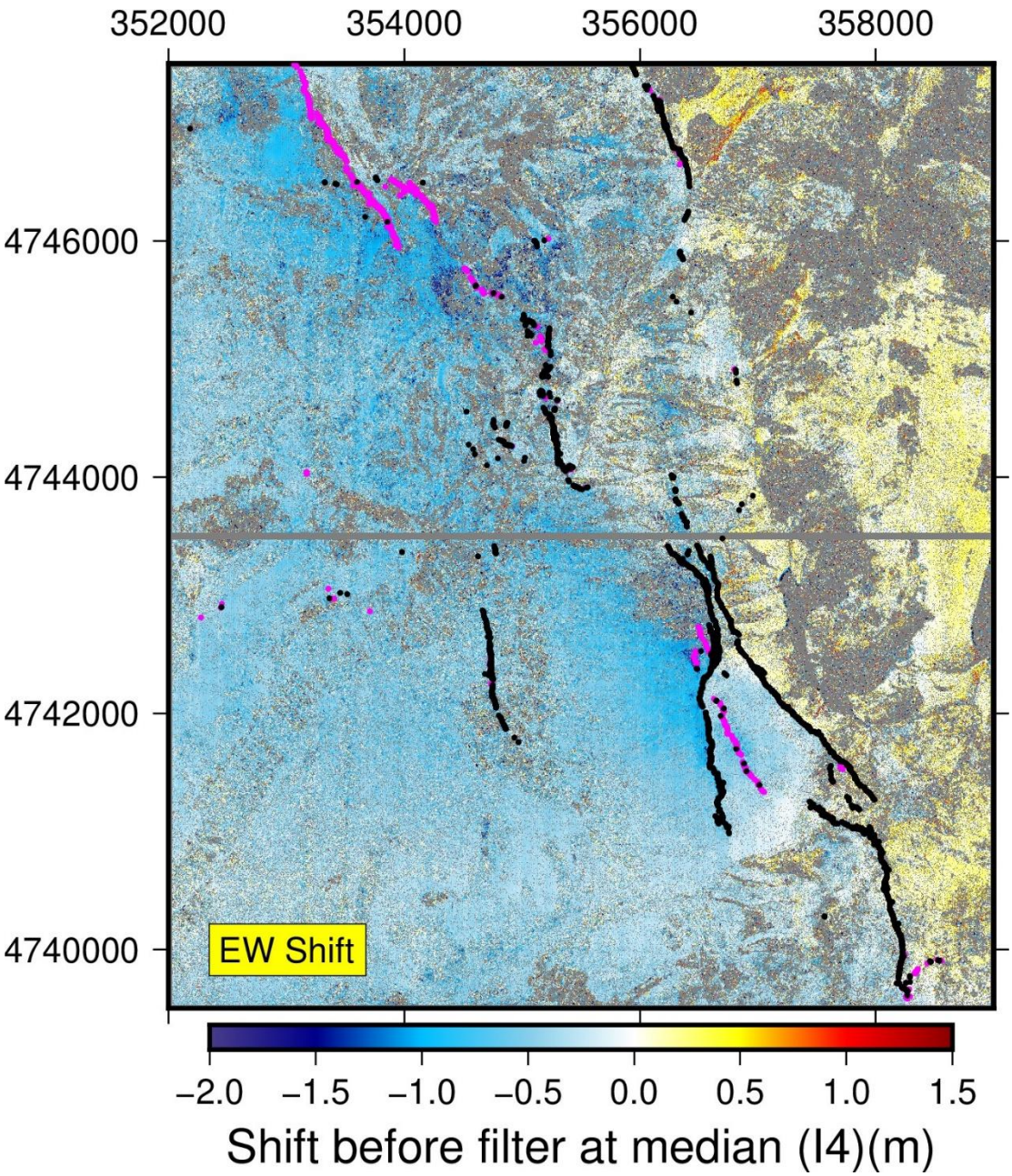

Figure 35: *Correlation tool output showing east-west results. The grey horizontal dividing line without data results from the split of the area processed into 2 sections. Black and magenta points are locations of co-seismic field measurements showing synthetic and antithetic normal faulting respectively (from Villani et al., 2018).*

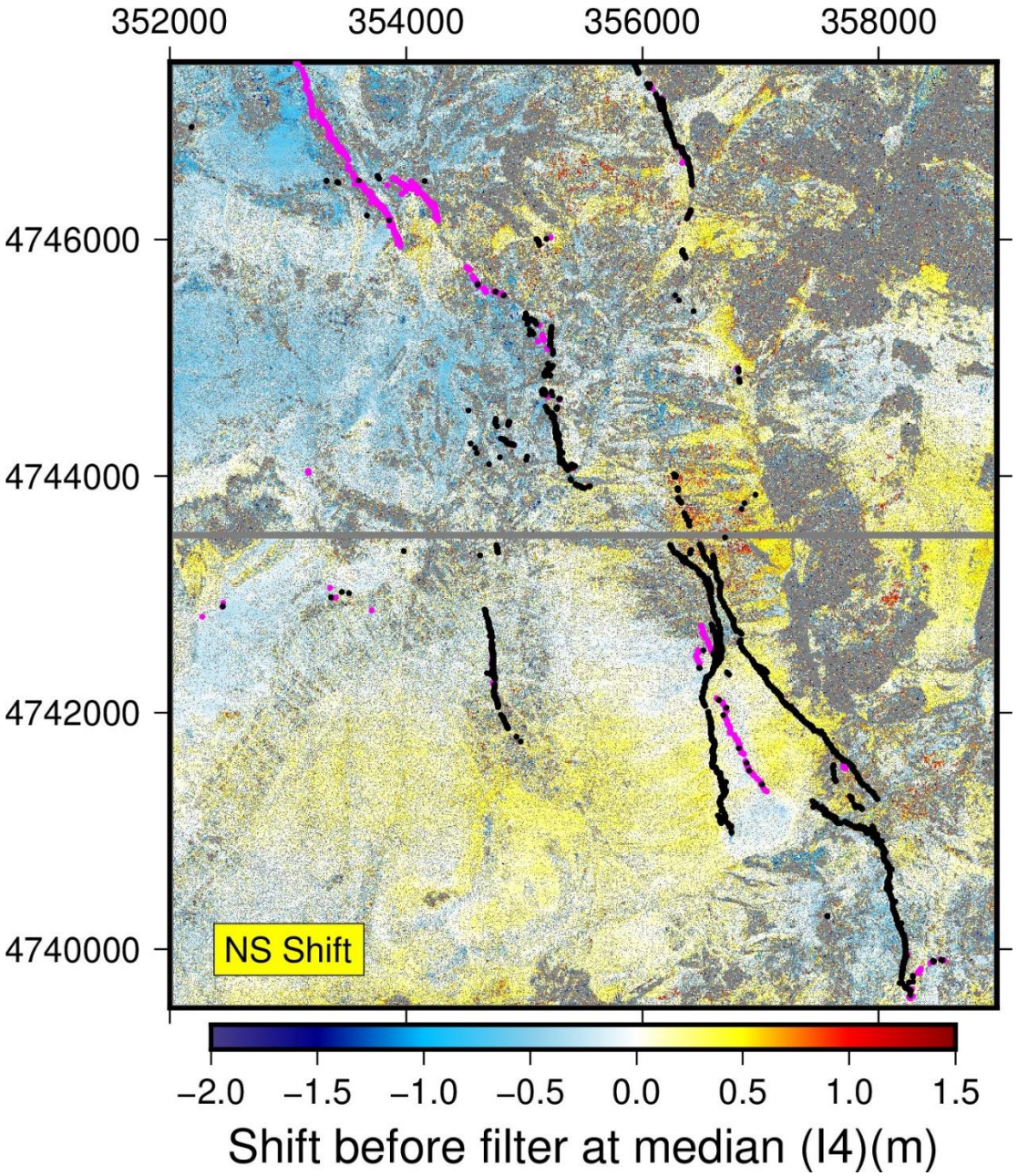

Figure 36: *Correlation tool output showing north-south results (otherwise caption as* ***Figure 35*** *above).*

3.4.3 Filtering the COSI-Corr correlation results using recursive filtering

In order to reduce the noise in low point density parts of the east-west and north-south displacement datasets from the correlation tool whilst preserving the low-noise high point density signals, I applied a recursive filter, based upon a threshold applied to each iteration of the filter by increasing window sizes. The filter, itself a refinement of decision filters such as median and Hampel filters (e.g. Pearson et al., 2016) and

developed by me in Matlab specifically for this research, runs recursively with increasing 2-dimensional sliding window sizes. On each run the filter calculates median values for horizontal displacement from the pixels within the window (ignoring NaNs), and the number of non-NaN pixels within the window. I ran the filter separately for the east-west and north-south components of horizontal displacement derived from the COSI-Corr tool. The filter applies a threshold at each filter stage to determine whether the preceding value (either the point's initial Z value (in this case, the east-west or north-south shift), or replacement median value as the case may be) is then replaced by the calculated median value for that window. The replacement continues with increasing window sizes unless and until the condition ceases to apply or the series of iterations concludes.

Here, the threshold I applied was a combination of two factors: a minimum percentage difference between the calculated median and the preceding window median value (set at 0.15, or 15%); and (as a multiplier of the first factor) a second factor assigning an importance to the percentage of non-NaN values within the window (itself set at 0.9 multiplied by the percentage of non-NaN values). The multiplier results in a lower threshold for minimum median difference in areas of low point density (and therefore replacement of a relatively higher proportion of values). In areas of high point density the minimum threshold is higher, retaining values which are not outliers, and which should more accurately represent the horizontal signal. The window sizes recursively applied (in point spacings of 4 m x 4 m) were 3, 5, 7, 9, 11, 13, 15, 17, 19, 21, 27, 33, 39, 45, 51, and 57. This gives a minimum window size of 12 m x 12 m and maximum window size of 228 m x 228 m, which I thought were appropriate given the scales of both near-fault detail and off-fault noisier areas, tested against results obtained using a number of other settings. The number of iterations was limited by computational capacity, which in turn restricted the area which could be filtered on each occasion.

In view of the size of the total area covered, for computational reasons I applied the filter in 2 groups of 6, which were split north and south (the respective areas used in the correlation tool process), a total of 12 sub-areas. The results from those sub-areas were then stitched together with averaging applied over overlapping fringes greater than the largest window size.

Although I also experimented with reducing the number of iterations and/or the maximum window sizes used in order to process a larger area at one time, the results showed either loss of detail in areas of high point density (if the number of iterations were reduced) or inability to replace outliers in areas of low point density or quality (if the maximum window sizes were limited).

The resulting filtered east-west and north-south horizontal shifts were then sampled onto the coordinates of the 1 December 2016 data, previously offset as described above by a bulk deduction of 4.1 m from the Eastings values. The extents of the resulting filtered east-west and north-south shifts that were applied to the 1 December 2016 data are shown in **Figure 37**.

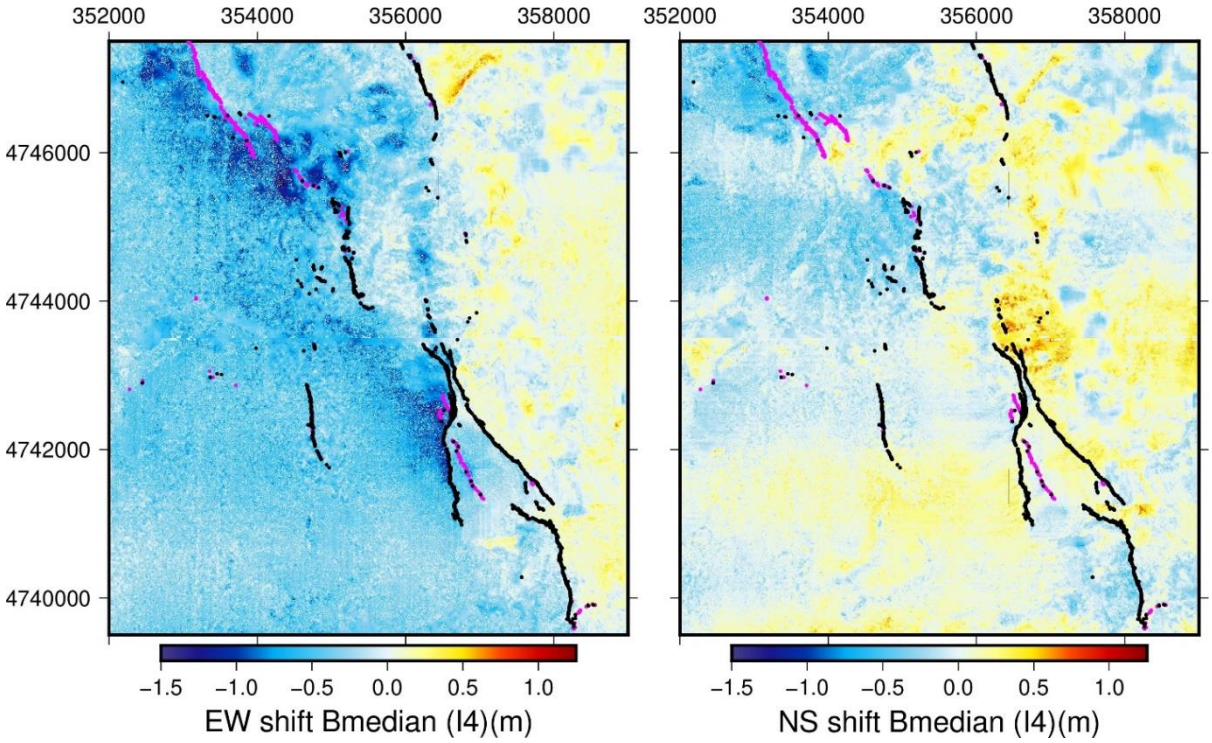

Figure 37: *Filtered COSI-Corr-derived east-west (LH) and north-south (RH) horizontal shifts, sampled onto 1 December 2016 point cloud data locations. Black and magenta points are locations of co-seismic field measurements showing synthetic and antithetic dips respectively (from Villani et al., 2018).*

As expected, the application of the recursive filter has removed outliers in areas of low point density, and replaced areas of low data density with median values, having removed outliers. The extent of the difference between the pre-filtered and post-

filtered offsets is shown in **Figure 38**. Areas of high data density are left largely unchanged by the filtering process.

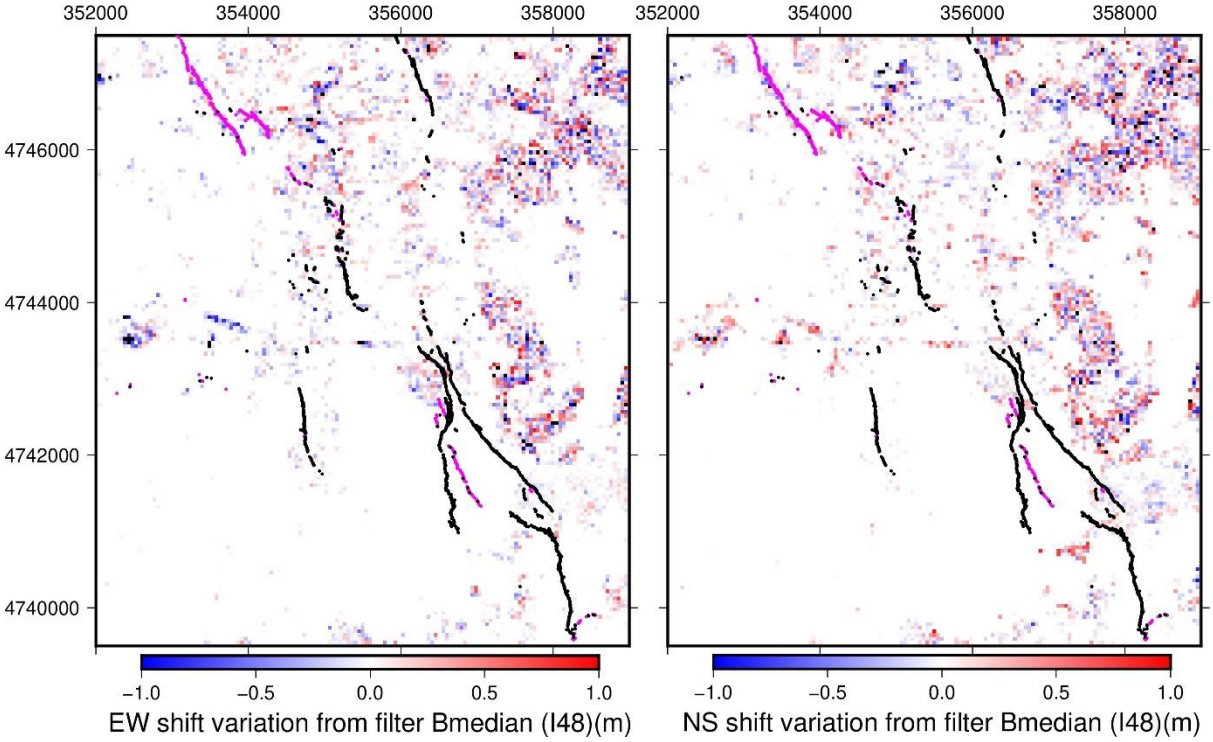

Figure 38: *Extent of difference between offset produced from use of correlation tool before filtering and after filtering, shown at gridded intervals of 48 m, east-west offset (LH) and north-south offset (RH) respectively. Black and magenta points are locations of co-seismic field measurements showing synthetic and antithetic dips respectively (from Villani et al., 2018).*

3.5 Differencing pre-processed Pleiades data to characterise vertical co-seismic deformation

I interpolated the filtered offset results onto the post-earthquake data using near-neighbour sampling, and applied the offsets to those data. I then derived the vertical difference between the pre-earthquake and adjusted post-earthquake datasets by subtracting a 4 m gridded dataset of the former cloud from a similarly gridded dataset of the latter cloud. The result is shown in **Figure 39**.

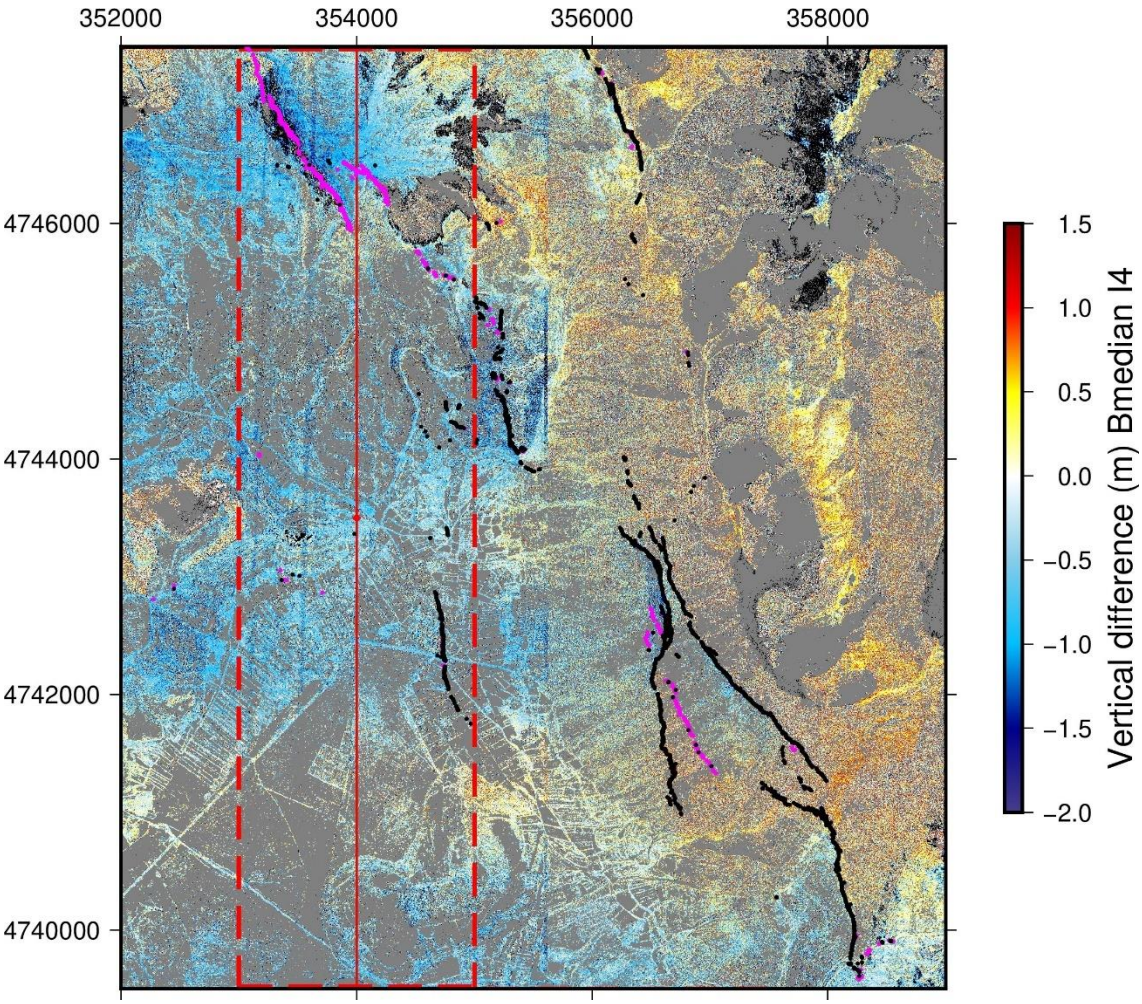

Figure 39: *Differencing result applying COSI-Corr derived horizontal shifts to post-EQ DEM, after bulk adjustments of 4.1m east and 2.25m vertically, 4m gridded data. Red dashed lines show spatial extent of data used in the profile in* ***Figure 40****.*

I again observed a sinusoidal effect to the west of Easting 355647 UTM 33T, the extent of which is shown by a profile through that data (on a north-south line), **Figure 40**. The data used for the profile are the vertical displacement results from an 8 km long strip (north-south) 2 km in width (east-west) centred on Easting 354000 UTM 33T (shown in red on **Figure 39**). The uneven sinusoidal effect appears to have a wavelength of approximately 2.5 km trending north-south, and an amplitude of ~0.5 m – 1 m. CNES (the French National Space Agency) have confirmed that the origins of this effect lay in the use of "some on board measures that are noisy" producing distortion in deriving orthoimages from Pleiades 1B satellite tri-stereo images (as used here). CNES have subsequently reconfigured the satellite to mitigate against this effect in the future.

Although I attempted to correct for this effect by deduction of the trend seen in the data from the vertical displacement results to the west of Easting 355647 UTM 33T, those attempts did not produce an acceptable result for the purposes of the inverse modelling. The sinusoidal effect is irregular. The area covered also includes parts which saw substantial amounts of co-seismic movement. Even with trying to mask those areas and deducting the resulting trend there was still a residual irregular signal which suggested that the data was not reliable. A second deduction of that residual trend did not materially improve the results.

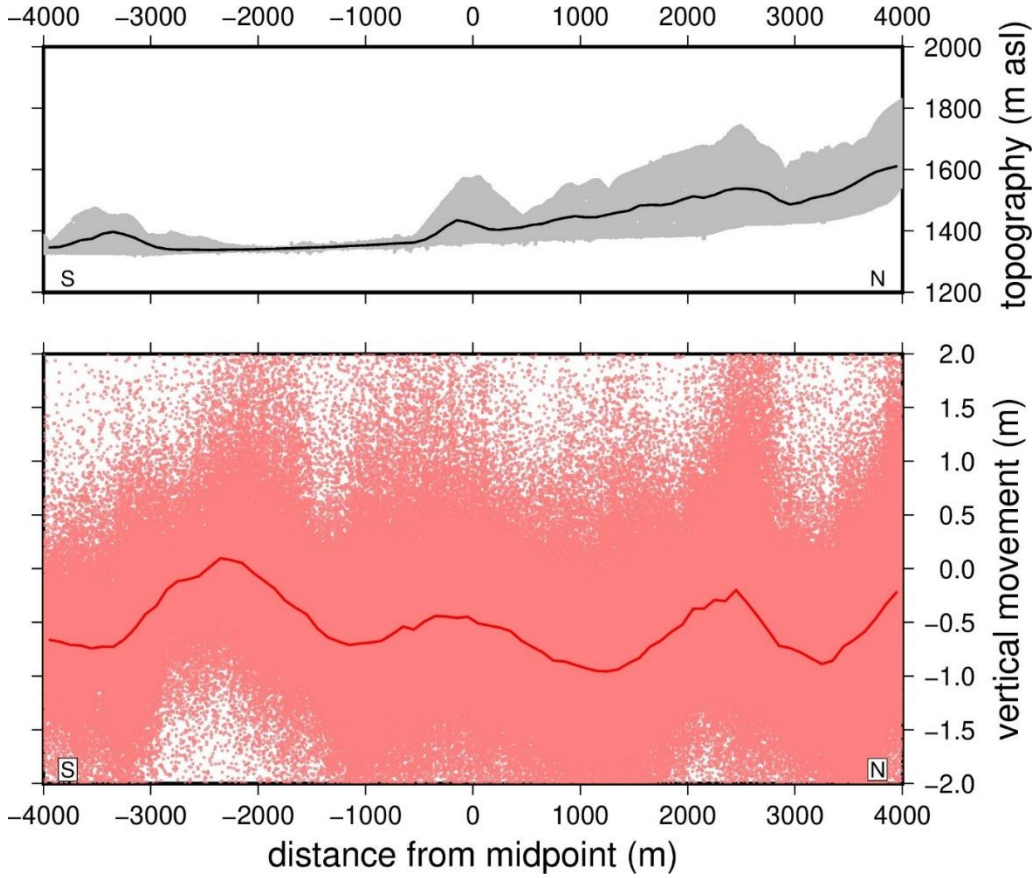

Figure 40: *Lower panel 2 km wide 8 km length median vertical displacement data profile (red line) centred on Easting 354000 UTM 33T (light red = data points used for median). Upper panel median topography (black line median against grey elevation data points).*

The area to the east of Easting 355647 UTM 33T covers the main area of co-seismic deformation around the Monte Vettore fault and its hanging wall. In view of the distortions apparent from the long-wavelength sinusoidal effect I therefore decided to

limit the extent of the Pleiades data used in the inversion to that area rather than introducing what seems clearly to be an artefact (**Figure 41**).

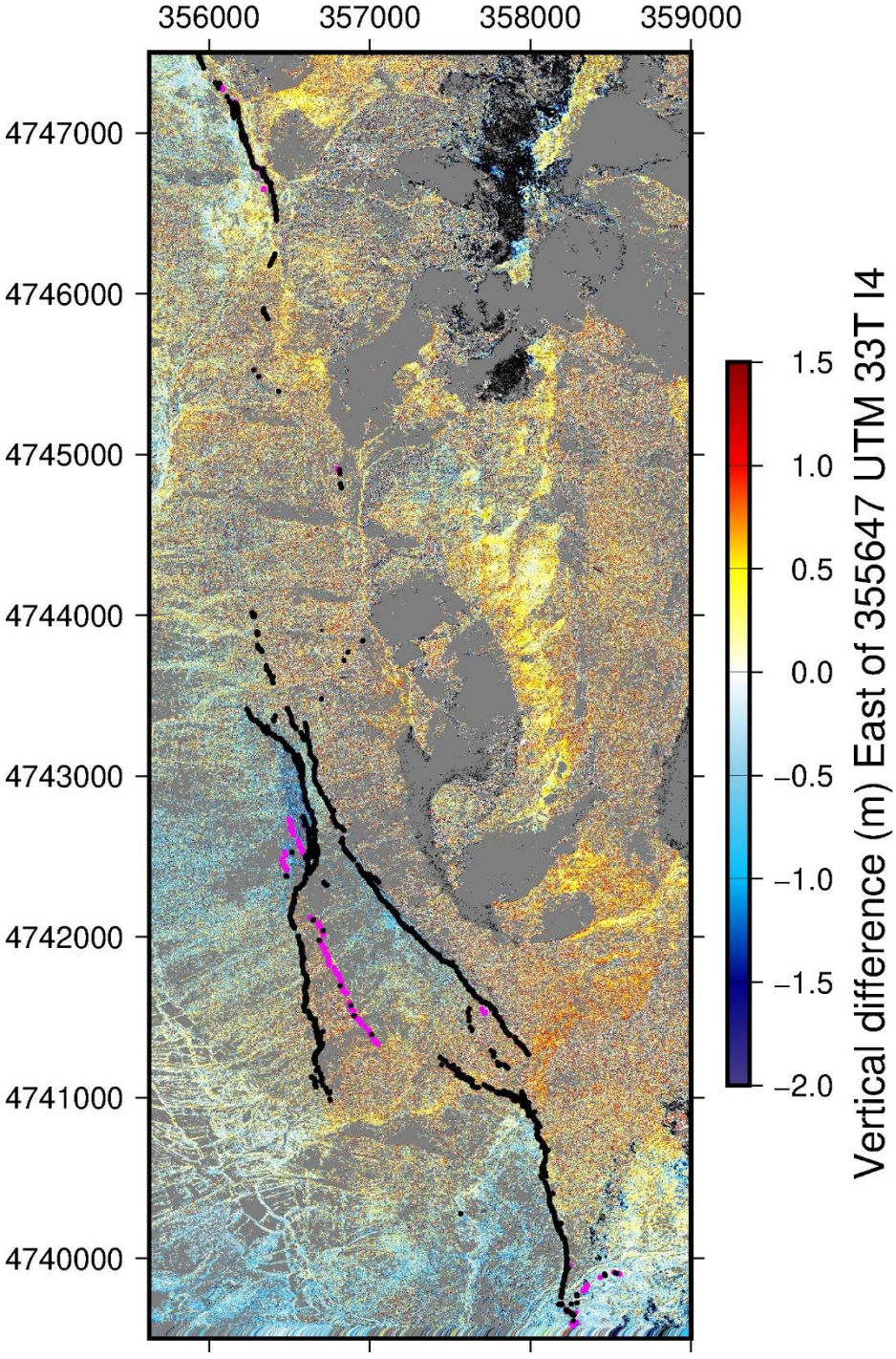

Figure 41: *Vertical differencing result applying filtered COSI-Corr derived horizontal shifts to post-EQ DEM, after bulk adjustments of 4.1m east and 2.25m vertically, 4m gridded data, extent limited to area east of Easting 355647 UTM 33T.*

This limits the results used here for modelling to an area which excludes one of the TLS sites covered in Chapter 5 below. However, in that Chapter I will present the results from an expanded area which has been processed in the same way.

I also experimented with the use of the ICP process (see **Chapter 2, para 2.2.5.2**) to see if it was possible to achieve a "3D" result, rather than what is essentially a 2.5D result. As input data, I used the post-earthquake point cloud, with bulk vertical and east-west alignments and filtered horizontal offset from the correlation tool with the unaltered pre-earthquake data. If successful, this would return a vertical displacement field, as well as what were expected to be relatively small horizontal adjustments additional to the previous horizontal offset. However, I found that the results using an initial window size of 40 m (and other trial window sizes) were very noisy, and did not yield a clear signal in any deformation field, even when visualisation of the results was limited by the exclusion of clearly erroneous values. I therefore decided not to use the results from the ICP process in the inversion.

3.6 Modelling set-up

3.6.1 Introduction

In order to model surface displacements, I jointly inverted eleven sets of geodetic data for slip across the time interval covering the Norcia earthquake, following the method of Floyd et al., 2016 which uses a modified version of the slipinv code (Funning et al. 2005). I assumed that surface displacements result from slip on multiple rectangular patches on a fault plane in an elastic half-space (Okada, 1985). I applied spatial smoothing (or regularisation) to the slip distributions using a Laplacian operator (Harris and Segall 1987), aiming to suppress instabilities in the inverse solution caused by noisy and/or incomplete data (Menke and Eilon, 2015). The datasets used for the inversion are described below. This method requires setting fault geometry for the fault segments identified, including dip, rake, fault slip depths, and patch discretisation (each discussed in further detail below). In order to reflect the detail of distributed slip seen at the surface in the Pleiades data, I adopted an approach of detailing relatively small features when setting the fault geometry in the areas covered by the Pleiades data, resulting in a total of nineteen fault segments.

3.6.2 Modelling input datasets

3.6.2.1 Selection of Pleiades data by area and proximity to main faults

As described above, I derived separate results from the Pleiades data for deformation in the t_x, t_y, and t_z dimensions (each comprising 3503751 data points for the eastern area). In order to make the data usable within the inversion process, and confining those datasets to the eastern area to avoid the bias from the sinusoidal effect, I then selected only points which were within 1 km of the modelled Monte Vettore and associated faults. This selection was aimed at excluding results from the footwall area which lies to the east behind the Monte Vettore ridge away from the main scarp and distributed deformation in the hanging wall. Many of those points were considered potentially to be unreliable due to the absence of data in one or more of the datasets, possibly due to shadow, snow coverage or near-vertical topography (see **para 3.3.2**). Median values were then taken over 120 m x 120 m blocks to reduce the data file sizes to ~1500 points due to computational restrictions within the modelling process.

3.6.2.2 ALOS and Sentinel-1 InSAR

The Pleiades pre-earthquake image (29th October 2016) post-dates the Visso earthquake on 26th October 2016. For consistency, I therefore chose InSAR datasets from the Sentinel-1 and ALOS-2 satellites which temporally cover only the Norcia earthquake (and not a combination of that earthquake and others). The InSAR data pairs identified covered 27th October and 2nd November 2016 (Sentinel-1) and 28th October and 11th November 2016 (ALOS-2). The InSAR data used in the inversion was in the form of previously processed and unwrapped interferograms with orbital correction, removal of topographic effects, manual rechecking and resampling as described in Walters et al., 2018, producing ~1500 line-of-sight data points per interferogram.

3.6.2.3 GNSS (Global Navigation Satellite System)

I used a short-baseline GNSS dataset for the Norcia earthquake, from Wilkinson et al., 2017, with t_x, t_y, and t_z results from 2 hanging wall/footwall pairs of near-fault campaign sites, with GNSS receiver pairs placed at a distance of ~6.2 km apart along strike either side of the main Monte Vettore Fault scarp. The pairs had respective

baselines of ~1.3 and ~1.8 km. I also used a regional GNSS dataset for the Norcia earthquake, from INGV, 2016, with t_x, t_y, and t_z results from the INGV CaGeoNet network, the Istituto Geografico Militare network, an INGV-RING continuous GPS station at Arquata del Tronto and other GPS instruments installed locally following the Visso earthquake.

The locations and coverage of the respective datasets are shown in **Figure 42**.

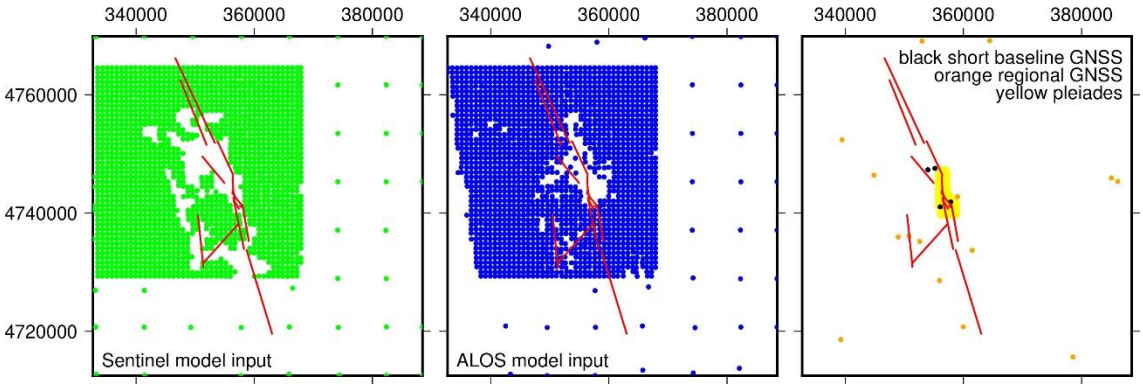

Figure 42: *Location and coverage of datasets used in modelling. Red lines modelled fault segments (see below). LH panel Sentinel InSAR, middle panel ALOS InSAR, RH panel far-field GNSS (orange), short baseline GNSS (black) and Pleiades data (yellow).*

3.6.3 Fault geometry model

3.6.3.1 Fault location in fault geometry model

In modelling the fault geometry, I defined a simplified array of faults, in order to relate geodetic measurements of slip at the surface to sub-surface slip. This approach is consistent with previous practice for geodetic modelling of complex (multi-segment) fault systems with events of similar size to the Norcia earthquake (e.g. Elliott et al., 2016, Floyd et al., 2016).

The choice of fault geometries relies in part upon the datasets modelled, and also upon additional geological or geophysical constraints. In this case, the far-field geometries adopted are based and rely upon the choice of geometries made in Walters et al., 2018 (see **Figure 26**).

The faults identified in figure 1c of Walters et al. as the Laga Fault, Pian Piccolo Fault, Norcia Antithetic Fault, the minor antithetic fault, and the two northern most

segments of the Monte Vettore fault lie outside the area covered by the Pleiades data I have used in the inversion. I have adopted their surface geometries without alteration, save for a small alteration to the dip of the Norcia Antithetic Fault, explained below.

I anticipated that the detail proved by the Pleiades data will enable me to retrieve higher-detail information on fault slip in the near-surface area than previous models have done. The model geometries of the fault structure in the area covered by the Pleiades data and the fault segments modelled therefore need to be in more detail and at finer scale than the far-field fault segments in order to ensure an acceptable fit of the model to the Pleiades data. I have therefore added to or adapted the nine model faults used by Walters et al., to give a total of nineteen fault segments. This has involved more detailed segmentation of the main Monte Vettore fault area, and the addition of more detailed synthetic and antithetic structures in its hanging wall.

The more detailed surface geometry of the faults is shown in **Figure 43**, showing respectively the wider fault geometry in the context of the extent of the coverage provided by the Pleiades data (LH panel), and the detail of the modelled fault geometry within that central area (RH panel).

By using the detail of the three Pleiades results (t_x, t_y, and t_z) and contemporaneous field data this enabled me to model the central section of the main Monte Vettore fault (between the Northings of 4747500 UTM 33T and 4739500 UTM 33T) as a section of interconnecting shorter segments at different strikes, including two spurs where the segments apparently continue into the hanging wall. The location of these segments is shown in red on **Figure 43**. In addition, the antithetic segments in the hanging wall of the main Vettore fault are modelled in more detail (in purple), as are the synthetic segments (in dark green).

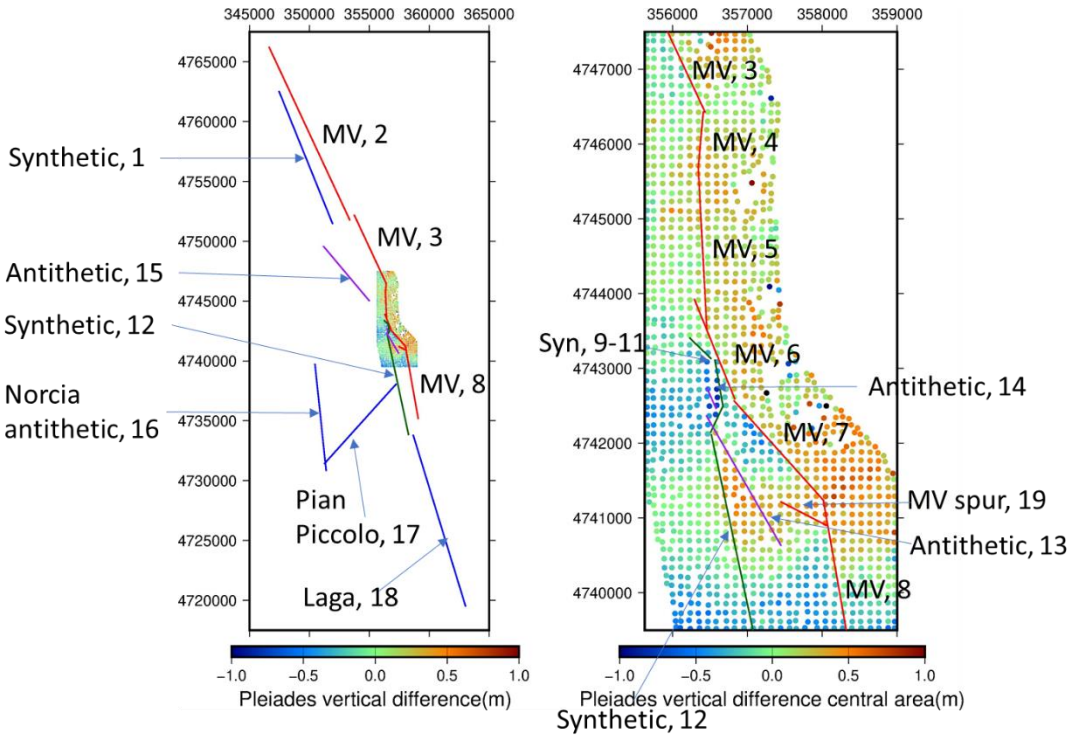

Figure 43: *Modelled fault surface geometry (LH panel), showing extent of Pleiades data coverage compared to wider area covered by InSAR and GNSS data. Red fault segments are the main Monte Vettore fault, dark green synthetic, purple antithetic and blue far-field fault segments. Detail of central area with extent of Pleiades data coverage (here showing vertical difference) (RH panel). The numbers shown are used to identify individual fault segments in the results section and elsewhere below.*

By way of comparison with the use of less detailed fault geometry in the area covered by the Pleiades data, **Figure 44** shows the vertical results from the Pleiades differencing, set against the surface geometry of the model faults used in Walters et al., 2018.

The model fault geometry used by Walters et al., 2018 is the most complicated geometry used in any of the previous published inversions. However, as this figure shows, the geometry used there does not fit well with the deformation patterns seen in the Pleiades results. It also leads to a worse fit of the model to the Pleiades data, especially in relation to the vertical results (see further, at **para 3.7.2.1** below).

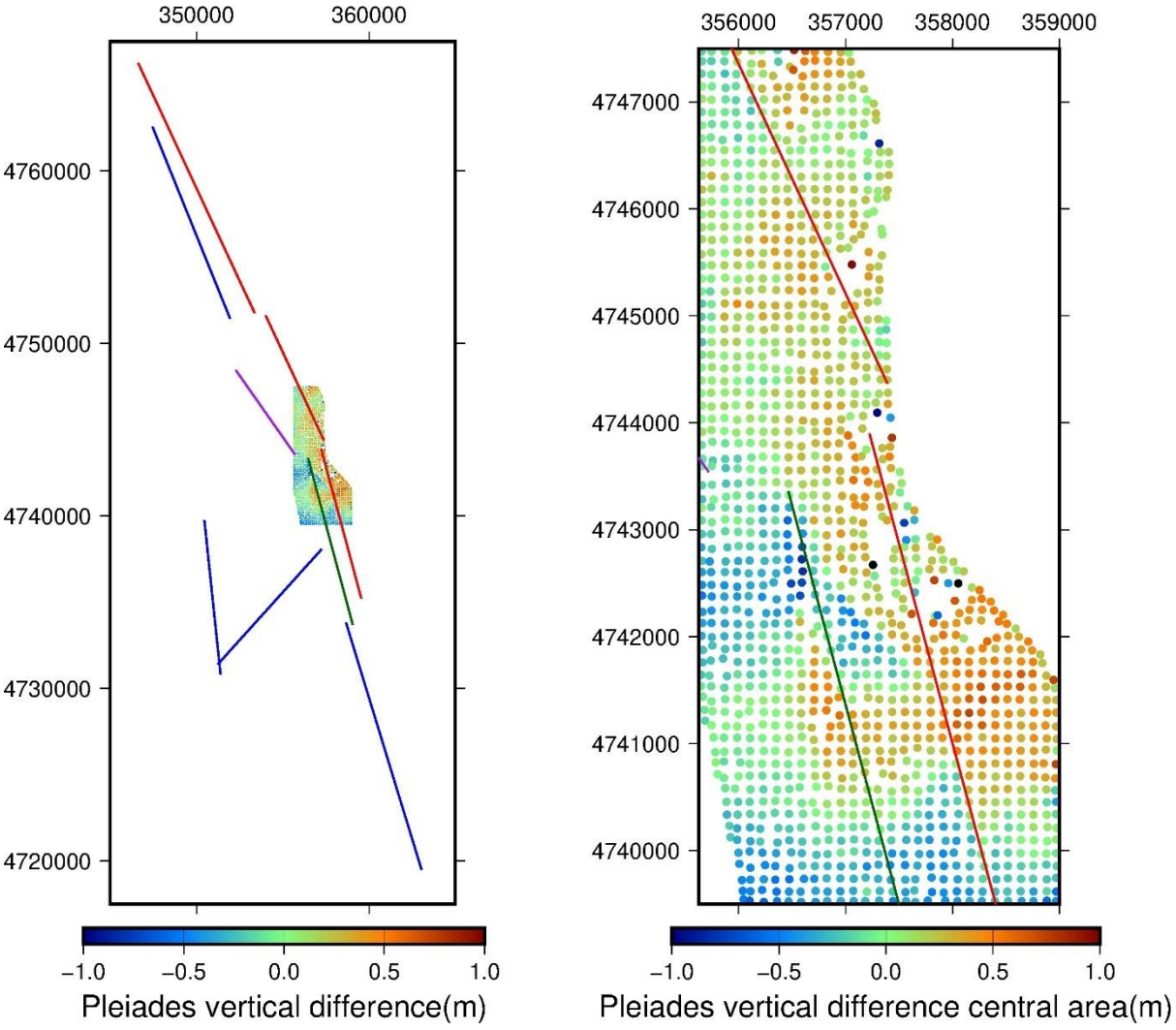

Figure 44: *Results of vertical differencing of Pleiades datasets, set against surface fault geometry used by [Walters et al., 2018](), LH panel showing far-field, RH panel detail of Pleiades results. Red fault segments are the main Monte Vettore fault, dark green synthetic, purple antithetic and blue far-field fault segments.*

By comparison, the fit of the geometry to the Pleiades "observed" data in the modelling process is visually much closer (**Figure 45**).

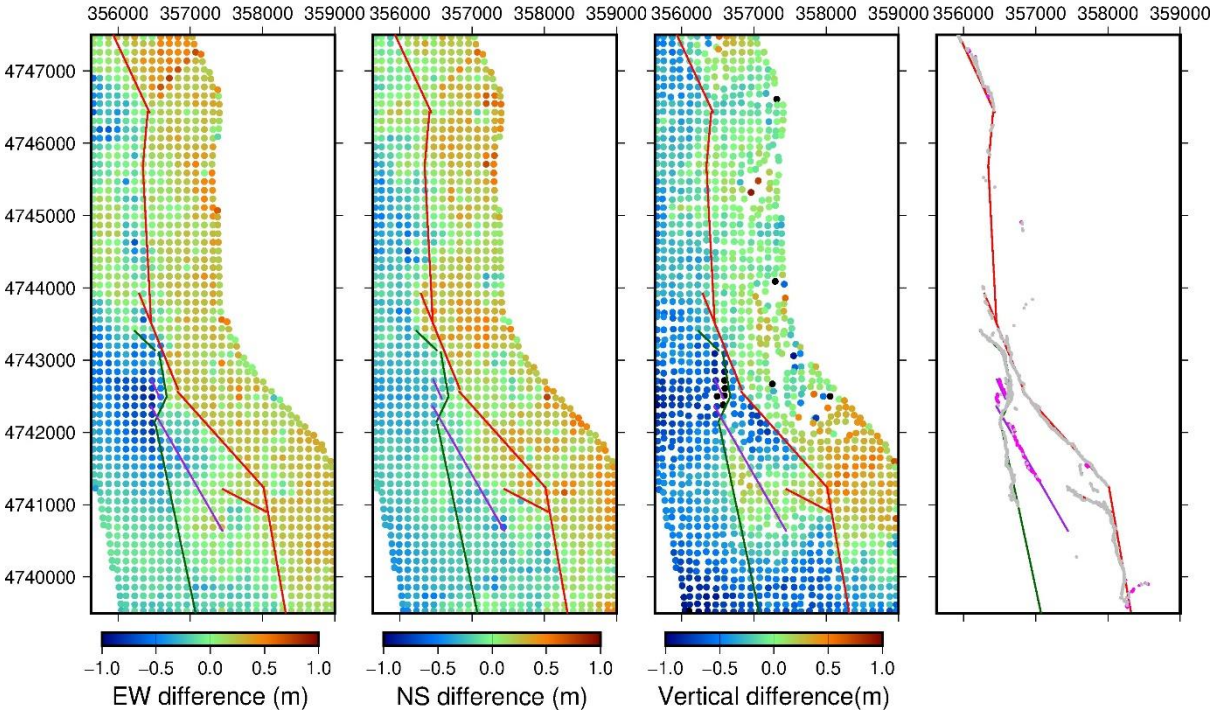

Figure 45: *Surface geometry of modelled faults in central area set against observed data from Pleiades differencing (east-west, north-south and vertical respectively, Panels 1-3). 4th panel shows fault geometry overlain by field locations recorded by Open EMERGEO Working Group (from Villani et al., 2018) with synthetic (grey) and antithetic (magenta) dip directions.*

In the area covered by the Pleiades data my initial choice of fault surface geometry was guided by a mixture of field observations (as recorded in 2016 by the Open Emergeo Joint Working Group, Villani et al., 2018, supplemented by Google Earth), and the Pleiades results themselves. I have divided the main Monte Vettore fault in this central area into segments with differing strikes, following the deformation pattern seen in the east-west and vertical displacement fields in the observed data in the model (and, to a lesser extent, the north-south displacement field).

Using the numbering of the fault segments given in **Figure 43**, I relied on field records to identify faults in one area of potential uncertainty at fault 4 (at ~4746000N) where the Pleiades signal is not clear. Spurs off the main structure (part of fault 6, and fault 19) are modelled as secondary structures, relying primarily on field data locations, but both are consistent with the Pleiades results in all three dimensions. Antithetic and synthetic structures are primarily guided in their detailed geometry by field data, but

faults 12 (synthetic) and 13 (antithetic) have both been extended to the south of the field data results, as the "horst" structure between those faults extends further south in the Pleiades vertical displacement results.

Although I considered adding 2 further shallow "spur" structures striking southwest-northeast at ~220^{o} from the main Monte Vettore fault at the junctions of faults 3/4 and 7/8 respectively, these are not shown in the field data, and the Pleiades data on their own did not justify those additions. The field data show another possible structure striking at ~210 ^{o} at the junction of faults 5/6 on the main Monte Vettore fault but this does not appear in the Pleiades data.

In my overall approach, I have also sought to avoid over-complicating the fault geometry to avoid "overfitting" the model to the data. The minor fault segments I have chosen to use were added incrementally and adjusted as the model developed and appeared to improve the model fit.

I compared our final results with an alternative model which omits some of the finer detail I used in the hanging wall, omitting faults 9-11 (synthetic), 14 (antithetic) and 19 (spur off the Monte Vettore fault) and elongating faults 12 (synthetic) and 13 (antithetic). Using this model with 14 fault segments, I found that in all cases, the fit of the model to data was marginally worse than the geometry I applied in both the far-field data (InSAR and far-field GNSS), and the near-fault data (Pleiades and relative GNSS – the latter in particular). Some of the modelled slip transfer from the main Monte Vettore fault to the main synthetic fault using this less detailed fault set-up was unrealistic, compared to the more diffuse deformation seen in the field at the surface. A table showing the relative RMS misfits for that alternative model appears in **Appendix 3A**, together with figures showing the geometry used in that comparative exercise and the resulting slip vectors.

3.6.3.2 Selection of dips/rakes/fault slip depths and patch discretisation within fault geometry model

In addition to the surface position of the fault segments, the model also requires individual settings of fault dip and rake. As with the surface position of the far-field fault segments (the Laga Fault, Pian Piccolo Fault, Norcia Antithetic Fault, the minor

antithetic fault, and the two northern most segments of the Monte Vettore fault), the dip selection for those faults is unaltered from the settings used in Walters et al., 2018, set at 40^{o} from horizontal. Two variable rake components are assumed for each of the segments, set at 90^{o} apart, to allow for the spatially varying rake suggested by field data showing varying degrees of oblique slip in most locations (Open EMERGEO Working Party, Villani et al., 2018).

Table 3.6 shows the strike, dip, rake, length, dip and patch discretisation used for each fault segment.

The two exceptions to following this approach for the far-field faults are the Norcia Antithetic fault and the Pian Piccolo fault. As noted in Walters et al., 2018, the Norcia Antithetic structure is not well-constrained. Initial tests with the dip of that fault set at 40^{o} to vertical resulted in improbable interaction between that fault and the Pian Piccolo fault at depth. The relocated aftershock clouds covering this fault segment in Chiaraluce et al., 2017 (**Figure 46**), suggest a structure with a significantly steeper dip, and with that as a guide, I have used a dip of 70^{o} from horizontal. Similarly, given the interaction between the Pian Piccolo fault at depth and the Norcia Antithetic fault and the Monte Vettore and the synthetic faults to the east of the Pian Piccolo fault, I tested a number of settings for rake for the Pian Piccolo fault as pure dip-slip appeared an unrealistic assumption. Ultimately, a setting with partial left-lateral slip was applied.

In each of these cases I applied a mask (by fixing slip at zero) to partially exclude areas where slip on fault patches would clearly overlap. In the case of the Norcia fault I masked patches at the southern end where slip on those fault patches would overlap with slip on the Pian Piccolo fault (allowing for their respective dips). Similarly, at the northeastern end of the Pian Piccolo fault I have masked areas which would coincide with slip on the Monte Vettore fault. In doing so, I have followed the approach taken in Walters et al., 2018 in this area (if not the exact geometry because of the differing dip applied for the Norcia fault).

Table 3.6 - Individual fault segment settings used within fault geometry model.

Fault no	Strike	Dip	Rake	Length (km)	Depth (km)	Number of patches (along strike)	Number of patches (down dip)	Patch length along strike (km)	Patch length down dip(km)
1	158	40	-135/-45	12	5	12	5	1.00	1
2	155	40	-135-45	16	5	16	5	1.00	1
3	155	40	-110-20	6.4	10	13	20	0.49	0.5
4	185	45	-80/10	0.75	10	3	40	0.25	0.25
5	177	45	-88/2	2.2	10	10	40	0.22	0.25
6	158	45	-127/-37	1.45	10	6	40	0.24	0.25
7	138	45	-147/-57	1.8	10	8	40	0.23	0.25
8	170	40	-135/-45	6.2	10	12	20	0.52	0.5
9	133	65	-132/-42	0.4	3	2	12	0.20	0.25
10	170	65	-95/-5	0.65	3	3	12	0.22	0.25
11	205	65	-60/30	0.4	3	2	12	0.20	0.25
12	168	50	-95/-5	8.5	3	17	6	0.50	0.5
13	330	70	-165/-75	2	1	8	4	0.25	0.25
14	335	70	-165/-75	0.3	1	1	4	0.30	0.25
15	320	40	-165/-75	6	2	6	2	1.00	1
16	354	70	-135/-45	9	5	9	5	1.00	1
17	222	40	-102/-12	9	8	9	8	1.00	1
18	163	45	-135/-45	15	10	15	10	1.00	1
19	118	45	-157/-67	0.7	3	3	12	0.23	0.25

Slip on the Norcia antithetic fault has been modelled down to 5 km, based on relocated aftershock data in Chiaraluce et al., 2017 where it intersects with the main Monte Vettore Fault (**Figure 46**).

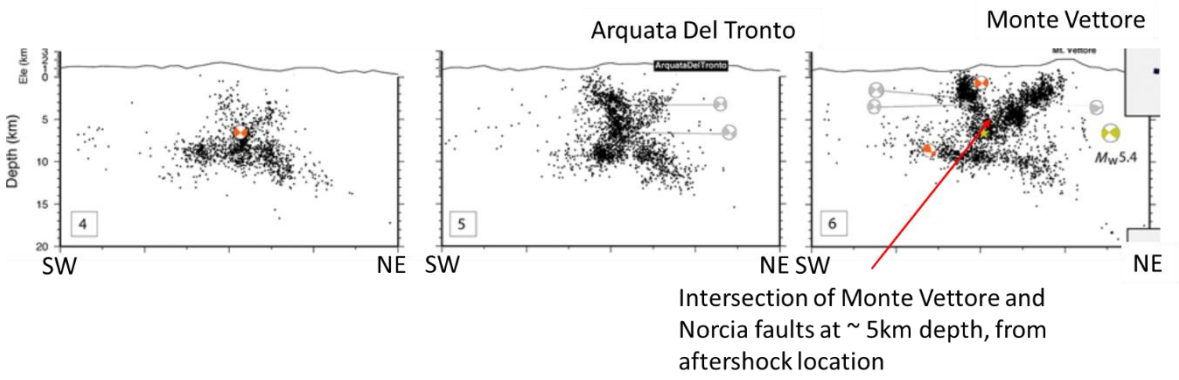

Figure 46: *Adapted extract from figure 3, Chiaraluce et al., 2017. Black dots, aftershocks' distribution with depth, centred on M_w 6.5 location. Sections are oriented orthogonally to the strike (155°) direction. For each section, focal mechanisms related to M_w ≥4:0 earthquakes are reported (grey, before the Norcia earthquake and orange, after the Norcia earthquake).*

The differences in the degree of discretisation used in each case are intended to reflect the relative extent of the detail in the datasets used in the inversion for the respective areas, without biasing the results.

A full table of the fault geometry is in **Appendix 3A.**

3.6.4 Inversion settings

3.6.4.1 Shear

Shear modulus (the response of material to shear stress) is set at 30 GPa, a typical figure for carbonate rocks. The Poisson ratio (the response of materials in directions orthogonal to uniaxial stress) is set at 0.25 (again, a typical value for carbonate rocks).

3.6.4.2 Offsets/ramps

In modelling slip on each patch I solved for line-of-sight offsets for the InSAR datasets. I also solved for an offset for each of the Pleiades and relative (short baseline) GNSS datasets to correct for any difference in relative positions of the datasets. I solved for x- and y-gradients (ramps) in respect of the Pleiades and InSAR datasets to remove any

inherent biases in those datasets. I applied a non-negative least squares constraint on the inversion to eliminate retrograde motion on the fault patches.

3.6.4.3 Relative weighting of datasets

In view of the considerable variance between the different datasets in terms of scale of geographical coverage, number of measurements, and the standard deviations within each dataset, I tested a number of variations in the respective weightings of the datasets to try to achieve the balance of overall relative weightings which best fitted all of the data without significantly increasing the misfits between the model and one or more of the datasets. I started with testing relative weightings of the Pleiades datasets and InSAR datasets and applied the inversion using only those datasets.

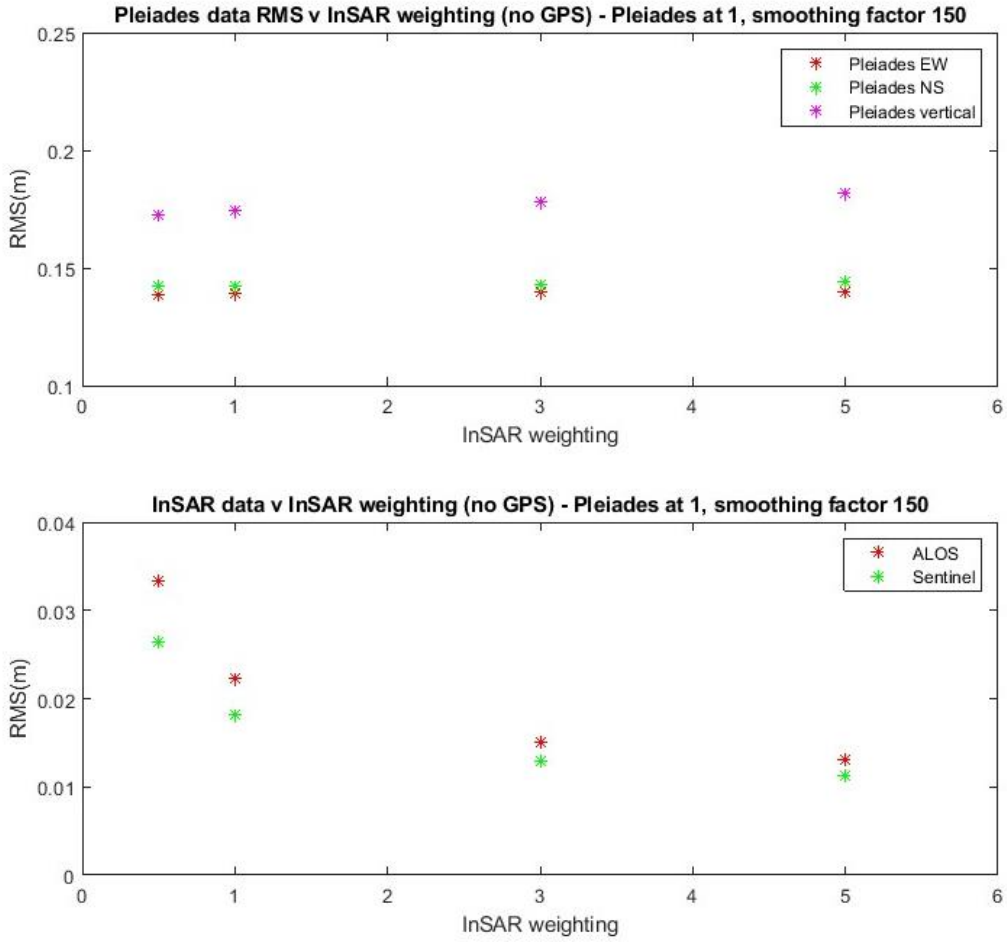

Figure 47: *Illustration of model RMS (Root Mean Squared) misfits between Pleiades (top panel) and InSAR (lower panel) datasets to model, using different weightings for InSAR datasets (Pleiades datasets weighting = 1 throughout).*

I subsequently added first the regional (far-field) GNSS then the relative (short baseline) GNSS datasets. In each case I was looking to achieve the best balance of outcomes in respect of misfits compared to standard deviation in sample areas of the datasets away from the areas of main deformation (**Figures 47 to 49)**.

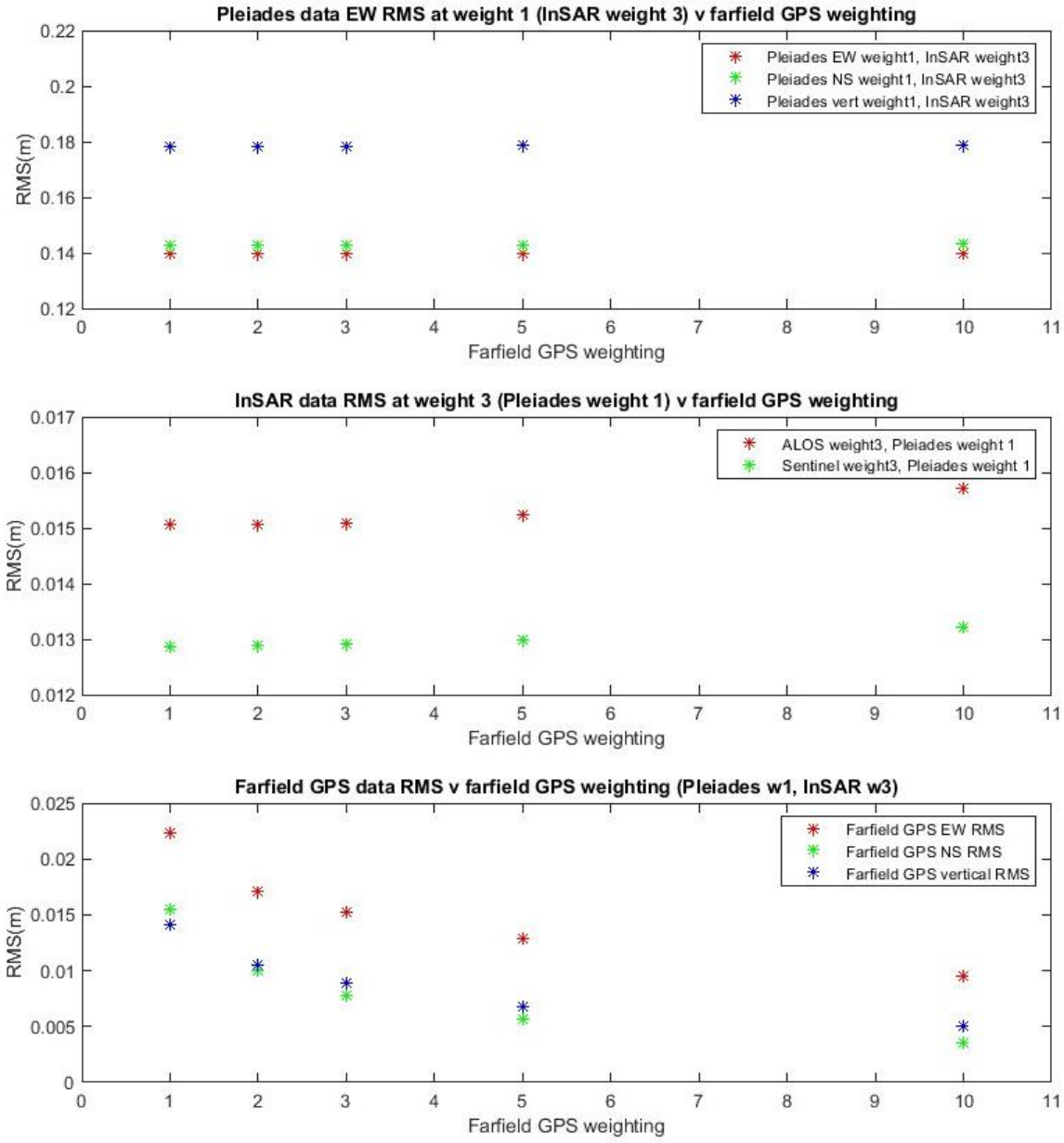

Figure 48: *Illustration of model RMS misfits between Pleiades (top panel) InSAR (middle) and farfield GNSS (lower panel) datasets to model, using different weightings for farfield GNSS datasets (Pleiades datasets weighting = 1, InSAR weighting = 3).*

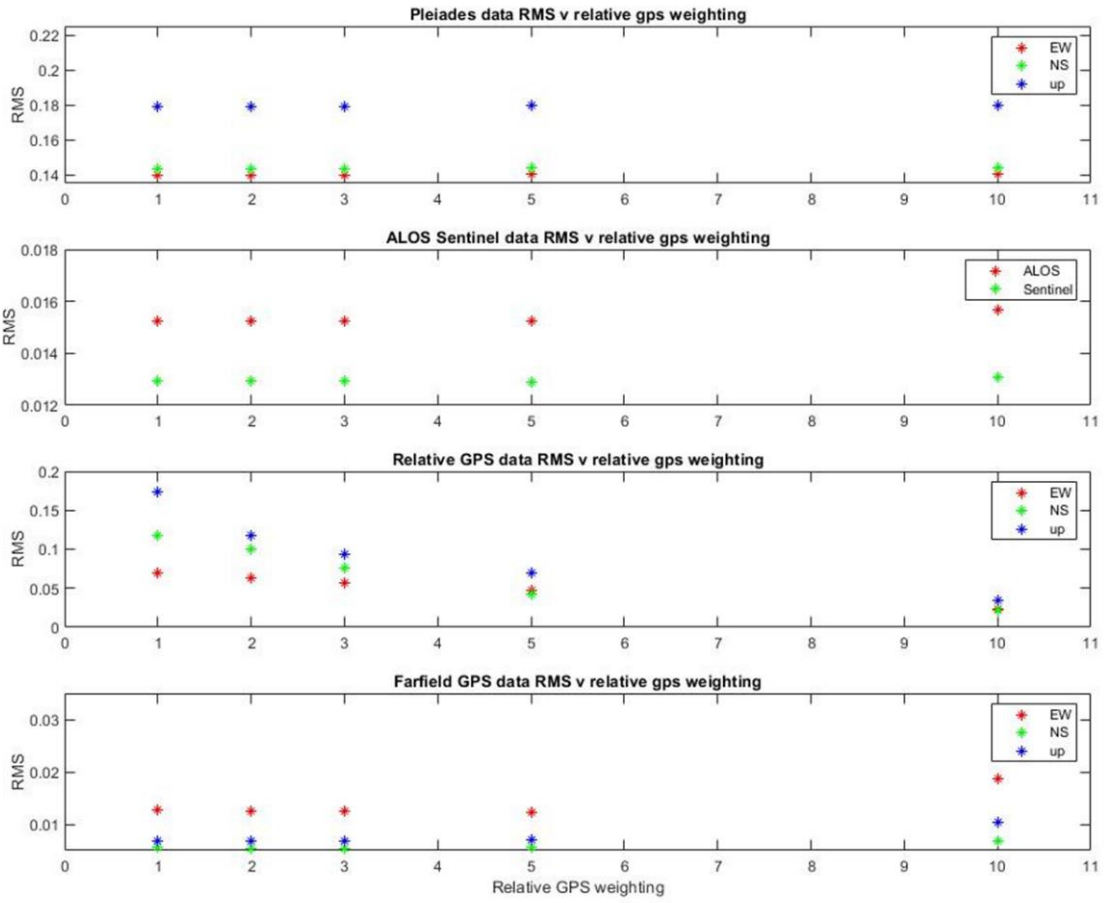

Figure 49: *Illustration of model RMS misfits between Pleiades (top panel) InSAR (upper middle), relative GNSS (lower middle) and Far-field GNSS (lower panel) datasets to model, using different weightings for relative GNSS datasets (Pleiades datasets weighting = 1, InSAR weighting = 3, far-field GNSS weighting = 5).*

I concluded that the best balance of weightings was Pleiades datasets (1), InSAR datasets (3), regional GNSS datasets (5), and relative GNSS datasets (5**).**

3.6.4.4 Choice of smoothing factor

The inversion is regularised using a Laplacian smoothing factor. The factor chosen is a balance between the smoothness of the overall result and its fit to the data. I tested various factors within what I considered to be reasonable bounds. I applied a smoothing factor of 150 as this represented a reasonable compromise between a range of factors. A lower smoothing factor (e.g. 100) increased the peak magnitude of slip and overall moment. Although not significantly affecting its spatial pattern, a lower smoothing factor of 100 resulted in patchy results for some of the far-field fault

segments. This effect was exacerbated using lower values still, such as 50, which produced unrealistic results. Improved RMS misfit values suggest that, with a lower smoothing factor, the model is perhaps overfitting to the Pleiades data. A higher smoothing factor (e.g. 200) has the opposite effect, with a reduced peak magnitude of slip and overall moment. Although less patchy, the overall effect was of over-smoothing, limiting the amount of near-surface detail. Figures showing the respective slip outputs by individual fault segments using smoothing factors of 100, 150 and 200, together with a table showing the respective RMS misfit values including use of a smoothing factor of 50 is in **Appendix 3A**. The comparative effect of the choice of differing smoothing factors on the final slip model is shown in **Figure 64** below in the modelling results section.

3.6.4.5 Using Monte Carlo techniques to assess uncertainties in slip

It is common practice with this type of inversion to check for 2-sigma uncertainties in slip using a Monte Carlo approach, perturbing each Pleiades, InSAR and GNSS dataset ~100-200 times with simulated realistic noise and inverting each of those perturbed collated datasets (e.g. Funning et al., 2005 Appendix B; Floyd et al., 2016). The standard deviation of those values for each fault patch is then used as an estimate of the 1-sigma uncertainty. Walters et al., 2018's Supplementary figure S6 shows the results of the use of those techniques on the far-field data used in this inversion. It was beyond the scope of this thesis to make a similar calculation in the time available.

3.7 Results of modelling

3.7.1 Overall model.

In summary, my final slip model (**Figure 50**) shows:

- slip is concentrated primarily at about 4-6 km depth on central segments of the main Monte Vettore fault (faults numbered 4-7), reaching ~4 m of slip in an area between Northings ~4742000-4745000 UTM 33T;
- there is widespread variation along strike at the near-surface on the main Monte Vettore fault, with predominantly left-lateral movement within the uppermost 1 km;

- there is distributed faulting involving the minor hanging wall faults and spurs from the main Monte Vettore fault (faults 9-11, 12-14 and 19), also showing left-lateral kinematics within the uppermost 1 km; and
- significant slip (up to ~5 m in one patch) is accommodated on the Pian Piccolo fault (fault 17) in a pattern which is heavily influenced by the neighbouring synthetic (fault 12) and Norcia (antithetic) (fault 16) fault patches, as well as the southern-most end of the Monte Vettore fault (fault 8).

The total moment release (M_o) is 1.547e+19 Nm, equivalent to ~M_w 6.7263.

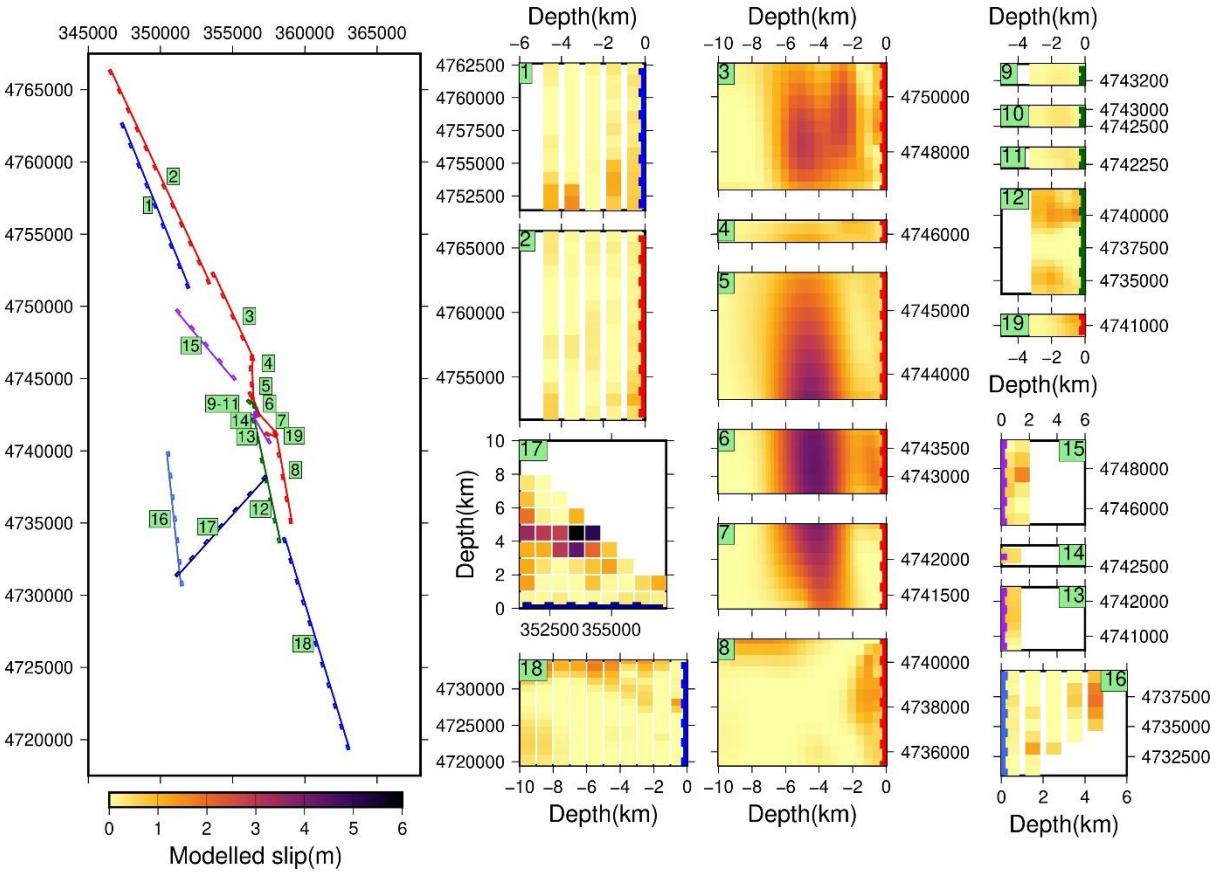

Figure 50: *Results of joint inversion showing slip on individual fault segments by discretised patch. The patches are projected to show dip relative to the surface in 2D. Location of the surface in each case is shown by a thicker line, with ticks showing dip direction. The numbers of each individual fault segment correspond to the locations shown in the plan figure (LH panel).*

Slip components (size and vector) are shown by individual fault segment in **Appendix 3A**.

A more detailed view of slip in the central area is shown in **Figure 51**. Both figures model interaction between slip on fault 7 (Monte Vettore) and faults 13 and 14 (antithetic), 12 (synthetic), and 19 (spur off the Monte Vettore fault). In particular slip is widely distributed between the main Monte Vettore fault and the subsidiary structures in the 2 km below the surface.

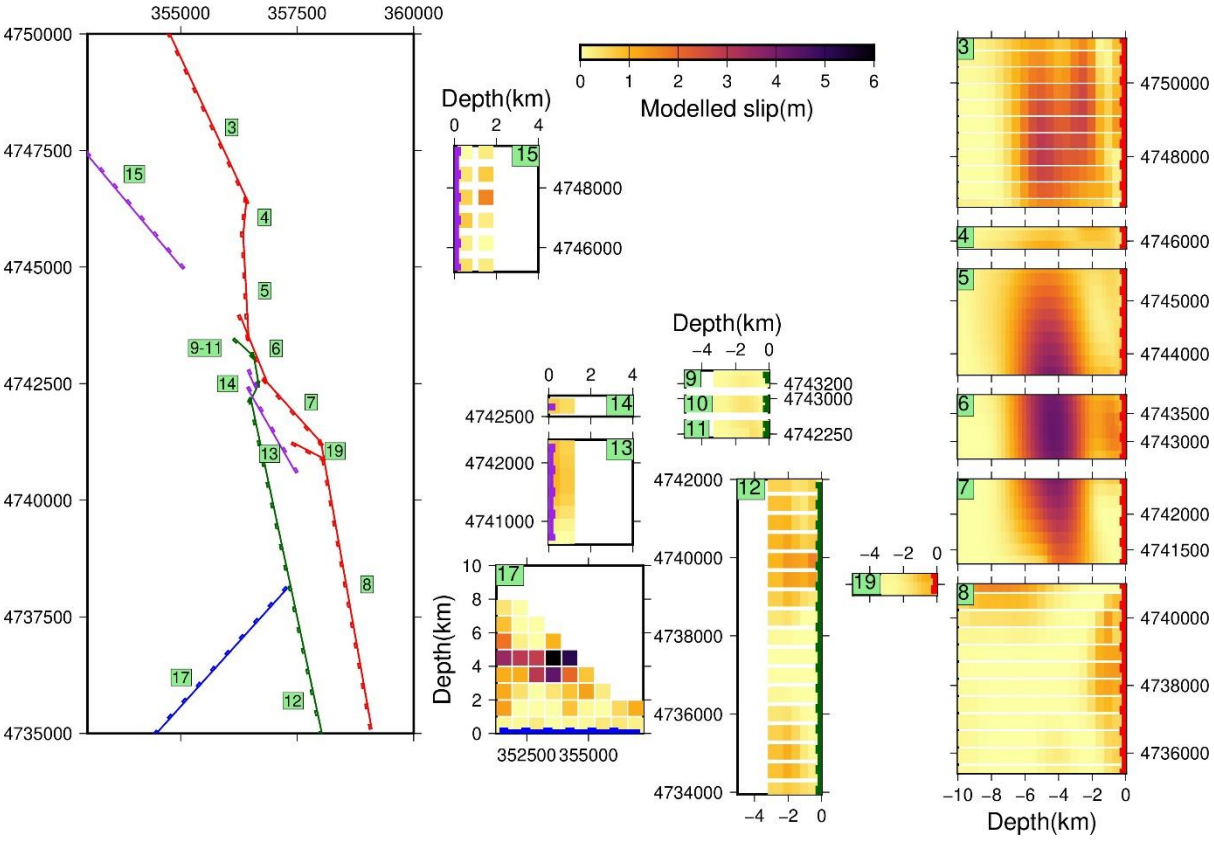

Figure 51: *Results of joint inversion in central area showing slip on individual fault segments by discretised patch. Location of the surface in each case is shown by a thicker line, with ticks showing dip direction. The numbers of each individual fault segment correspond to the locations shown in the plan figure (LH panel).*

In order to aid visualisation in a summary figure the slip vectors slip vectors at depth for the central area have been down-sampled to 1 km x 1 km patches, although in many case the patches modelled for the central area were smaller in size (typically ~0.25 km x 0.25 km) (**Figure 52**).

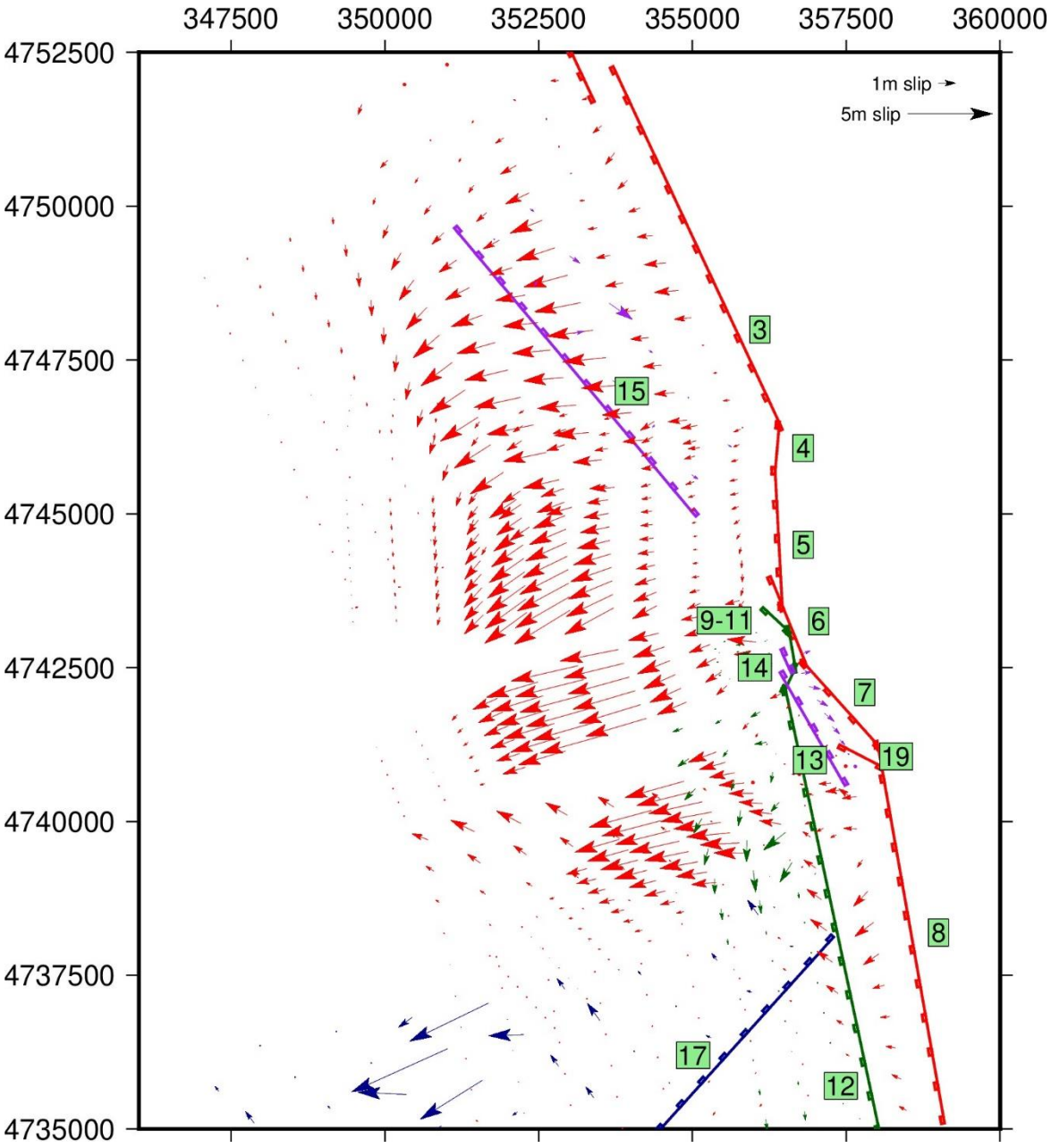

Figure 52: *Orientation and magnitude of slip vectors resulting from joint inversion in central area showing slip at depth projected in 2D onto the surface, down-sampled to ~1 km x 1 km patches. Colours of vectors shown match faults shown at surface.*

More detailed zoomed-in figures of near-surface slip with less down-sampling are shown in **Figures 54 and 55**.

As some of the fault patches show little or no slip and therefore are invisible on this figure, **Figure 53** shows the size of the slip vectors by fault patch for the same area, including patches with zero slip.

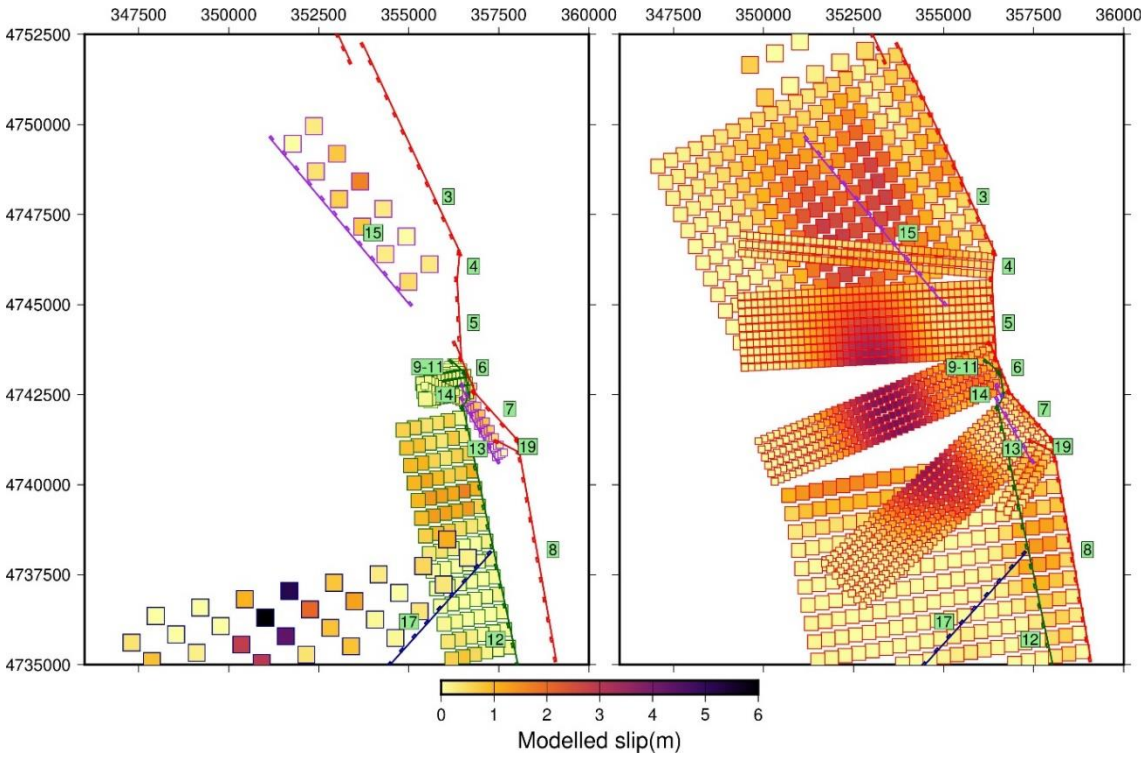

Figure 53: *Illustration of magnitude of slip vectors by fault patch in the central area split for ease of visualisation between Monte Vettore fault segments (RH panel) and other faults (LH panel).*

A more detailed figure showing slip in the upper-most 3 km in the area of main co-seismic slip, down-sampled at ~0.5 km gives a clearer image of the relationship between slip in the uppermost 1 km and down to ~5 km below that (**Figure 54**). A further zoomed-in figure without down-sampling shows the detail of slip in the uppermost 1 km (**Figure 55**). The slip vectors in the top 1-2 km depth differ significantly in both orientation and location from those at greater depth, with slip being partitioned onto minor structures in the near-surface, and at vectors oblique to the largely regular vectors (towards ~205^{o}) at greater depth on the principal structures.

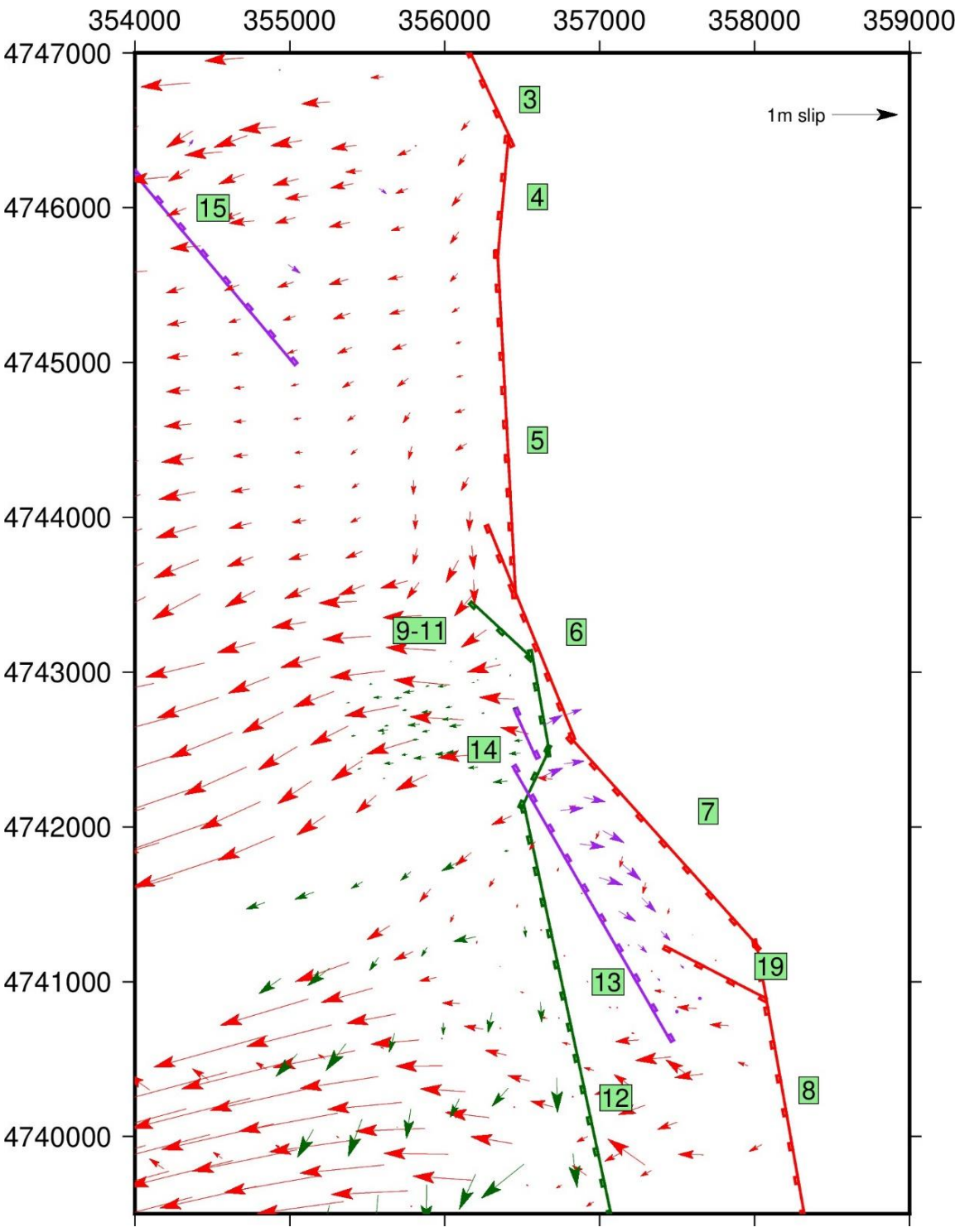

Figure 54: *Orientation and magnitude of slip vectors resulting from joint inversion in central area showing detail of slip at depth in upper ~3 km below surface, projected in 2D onto the surface, down-sampled to ~0.5 km x 0.5 km patches. Colours of vectors shown match faults shown at surface.*

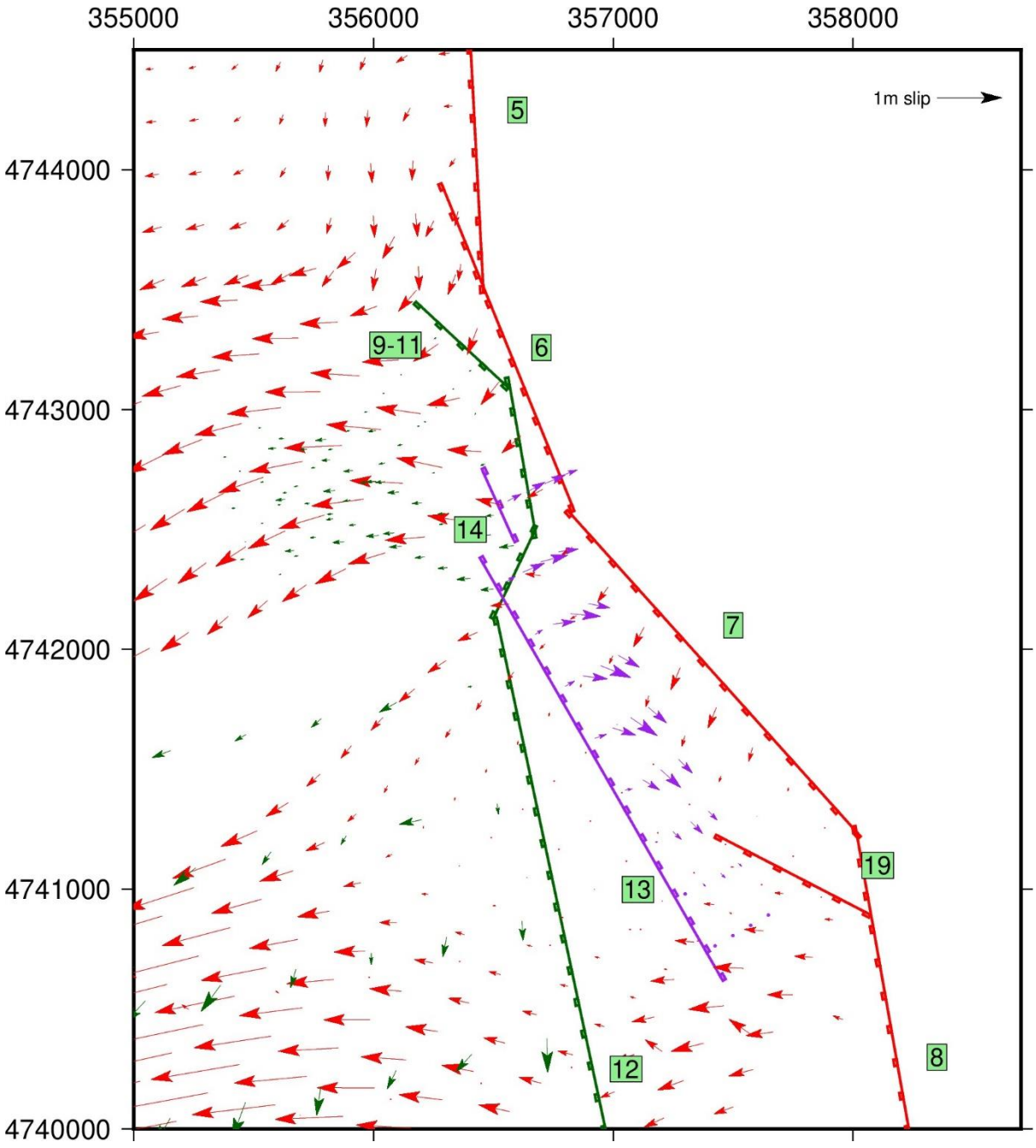

Figure 55: *Orientation and magnitude of slip vectors resulting from joint inversion in central area showing detail of slip in near-surface area projected in 2D onto surface, without down-sampling. Colours of vectors shown match faults shown at surface.*

Figure 56 shows slip on the Pian Piccolo fault (fault 17) and the faults adjacent to it (fault 16 Norcia antithetic, fault 12 synthetic, fault 8 part of Monte Vettore, and fault 18 Laga). The modelled interaction between fault 17 and its neighbours can be seen more clearly from this figure.

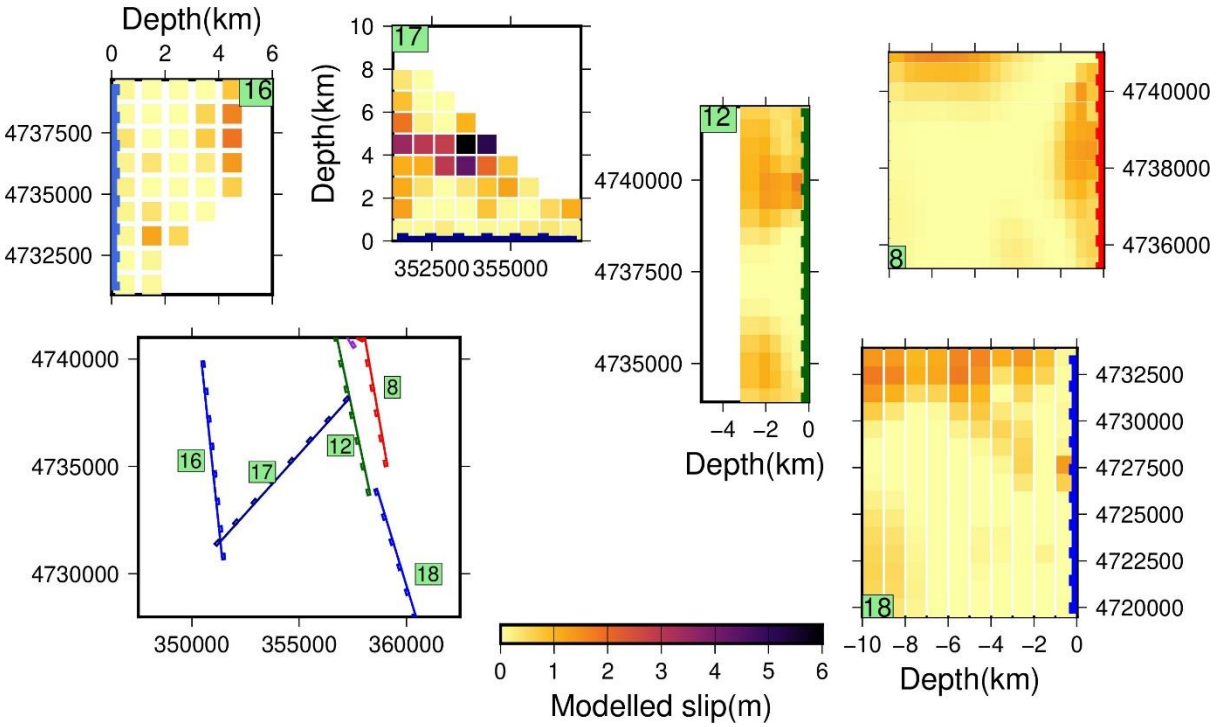

Figure 56: *Results of joint inversion in Pian Piccolo area showing slip on individual fault segments by discretised patch. Location of surface in each case shown by a thicker line.*

The slip vectors at depth for the Pian Piccolo area are shown in **Figure 57**. As before, in order to aid visualisation the slip vectors have been down-sampled to 1 km x 1 km patches.

3D views of the overall displacements over the wider area (respectively from SW and NE perspectives) are shown in **Figure 58**.

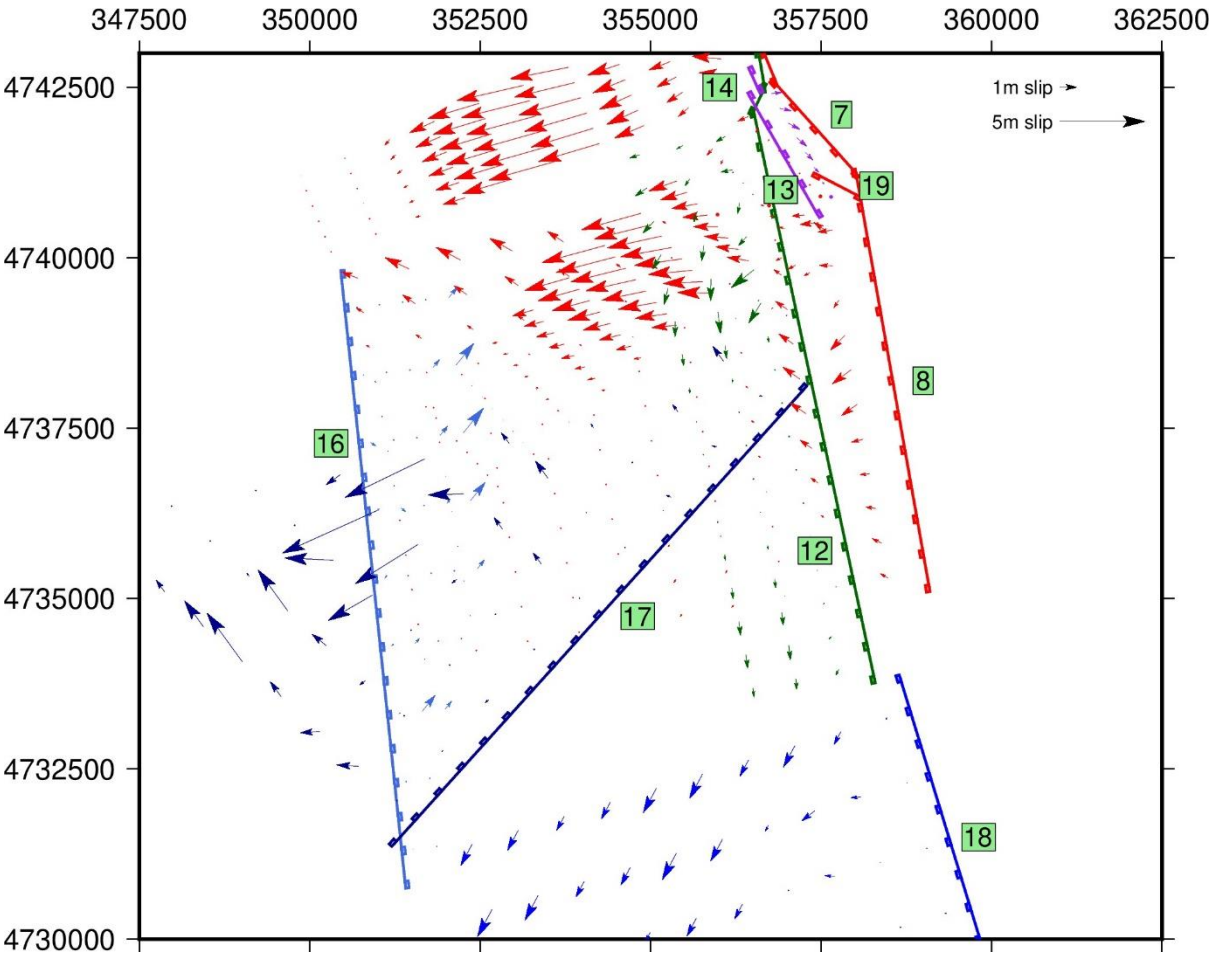

Figure 57: *Orientation and magnitude of slip vectors resulting from joint inversion in Pian Piccolo area showing slip at depth projected in 2D onto the surface, down-sampled to ~1 km x 1 km patches. Colours of vectors shown match faults shown at surface.*

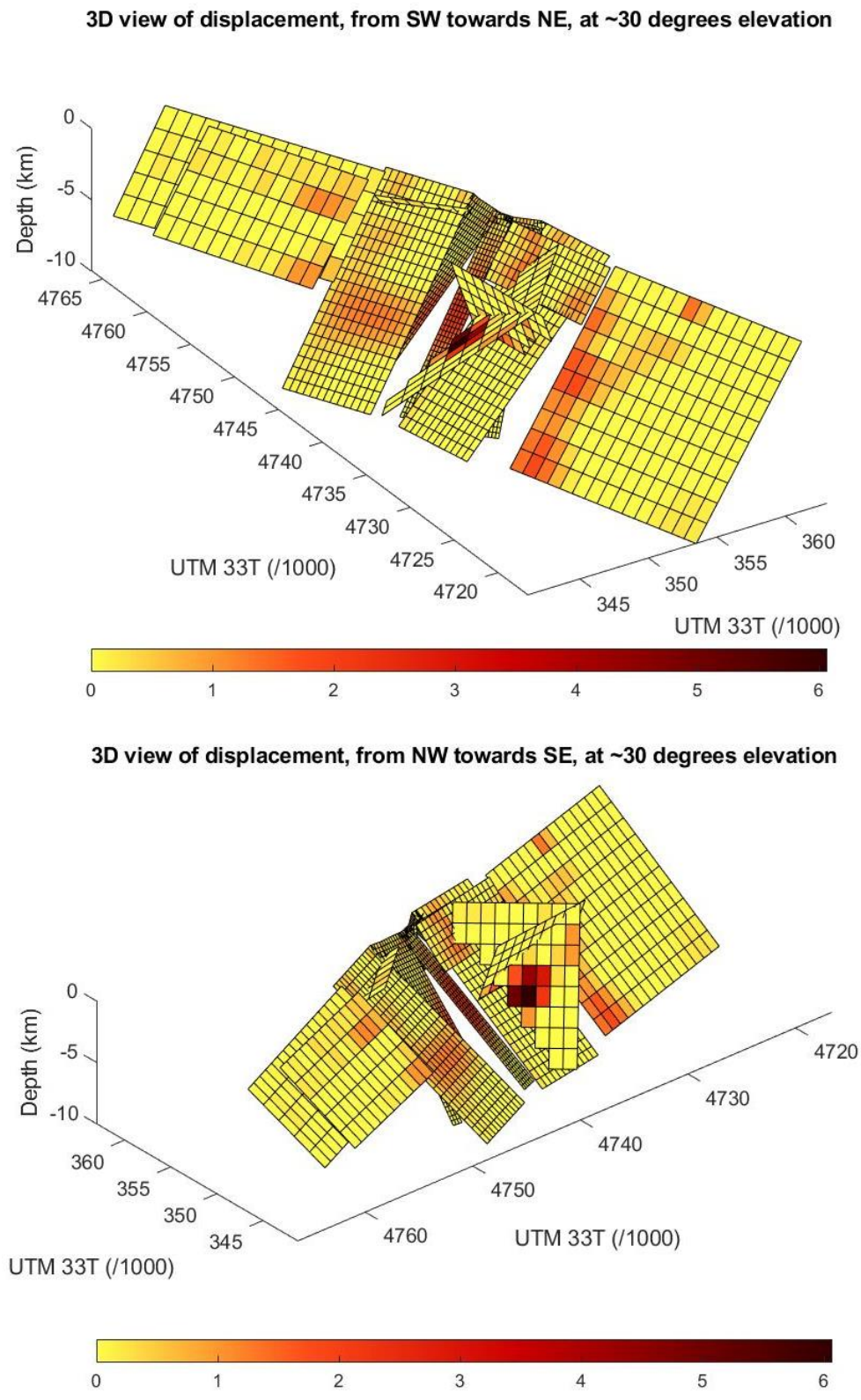

Figure 58: *Displacement observed in 3D, viewed from elevation of ~30^{o}, from southwest towards northeast (top) and northwest towards southeast (bottom), note slight differences in colour scale from previous figures.*

3.7.2 Fit to datasets – data uncertainties including RMS values and visualisation of model v observed values.

3.7.2.1 Overall fit

The overall Root Mean Squared (RMS) misfit value from the joint inversion model is 0.115 m (figure to 3 d.p.). However, the various datasets have different levels of noise/standard deviation, therefore the fit to each individual dataset is discussed below. The comparative figures for standard deviation of the datasets and RMS misfits are set out in **Table 3.7**.

3.7.2.2 Fit of model to individual datasets

Table 3.7 Fit of model to individual datasets. Standard deviation values for Pleiades and InSAR datasets are based upon sample areas away from the main co-seismic deformation. Standard deviation values for GNSS datasets are for the whole dataset used in the joint inversion.

Dataset	Standard deviation (m)	RMS misfit (m)
Pleiades east-west	0.1148	0.1399
Pleiades north-south	0.1141	0.1438
Pleiades vertical	0.1805	0.1823
ALOS	0.0248	0.0154
Sentinel	0.0253	0.0131
Far-field GNSS east-west	0.0452	0.0122
Far-field GNSS north-south	0.0268	0.0062
Far-field GNSS vertical	0.0615	0.0069
Relative GNSS east-west	0.2670	0.0477
Relative GNSS north-south	0.1559	0.0434
Relative GNSS vertical	0.4078	0.0691

(a) Pleiades datasets

Standard deviation values for the Pleiades datasets used in the inversion were calculated using an area of 1.8 km^2 in the footwall, away from the main area of deformation. Observed, modelled and residual values are shown below (**Figures 59 to 61)**. The model smooths some of the noisier elements of the input data, whilst maintaining a high level of detail in the near-fault areas where most co-seismic

deformation occurred. The east-west and vertical residuals highlight the possible existence of 2 southwest-northeast trending minor structures in the footwall, in each case originating near bends in the main Monte Vettore fault segments where the strike changes from ~165^{o} to nearer north-south (although, as explained above, those have not been included in the geometric model).

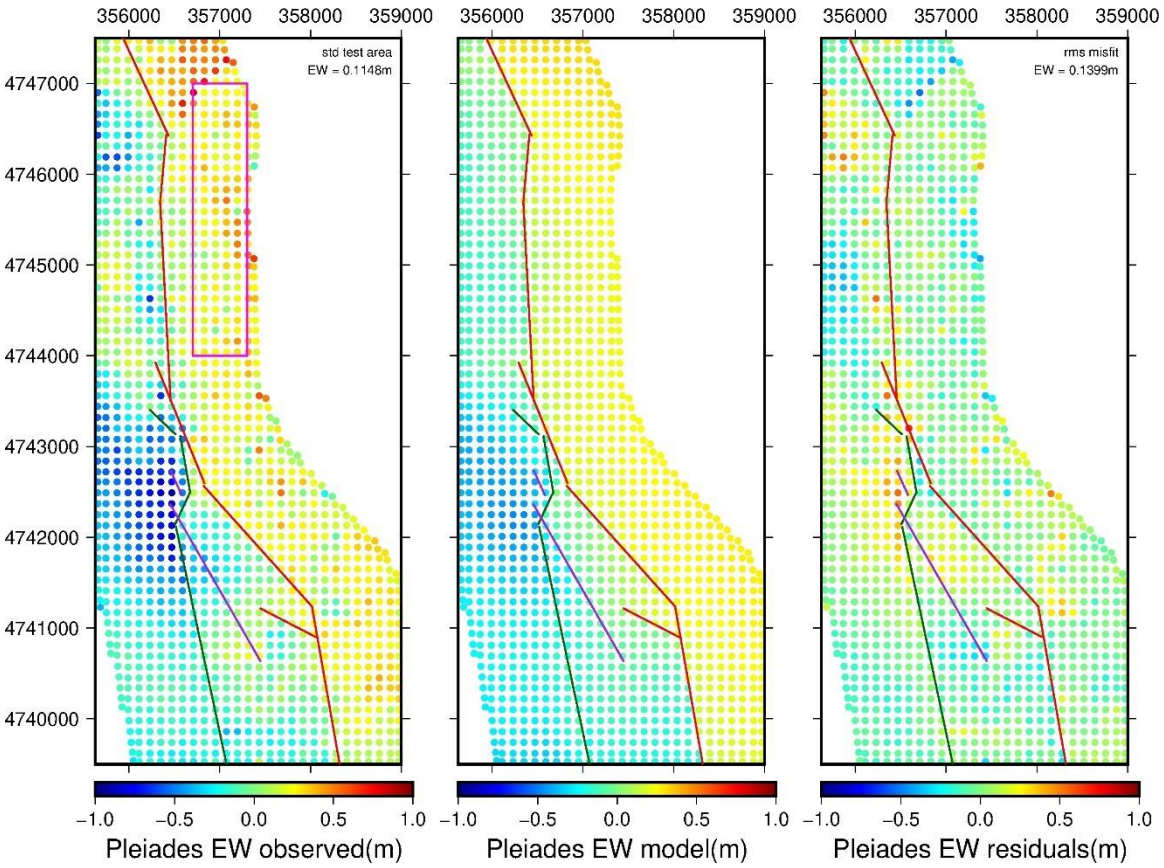

Figure 59: *Observed (LH panel), model (centre) and residuals (RH) data for Pleiades east-west displacement dataset used in joint inversion. Magenta box shows area used for standard deviation calculation for observed data. Surface traces of modelled fault segments for this area are shown in red (Monte Vettore fault), purple (antithetic) and dark green (synthetic).*

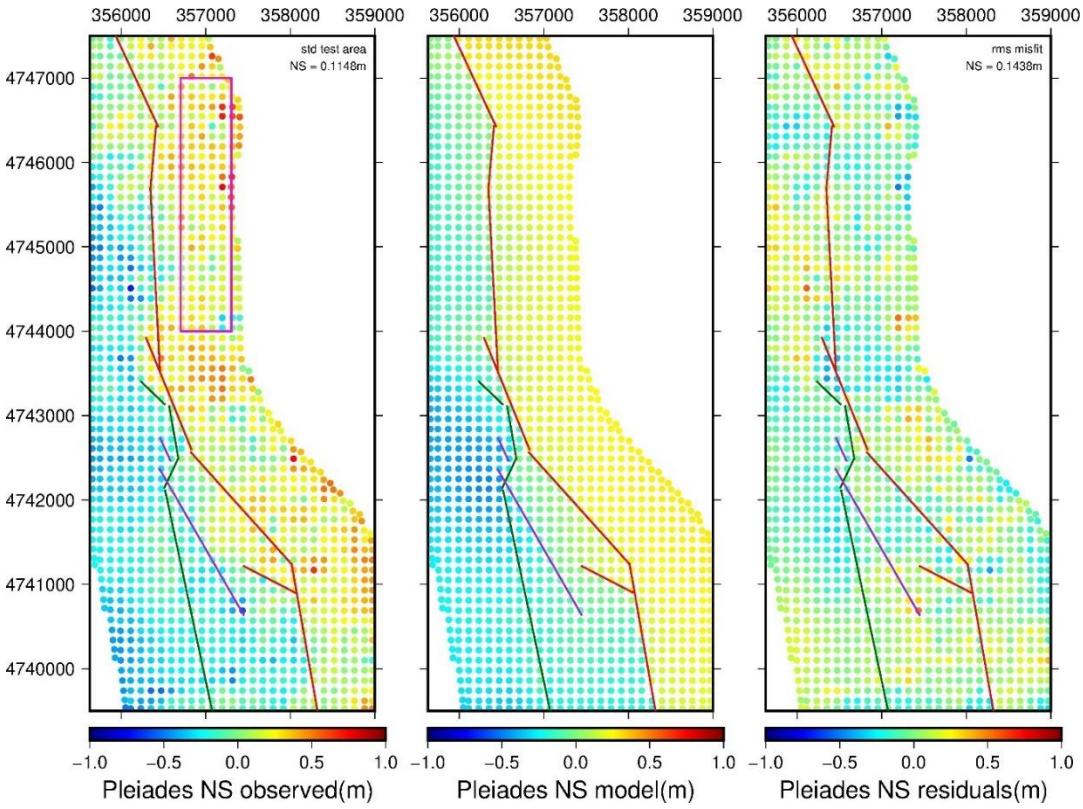

Figure 60: *Observed (LH panel), model (centre) and residuals (RH) data for Pleiades north-south displacement dataset used in joint inversion. Magenta box shows area used for standard deviation calculation for observed data. Surface traces of modelled fault segments for this area are shown in red (Monte Vettore fault), purple (antithetic) and dark green (synthetic).*

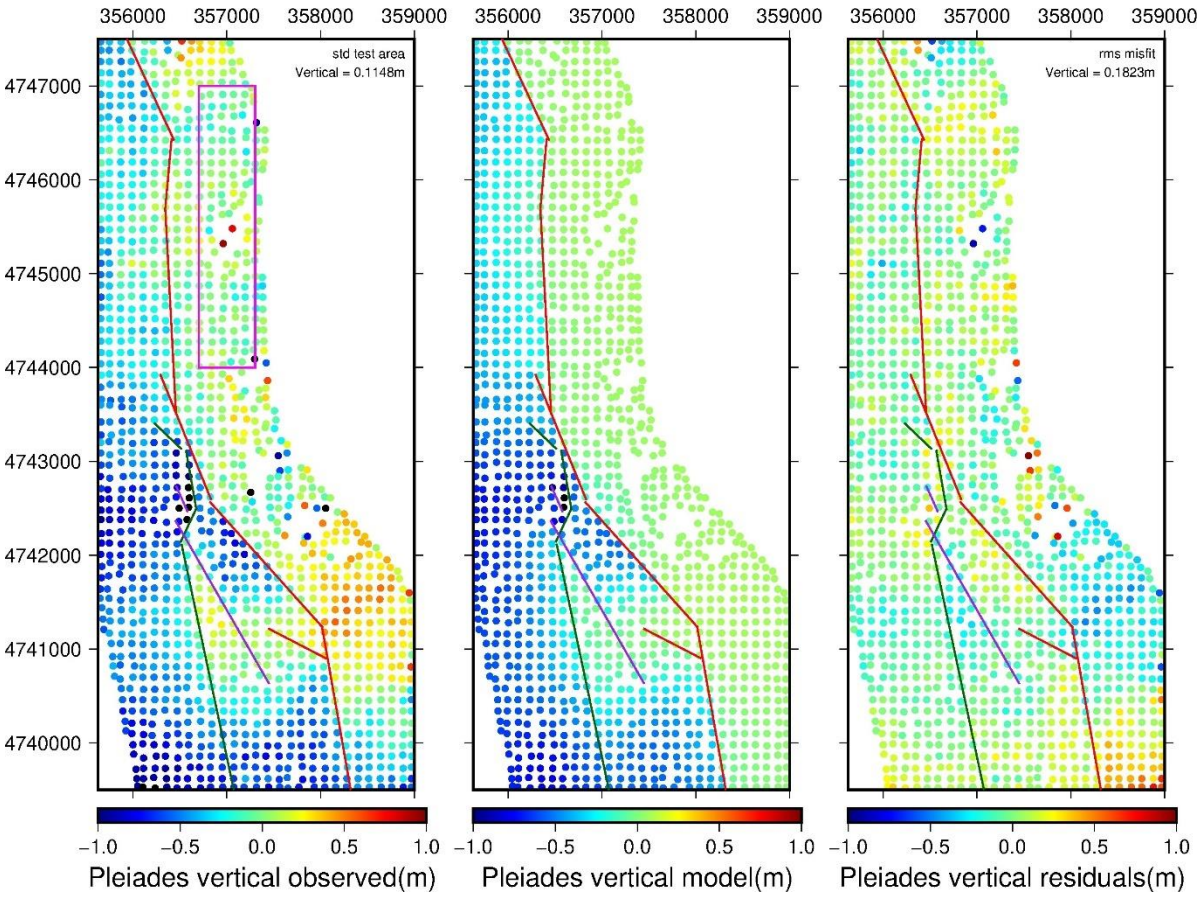

Figure 61: *Observed (LH panel), model (centre) and residuals (RH) data for Pleiades vertical displacement dataset used in joint inversion. Magenta box shows area used for standard deviation calculation for observed data. Surface traces of modelled fault segments for this area are shown in red (Monte Vettore fault), purple (antithetic) and dark green (synthetic).*

(b) InSAR datasets

Standard deviation values for the ALOS and Sentinel InSAR datasets used in the inversion were calculated using an area of 112 km^2 in the footwall, away from the main area of deformation. Observed, model and residual values are shown in **Figure 62**. In both case residuals are < ~5 mm except directly adjacent to the areas of main co-seismic deformation.

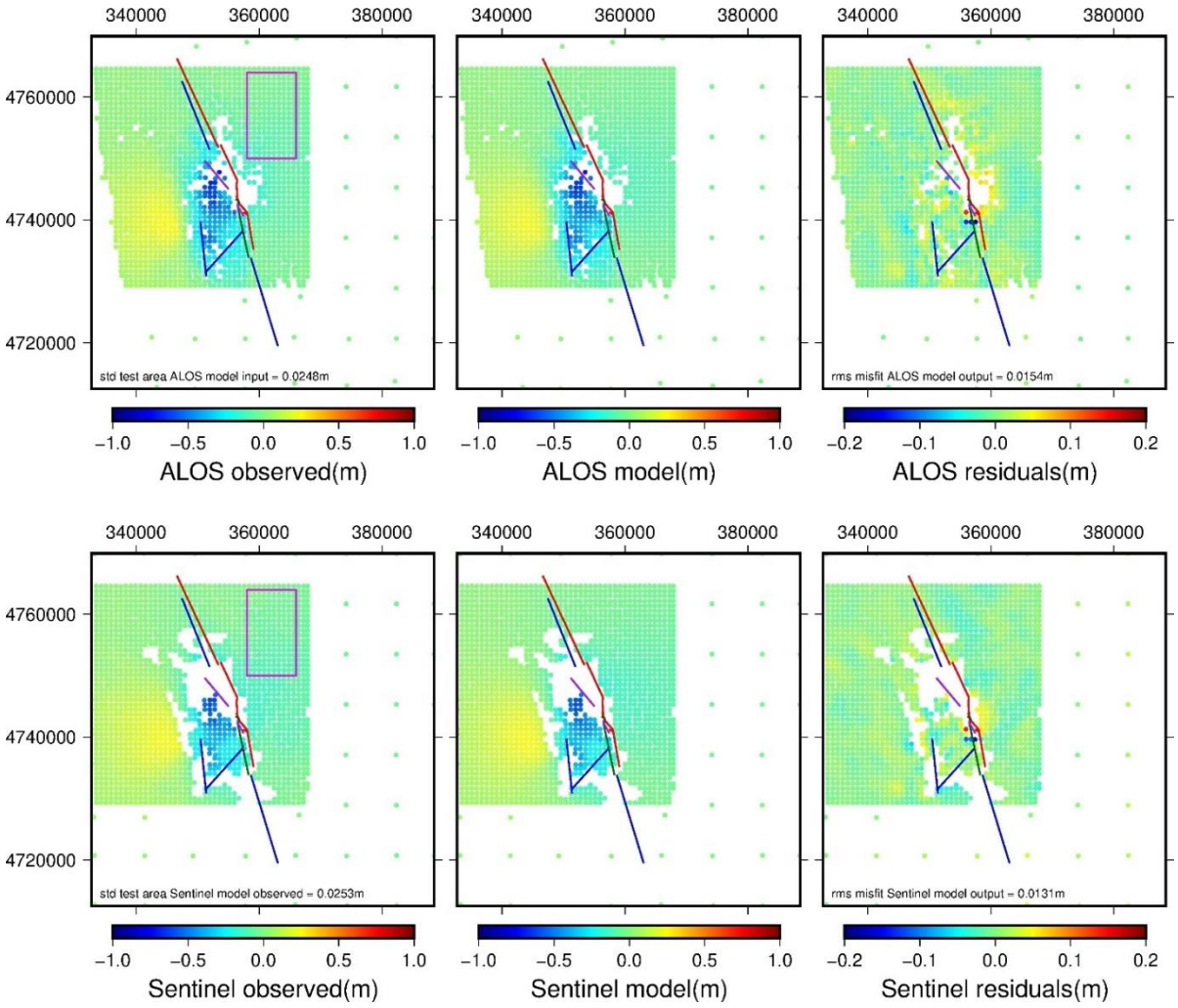

Figure 62: *Observed (LH panel), model (centre) and residuals (RH) data for ALOS (upper) and Sentinel (lower) datasets used in joint inversion. Magenta box shows area used for standard deviation calculation for observed data. Surface traces of modelled fault segments are shown in red (Monte Vettore fault), purple (antithetic), dark green (synthetic), and blue (far-field). Note different scale used for residuals.*

(c) Far-field and short baseline GNSS

Standard deviation values for the far-field GNSS datasets were based upon the full geographical extent of the datasets, rather than a selected test area. Standard deviation values for the short baseline GNSS datasets were based upon the full geographical coverage of the datasets, rather than a selected test area (there are only 4 locations involved). The limited number of results suggests that a standard deviation figure statistic is unlikely to be particularly helpful in comparing fit to data. Observed,

model and residual values are shown in **Figure 63**. Note the different scale used for the residuals (RH panels).

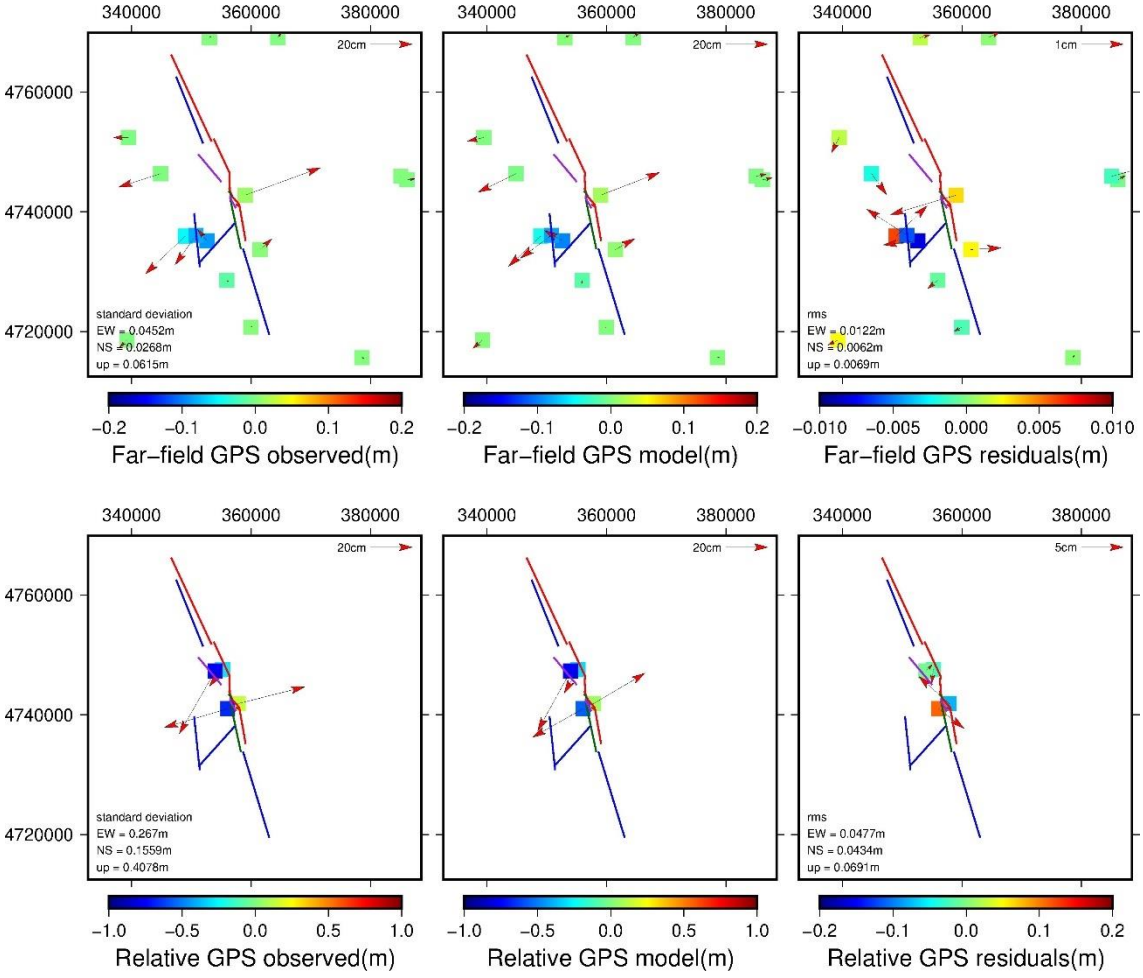

Figure 63: *Observed (LH panel), model (centre) and residuals (RH) data for relative GNSS (upper) and short baseline (relative) GNSS (lower) datasets used in joint inversion. Arrows show combined east-west and north-south horizontal displacement, scale and squares indicate vertical displacement. Surface traces of modelled fault segments are shown in red (Monte Vettore fault), purple (antithetic), dark green (synthetic), and blue (far-field). Note use of different scales for residuals.*

3.7.2.3. Smoothing factors applied

The comparative effect of the choice of differing smoothing factors applied by way of regularisation is shown in **Figure 64**. A smoothing factor of 150 (as opposed to either higher or lower values, in this case 200 and 100 respectively) appears to achieve a balance between an over-smoothed model and one with high levels of noise.

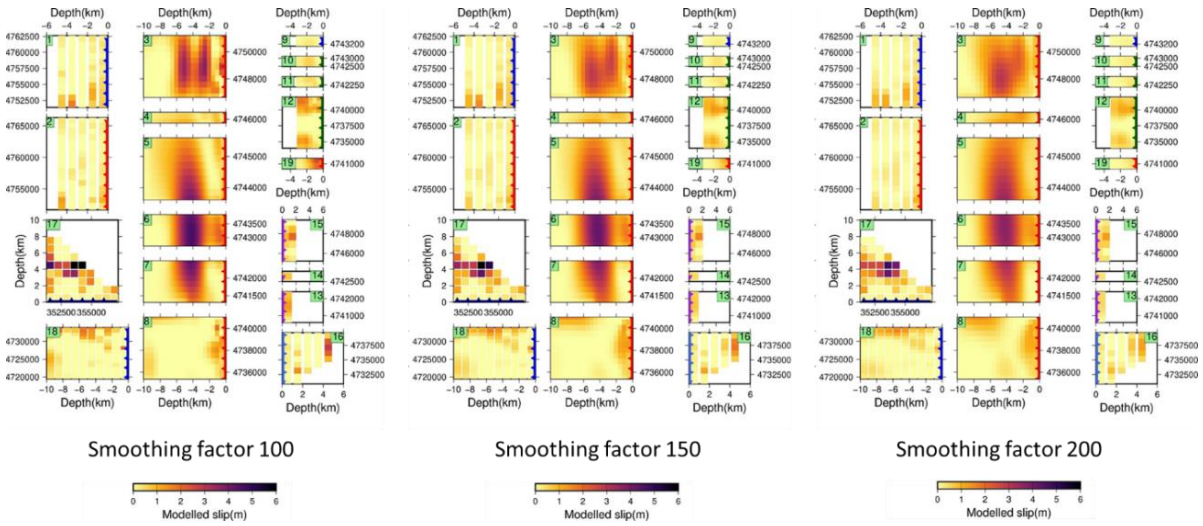

Figure 64: *Comparative overall slip results using differing smoothing factors (respectively 100, 150, and 200, from Left to Right – larger scale figures are in* ***Appendix 3A****).*

3.8 Discussion

3.8.1. Introduction

In discussing the modelling results I will concentrate on two main areas:

(1) the distribution of slip between the main Monte Vettore fault segments and the ancillary synthetic and antithetic structures in its hanging wall; and

(2) the relationship between the Pian Piccolo fault segment (fault 17) and its neighbours, including the Norcia antithetic fault segment to the west (fault 16), the southern-most Monte Vettore fault segment (fault 8) and synthetic structure in the hanging wall (fault 12) to the east.

In both cases I aim to compare the results of my modelling with the results from previous inversions, assessing:

- whether my model is justified in terms of fit to data;
- is the modelled slip realistic on both large and individual fault segment scale;
- does the modelled slip help lead to a better understanding of the kinematics of the Norcia earthquake; and
- does the model shed light on the distribution of slip on complex fault networks?

I will also assess whether the addition of complexity to the data and geometry in the central area covered by the Pleiades data where co-seismic deformation was greatest has been at the expense of the fit of the model to data outside that central area.

Finally, I will also consider briefly the extent of differences between my results from the Pleiades data, and those obtained from the only previously published inversion to have used that data, Delorme et al., 2020. More detail on this last aspect is contained in **Appendix 3B**.

3.8.2 Modelling results - overview of slip at depth

At depth, my results show maximum slip of ~ 4-5 m concentrated on one main area, the Monte Vettore fault segments 5, 6 and 7 at 3-6 km depth, with little slip below 6 km depth, and with slip decreasing towards the surface. Slip vectors at depth are principally oriented towards ~250^{o}. The location of the main area of slip at depth coincides with results from other models (e.g. Cheloni et al., 2017 and Walters et al., 2018) (see **Figures 27 and 67**).

The continuation of the Monte Vettore fault (fault 8) to the south of the central area shows slip of up to ~ 1 m at depth below 6 km at its northern-most end, and elsewhere slip of < ~ 0.5 m in the top ~3 km below the surface. The Laga fault (fault 18) also shows slip of ~ 1 m at its north end, at ~5-9 km depth, but elsewhere there is a patchy picture with little slip overall near the surface. In showing slip at depth in some areas to the south of the region, my model agrees with several previous models. Walters et al., 2018 show slip on the Laga fault at ~6-7 km depth (but little at the surface). Each of Cheloni et al., 2017, Sconamiglio et al., 2018, Xu et al., 2017 and Cheloni et al., 2019 identifies a patch of slip at depth towards the southern-most part of the region (see for example, **Figures 27 and 28**).

A common feature of all of the models is a complex pattern of near-surface deformation, and, with it, high levels of uncertainty. A feature noted by some (e.g. Xu et al., 2017 and Cheloni et al., 2019) is a degree of left-lateral strike-slip motion in the near-surface deformation. Both complexity and left-lateral strike-slip motion are present in my model (and discussed in more detail below).

My model retains the essential far-field geometry of the Walters et al., 2018 model. A possible concern in respect of fit of my model to the far-field data is that the addition of near-fault data in the form of the Pleiades results and more complex geometry might have worsened the fit to the far-field data. However, my results (**Table 3.7**) confirm that the model geometry and addition of Pleiades datasets have not materially impacted the fit of this model to the far-field data.

The estimated seismological magnitude from the inversion is, at ~M_w 6.73 (moment 1.547 x 10^{19} Nm), higher than the previous estimated magnitudes of M_w 6.6 (Walters et al., 2018) or M_w 6.5 (INGV - cnt.rm.ingv.it). This discrepancy may be explained by the addition of the Pleiades data showing surface movement due to distributed faulting close to the main Monte Vettore fault, which was not previously incorporated into the earlier models. The Pleiades data also covers a period of a month post-earthquake when some afterslip may be expected. It is possible that the addition of detail of distributed faulting at the surface not used elsewhere has corrected what is otherwise an underestimate of moment by using solely datasets which do not pick up that detail. However, that is unlikely on its own to significantly impact the moment calculation. The inclusion of an element of afterslip would appear to be a more likely explanation for the difference.

3.8.3 Modelling results - distributed near-surface slip on the Monte Vettore fault and in its hanging wall.

Does my extra detail in the central area covered by the Pleiades data improve the modelling results compared to previous studies? My main aim is perhaps different from some of the previous models, in that I am interested primarily in shallow slip distribution. The most detailed fault geometries used to date only use a maximum of 4 fault segments in their model in this central area, whereas I used 13 fault segments in this central area. My approach identifies detail of near-surface slip distribution in the near-fault areas which is not available through the other modelling strategies, and reduces the level of uncertainty.

In the central area, the typical co-seismic rake recorded at the surface of 80° for a fault segment within the Monte Vettore fault segments dipping at 71° and striking at 141°

results in a plunge of ~68° towards an azimuth of ~204° (Galderisi and Galli, 2020), and see **Figure 65** for co-seismic results in the central area. My model shows predominantly dip-slip displacement below ~ 2 km depth on the main Monte Vettore fault, trending towards ~250° (**Figures 43 and 45**). However, within the top 2 km below the surface, my results show a strong strike-slip (left-lateral) element on the main and synthetic faults, with varying trends (**Figure 46**). This left-lateral element coincides with the results found by Xu et al., 2017 and Cheloni et al., 2019.

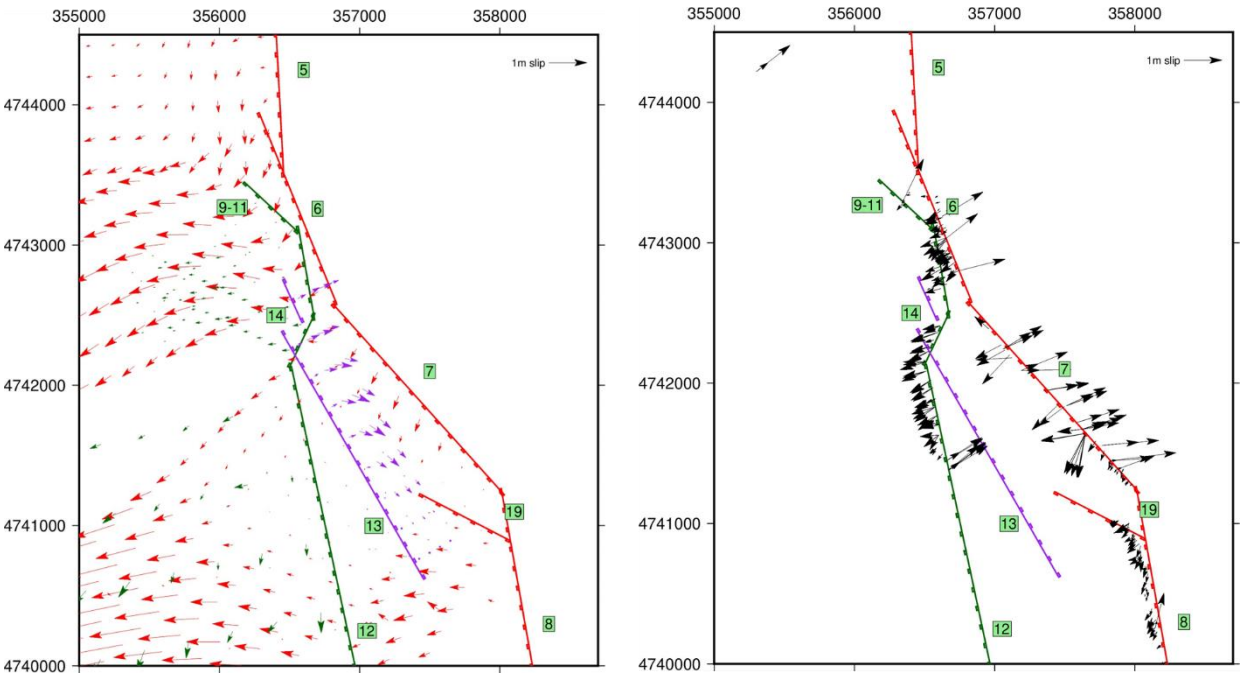

Figure 65: *Comparison of near-surface modelling results in the central area (LH panel) with field results at the surface for the same area from Villani et al., 2018 (RH panel). Field results are shown where there are recorded measurements of slip vectors plus either combined offset, or both opening (heave) and throw.*

In each of fault 4, the southern end of fault 5, the northern end of fault 6, fault 7 and the synthetic fault 12 slip vectors are modelled in the top 1 km below the surface as towards ~180°-205°, which matches the slip measured at the surface. At the northern end of fault 5 the slip vectors are more intermediate (at ~230°). See also the individual segment slip details in **Appendix 3A.**

Galderisi and Galli report the co-seismic field data for the antithetic faults as slickenlines trending towards 101°. In respect of my faults 13 and 15 (both antithetic), below ~1 km my modelled results show the trend of the slip is towards ~150°-160°. In the top 1 km below the surface, however, the trend is generally towards ~90°-110°, which also compares well with the co-seismic data.

Other models also show predominantly dip-slip displacement at depth which is consistent with my model below ~2 km depth. However, my modelling also shows near-surface slip distribution that is consistent with field measurements, with transfer of slip to neighbouring minor fault splays, as well as slip vectors that are oblique to the main dip-slip vectors seen at greater depth. This extensive and complex distribution of slip is consistent with the behaviour expected of immature fault systems such as the VBFS (Dolan and Haravitch, 2014). The complexity of the fault system is itself a reflection of its immaturity (Wesnousky, 1988).

The antithetic structures in particular seem to play an important part in this process of slip transfer with reduced amounts of near-surface slip on the main fault segments (notably faults 5 and 7) in areas where those are adjacent to antithetic faults, in addition to the oblique slip vectors noted above.

The synthetic structures also play a part in the distribution of slip within the hanging wall of the main Monte Vettore fault, with the modelling of fault 12 in particular showing the same near-surface oblique slip vectors, with an azimuth of ~ 180-205° where that fault overlaps with antithetic fault 13.

The respective geometries of the main Monte Vettore and antithetic structures trend slightly towards near-convergence in the hanging wall below the junction of faults 6 and 7, suggesting that those structures coincide at different depths over their lengths. The respective geometries of the synthetic structures here also trend towards convergence in the same area of the hanging wall below the junction of faults 6 and 7. Indeed, the synthetic and antithetic structures cross at one point in a complex pattern at the surface. This surface complexity must also reflect a very complicated pattern at shallow depths.

The geometry of the main Monte Vettore fault itself in this central area is likely to have played an important part in the distribution of slip, and the development of the pattern of minor structures in the hanging wall over time. This central area (equivalent to my faults 6 and 7) was identified as a bend in the fault, and an area where the co-seismic slip is significantly higher than neighbouring fault segments (Iezzi et al., 2018). Based upon an analysis of the surface ruptures, the strike of the fault changes from the overall strike by ~28^{o}, with field measurements of dip at the surface increasing to ~70-88^{o} compared to dip of ~50-70^{o} on neighbouring faults (ibid). That study also found long-term throw in this area at a maximum compared to throw elsewhere on the fault, suggesting that the bend (and its co-seismic effects over time) are a persistent feature.

Several studies have found that fault bends and step-overs produce the most complex rupture zones (e.g. Johnson et al., 1998, Teran et al., 2015), with slip transferred from the main fault onto mechanically more favourably oriented steeper-dipping distributed minor faults (ibid). It has been suggested that lateral components of slip have a tendency to be accommodated preferentially on near-vertical fault strands through slip partitioning (e.g. Bowman et al., 2003). This transfer of slip onto more favourably oriented structures and possibly partitioning of slip at a fault bend, particularly at the near-surface where lower normal stress values apply and where the hanging wall material is likely to be relatively unconsolidated, appears a reasonable explanation for what has happened in this central area. The deviations in the strike of the main Monte Vettore fault in the central area and changes of dip have introduced geometries on some of the fault segments which do not fit well with the regional stress patterns, and to allow for those differences slip (particularly its lateral components) has been transferred to steeper-dipping subsidiary structures in the hanging wall within the top ~1-2 km below the surface.

Much of the surface material involved in the hanging wall is either unconsolidated material in the form of slope deposits (Coltorti and Farabollini, 1995), or prone to landslides. The bedrock in the footwall is almost exclusively limestones and marls (Pierantoni et al., 2013), and there is generally little difference along strike. However, Fault 7 includes the area containing the massive limestone outcrop of the Scoglio dell'Aquila, whereas the neighbouring geology is mapped as Carnelian limestone (ibid).

The model of slip in the area below the Scoglio dell'Aquila outcrop shows hardly any slip on the main fault between 500 m and 1.5 km depth, but there is slip on the antithetic fault 13 which is separated from it by less 500 m at this point on the surface. This suggests that differences in lithology may also have played a part in the distribution of slip in this one specific area, although probably not elsewhere.

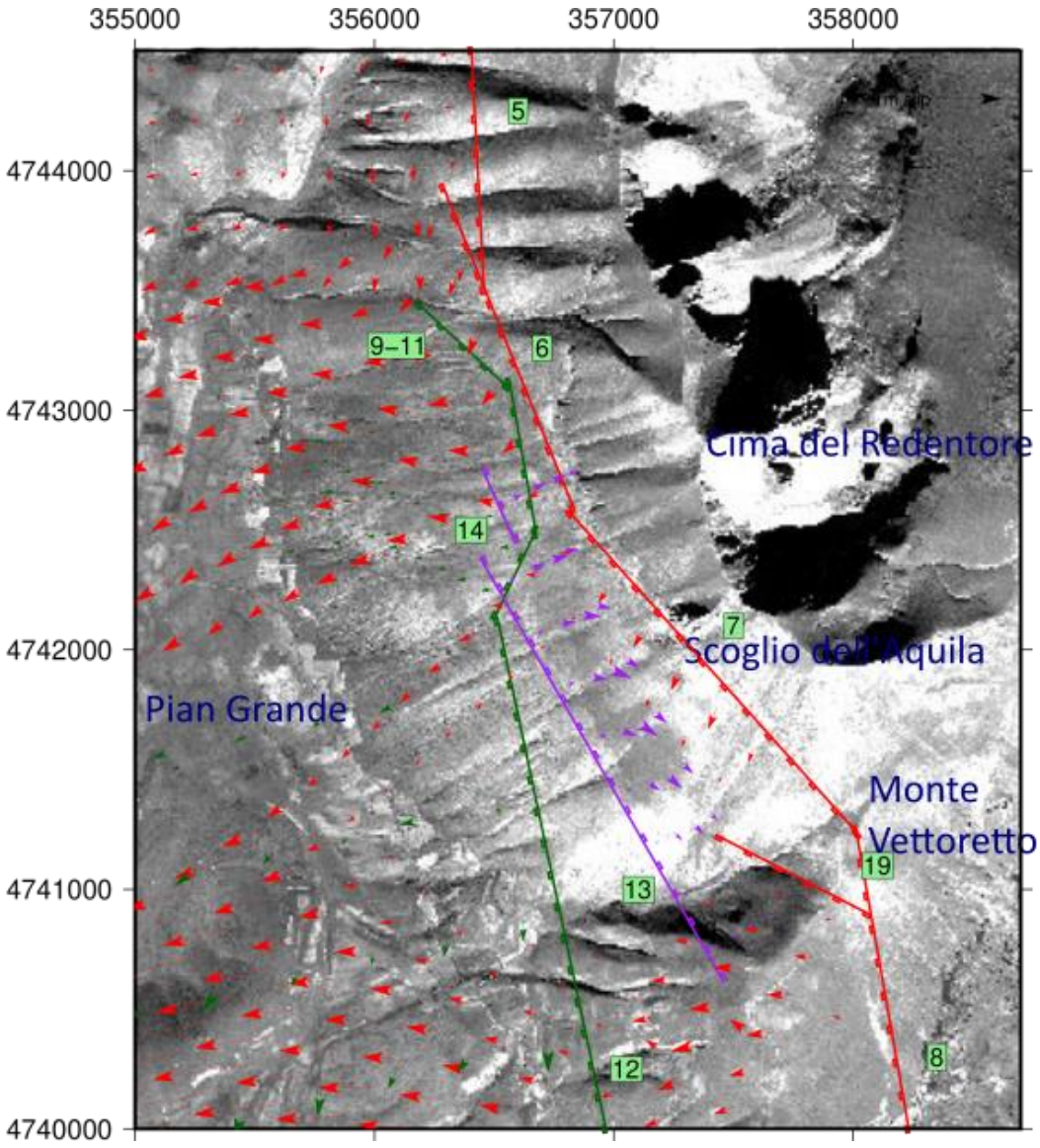

Figure 66: *Detail of slip vectors and modelled fault geometry (from* ***Figure 55*** *above) superimposed onto Pleiades-derived image of central area, showing slip from Monte Vettore fault 7 transferred onto faults 13 (antithetic) and 12 (synthetic) in hanging wall with near-surface strike-slip vectors where fault 7 deviates from overall strike of Monte Vettore fault.*

By superimposing the slip vectors onto a Pleiades-derived image of the area around the Scoglio dell'Aquila outcrop, the role of the minor structures in the hanging wall below the Scoglio dell'Aquila outcrop can be seen more clearly (**Figure 66**).

Away from the areas of distributed slip, other modelled near-surface slip vectors are more generally consistent with the dip-slip vectors at depth. Slip on the "spur" from the Monte Vettore fault (fault 19), is predominantly right-lateral within the top ~1-2 km below the surface, which (given its strike of 118^{o}) aligns with the slip seen elsewhere at depth. The limited amount of slip on the minor synthetic fault segments (9-11) also aligns with the slip seen elsewhere at depth (with an azimuth of ~250^{o}), with relatively little slip apparently transferred from the neighbouring Monte Vettore fault segment (fault 6). This suggests that, although slip is distributed considerably in some areas in the near-surface, in other areas there is consistency in the slip vectors. This in turn implies that slip on the main Monte Vettore fault below ~2 km depth properly represents slip at depth, and that the distribution of slip in the central area is a relatively confined local feature, governed largely by changes in the fault geometry of the main Monte Vettore fault in this particular area. There does not seem to be any need to imply particularly complicated fault geometry at depths below ~2-3 km in either the central area or further afield in the area modelled.

The values for near-surface slip of up to ~1 m are in line with expected values compared to field results from the surface. Although field results reported up to >2 m of slip in a few locations on the main Monte Vettore fault (e.g. Villani et al., 2018), the highest values include areas of possible landsliding, and the mean value for throw recorded for "co-seismic rupture with offset" (N=4677) for all locations with co-seismic slip was 24 cm with a maximum of 221 cm (ibid). For "co-seismic ribbon on bedrock" (N=837) the equivalent values were 69 cm and 260 cm (ibid).

As to whether the model is biased towards fitting the Pleiades data, a comparison between the standard deviation values for the observed Pleiades data calculated on a sample area away from the area of main deformation and the RMS misfit values from the model suggests close alignment without overfitting the model to the Pleiades data.

3.8.4 Modelling result - modelled slip on the Pian Piccolo fault and its neighbours

Slip on the Pian Piccolo fault (fault 17) is heavily influenced by its proximity to other structures (notably fault 16 (Norcia)) and by its location within the Monte Vettore hanging wall. Untangling the interrelationships between these structures is complicated by the modelling of the structures as largely rectangular features when in nature they will not be as regular in shape. It is relevant to note that the Pian Piccolo fault appears to have acted as a structural barrier to northwards propagation of the 24th August 2016 Amatrice earthquake which initiated on the Laga fault and then propagated northwards onto the south end of the Monte Vettore fault, but apparently without rupturing beyond the Pian Piccolo fault (e.g. Walters et al. 2018). This is likely to have resulted in accumulated stress on the Pian Piccolo fault, but also an area of stress shadow on the footwall side of the Pian Piccolo fault where slip was observed on the south end of the Monte Vettore fault during the Amatrice earthquake. It also relevant to note that the exact location of the (blind) Norcia antithetic fault is not well constrained by the geodetic data (Walters et al., 2018).

Slip at depth on the Pian Piccolo fault is split into two principal slip vectors, in separate patches. One slip vector is essentially dip-slip (trending towards ~340^{o}), which is observed at the mid-point of the Pian Piccolo segment between 2 and 4 km depth and at greater depth (5-7 km) where the Pian Piccolo fault crosses the Norcia antithetic fault (fault 16). The second slip vector mirrors almost exactly the direction of slip towards ~250^{o} on the main Monte Vettore segments (faults 6 and 7), with slip of ~2-6 m at depths of 4-6 km in its southwest half. The slip towards ~340^{o} nearer the surface appears to be in an area where there is little or no direct interaction between the Pian Piccolo fault and its neighbours. The slip towards ~250^{o} below this patch appears to be heavily influenced by the slip vectors at depth on the main Monte Vettore fault, and presumably arises because of the interaction of those faults (the aftershock data show the faults interact at ~5 km depth – Chiaraluce et al., 2017, and **Figure 46**).

The slip values seen on the Pian Piccolo fault are at their maxima (~4-5 m) at this point. Although those values might appear anomalous, the Ridgecrest, California earthquake sequence in 2019 provides an example of where the modelled highest levels of slip at depth on the northwest-southeast trending structures following the later M_w 7.1 event

were concentrated adjacent to where the earlier M_w 6.4 event had ruptured southwest-northeast trending structures orthogonal to those structures (see Ross et al., 2019, Figure 5). Although as largely strike-slip motion on near-vertical structures those faults are not directly analogous to the Monte Vettore and Pian Piccolo faults, this example nevertheless shows that maxima can occur where mutually orthogonal trending faults interact in a sequence (in this case, bearing in mind the likely previous stress build-up on the Pian Piccolo fault associated with the Amatrice earthquake -see **Figure 67**).

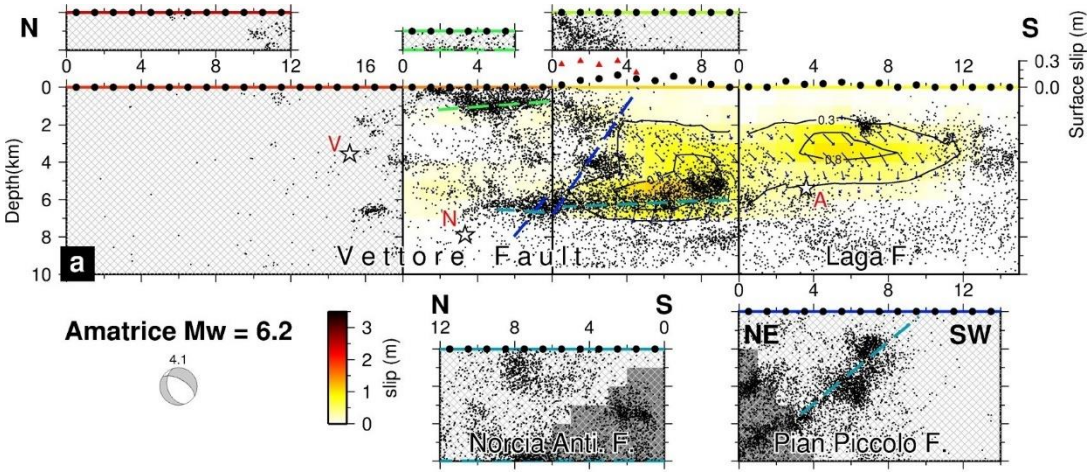

Figure 67: *Modelled slip associated with the Amatrice earthquake, from Walters et al, 2018. Slip on the Laga fault largely stops at the boundary of the modelled Pian Piccolo fault, shown in dark blue on upper panel.*

The final slip patch below this area (and further away from the Monte Vettore fault) reverts to the ~340° trend seen nearer the surface at the northeastern end. This would suggest that at this depth there is no longer the interaction with the Monte Vettore fault and possibly that slip on the Pian Piccolo fault continues below the interaction of the two faults, rather than terminating where the 2 faults meet.

In this latter area, the 3D geometry of the Pian Piccolo fault shows that it intersects the steeply-dipping antithetic Norcia fault (see **Figure 58**). However, the Norcia fault appears to have little or no effect on slip on the Pian Piccolo fault. The Norcia fault shows left-lateral/dip-slip movement towards ~45° at ~2-3 km depth at its south end near its junction at the surface with the Pian Piccolo fault, and at ~4-5 km depth

further away, at the northern-most end of the Norcia fault. Both of those slips would appear to be influenced by the slip towards ~340^{o} at this end of the Pian Piccolo fault.

The Pian Piccolo fault is a blind structure, with no rupture reaching the surface. The model (**Figures 56 and 57**) accurately reflects that: slip on the Pian Piccolo fault itself is largely confined to slip below 3 km except at the northeast end where slip of < ~20 cm is modelled at the near surface.

In the hanging wall of the south end of the Monte Vettore fault (fault 8), there is little if any slip at depth. At ~2 km depth, however, where the hanging wall coincides with the approximate location in the footwall of the Pian Piccolo fault, slip vectors are towards ~340^{o} (compared to ~250^{o} nearer the surface). In the same area there is no slip observed on the synthetic fault (fault 12) until several km away from the Pian Piccolo fault. This suggests that the stress shadow from the Amatrice earthquake significantly limits slip in this area during the Norcia earthquake, with the slip on the Pian Piccolo fault dominating where the structures interact. It is possible that at least some slip is being transferred from the Monte Vettore fault onto the Pian Piccolo fault although, given the slip vectors involved, that appears unlikely.

Figure 68 shows detail of the slip vectors in this area, with very little slip overall in the area where the northeastern end of the Pian Piccolo fault coincides with the hanging wall of the Monte Vettore fault.

In terms of near-fault and near-surface slip, the slip results in this area seem to be a sensible match to the field data. The areas where surface ruptures have been mapped in the field include the northern parts of the synthetic fault (fault 13) and Monte Vettore fault (fault 8) (see **Figure 65**), which matches the modelled results seen on individual fault segments. There are no areas where the model predicts significant slip at or near the surface when the faults are known to be blind. The influence of the Pleiades data and use of more detailed fault geometry is in any event likely to be limited in this area (the Pleiades data I have used only just stretches as far south as the northeastern end of the Pian Piccolo fault at its surface).

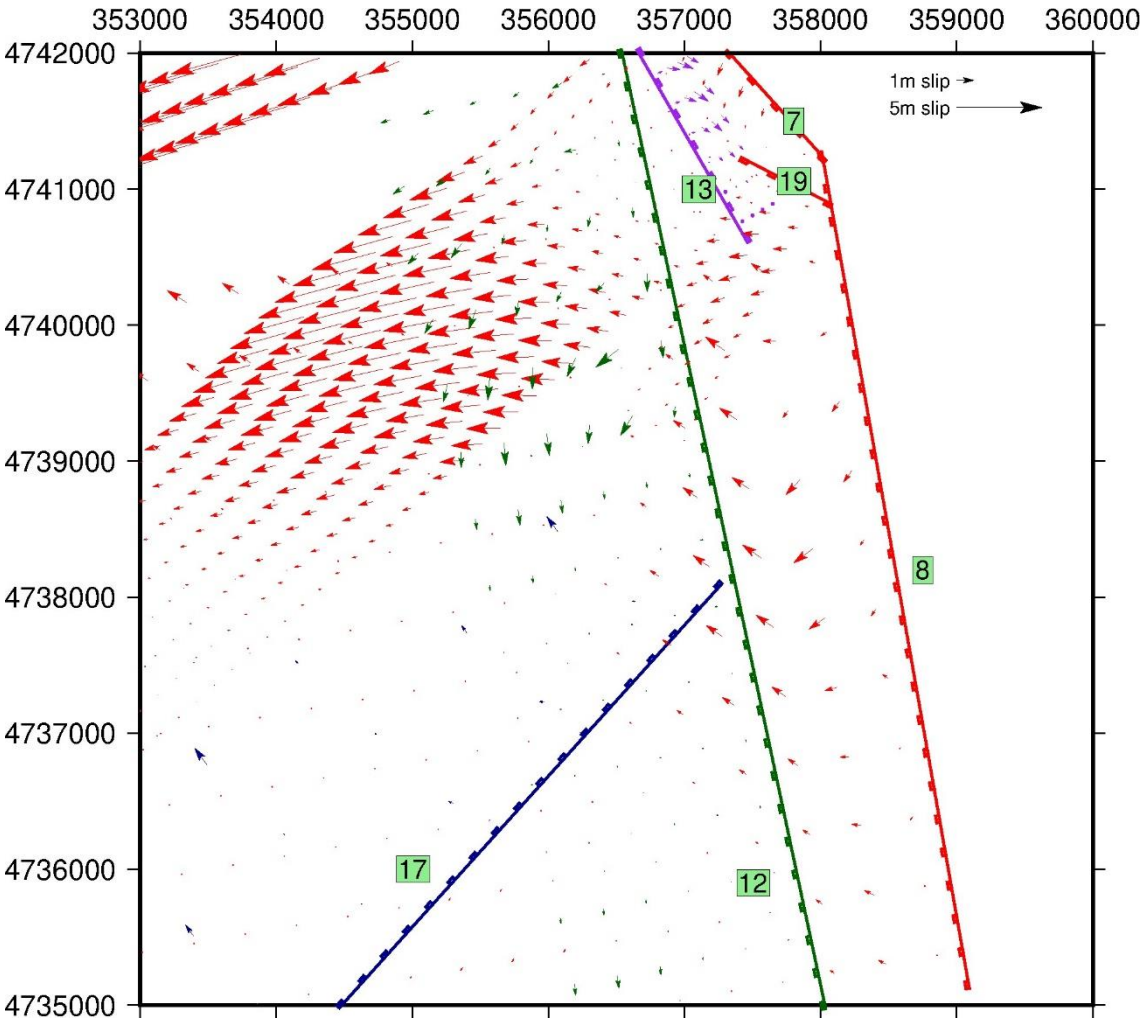

Figure 68: *Detail of orientation and magnitude of slip vectors resulting from joint inversion in central area showing detail of slip in near-surface area projected in 2D onto surface, without down-sampling, in the area where the northeast end of the Pian Piccolo fault (fault 17) coincides with the hanging wall of the Monte Vettore fault (fault 8) and the synthetic structure (fault 12) in the hanging wall. Colours of vectors shown match faults shown at surface.*

The slip pattern on the Pian Piccolo fault largely matches the previous modelling in Walters et al., 2018. There, slip at depth on the Pian Piccolo fault was split into two elements, largely left-lateral strike-slip towards the southwest at ~2-3 km depth, and at lower depths, dip-slip. However, their model of slip on the Norcia Antithetic fault (**Figure 69**) shows dip-slip with right-lateral kinematics (compared to the left-lateral

kinematics observed in my model at depth

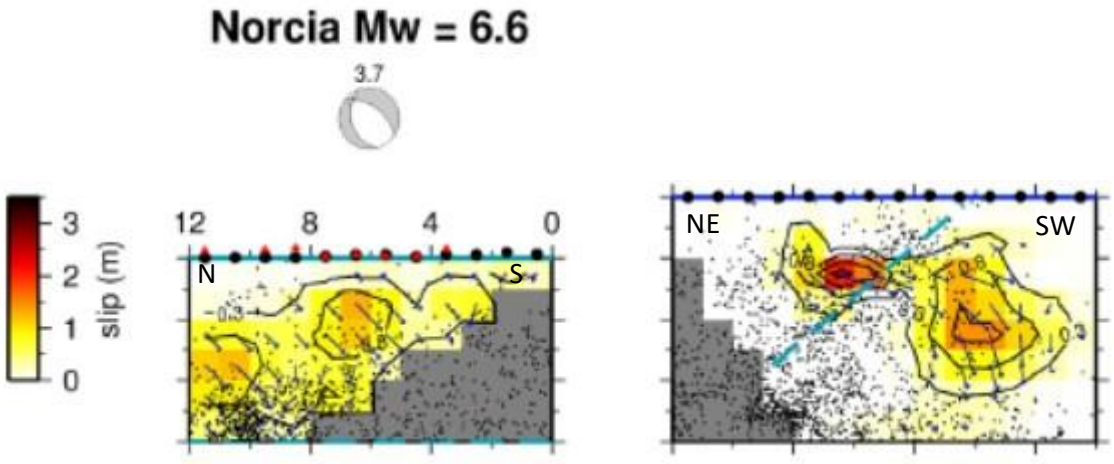

Figure 69: *Adapted from Walters et al., 2018, figure 7, slip vectors from inverse modelling of the Norcia earthquake for the Norcia Antithetic Fault and the Pian Piccolo Fault. Blue line shows intersection of the modelled faults, black dots show aftershocks following the earthquake.*

Cheloni et al., 2017 also model slip on the Norcia Antithetic fault as being dip-slip with left-lateral kinematics, with slip on the Pian Piccolo fault being dip-slip with right-lateral kinematics. This suggests that slip at depth on the Norcia antithetic fault on my model is more influenced by its interaction with the Pian Piccolo fault than wider regional slip kinematics.

3.8.5 Modelling results – comparison with the results of Delorme et al., 2020

In summary, and as I set out in more detail in **Appendix 3B**, Delorme et al.'s Pleiades input data for their inversion (1) are noisy compared to my differencing results, (2) include data from an area which I (and Delorme et al.'s figure S1) have identified as being subject to a long-wave sinusoidal distortion, and (3) suffer from uncorrected topographic and regular spatial aliasing artefacts. Therefore, the reliability of the Pleiades data set within Delorme et al.'s inversion must be open to considerable question. Whilst more limited in area, my Pleiades data results appear to be more robust as a result of my approach to differencing the datasets and omitting the more questionable areas of data outside the main areas of co-seismic displacement. I

consider that they therefore provide a more reliable source of detailed near-fault data for the joint inversion.

As an example, **Figure 70** shows the different results from deriving horizontal displacement in an east-west direction (explained in more detail in **Appendix 3B**).

In my joint inversion I have in any event disregarded the data shown to the left of my figure due to the sinusoidal effect shown particularly in the north-south and vertical displacement results. However, even discounting that, the noise in the east-west displacement field is significantly reduced in my results, notably in the footwall, with values much reduced from the up to > 1m east displacement seen in the Delorme et al. results (their colour palette is in pixels (50 cm)).

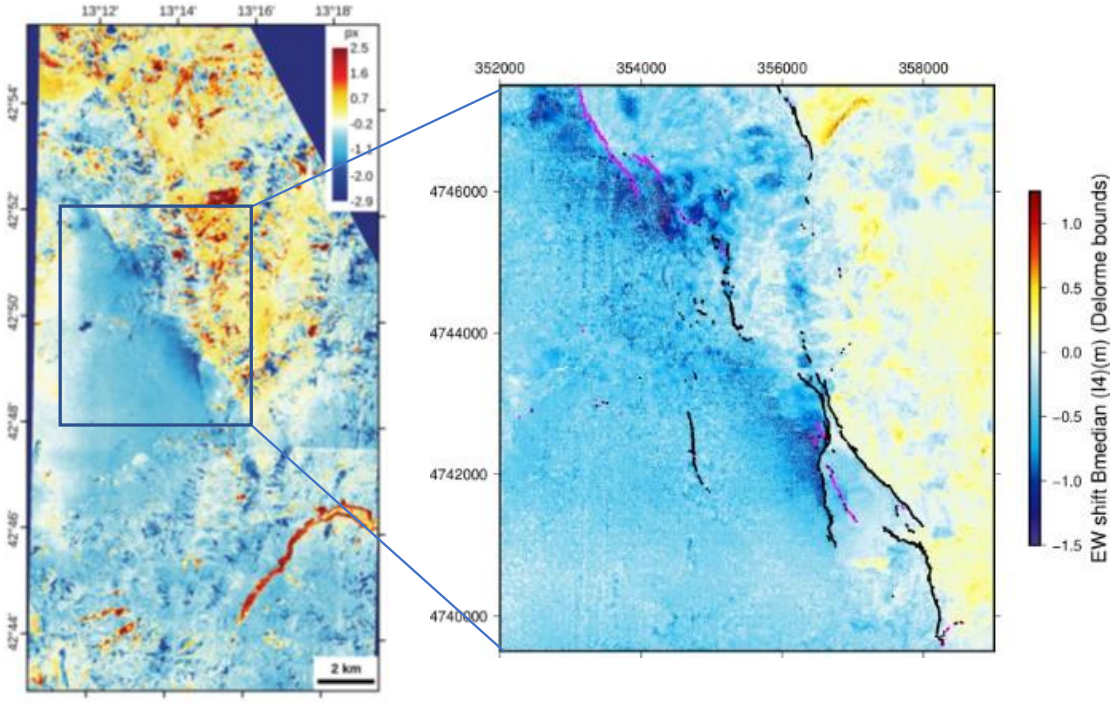

Figure 70: *Comparison of Delorme et al, 2020 east-west displacement (from their Figure S1) (LH panel) with my east-west displacement values for the area shown (RH panel), using the same colour palette as far as possible.*

Using my Pleiades input data, and adopting a more detailed approach to the geometry used in the modelling set-up, I have also been able to model near-surface detail over an extended area, without having to adopt the selective approach adopted by Delorme et al. of using a limited profile across the area of greatest displacement. That

approach, in any event, did not enable Delorme et al. to reach any definite conclusions as to the nature of near-surface distributed faulting - they identified a previously unreported level of complexity in co-seismic deformation at shallow depth, but acknowledged that the short spatial wavelength involved was too short for their large-scale inversion to capture it.

3.9 Conclusion

Previous models of near-fault slip distribution in the complicated extensional setting of the Apennines, and in particular the Monte Vettore fault area, have agreed on one common conclusion, namely that detailed modelling of near-surface complexity visible on the surface through the presence of ruptures is very difficult if not impossible to achieve with the conventional geodetic datasets of InSAR and GNSS, even when supplemented by field evidence. In this case, my approach has been to supplement those conventional datasets with very high resolution optical satellite data from the Pleiades satellite constellations from before and after the Norcia earthquake of 30th October 2016 in the form of DEMs which have been carefully aligned and correlated to remove artefacts. I have used denoised displacements derived from those data to add a level of complexity to near-fault surface movement, and to model the fault geometry in that area in more detail. This has resulted in a model which has a close fit to the Pleiades data without losing the fit to the far-field geodetic data. In doing so, I have revealed a level of detail in near-surface distributed slip in the near-fault region which has not previously been available.

As stated above, I have not conducted an analysis of slip uncertainties using a Monte Carlo technique, which could have been useful as a final check of the fit of the model to the data to increase confidence in the results. However, I adopted an iterative approach to assessing weighting of the datasets, and smoothing factor and individual settings such as dip and rake were adjusted over time when (for example) slip vectors appeared to be constrained by the rake settings. The close fit of the model to the individual datasets (including the Pleiades data), the extensive iterations of the constituent parts of the set-up of the model geometry and slipinv settings, and the previous uncertainty analysis in Walters et al., 2018 of the fit to the far-field data all

provide reassurance that the reliability of the results is not significantly impaired as a result.

Of particular note from my results are the extent to which slip is transferred from the principal fault plane onto neighbouring minor structures in the hanging wall, and how movement observed in the top kilometre below the surface (predominantly strike-slip in this case) digresses from dip-slip displacement observed at lower depths. These give a clearer picture of the kinematics involved in the Norcia earthquake and the diffuse nature of the near-surface displacement.

The particular geometries involved in the bends in the central area of the Monte Vettore fault (and the accompanying changes in near-surface dip) have resulted in what appears to be a relatively localised, but complex area of near-fault distributed faulting, in which co-seismic slip on the main Monte Vettore fault is transferred onto minor hanging wall structures which themselves have complicated geometries. In places, this transfer appears to be of at least partially partitioned slip, with lateral slip transferred onto more steeply-dipping structures oriented more favourably compared to the regional stress regime. The relatively unconsolidated nature of the hanging wall material, and the lower stress regime within the top 2 km below the surface have allowed a complex pattern of antithetic and synthetic faults to form over time in the hanging wall of the Monte Vettore fault, in which during the Norcia earthquake the antithetic structures seem to have played the most important part in the transfer of slip. There is no particular reason to assume that this geometrical complexity continues with depth. Nevertheless, the extent and nature of the distributed faulting and slip transfer, in particular in an area with fault bends, is an important consideration for those looking to develop seismic hazard assessments using models incorporating field data. Failure to recognise and to take into account the distributed nature of faulting is likely to lead to misinterpretation of the results derived only from surface displacement on the primary structures.

The particular role of the Pian Piccolo fault within the overall of the Norcia earthquake has been clarified, if not entirely resolved. Having previously acted as a barrier to the propagation of the Amatrice earthquake, it lay at a boundary between stress build-up

(to the northwest) and stress shadow (to its southeast). During the Norcia earthquake it appears to have ruptured simultaneously with its neighbouring Monte Vettore and Norcia antithetic faults, in a way that has meant that its expected slip pattern has been secondary to the principal slip vectors of the Monte Vettore fault, which have dominated where the faults have interacted at depth. However, its slip vectors have in turn dominated over slip on the Norcia antithetic fault where those faults interact.

My method improves upon the previous model produced by Delorme et al., 2020 using the same Pleiades data by taking an alternative approach to deriving horizontal and vertical displacement from those data, with careful application of correlation and outlier filtering techniques. This has eliminated many of the artefacts seen in that study, and I have avoided the use of data in outlying regions which I consider are questionable. The result is more reliable near-fault displacement fields which have then been used successfully in my joint inversion, which in turn has meant that I have been able to derive detail of near-surface slip which was previously lacking.

These results give insights into how to use high-resolution optical satellite data in conjunction with other geodetic datasets on future occasions to model near-surface slip distribution in active tectonic regions of similar complexity.

CHAPTER 4. Using repeat post-seismic Terrestrial Laser Scanning to test the reliability of fault scarps as evidence of co-seismic deformation following the 30th October 2016 M_w 6.6 Norcia earthquake - Meterff site

4.1 Introduction

4.1.1 Overview

The accuracy of seismic hazard models such as the national and regional hazard models in the Global Earthquake Model (https:/hazard.openquake.org/gem) depends upon the availability of reliable earthquake records in active tectonic regions and long-term slip rates on faults. A variety of methods are commonly used to obtain evidence of co-seismic and post-seismic deformation for modern earthquakes (e.g. seismology, InSAR, GNSS), but those techniques are all limited to the last few decades (in the case of InSAR and GNSS) or the last century (seismology). Earthquakes in relatively slowly deforming regions like Italy can typically have recurrence intervals of hundreds or thousands of years on each fault (e.g. Pantosti et al., 1996). Fault scarps are therefore a key component alongside historical records, palaeoseismology, and larger-scale geomorphology used to investigate older earthquakes beyond the availability of instrumental data. In this Chapter, I will focus on one fault scarp in order to investigate how reliable that scarp is as evidence of the Norcia 2016 earthquake which resulted in additional displacement along the scarp.

4.1.2 Fault scarps – uses and advantages

Earthquakes nucleate at depth, and the majority of their moment release will also occur at depth (Scholz, 1988). However, some of the distributed slip may reach the surface, with the slip seen at surface related empirically to the magnitude of the earthquake and subsurface slip (Wells and Coppersmith, 1994). Where that slip ruptures the surface, it may give rise to recognisable landforms in the form of a fault scarp (or “tectonic landform coincident, or roughly coincident, with a fault plane that has dislocated the ground surface” – Stewart and Hancock, 1990). A fault scarp

preserved in the surface may be evidence of an individual, historic earthquake, or, more probably, a succession of earthquakes over time along the same fault plane (e.g. Wallace, 1977).

Contemporaneous written records may exceptionally date back up to a thousand years or more and provide an overall idea of the extent and nature of a seismic event. However, they depend on the extent and accuracy of record-taking. Contemporaneous records are often based upon an assessment of the intensity of shaking (ground motion) produced by an earthquake, judged by its effects in a specific built-up locality. That locality may be many miles away from the epicentre in conditions which will differ from modern conditions (e.g. Ambraseys, 1971). The complexity and distributed nature of a fault network such as in central Italy might mean that it is difficult attributing a significant shaking event to a particular fault within that system. Contemporaneous records are therefore unlikely to be reliable as a guide to co-seismic near-fault displacement in all cases.

Trenching in specific areas across fault scarps may provide insight into the dates of previous events using Quaternary dating techniques, and, to some extent, the magnitude of the events as seen in those specific locations (e.g. Schwartz and Coppersmith, 1984, Galli et al., 2018). However, palaeoseismic evidence from trenching is expensive to collect, limited by site accessibility, and very site-specific. It may not, for example, identify widely distributed faulting (Michetti et al., 2005), nor along-strike variability. It is also dependent upon the quality and temporal extent of the sedimentary record, which is likely to vary. Trenching on its own is therefore unlikely to give a reliable picture of the extent of any distributed faulting, and will need to be combined with other available evidence as part of an integrated study (ibid).

Fault scarps as a record of slip may stretch back further than historical records, and are a potential source of more localised, detailed or grain scale information than historical or larger-scale geomorphological features. They can potentially provide information not just as to the extent of shaking, or longer-term tectonic uplift (e.g. Wallace, 1977, Bucknam and Anderson, 1979), but also the type of slip (e.g. Villani et al., 2018), and potentially the long-term pattern and magnitude of slip (e.g. Papanikolaou et al., 2005,

Wei et al., 2021). Unlike trenching, it is relatively easy and inexpensive to collect data at multiple places along an exposed fault scarp using either fieldwork or remote surface observation techniques (e.g. Wilkinson et al., 2015, Hodge et al., 2020).

4.1.3 Biases within fault scarps

In order to use scarps as a cumulative record of the tectonic history of an area (that can give access to long term slip rates) we need to assess three things that can potentially impact upon the reliability of fault scarps as evidence:

1) The distribution of co-seismic slip between on-fault and near-fault deformation. Scarp reliability depends on how the co-seismic slip was distributed;
2) The extent and nature of afterslip. Again, the reliability of the fault scarp record depends on the distribution of slip between on-fault and near-fault processes. This may be related to 1) above depending on the properties of the fault in the near-surface;
3) Geomorphological processes such as weathering or gravitational erosion. These will most likely happen during the afterslip period when scarps are being degraded but conceivably could also occur during a co-seismic event and during the interseismic period when erosional processes will continue to operate. Here the reliability is dependent on the preservation potential of the scarp and the surrounding area.

The first of these issues is addressed in Chapter 3. In this Chapter I concentrate primarily on the second and third of these issues.

4.1.4 The use of Terrestrial Laser Scanning ("TLS") as an investigatory technique for post-seismic slip and geomorphological processes.

Following advances in differencing techniques in the last 10 years, airborne LiDAR images acquired by UAVs or aircraft ("ALS") have been used to investigate co-seismic deformation at centimetre to sub-metre scale which is below the resolution of even very high resolution optical satellite data. This has typically been done by comparing airborne TLS results with other datasets. ALS has been used successfully to derive three-dimensional co-seismic displacements by differencing pre-and post-earthquake

datasets using ICP algorithms (e.g. Nissen et al., 2014, Nissen et al., 2017, Scott et al., 2018, Lajoie et al., 2019). However, even using ALS, the window sizes required in such techniques to reduce errors may exceed the scale at which the co-seismic deformation is measured (Nissen et al., 2012). The scales at which post-seismic deformation need to be measured are likely to be smaller still in scale. Post-seismic deformation might, in unusual cases, exceed the co-seismic deformation (Freed et al., 2007). However, the more normal and expected position is that post-seismic deformation is orders of magnitude smaller than the co-seismic deformation (e.g. Freed et al., 2006). Although post-seismic deformation may not be confined to the immediate area of the scarp itself, over a period of a few years following a medium-sized earthquake the surface manifestation of such deformation is unlikely to exceed a scale of perhaps a few centimetres (e.g. Wilkinson et al., 2012, Freed et al., 2006).

High-resolution tripod-based TLS scans taken on different occasions have been used successfully in measuring post-seismic displacement at millimetre/centimetre scale (e.g. Wilkinson et al., 2010, Wilkinson et al., 2012, DeLong et al., 2015). They have also been used to measure co-seismic displacement of less than 20 cm in a particular case where TLS scans were available from immediately before and after an earthquake (Wedmore et al., 2019), and landforms associated with co-seismic slip in the 2010 M_w 7.2 El Mayor Cucapeh earthquake using results from scans taken a couple of weeks after the earthquake (Gold et al., 2013).

Wilkinson et al., 2012 used repeat TLS surveys over a period from 8 to 124 days after the L'Aquila, 2009 earthquake to measure post-seismic deformation in 3D at 5 sites over that time period by measuring millimetre-scale partitioned post-seismic displacement. **Figure 71** (combining Figures 4 and 5 from Wilkinson et al., 2012) shows the extent of continuing deformation at two of those sites, PAG and SP. PAG was measured in the field as having a vertical offset of ~7.5 cm after the earthquake, but the post-seismic deformation measured was in the order of 1-2 cm. DeLong et al., 2015 measured centimetre-scale post-seismic deformation associated with the 2014 M_w 6.0 Napa earthquake over a period of 59 days using repeat TLS, including vertical deformation spread over a zone of several tens of metres.

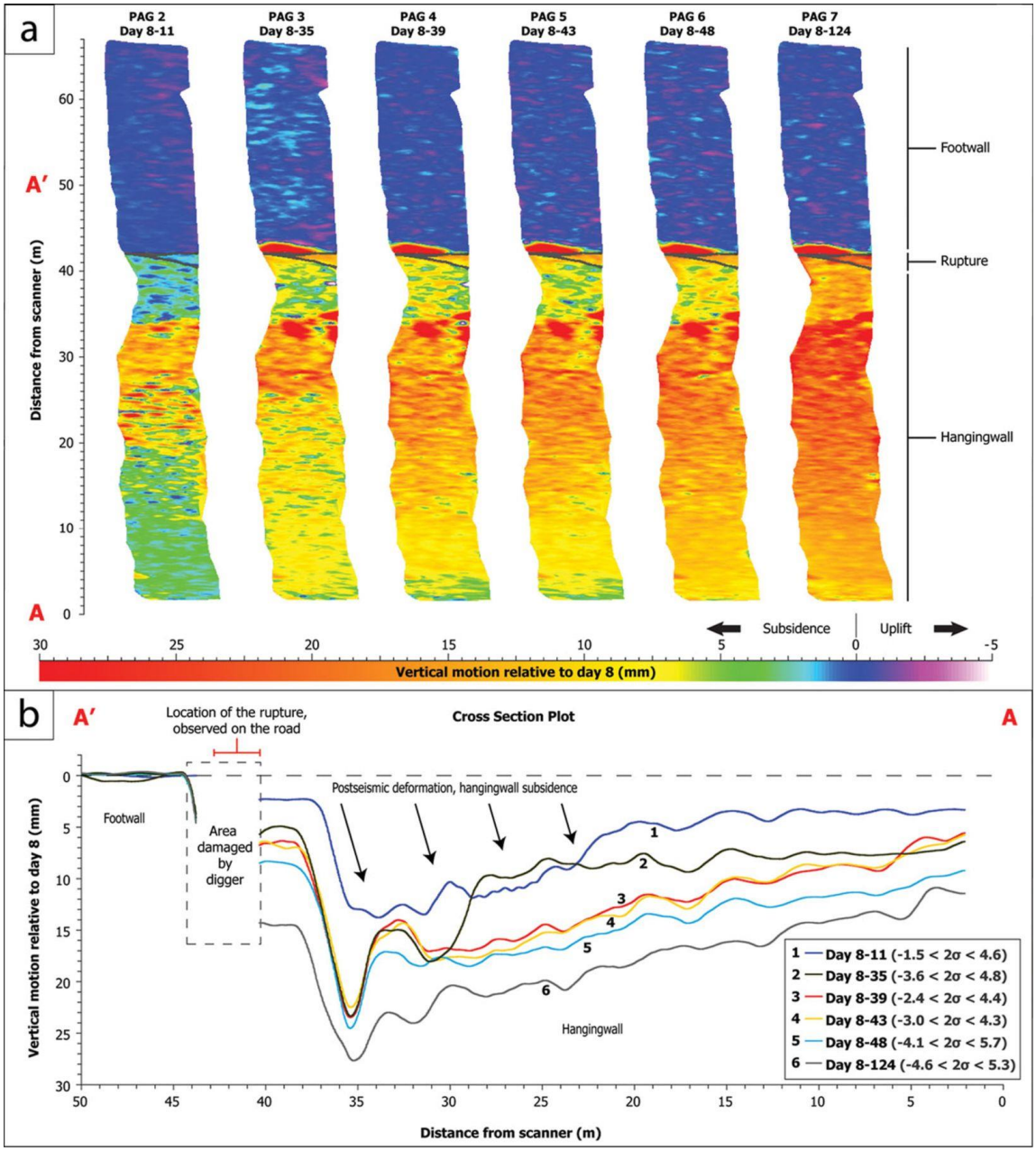

PAG site

(**Figure 71** continued on next page)

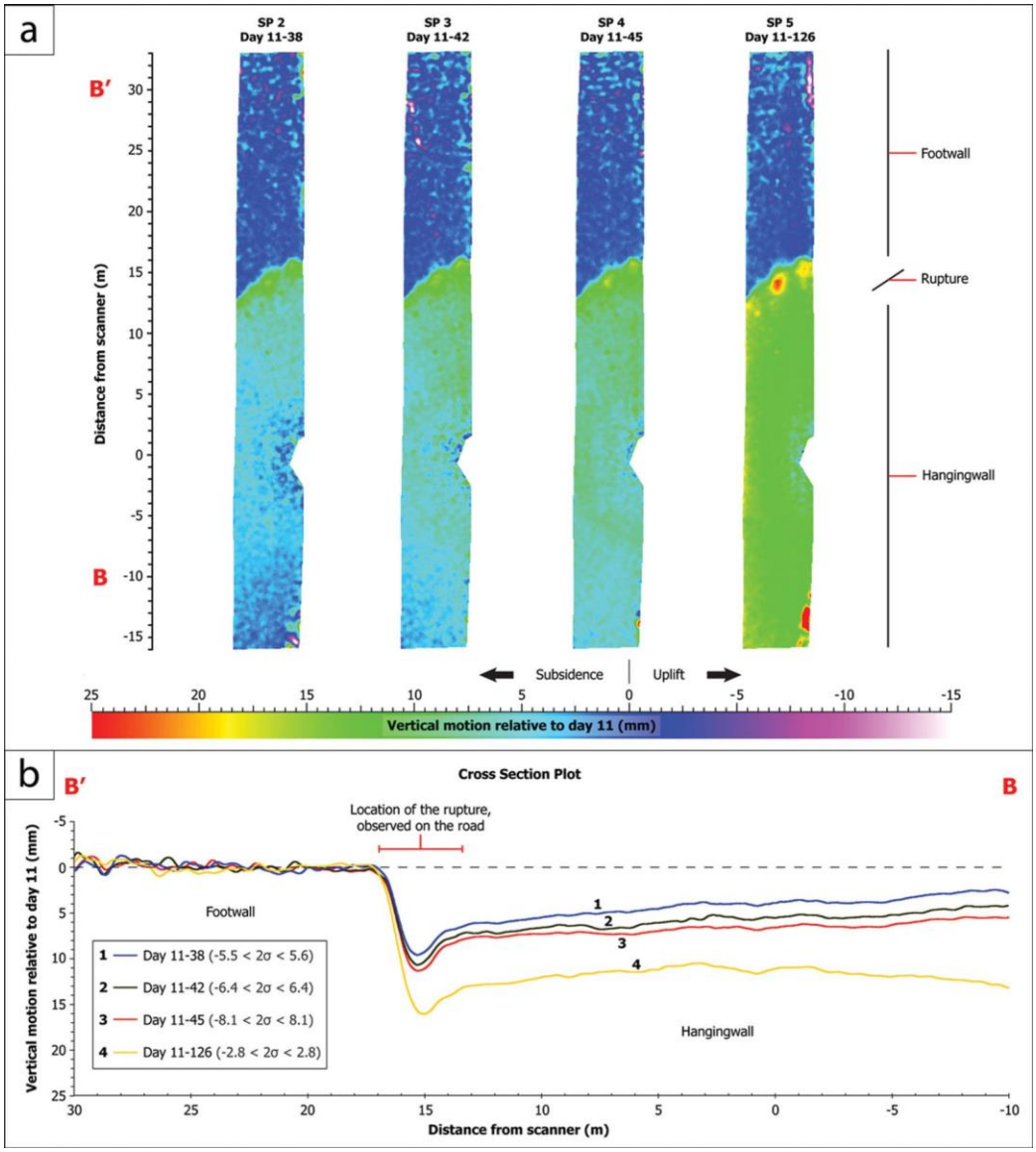

SP site

Figure 71: *From Wilkinson et al., 2012, post-seismic deformation at sites PAG and SP. In each figure (a) colour map plots showing vertical motion values in a footwall static reference frame (b) cross sectional plots taken perpendicular to the main strike of the ruptures.*

Wedmore et al., 2019, used pre- and post-seismic TLS scans separated by 8 days on a site at Bove Road (near the Frontignano ski resort in Umbria, central Italy), either side of the 2016 6.6 M_w Norcia earthquake. The results from those scans were differenced using the ICP algorithm (Nissen et al, 2017 – see **paragraph 2.2.6.2**). The study showed co-seismic vertical deformation sharply delineated on the fault itself, but with

horizontal motion distributed over an 8 m-wide zone, with ~50% of movement occurring away from the fault. **Figure 72** shows the data as medians of across-strike values. The co-seismic deformation recorded at the Bove Road site was of the order of a maximum of ~12 cm (Villani et al., 2018).

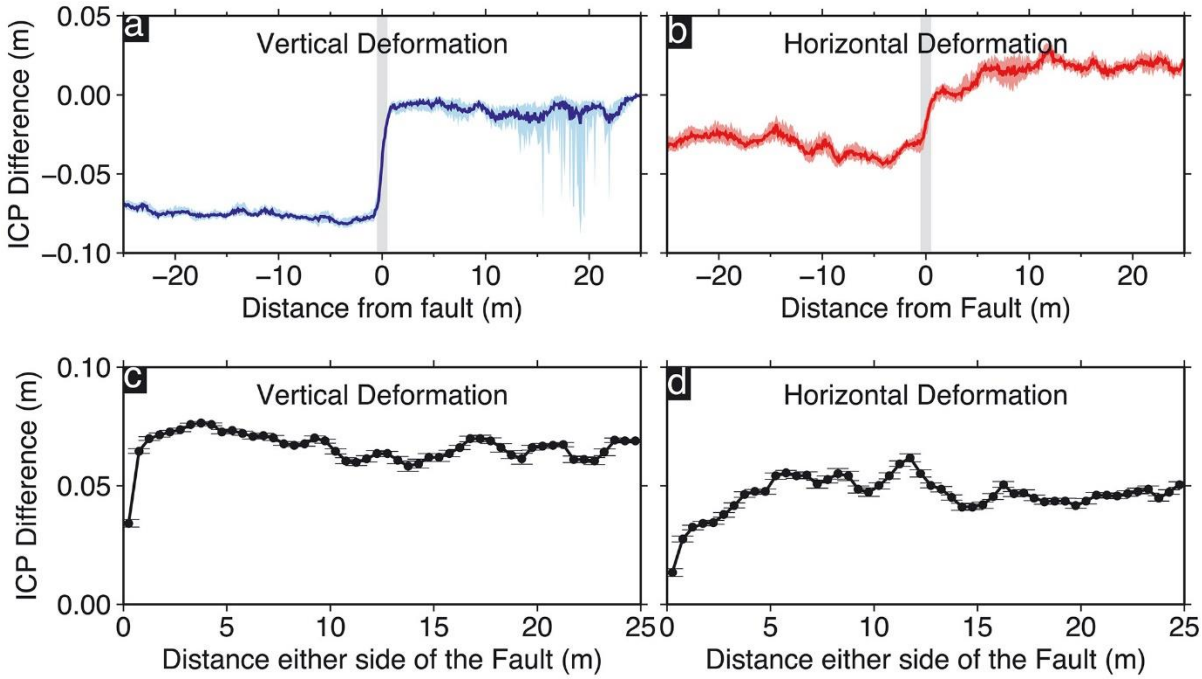

Figure 72: *From Wedmore et al., 2019, showing across-strike medians of vertical ((a) and (c)), and horizontal ((b) and (d)) co-seismic displacement from the Norcia earthquake, respectively distance from fault and distance either side of fault.*

The advantages of using TLS in this way compared to other techniques are:

- It allows for relatively easy and inexpensive investigation of multiple sites involving less time in the field than (say) trenching;
- Repeat scans over a period of time, by return visits to the same sites, allow investigation of longer-term trends;
- TLS gives greater resolution both in the level of spatial detail which can be obtained, and temporally.

In this study I use the differential TLS approach to assess the reliability of scarps and the extent to which the spatial and temporal biases have affected their ability to record long term cumulative slip. In this case, the TLS data were obtained on multiple

visits over 3 years to fault scarp sites which saw co-seismic surface deformation in a medium-sized earthquake (Norcia, 30th October 2016 M_w 6.6) in an active tectonic region (the Apennines, Central Italy).

4.1.5 Acquisition of TLS data in 2016, 2017 and 2019.

In the few days following the Norcia earthquake, a team from the University of Leeds, with Italian colleagues, scanned approximately a dozen sites where surface ruptures were apparent around the areas of greatest deformation seen in the form of new surface ruptures in the hanging wall of the MVFS. The sites covered a mixture of main fault, synthetic and antithetic structures. In 2017 further scans were taken of the majority of the same sites in either the spring or autumn (in some cases, both) by teams from Leeds and Durham Universities.

For this study, I scanned a number of those sites again in August/September 2019 (details and dates of all scans used in this study are given in Chapter 5).

In this Chapter, I concentrate on one of those fault scarps called Meterff. I investigate the processes which operate to degrade the scarp and the near-fault area in the 3 years following the Norcia earthquake.

4.2 Meterff site – description and co-seismic data

4.2.1 Choice of meterff site, location and description.

The Meterff scarp adjoins the Valle delle Fonti, near Castelluccio di Norcia, at ~UTM 33T 355350/4744100. The site was scanned in 2016 (post-Norcia earthquake), September 2017, and September 2019. It is a synthetic hanging wall splay ~1.5 km west/northwest of the main co-seismic deformation from the Norcia earthquake on the MVFS along the Cordone del Vettore, and ~2 km northeast of the Castelluccio di Norcia hilltop village. It lies at ~1425 m above sea level. The section of the scarp visible from the valley floor is approximately 100 m in length, although the scarp continues for a further ~250 m towards the north (**Figure 73**), and in turn is the southern-most surface rupture of a complicated series of synthetic and antithetic fault surface ruptures which extends over ~2 km northwards. The slope dips at ~35^o towards the southwest, with the fault scarp having an overall strike of ~150^o (veering towards ~170^o at the northeast-most end).

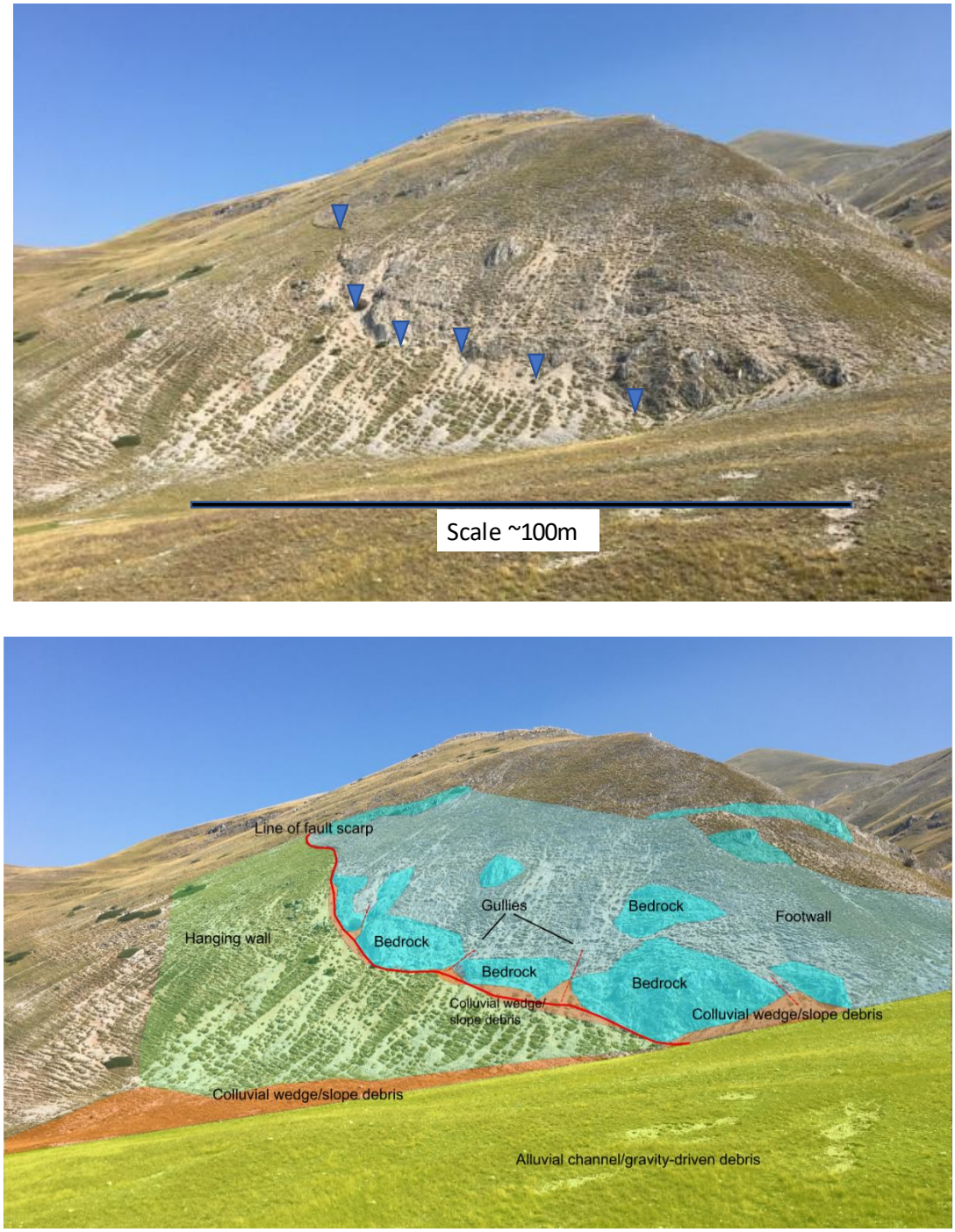

Figure 73: *Meterff fault scarp, photo taken on 30 August 2019, at UTM 33T 355224/4744125 looking NNE across an alluvial channel, line of scarp marked with blue triangles (upper panel). Annotated with my interpretations of the main areas of bedrock and debris deposits, and relative positions of footwall and hanging wall (lower panel). Red line shows my interpretation of the line of the fault scarp. Undifferentiated areas of footwall and hanging wall are primarily scree and loose deposits.*

At the foot of the slope there is a run-off from the more elevated slopes to the east (which exceed 2085 m in elevation), with unconsolidated material likely to be of either alluvial or gravity-driven origin (perhaps from avalanches). The scarp site is largely clear of significant vegetation, reasonably accessible, well covered by data from the 3 TLS scanning visits, and apparently sufficiently isolated from other surface ruptures in 2016 to be studied as a single entity (albeit one which is a synthetic or relay structure within the hanging wall of the main Monte Vettore fault system).

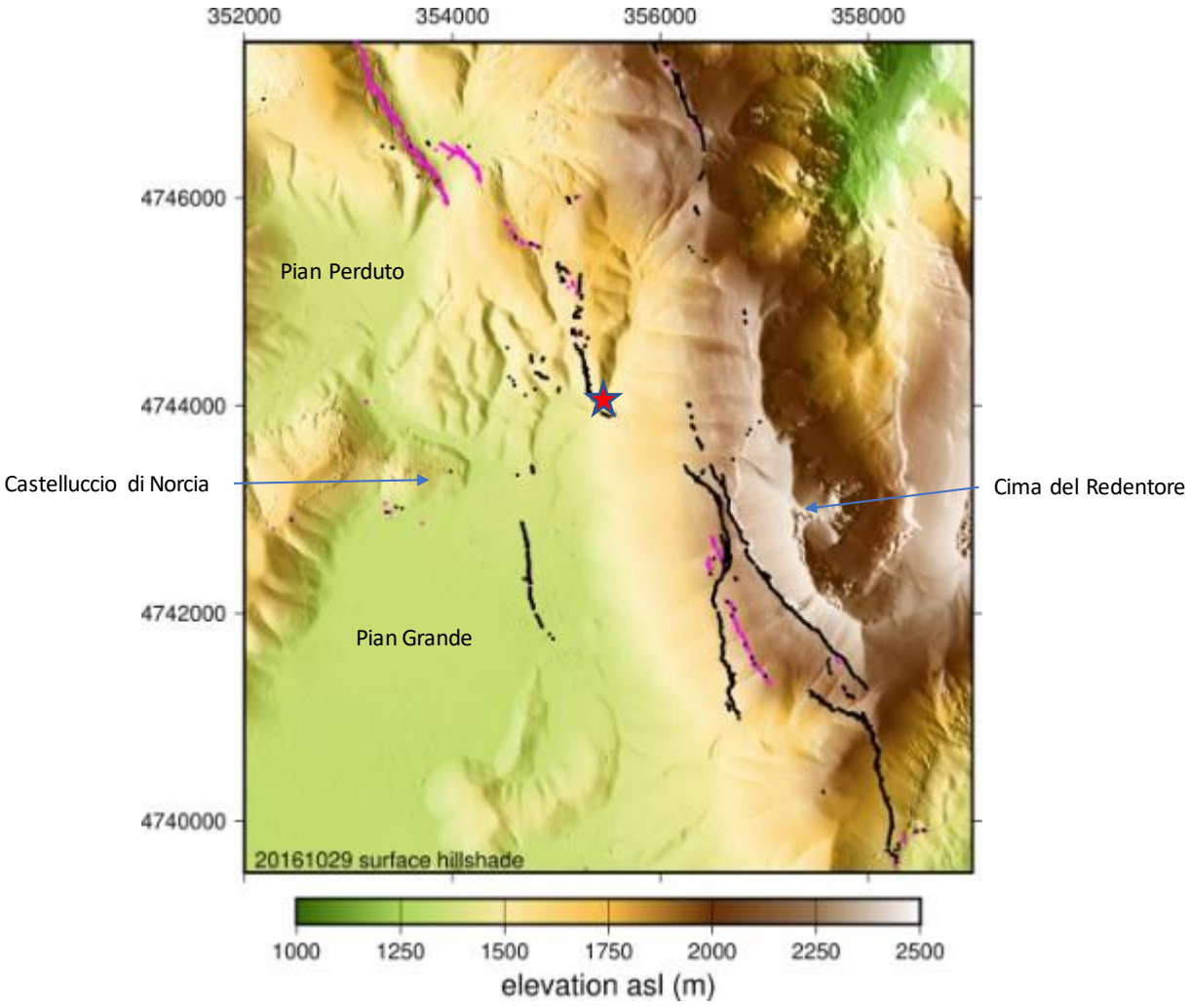

Figure 74: *Surface DEM from Pleiades data from 29th October 2016, Meterff site marked by red star. Sites mapped by the Open EMERGEO Joint Working Group in 2016/2017 (Villani et al., 2018) shown in black (synthetic dip) and magenta (antithetic dip).*

The Meterff scarp saw up to a metre of vertical co-seismic vertical displacement, as recorded in the database in Villani et al., 2018. **Figure 74** puts this site in the context of the other co-seismic field results recorded by the Open EMERGEO Joint Working Group (data from Villani et al., 2018, results covering both the Norcia and Visso earthquakes), as well as showing the surrounding geomorphology.

4.2.2 Geological setting of Meterff site.

The geology of this area was mapped most recently by Pierantoni et al., 2013. At the time, the fault trace that gave rise to the Meterff surface rupture in 2016 was apparently unknown, and it did not feature on the 2013 map although the scarp shows signs of previous movement, with exposed bedrock of up to ~2 m in places above the new scarp in 2016. It is, however, now shown on the ITHACA Catalogo delle Faglie Capaci (Catalogue of Capable Faults) (http://sgi.isprambiente.it/ithaca/viewer/index.html).

The Meterff site is within an area shown on the Pierantoni map as being a single limestone unit, Calcare Massiccio (massive limestone), set within slope deposits to the east and south, bordered to the northwest by Scaglia Variegata and Carnelian (micritic) limestone units and to the west by the Maiolica unit (**Figures 75 and 76**). The Calcare Massiccio is the oldest outcropping unit (Jurassic), consisting of white, grey or pale-brown limestones, massively or coarsely bedded in several metre-thick cycles, indicating a peritidal depositional environment ranging from subtidal to supratidal conditions (Pierantoni et al., 2013). The Carnelian micritic limestones comprise medium-thick beds, grey or dark brown in colour, with frequent calcareous turbidites (including megabreccias of the Calcare Massiccio from neighbouring structural highs). The Maiolica unit consists of white and ivory micrites, thin-medium bedded, dating from the Upper Tithonian-Lower Aptian age (the Jurassic/Cretaceous border). The Scaglia Variegata units date from the Cretaceous-Oligocene, red, grey and green limestone and marly limestones arranged in thin-medium beds alternating with marls (ibid).

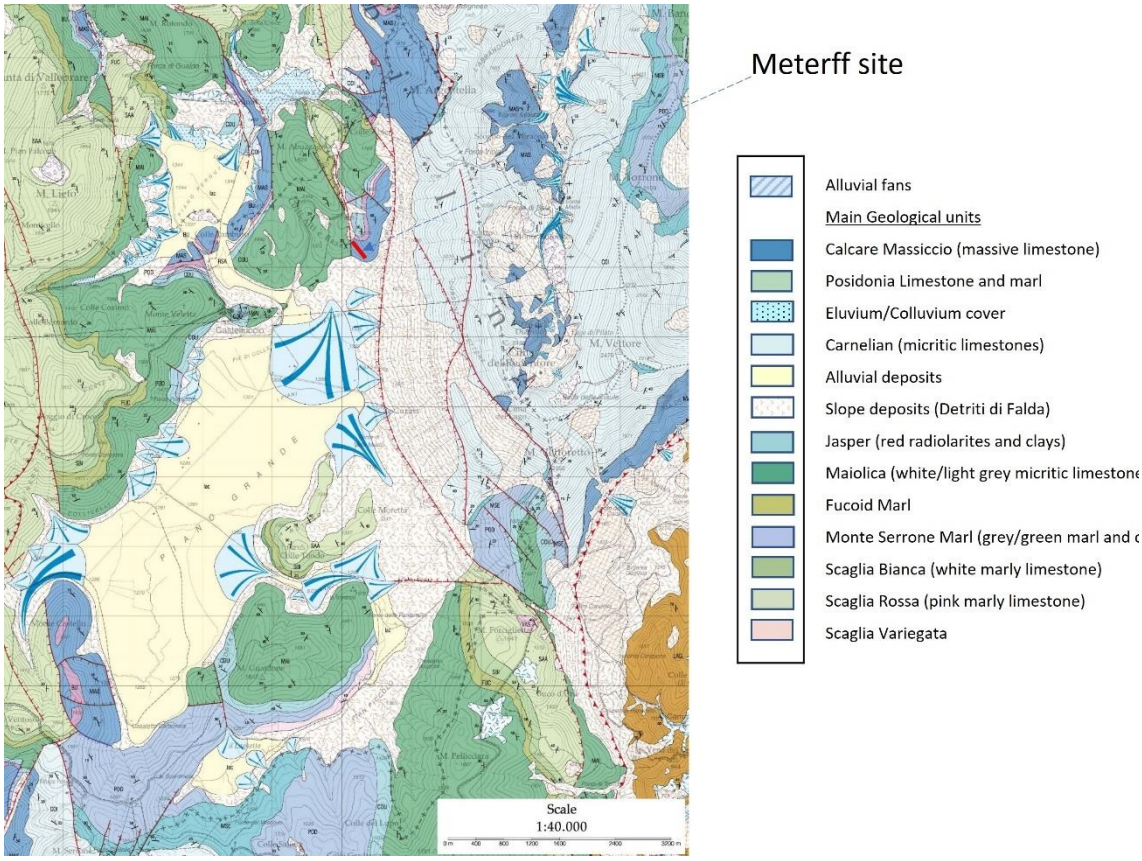

Figure 75: *Geological map of area of region covering Meterff site, from Pierantoni et al., 2013, with translations of the main geological units where appropriate. Meterff site added in bold red line. Known fault traces at that time marked in red, with ticks on hanging wall side.*

Previous tectonic activity has resulted in the downthrow of the later Maiolica unit to the west so that it now outcrops next to the Calcare Massiccio (**Figure 76**). The majority of the faulting shown in Pierantoni et al.'s 2013 map in the immediate area around the Meterff fault scarp is normal faulting synthetic to the main Monte Vettore fault, trending ~north-south. Further to the north and west the faulting shown is antithetic normal faulting. There are also what appear to be shorter segments to the north of the Meterff scarp linking the north-south faulting trending at ~150-160^{o} (probably as relay structures).

There also appears to be a synclinal structure, with beds dipping at ~40/50^{o} to the west in the Calcare Massiccio and Carnelian units, changing to ~30^{o} dip to the west and then ~40^{o} dip to the east in the Maiolica unit (**Figure 76**).

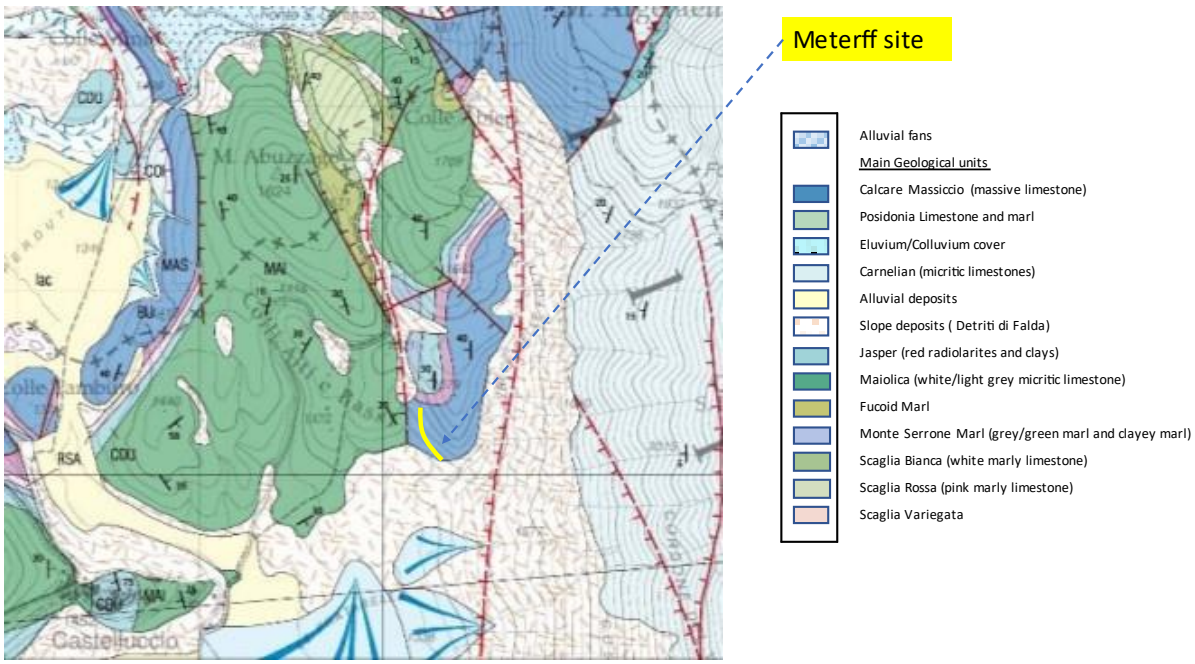

Figure 76: *Detail of* ***Figure 75*** *above, showing area immediately surrounding the Meterff site (added in yellow)*

4.2.3 Co-seismic results, from fieldwork.

The Open EMERGEO Joint Working Group recorded slip at a number of locations along the Meterff scarp (**Figure 77)**.

Maximum slip recorded was ~1 m (giving the location its name). Locations where field measurements were taken with slip measurements (35 out of ~58 locations recorded) largely coincide with areas of exposed bedrock, rather than colluvial wedge/slope debris. Smaller values typically coincide with locations where the rock type is recorded as either “debris” or “Bedrock/debris” (although rock type was not recorded in many instances).

Co-seismic “slip vector trends” recorded showed slight left-lateral kinematics, plunge being predominantly towards ~225^{o}. Recorded rakes were similar at ~-72^{o} in a plane striking towards ~150^{o} and dipping at ~70^{o} (which produces a plunge of ~63^{o} towards an azimuth of ~197^{o}) (there were < 5 measurements in either case) (all data from Villani et al., 2018). The individual measurements are in **Table 4.2.3** below.

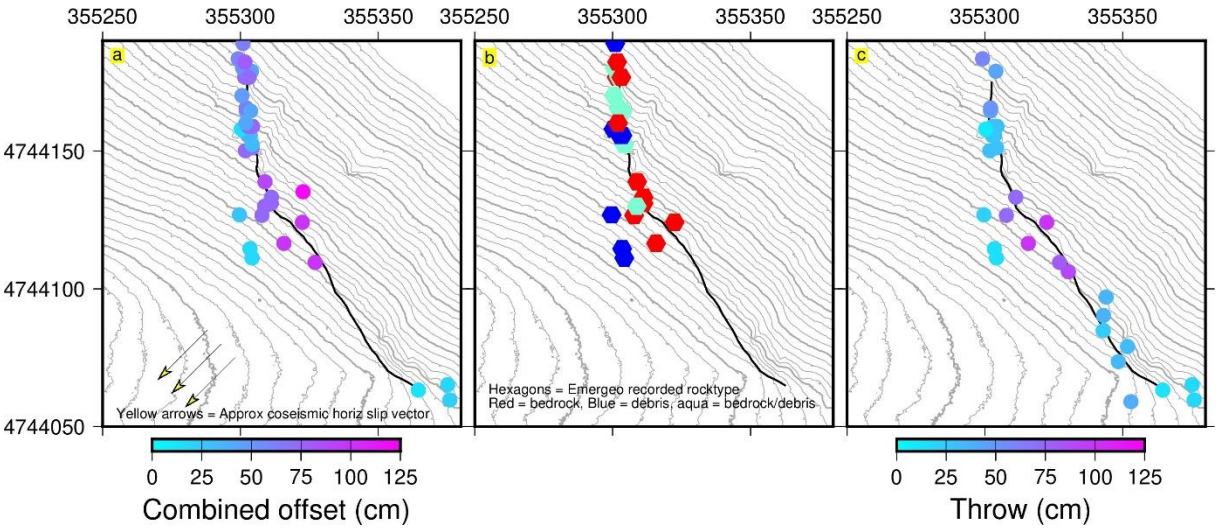

Figure 77: *Open EMERGEO field locations, showing: (a) combined co-seismic offset data (from locations where both throw and heave were measured, or offset was measured), and approximate slip vectors, with height contours at 2 m intervals; (b) recorded rock types (Red = bedrock, blue = debris, aquamarine = bedrock/debris); and (c) throw (in all cases, whether heave/opening was also measured) (data from Villani et al., 2018).*

Table 4.2.3 Table of Emergeo field measurements for Meterff site showing either rake or plunge and slip vectors.

Emergeo reference	Strike	Dip Direction	Rake	Slip vector trend	Plunge
6198	148	238	-70	n/a	n/a
6086*	n/a	277	n/a	277	-70
6258	158	248	-72	n/a	n/a
2058	n/a	n/a	n/a	223	55
6259	150	240	-72	n/a	n/a
2059	n/a	n/a	n/a	226	52
2060	n/a	n/a	n/a	234	36

(* This record appears anomalous, with slip vector trend matching dip direction)

Those approximate vectors are shown on **Figure 77 (a)**. There was inconsistency between the EMERGEO field teams as to whether measurements were of throw, throw and heave (opening), or offset. The combined offset **Figure 77 (a)** records where either offset, or both throw and heave were measured.

In Galderisi and Galli, 2020, the co-seismic slickenlines results for the Colli Alti fault (which the Meterff scarp appears either to be part of, or to link to) were summarised as a fault plane strike of 152°, with 67° dip, and slickenlines trending towards 196°, plunging at 59° (a rake of -68°), with left oblique kinematics.

4.2.4 Inverse Modelling of co-seismic slip using shallow slip distribution models.

I cautioned in Chapter 3 about the distorting effect of a north-south sinusoidal feature observed in the vertical deformation results from differencing the Pleiades data west of Easting 355647 UTM 33T. I have excluded that area from the inverse modelling results presented in that Chapter. However, in order to see if the model fits with these field data, I repeated the modelling using a further, 20th, fault segment representing an extended Meterff fault segment, using results from the Pleiades data which include the "sinusoidal" area as well as the area used in the previous inversion. Before doing so, to try to lessen the sinusoidal effect by correcting for it, I extrapolated the results from a profile of the vertical displacement results from an 8 km long strip (north-south) 2 km in width (east-west) centred on Easting 354000 UTM 33T (see **Figure 40** in Chapter 3), and deducted the trend seen from the results in the "sinusoidal area" (ie the area to the west of Easting 355647 UTM 33T). This correction did not succeed in completely removing the effect, but lessened it. I then limited the Pleiades results used in the joint inversion to results from within I km of the modelled fault segments including the additional Meterff segment (see **Figure 78**), and applied a spatial mean filter of 120 m x 120 m to reduce the size of the input files for the inversion.

In this inversion I modelled the fault segment including the Meterff scarp area as a separate, synthetic, structure in the Monte Vettore hanging wall with a strike of 170°, dip of 65°, length of 1400 m and a depth of 3 km, centred on UTM 33T 355250/4744550. This places the segment as extending to the north beyond the area studied here using TLS, with that area lying towards the south end of the modelled fault segment. The fault segment is discretised into fault patches of ~ 0.5 km x 0.5 km, reflecting the detail provided by the Pleiades data, but also that the data may not be as reliable in the "sinusoidal" area compared to the area further east. Other settings and geometries were unchanged from the joint inversion presented in Chapter 3 and I do not therefore repeat them here.

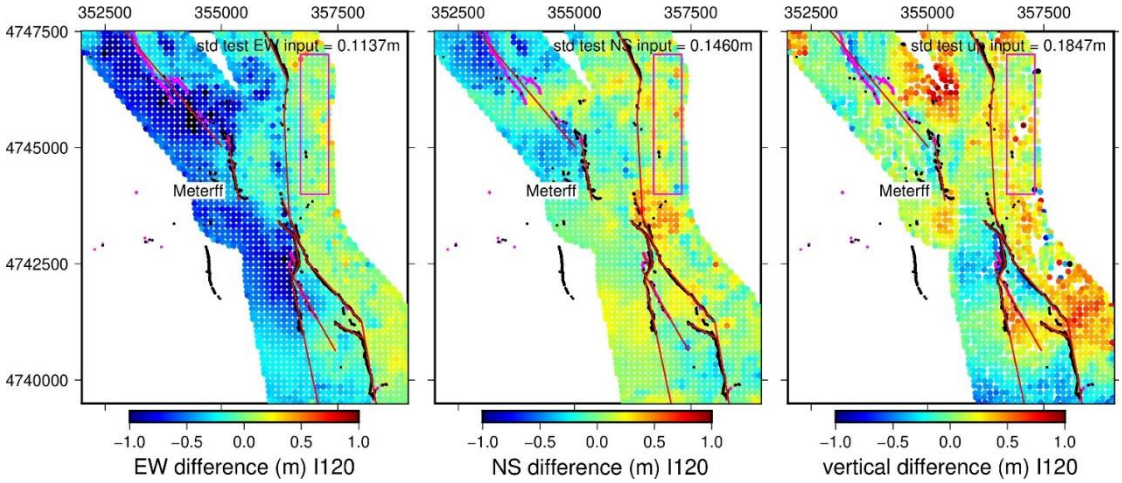

Figure 78: *Pleiades input data for the extended area used for the joint inversion including the "new" Meterff fault segment used in the model geometry. Black markings show the locations of co-seismic synthetic dips recorded by the Open EMERGEO Joint Working Group, magenta markings antithetic dips.*

Table 4.2.4 Table of RMS (Root Mean Squared) misfits of model using extended area for Pleiades data to datasets compared to Standard deviation (std) figures for those datasets and to RMS values from inversion without extending the Pleiades data area.

Dataset	Standard deviation (m)	RMS misfit (m)	RMS misfit using extended data (m)
Pleiades east-west	0.1148	0.1399	0.1606
Pleiades north-south	0.1141	0.1438	0.1719
Pleiades vertical	0.1805	0.1823	0.1919
ALOS	0.0248	0.0154	0.0178
Sentinel	0.0253	0.0131	0.0144
Far-field GNSS east-west	0.0452	0.0122	0.0132
Far-field GNSS north-south	0.0268	0.0062	0.0063
Far-field GNSS vertical	0.0615	0.0069	0.0073
Relative GNSS east-west	0.267	0.0477	0.0838
Relative GNSS north-south	0.1559	0.0434	0.0877
Relative GNSS vertical	0.4078	0.0691	0.0734

The result of the model in the case of the new fault segment incorporating Meterff is shown in **Figure 79**. This shows largely dip-slip displacement of up to ~ 0.5 m towards ~ 250-260^{o} at ~ 1-2 km depth in the centre of the fault segment, but lower figures for slip towards the ends of the fault segment and towards the surface.

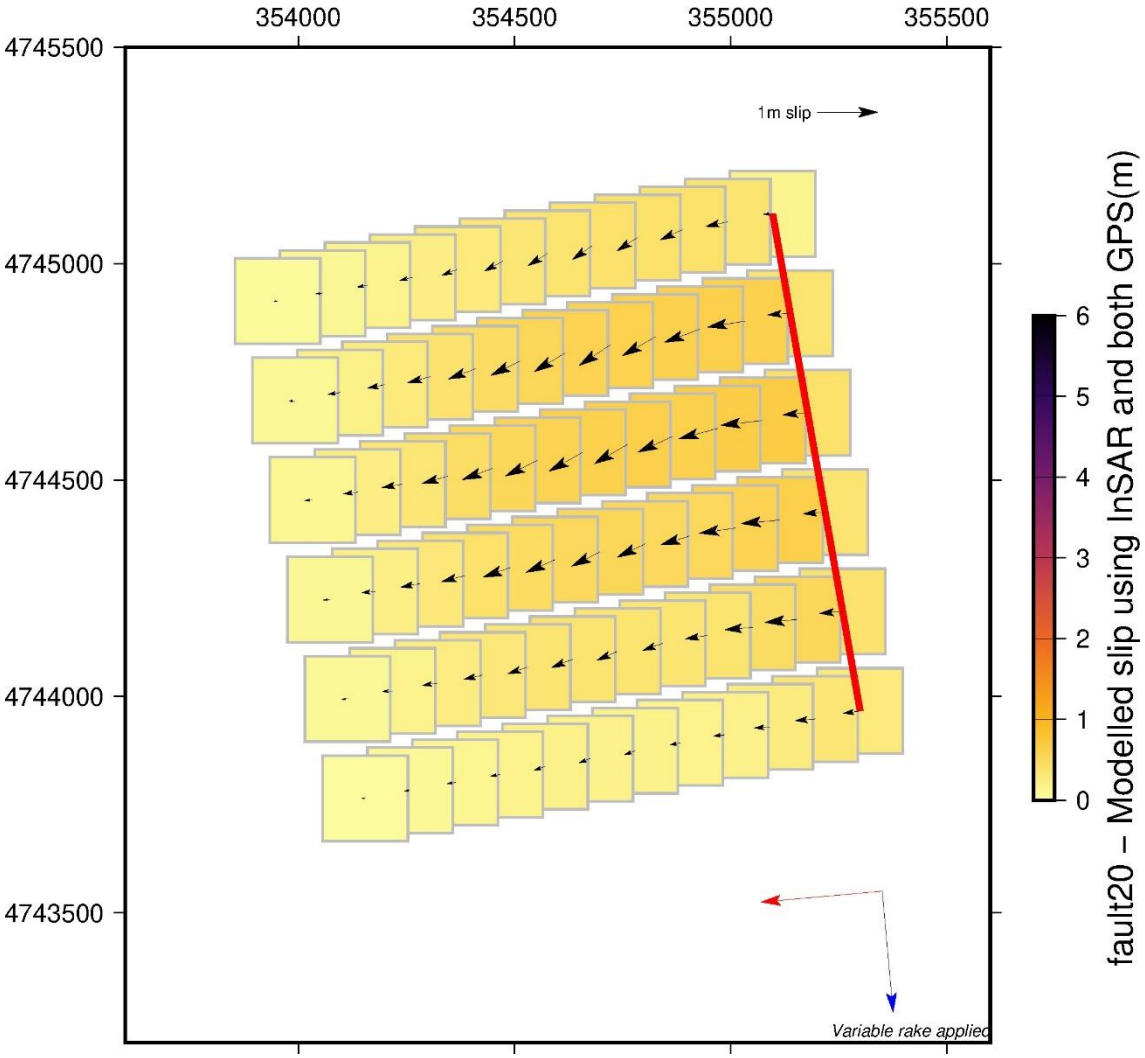

Figure 79: *Modelled co-seismic slip vectors for the additional fault segment including Meterff as part of the joint inversion using the extended area of Pleiades data.*

4.3 Scan acquisition

The first scan of the Meterff scarp using TLS was conducted by a team from the University of Leeds on 31st October 2016, the day after the Norcia earthquake. Their drawing of the field site is shown in **Figure 80**. A single panoramic scan was taken with a tripod-mounted RIEGL VZ-1000 scanner, positioning 3 registration targets in the

hanging wall of the fault to reference the scan globally, using GNSS.

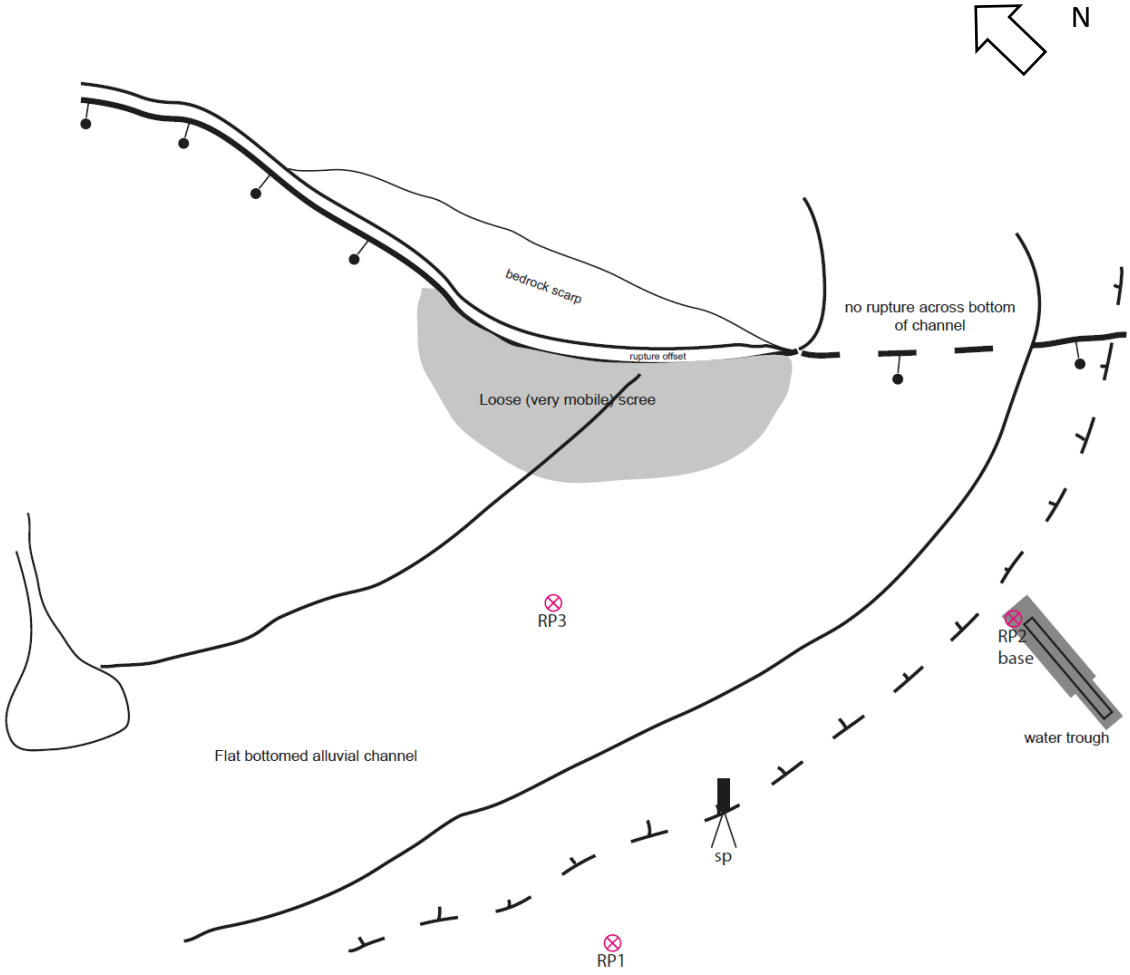

Figure 80: *Drawing by University of Leeds team of TLS field site at Meterff (UTM 33T 355224/4744125) on 30th October 2016.*

The scan position used by the University of Leeds team was at the top of a raised bank across a flat-bottomed alluvial channel from the main bedrock scarp looking ~northeast towards the slope. A field photo from 2016 is shown in **Figure 81**.

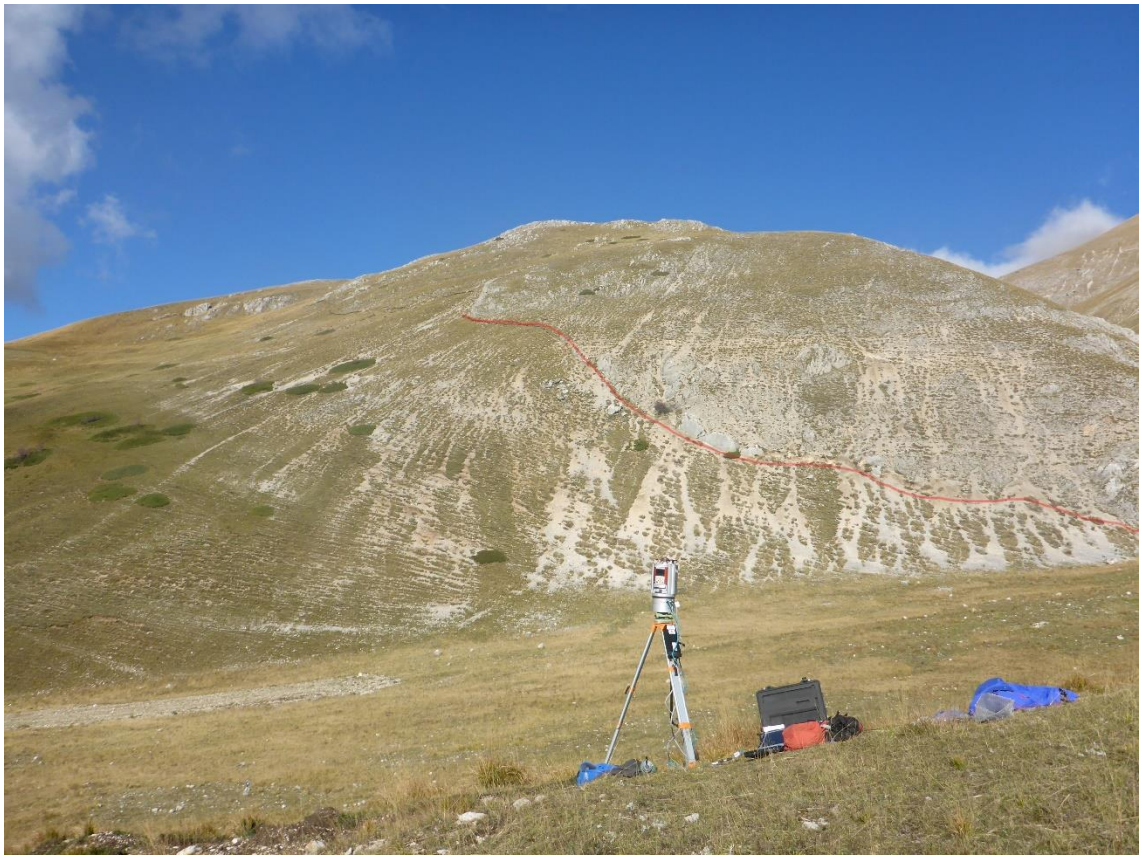

Figure 81: *Field photograph of Meterff site on 30 October 2016 looking northeast (photograph taken by Luke Wedmore, then University of Leeds), line of approximate fault trace marked in red.*

The same approach was followed in 2017, with the Leeds and Durham team using a RIEGL VZ-4000 scanner on 3rd October 2017. A single panorama was shot from approximately the same position on the top of the raised bank opposite the fault scarp, using similar registration targets. However, the GNSS coordinates for those registration targets in both 2016 and 2017 do not appear to have been saved successfully, with recorded coordinates (including height) bearing no relationship to the actual position of the scarp.

In 2019 we used 2 scan positions, one of which matched approximately the previous scan and reflector positions on the raised bank overlooking the alluvial channel, the other being halfway across the alluvial channel towards the fault scarp (see **Figure 82**, my drawing of the scan site in 2019).

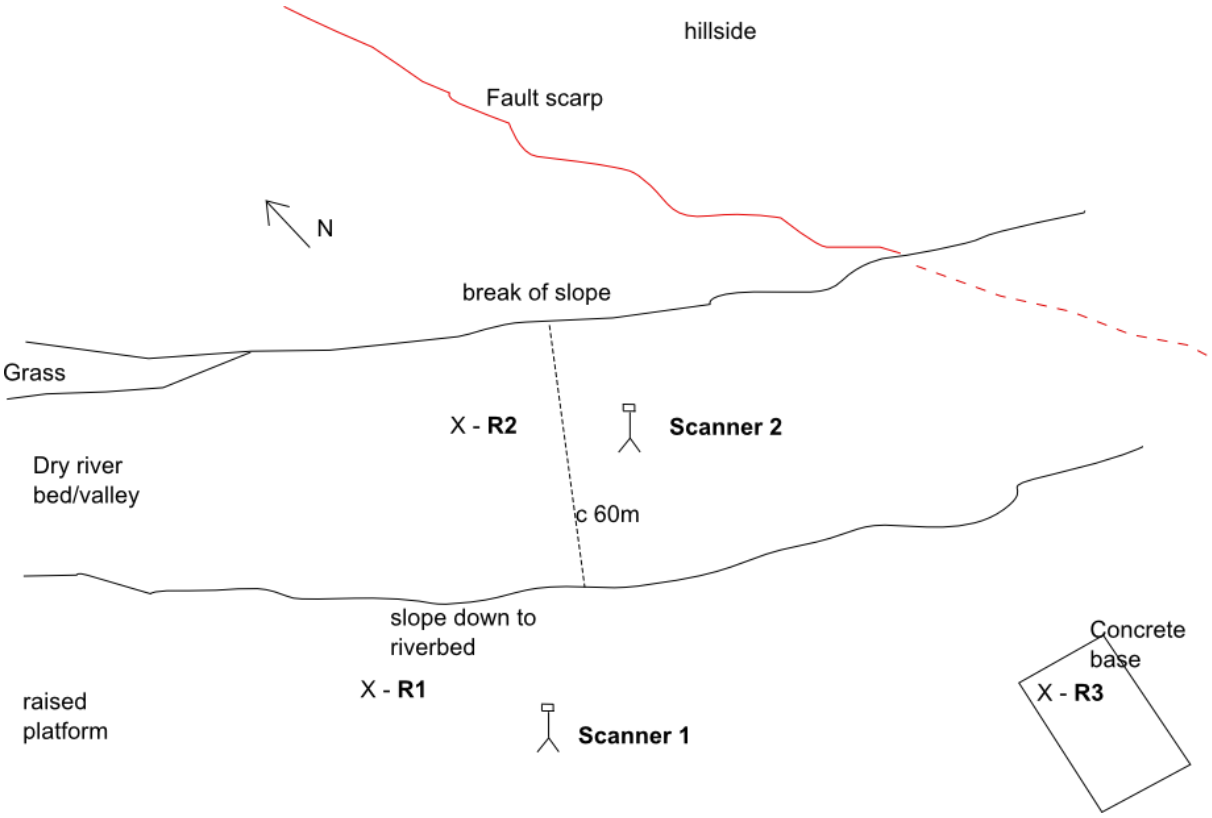

Figure 82: *Field drawing of scanner (Scanner 1, 2) and reflector (R1-R3) positions used on 30 August 2019 at UTM 33T 355224/4744125.*

In total we took 4 scans on 30th August 2019, using a tripod-mounted Leica C10 Scanstation scanner. From the raised position we took medium and high resolution panorama scans (360°). From the alluvial bed position we took a medium resolution panorama, and a high resolution window ~ 20m high along the main fault scarp. Using similar positions for the registration targets as previous scans, I used those positions to reference the scans globally using RTK (real-time kinematic positioning) GNSS, and then to tie the 4 scan datasets together internally using Cyclone 9.1.3 software. Note the water trough shown in the 2016 drawing is no longer present having been removed by an avalanche in the 2016/2017 winter, although the concrete base remains.

4.4 Processing scans

4.4.1 Pre-processing Meterff TLS data

In each case, using the relevant proprietary software (RiScan Pro 2.4 in the case of the RIEGL scans and Cyclone 9.1.3 in the case of the Leica scans), I manually cleaned the

scans to remove noise from scan returns caused either by atmospheric anomalies such as dust or distant topography, cut the size of the scans to the usable areas surrounding the Meterff fault scarp, and exported the point clouds. In the case of the 2019 scans, I also co-registered the multiple scans internally, as described above. I then used a spatial filter in Cloud Compare software (CloudCompare v2.10.2) to remove points closer than 2 cm to each other in each of the point clouds to achieve equivalent resolutions between the scans, and to reduce the point clouds to manageable size.

I considered using a "lowest" point filter to remove the seasonal effect of vegetation. I experimented with using a filter with decreasing area window sizes containing increasing point densities to select the lowest points in each window, removing points above the lowest point elevation (retaining the ground surface detail in areas of high point density). However, I found that, even using window sizes as small as 25 cm x 25 cm the filter reduced the number of remaining points within the datasets to a resolution which made it difficult to align the point clouds reliably for subsequent differencing. There is, in any event, relatively little vegetation in the scan site area in either the footwall or hanging wall adjacent to the fault scarp. I did not therefore feel that a "lowest" point filter was justified here, compared to other noise filtering techniques.

4.4.2 2D Pre-alignment of Meterff TLS point clouds

In the light of the erroneous coordinates for the 2016 and 2017 scans, and using the 2019 GNSS positions as a guide, I applied bulk shifts to the recorded coordinates of the earlier scans, to move the scans into the same rough location as the 2019 scans. In both cases I then used the CloudCompare Rotate/Translate tool to manually rotate the scans around their respective Z axes, to approximately line up the scans horizontally to the 2019 scan. I then applied bulk translations of the vertical coordinates of the 2016 and 2017 scans using the same tool, translating solely along the Z axis (fixing the X and Y axes). Once the scans were approximately aligned I then applied the CloudCompare rough alignment tool using tie points in each of the pairs of scans to align the 2016 point cloud more precisely to the coordinates of the 2019 reference cloud by a rigid transformation (producing a combined matrix showing the rotation about 3 axes, X, Y and Z, and a 3D translation vector). I then roughly aligned the 2017 point cloud to the

aligned 2016 cloud, and the 2019 cloud to the 2017 aligned cloud, using tie points in each respective pair. Once roughly aligned in this way, I used the point-to-point ICP algorithm within CloudCompare to precisely reference the later point cloud in each pair of point clouds to the earlier point cloud using a nearest neighbour comparison, making allowances for the respective degrees of overlap between the point cloud pairs. Although I tried using various patches within the footwall to derive a matrix as a reference point to align the clouds using a rigid transformation I was unable to do so satisfactorily. I concluded that the extent of continued erosion in the footwall over time was introducing distortions in the matrix, which were then amplified when the transformation was applied to the later point cloud. Using the whole point clouds to reference the later cloud to the earlier cloud seemed to produce a more reliable result in each case (specifying the degree of overlap between the clouds when using the CloudCompare fine registration tool). That was the approach I adopted in each case for this site.

4.4.3 Use of ICP algorithm in differencing Meterff data

Once the respective pairs of point clouds were aligned using the method described above, I then used the windowed point-to-plane algorithm within Matlab which is described in Chapter 2, paragraph 2.2.6.2 as a method of deriving a "3D" differencing result (yielding all three components of deformation, east-west, north-south and vertical outputs, through a single process) (Bouaziz et al., 2013, Chen and Medioni, 1992, Nissen et al., 2012, Nissen et al., 2017). In each case, in differencing the pairs of datasets I used local windows of 1 m x 1 m, with a buffer zone or fringe of 0.4 m to allow for horizontal displacement (larger than the expected maximum post-seismic deformation where the maximum co-seismic deformation recorded in the field was 1 m), and a sliding window of 0.2 m (which means that adjacent cells overlap by 80%).

In order to illustrate the processes I followed in differencing the datasets and the consequences of the stages involved, as an example I show below the results obtained for the vertical displacement seen between the 2016 and 2019 scans. **Figure 83** shows respectively the unfiltered ICP results (a) and the same results with a median filter applied on a grid of 1m x 1m (b).

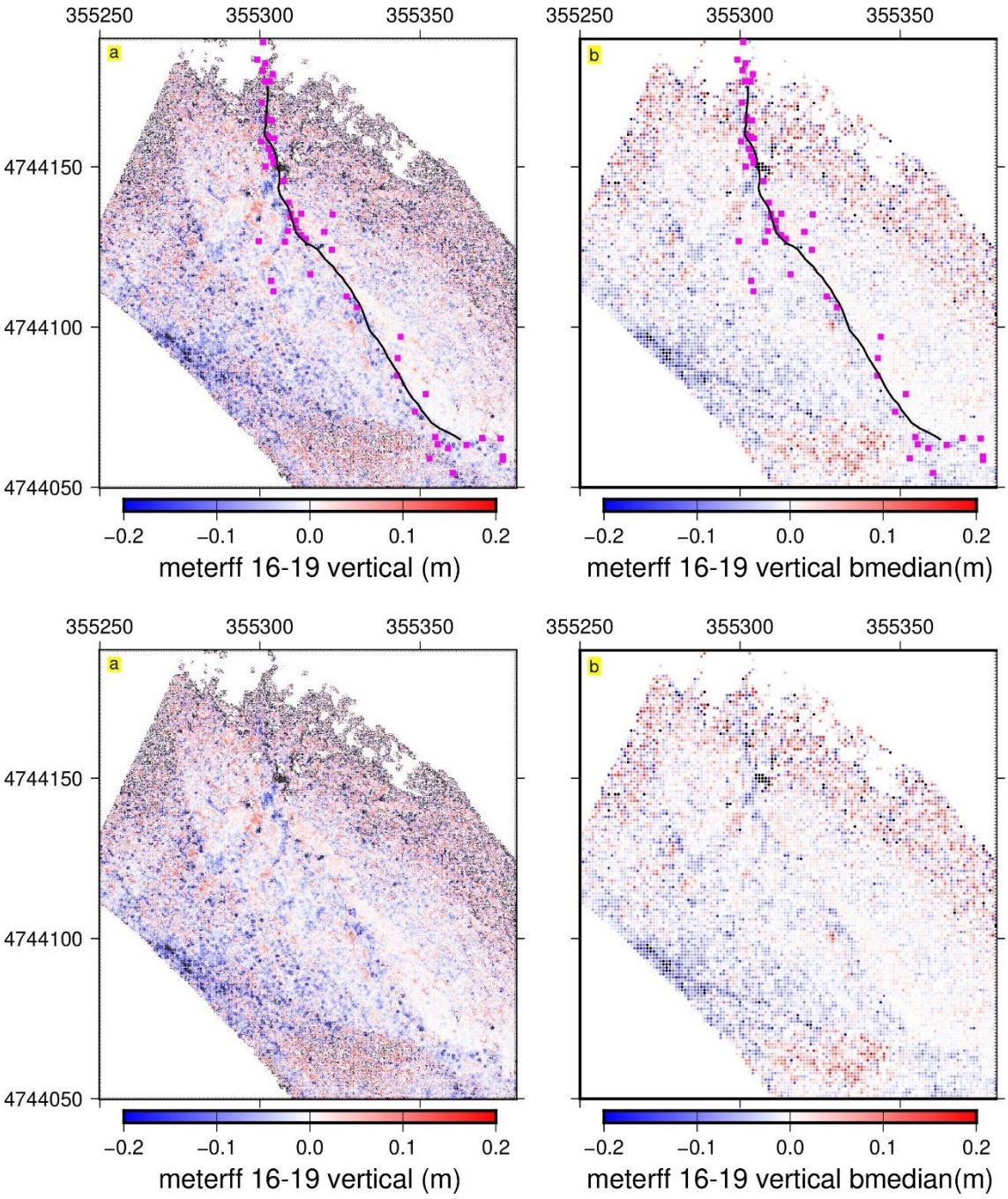

Figure 83: *ICP results showing vertical displacement between 2016 and 2019 scans, (a) shows results without filtering; (b) shows results with median filter on a 1m x 1m grid. Magenta squares (this and subsequent figures) are the location of the co-seismic field measurements by the Open EMERGEO Working Group (Villani et al. 2018). My best estimate of the fault scarp line is shown in black (lower panels show the same results without the scarp line and field locations).*

Although the colour palette used here is limited to +/- 20 cm vertical movement, the ICP results contain considerable amounts of noise, especially away from the area immediately adjacent to the fault scarp and the figure saturates at both negative and positive values. Even using the median figure (RH panel), the maximum displacement shown is between ~-1 m and +70 cm. Similar amounts of noise were seen in the results from the other ICP results (for 2016/2017 and 2017/2019) and in the east-west and north-south dimensions.

In **Figure 83** and the following figures I have shown an estimated fault scarp line, which I drew using ArcGIS Pro, based upon a DEM from the 2019 dataset, allied to my photographs of the site, and Google Earth imagery.

4.4.4 Further filtering of ICP results for TLS to remove noise and isolate signal

Given the noise in the initial results from the ICP algorithm, and in light in particular of the initial manual alignment (through CloudCompare) of the 2016 and 2017 point clouds relative to the 2019 point cloud, I then solved for possible ramps in each of the three dimensions. Before doing so, I removed results which exceeded displacement of 30 cm in any of the 3 dimensions. As a visual comparison also showed that there were some areas where there were few if any results in the scans for one or other of the point cloud pairs, I then used a spatial selection to select only the ICP results which were within 50 cm of both sets of data in each pair (to avoid “false” results from the algorithm calculating a transformation for a window in which one or both of the datasets had very little or no data). After that I detrended the remaining ICP data by applying a best fit plane correction by way of deduction from the ICP results. The results of those combined processes are shown in **Figure 84** (again, showing the vertical displacement results between 2016 and 2019 as an example).

The effects of this selection and detrending stage are shown in **Figure 85**. In this case, detrending by the application of a ramp makes only a small difference (the overall ramp difference from west to east is ~1.2 cm). The larger scale removal of noise by the application of selection and removal of displacement values exceeding +/- 30 cm excludes mainly peripheral data, and very little data is removed from the vicinity of the fault scarp itself.

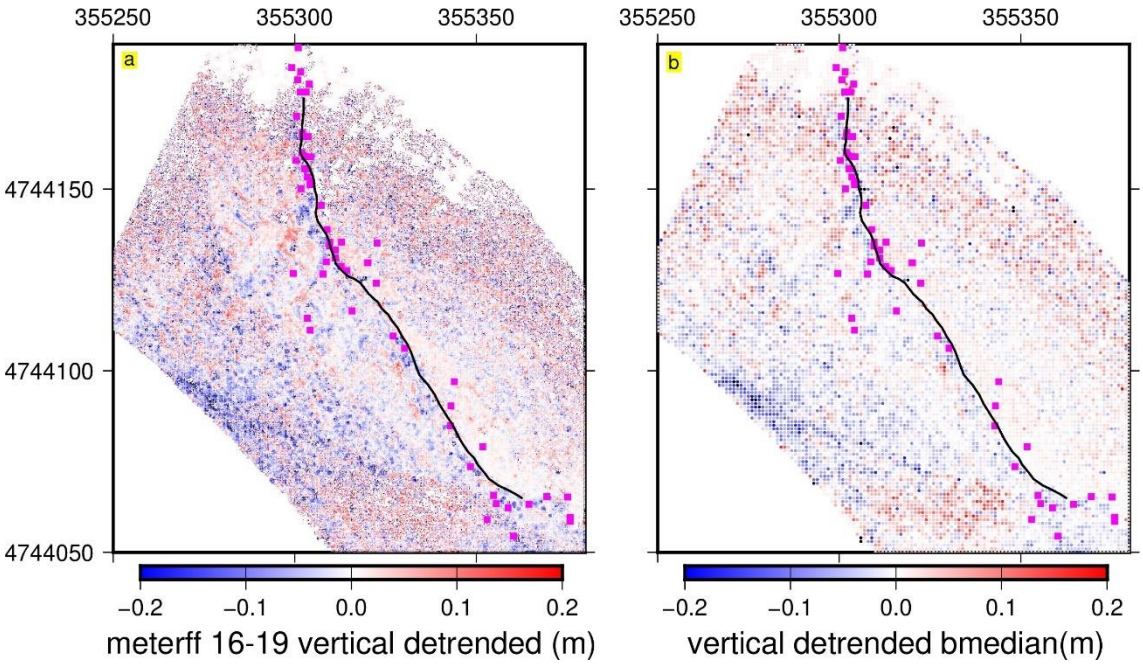

Figure 84: *ICP vertical displacement results between 2016 and 2019 scans, (a) after detrending and selection of areas where datasets overlap, (b) with 1m x 1m grid median filter.*

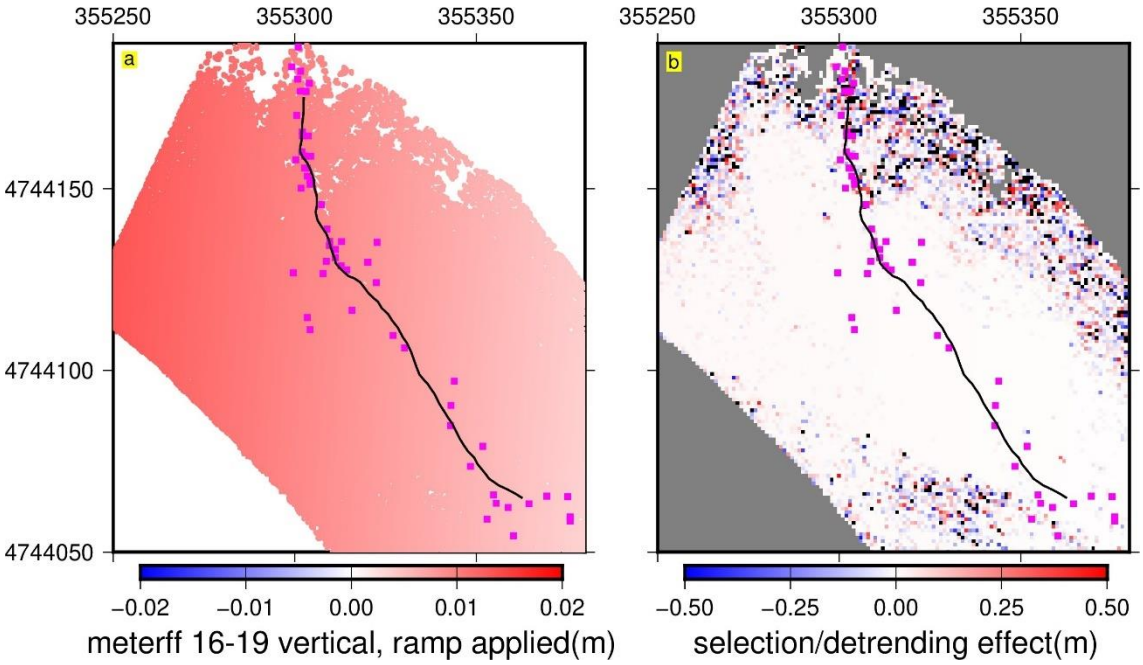

Figure 85: *(a) Ramp applied to detrend ICP vertical displacement results, (b) overall difference between ICP vertical displacement results and results after selection of common areas, exclusion of points exceeding +/- 30 cm displacement, and detrending.*

Although the results of this selection and detrending clarified the signal, the results remained noisy in places, with some anomalous individual results particularly in areas away from the main fault scarp. I therefore applied a final stage of a recursive filter to a 1 m x 1 m gridded median dataset of the detrended ICP results aiming to replace outliers with median values. The filter uses iterations involving increasing local window sizes of 3 x 3 points up to a maximum of 15 x 15 points (3, 5, 7, 11, 15). The filter calculates outlying values within each iteration which fail to meet a threshold set as a minimum variance (here 0.04 or 4%) between the median of the values in that window and that value (or the preceding window median if it has been replaced in an earlier iteration) and/or a minimum required level of non-NAN values in that window (here 0.4 or 40%). Those outliers are replaced by the median value at each stage, unless and until the threshold is no longer passed, or the series of iterations concludes by reaching its maximum window size.

The results from this final processing step are shown in **Figure 86**, discussed in more detail in the Results section.

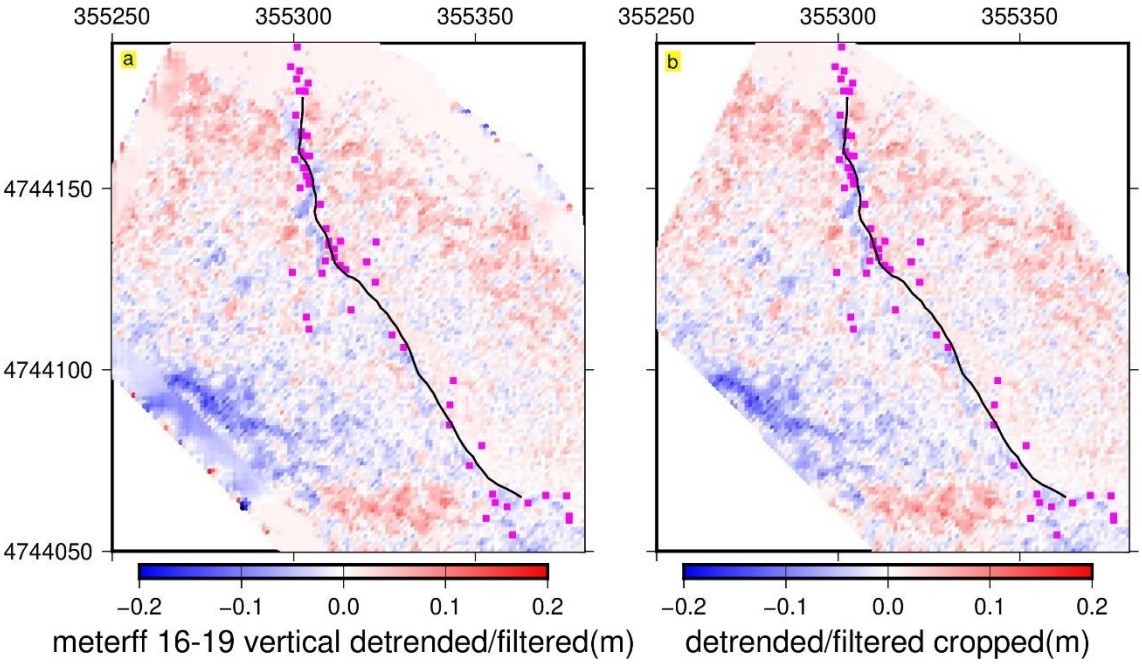

Figure 86: *Vertical differencing between 2016 and 2019 results after ICP, detrending and recursive filtering, (a) full filter results, (b) cropped to extent of previous figures.*

The filtering step requires the data to be gridded, therefore I have only used the median filtered results from the previous (detrending) step. Due to the use of increasing window sizes in the recursive filtering process, used on a cropped dataset on a grid (as here), the filter adds a surrounding border (shown in the LH panel below). It also replaces NaN values with values based upon medians of surrounding non-NaN values.

For comparison with results shown in previous figures, panel (b) shows the results cropped to the same polygon outline area as those previous figures.

The difference in results from this final de-noising step are shown in **Figure 87**. (a) shows the data points which have been filtered out by the application of the recursive filter. (b) shows the overall extent to which the combined steps of data selection, detrending and recursive filtering have removed noisy data from the original results from ICP (cropped to the same polygon as in the figure above to exclude the surrounding border applied in the recursive filtering process).

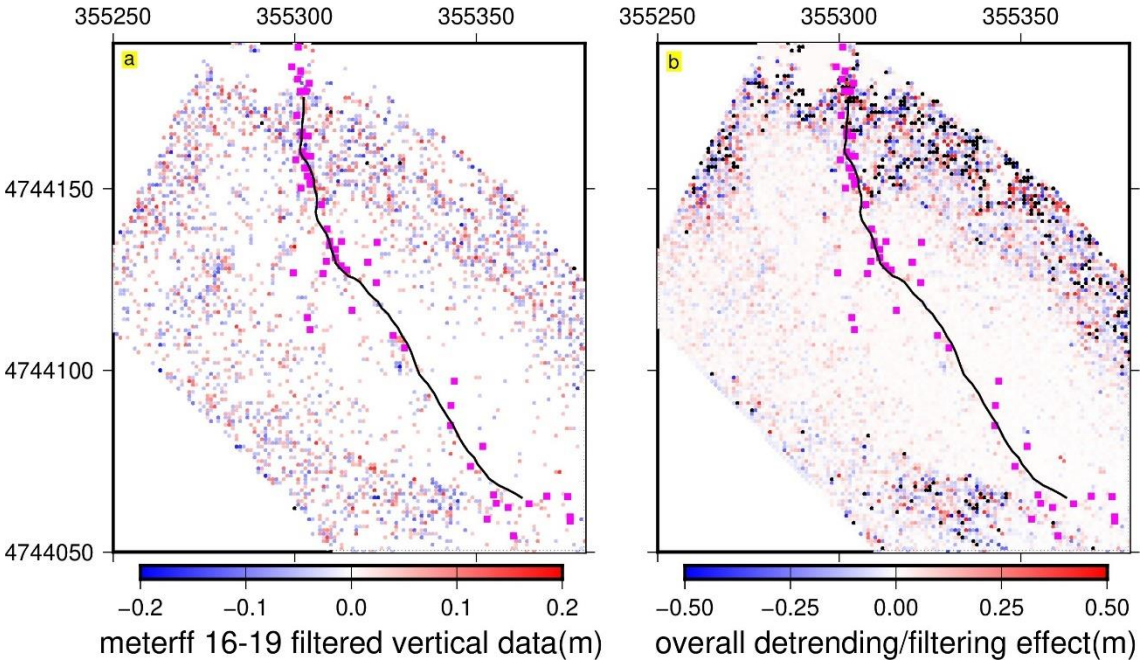

Figure 87: *Effects of the application of the recursive filter. (a) Extent of data removed from the previously detrended results by the recursive filter. (b) Combined effect of the selection and detrending processes, and recursive filtering. Note that different scales are used in the respective panels.*

I experimented with using other threshold figures for the recursive filter, but found that overall across the various detrended results, the settings shown here achieved the best balance between retaining the signal in the near-fault scarp area whilst removing noise from areas further away from the scanners (in particular, further up the slope, and in the comparatively horizontal alluvial channel area at the foot of the slope where the returns would be expected to be less reliable than on the steeper hillside beyond).

4.5 Results

4.5.1 Differencing results

I processed 3 "pairs" of scans through the differencing steps described above, obtaining east-west, north-south and vertical differencing results for each of the 2016/2017, 2017/2019, and 2016/2019 point cloud pairings. Each of the point clouds was cropped to broadly the same overall central area, although in the case of the pairs involving the 2019 scan the area is slightly smaller as the 2019 scan did not cover as much of the footwall as the earlier scans. In each case below I will show the detrended, and recursively filtered results, although I also show the unfiltered (but detrended) results in each case in **Appendix 4**.

(a) 2016/2017

The time difference between the 2016 scan and the 2017 scan is approximately 11 months.

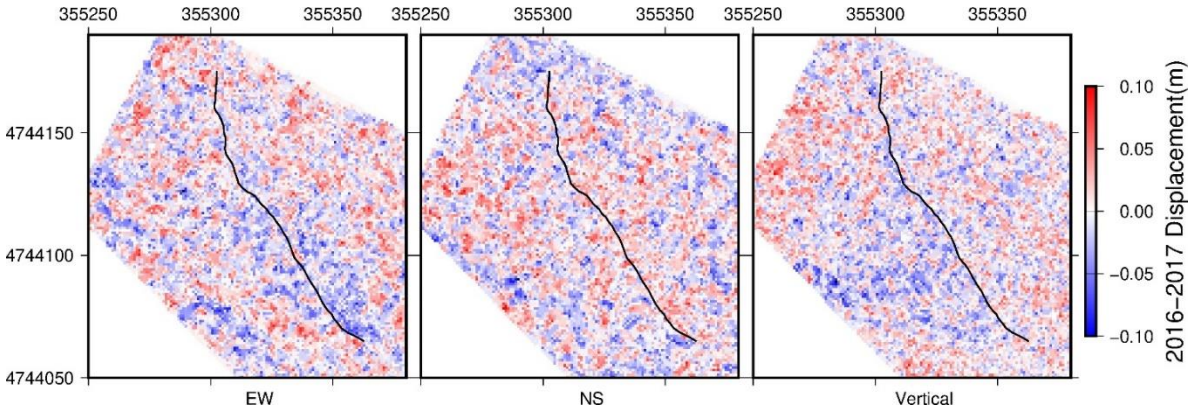

Figure 88: *Results of displacement in east-west, north-south and vertical components between 2016 and 2017 scans.*

The differencing results for east-west, north-south and vertical displacement are shown in **Figure 88**. The post-seismic displacements observed are much smaller in scale than the co-seismic displacements.

In order to visualise the combined displacements in one combined figure, **Figure 89** shows the overall horizontal slip vectors, set against a background of the vertical results, in both cases using median filter gridding at intervals of 5 m x 5 m.

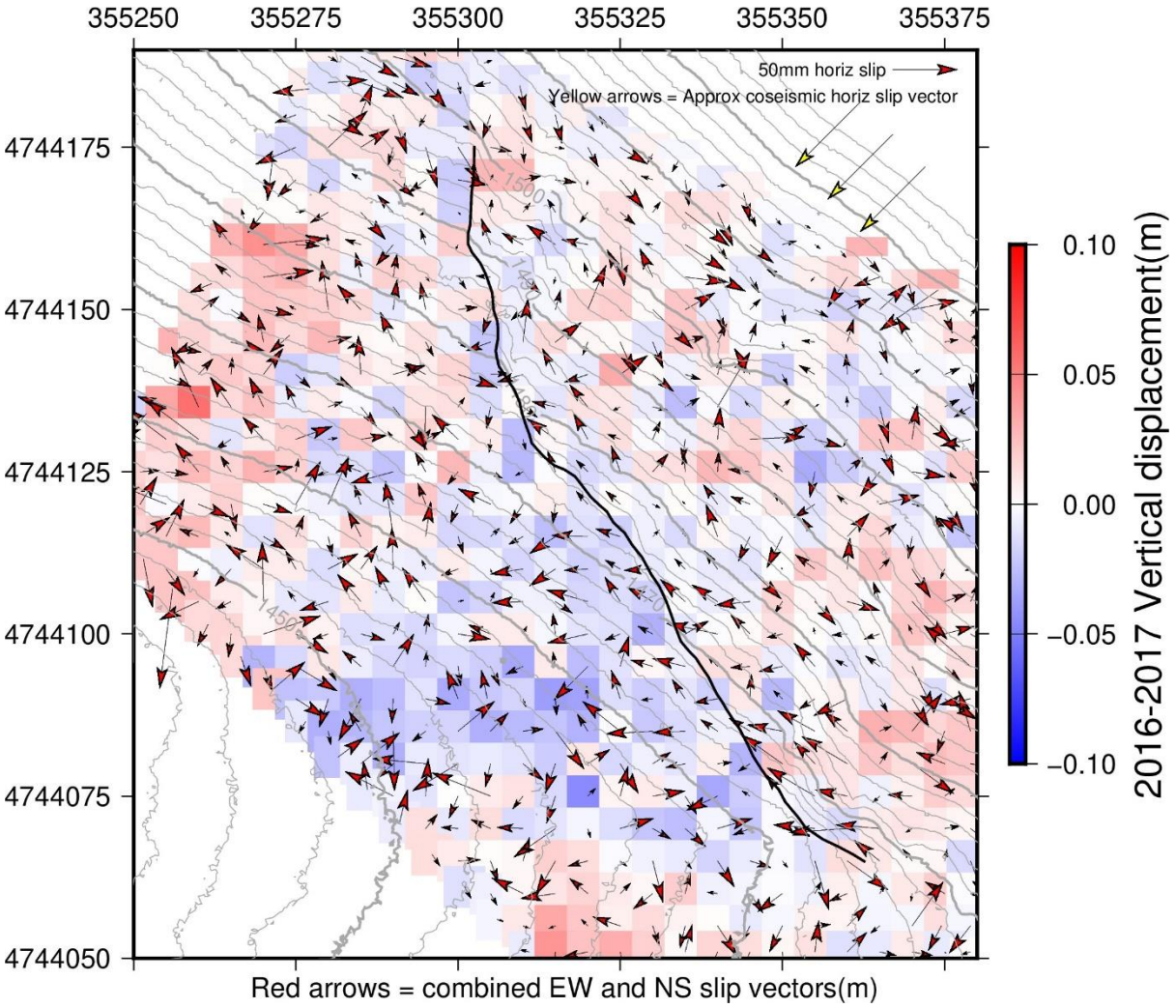

Figure 89: *Combined horizontal slip vectors for 2016–2017 (red arrows) set against a background of vertical displacement, in each case results are median values at 5m intervals.*

Horizontal slip vectors show little clear pattern. However, the hanging wall is displaced downwards relative to the footwall by up to ~2-3 cm, particularly adjacent to the fault

scarp, although the displacement is not uniform throughout and is more prominent in the lower slope areas.

This vertical displacement can be seen in a stacked scarp-perpendicular profile (**Figure 90**). Further away at ~10-30 m from the scarp the downwards vertical displacement in the hanging wall continues in the lower parts of the slope.

Individual scarp-perpendicular profiles show similar results (although the profiles vary by location). An example is shown in **Figure 91**. In this particular example, the north-south movement immediately next to the scarp is more pronounced than in the stacked profile.

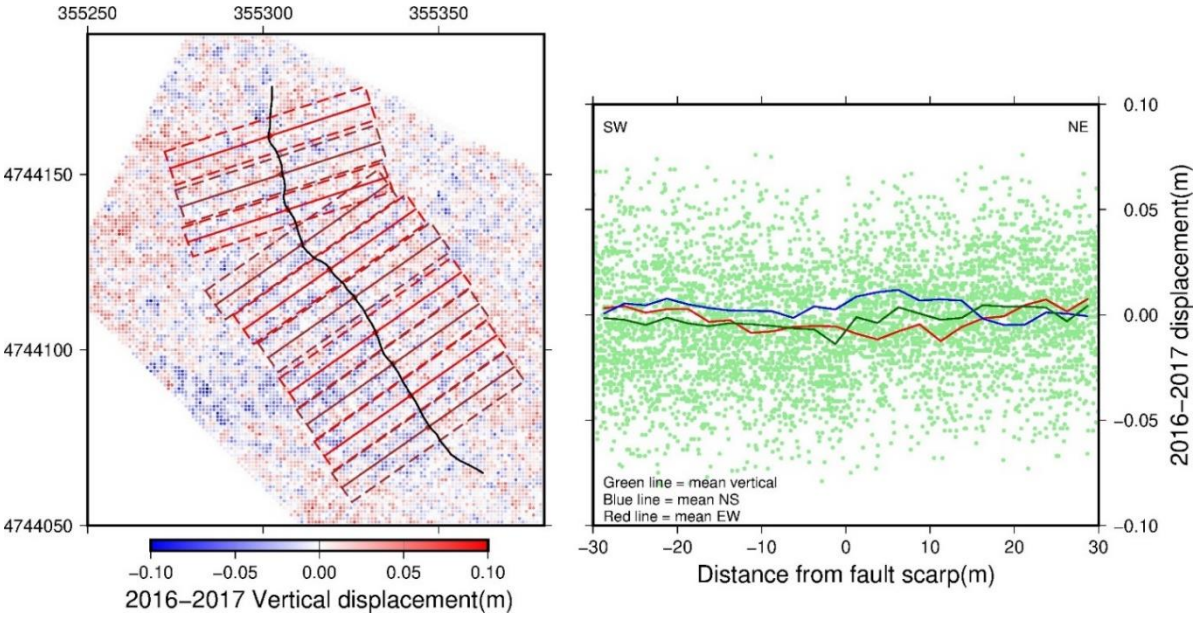

Figure 90: *Stacked profiles perpendicular to the fault scarp (LH panel shows the individual profiles in plan view against the 2016–2017 vertical displacement results, RH panel (for this and following figures) shows mean east-west (red line), north-south (blue line) and vertical (green line, individual results in light green) displacement). Negative values represent west, south and downwards movement respectively.*

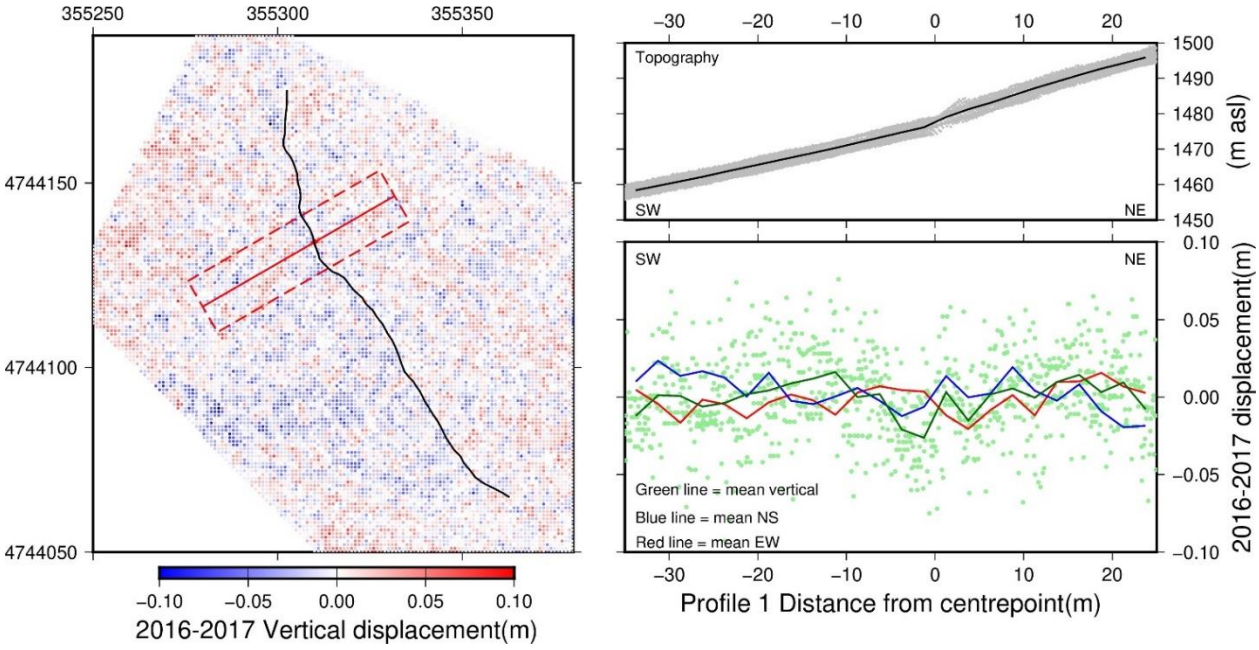

Figure 91: *Example individual profile showing 2016–2017 displacement (description of content as in previous figure). Top right panel shows topographic profile of slope.*

(b) 2017/2019

The difference in time between the 2017 and 2019 scans is ~ 22 months, with 2 intervening winters. The differencing results for east-west, north-south and vertical displacement are shown in **Figure 92**.

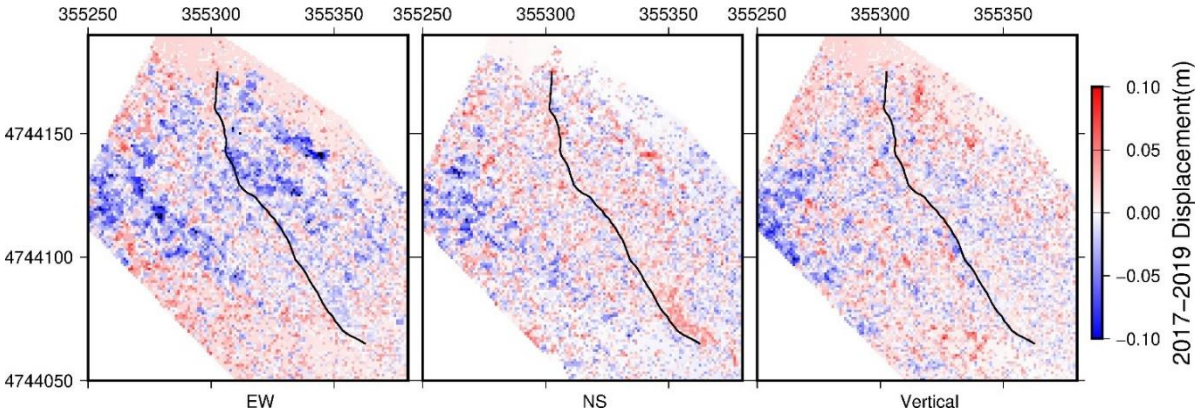

Figure 92: *Results of displacement in east-west, north-south and vertical components between 2017 and 2019 scans.*

Here, the results show more regular displacement in the horizontal vectors, and a perhaps more mixed picture in relation to the vertical displacement. **Figure 93** shows the respective horizontal and vertical displacement represented on a single figure.

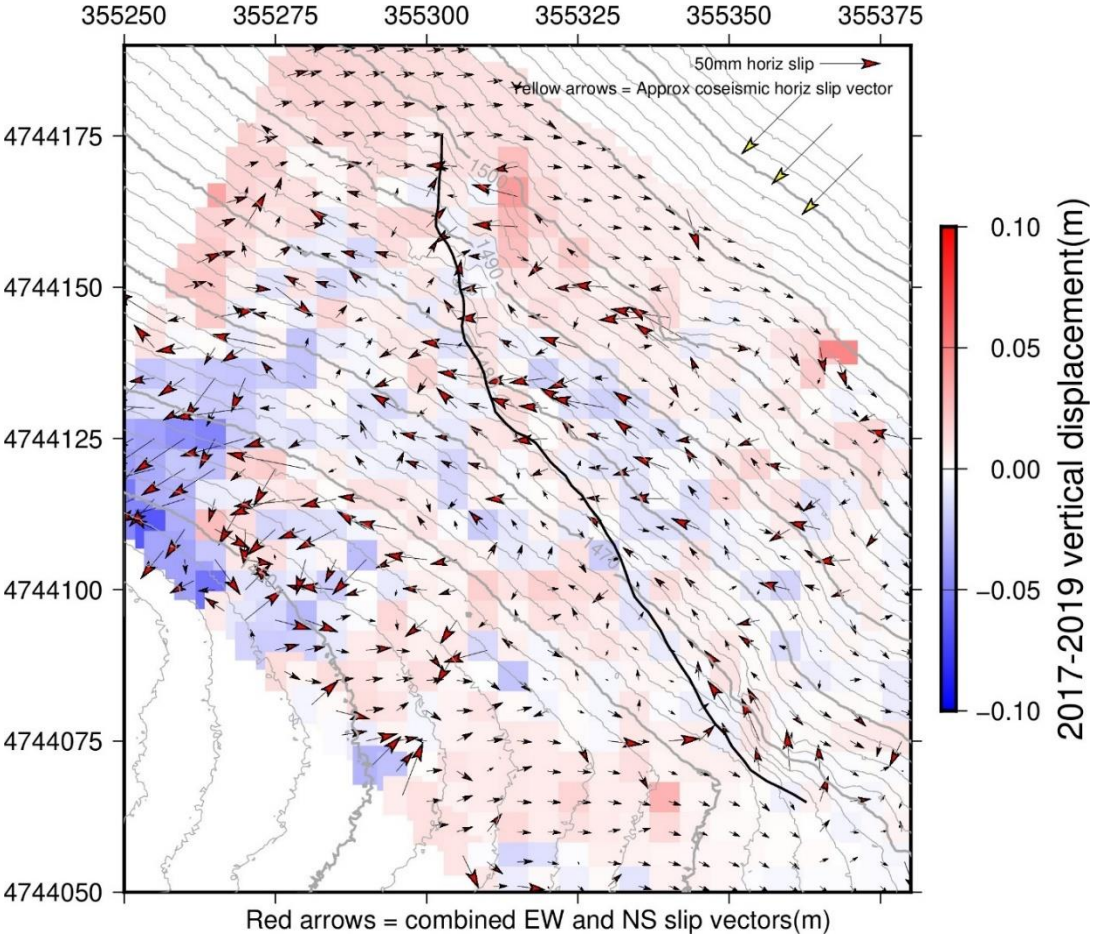

Figure 93: *Combined horizontal slip vectors for 2017–2019 (red arrows) set against a background of vertical displacement, in each case results are median values at 5m intervals.*

With the exception of the area to the far left of this figure, where the slope coincides with the edge of the alluvial channel, little relative vertical displacement is observed across the scarp. The more prominent feature is the WNW/SSE movement of the footwall and hanging wall relative to each other, particularly in the lower parts of the slope. As before, a stacked profile perpendicular to the scarp shows this effect (**Figure 94**), particularly with regard to the east-west element of that relative movement.

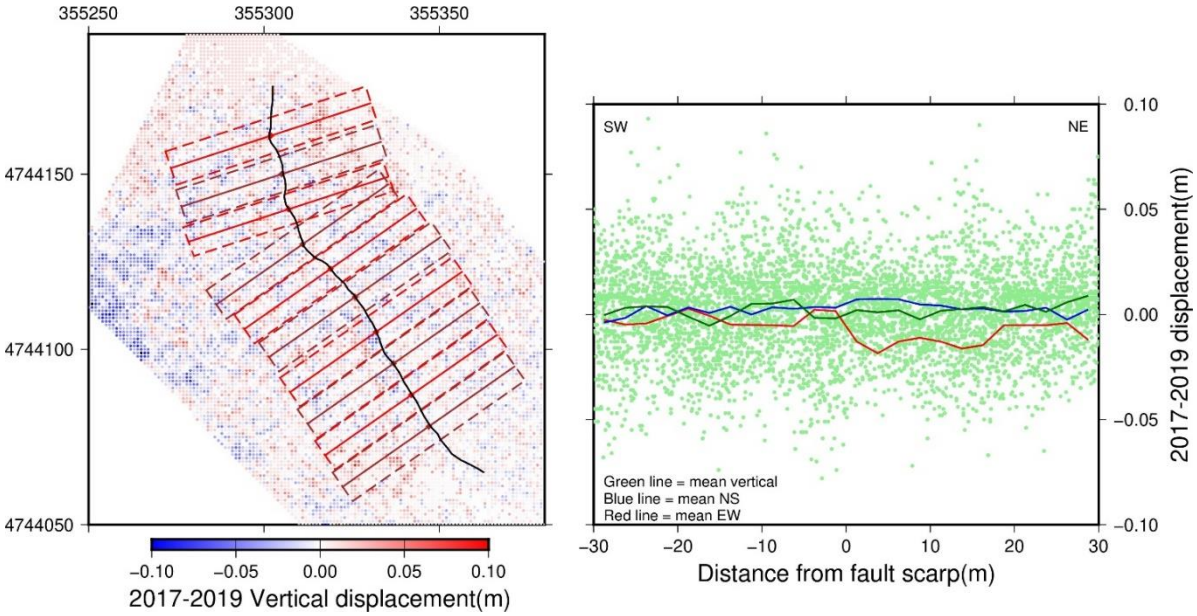

Figure 94: *Stacked profiles perpendicular to the fault scarp (LH panel shows the individual profiles in plan view against the 2017–2019 vertical displacement results, RH panel description as in* ***Figure 90****.*

Figure 95: *Zoomed-in 2019 photograph showing line of possible secondary scarp (blue arrows****)***

There is also vertical displacement of up to ~2 cm in the footwall above the fault scarp, roughly along the 1490 m contour line, with a trend of ~ 135°. Here, the lower part of the slope is displaced downwards relative to the upper part of the slope. The line along which the displacement is most noticeable seems to follow the position of a smaller surface feature seen in the 2019 photo **(Figure 73**) which largely follows the contour lines. **Figure 95** is a zoomed-in copy of that photo.

A stacked profile from the 2017–2019 difference results with profiles taken perpendicular to a line striking at 135° supports the conclusion that there is downward displacement towards the southwest along that line (**Figure 96**), although the displacement is only of the order of ~1 cm. There is also a change in east-west displacement of similar magnitude at the same point.

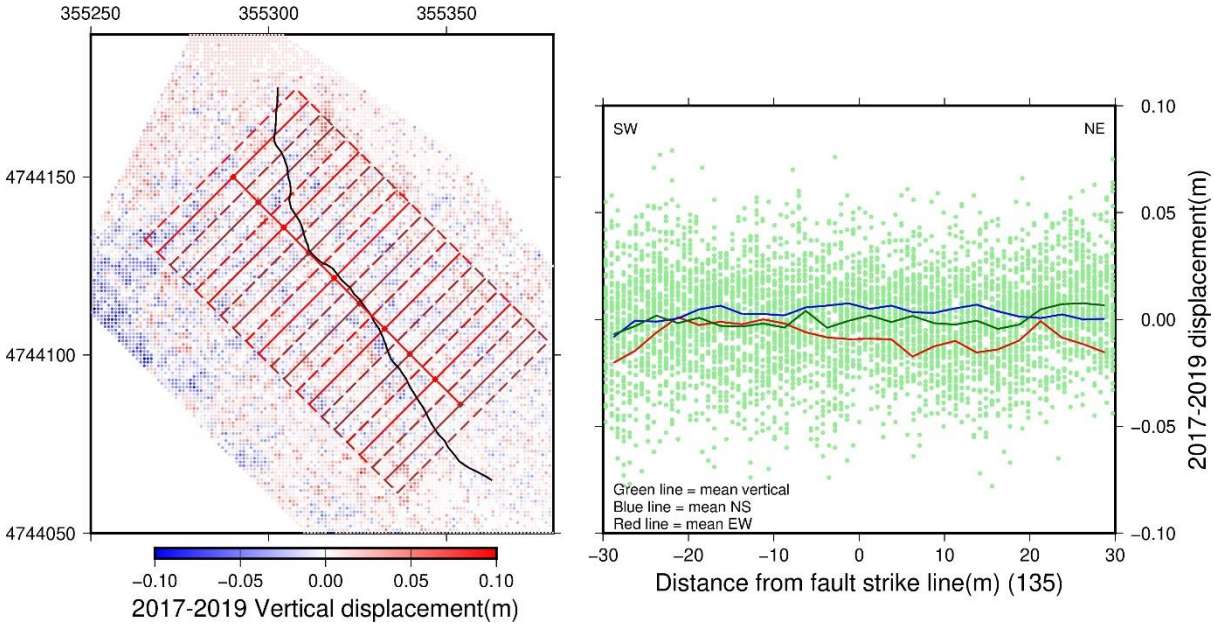

Figure 96: *Stacked profiles for 2017–2019 displacement perpendicular to a line striking 135° shown in red on LH panel (LH panel in plan view against the 2017–2019 vertical displacement results, RH panel description as in* ***Figure 90****.*

I used ArcGIS Pro with the aid of the photograph, and a high resolution DEM of the area, to draw a line following the line of this surface feature with a strike of ~135°. **Figure 97** is an updated version of **Figure 93** with that line shown in dashed dark green.

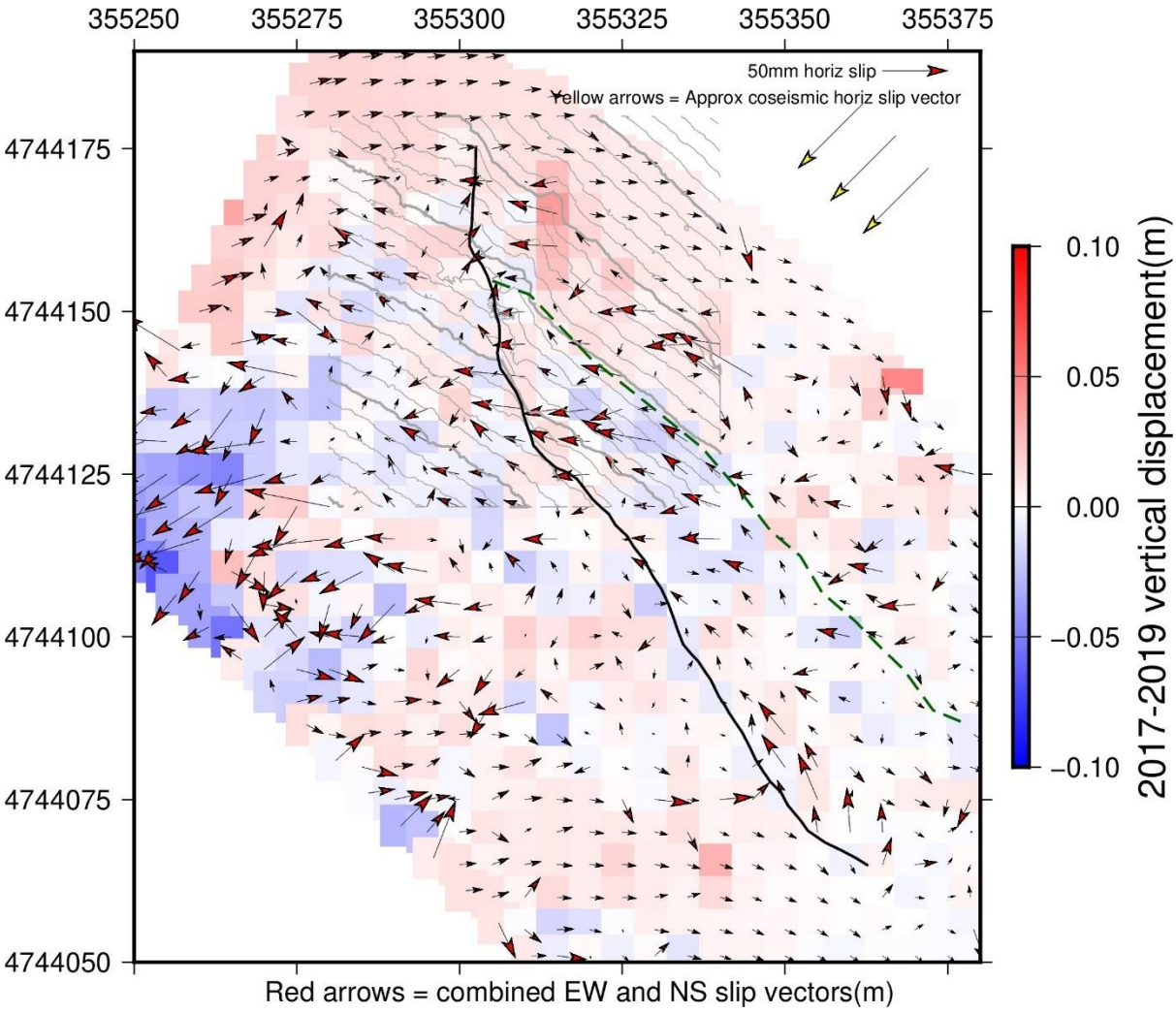

Figure 97: *Combined horizontal slip vectors for 2017–2019 (red arrows) set against a background of vertical displacement, in each case results are median values at 5m intervals. Dashed green line shows line of possible second surface feature.*

(c) 2016/2019

The time difference between the 2016 and 2019 scans is ~33 months, with 3 intervening winters.

The differencing results for east-west, north-south and vertical displacement are shown in **Figure 98**.

The horizontal slip vector results broadly match the vectors observed in respect of the 2017–2019 pair of scans, with up to ~ 3 cm west/WNW movement of the footwall relative to the hanging wall. The relative vertical displacement along the fault scarp is

similar to the pattern seen in the 2016–2017 results (although with a slight offset - the 2016–2019 values show slight uplift in the footwall as well as downthrow in the hanging wall, whereas in the 2016–2017 results the footwall is largely static).

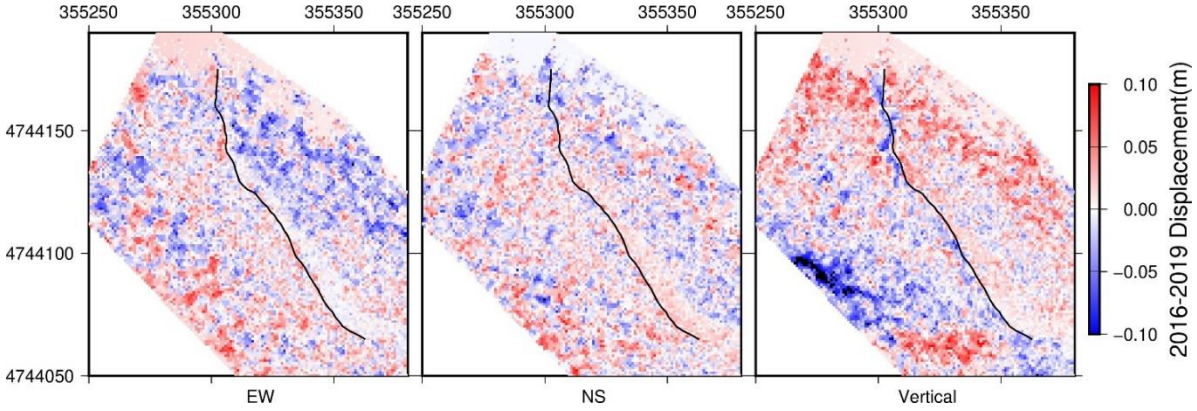

Figure 98: *Results of displacement in east-west, north-south and vertical components between 2016 and 2019 scans.*

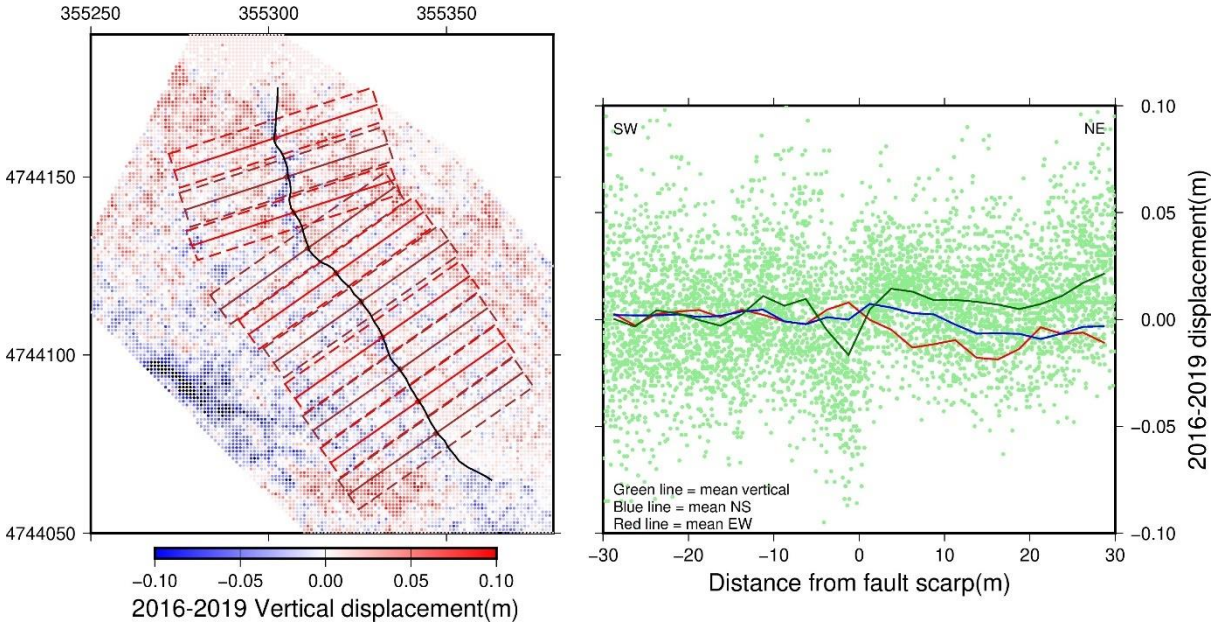

Figure 99: *Stacked profiles perpendicular to the fault scarp (LH panel shows the individual profiles in plan view against the 2016–2019 vertical displacement results, RH panel description as in* ***Figure 90****.*

Overall, the relative vertical displacement along the fault scarp is is in the order of 3 cm. This is shown in **Figure 99** (stacked, scarp-perpendicular profiles).

Figure 100 shows the results represented on a single figure.

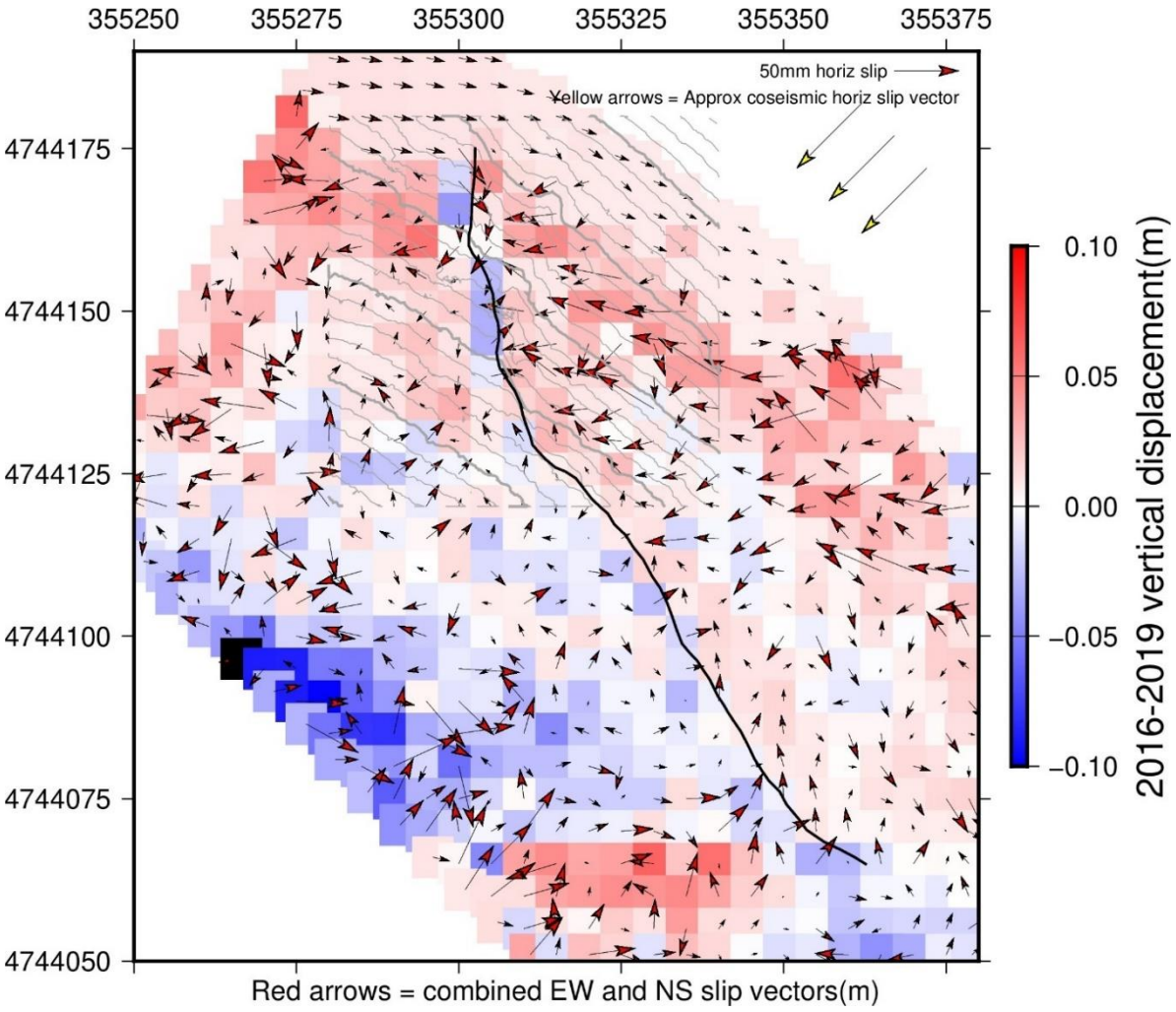

Figure 100: *Combined horizontal slip vectors for 2016–2019 (red arrows) set against a background of vertical displacement, in each case results are median values at 5m intervals.*

An example of a single profile shows vertical displacement of up to ~ 5 cm (**Figure 101**) (the example shown is for the same profile as in the results for 2016–2017 above, which includes the section of the fault scarp at which field measurements recorded the greatest co-seismic vertical displacement). As in relation to 2017–2019, the results also show relative vertical displacement along a line which roughly follows the 1490 m contour. In this case, the effect is more pronounced, with overall relative offset of ~ 3-4 cm.

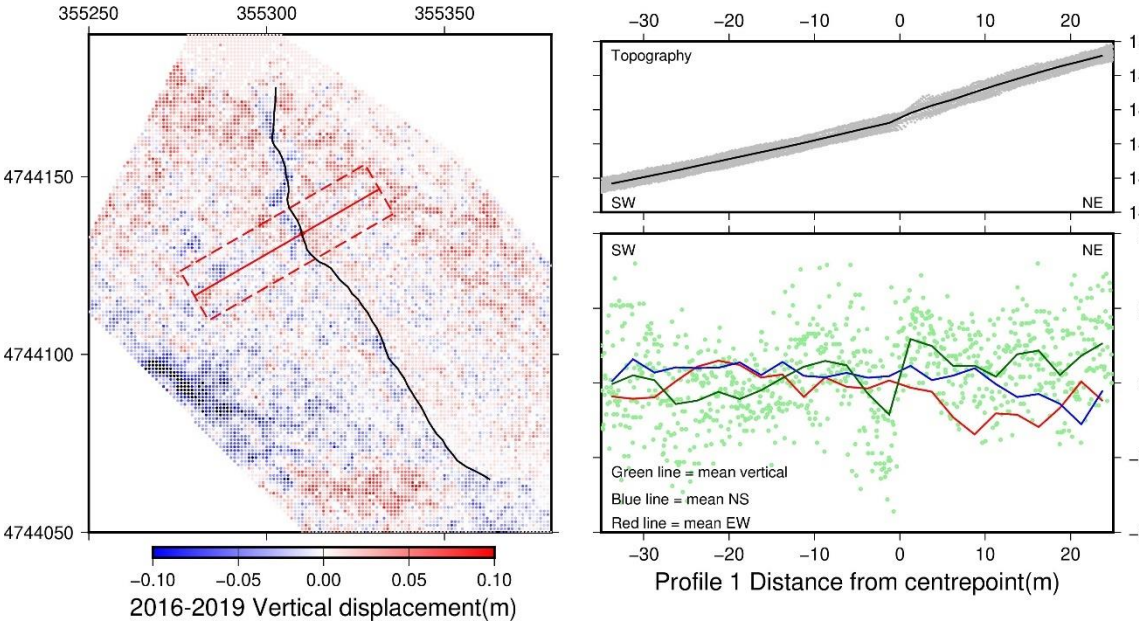

Figure 101: *Example individual profile showing 2016–2019 displacement (description of content as in previous figure).*

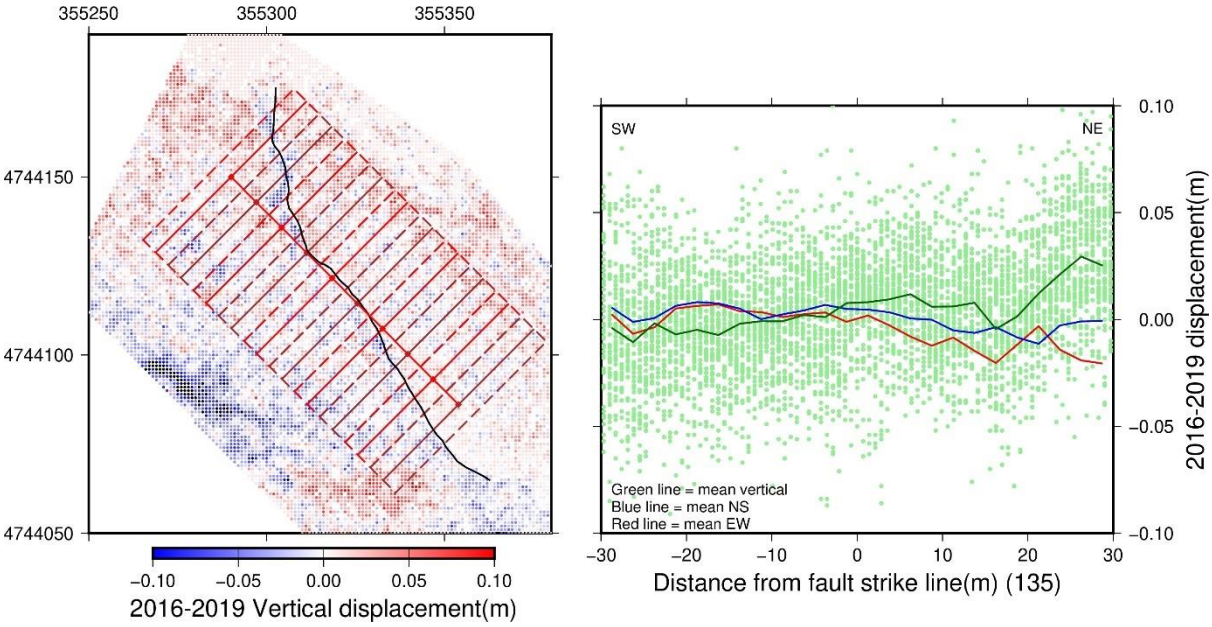

Figure 102: *Stacked profiles for 2016–2019 displacement perpendicular to a line striking 135^{o} shown in red on LH panel (LH panel in plan view against the 2016–2019 vertical displacement results, RH panel description as in* ***Figure 90****.*

A stacked profile perpendicular to a line striking at 135 ^{o} shows both this vertical displacement, and a change in the horizontal slip vectors at the same point (**Figure 102**).

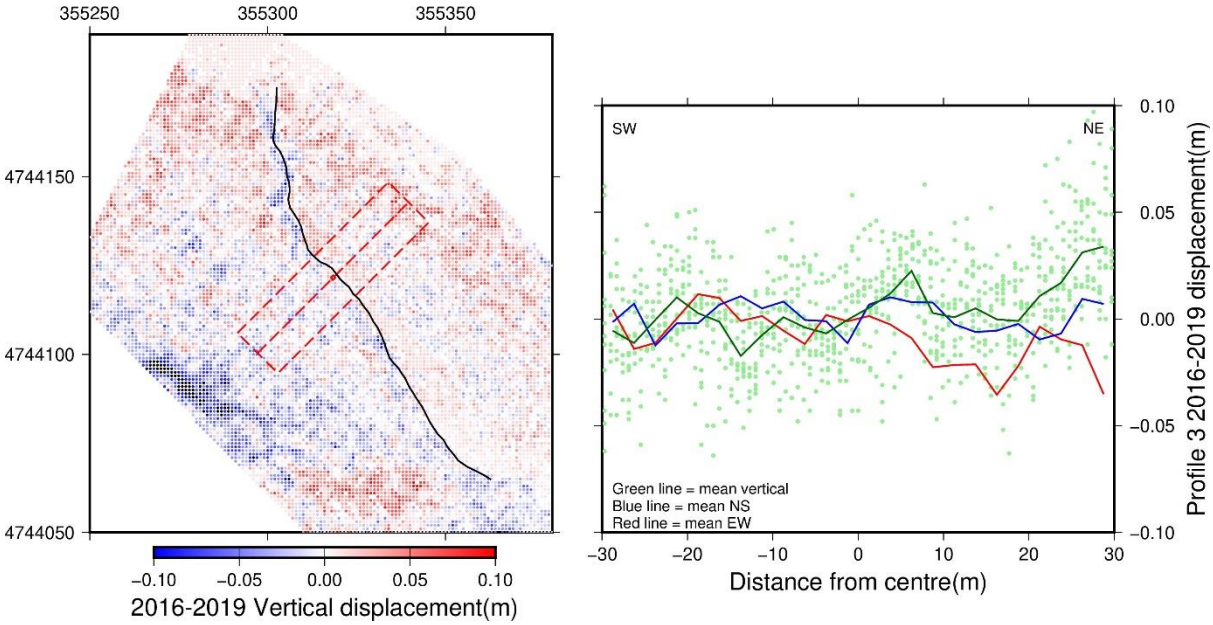

Figure 103: *Example individual profile for 2016–2019 displacement perpendicular to a line striking 135^o shown in red on LH panel (LH panel in plan view against the 2016–2019 vertical displacement results, RH panel description as in* ***Figure 90****.*

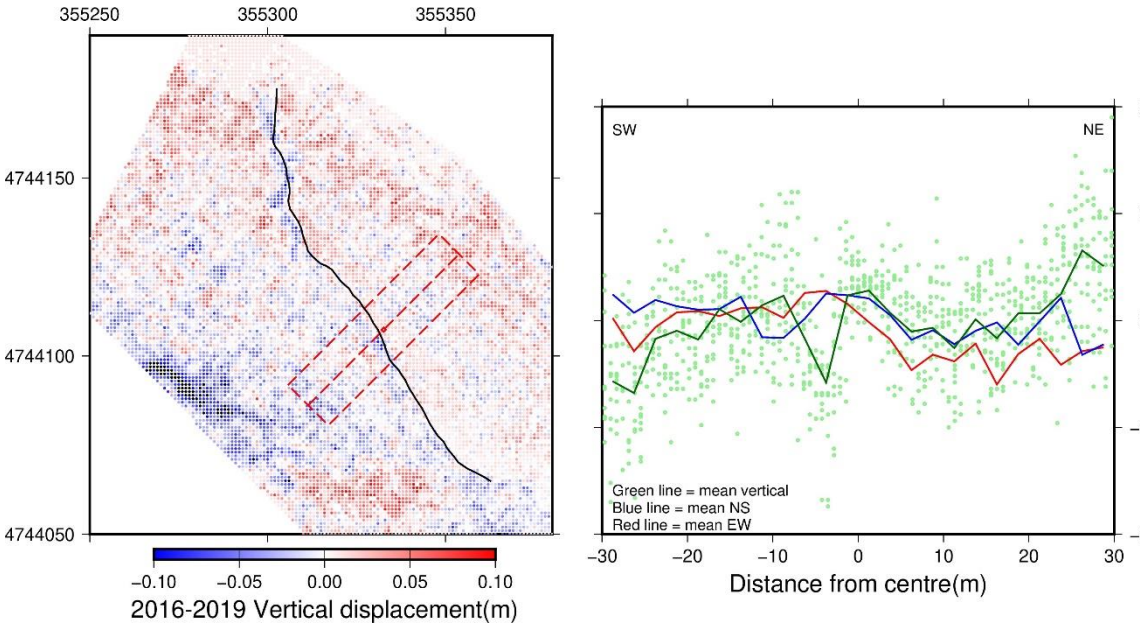

Figure 104: *Example individual profile for 2016–2019 displacement perpendicular to a line striking 135^o shown in red on LH panel (LH panel in plan view against the 2016–2019 vertical displacement results, RH panel description as in* ***Figure 90****.*

Individual profiles with the same geometry (along a 16m wide and 60 m long swath based upon lines with bearings of 45^o) show similar results. **Figures 103** and **104** show

two examples, both of which show downward displacement of ~3 cm with an element of ~1-3 cm westerly movement at ~18 m from the centre point of the swath (which places the movement at along the line marked in **Figure 96**).

(d) Internal consistency of the results

As a check as to the extent to which the results are consistent between pairs of scans, I have compared the gridded results for east-west, north-south and vertical displacement of the 2016–17 results added to the 2017–19 results, against the 2016–2019 results. Ideally, those results should match if the results are internally consistent. Details of the results are in **Appendix 4**.

In each case the results are not exact matches and in particular there seem to be offsets in the east-west and north-south results. However, the principal features of the 2016–2019 results in terms of relative motion (downthrow of the hanging wall relative to the footwall, relative northwest displacement of the footwall relative to the hanging wall, and vertical displacement within the footwall along a line roughly parallel to the contours) are reasonably well reflected in the combined 2016–2017 and 2017–2019 results. Given the amount of noise in the data, this result appears satisfactory as an exact match was unlikely.

4.5.2 Modelling shallow slip using Meterff TLS differencing results.

In order to model near-surface slip, I jointly inverted the three sets of TLS results across each of the post-seismic 3 time intervals, following the method of Funning et al., 2005, Floyd et al., 2016. As in Chapter 3, I assumed that surface displacements result from slip on multiple rectangular patches on a fault plane in an elastic half-space (Okada, 1985).

4.5.2.1 Fault geometry model

I initially used a model involving two simplified contiguous fault segments at differing strikes (168° and 142° respectively) to represent the visible Meterff scarp location used in this study. I refer to those respectively as the upper and lower Meterff segments. I also experimented with a third segment of 100 m length and strike of 134° further up the slope following the contour-parallel feature mentioned above (referred

to below as the top segment). Its addition significantly improved the fit to the TLS data in relation to the inversions of the later scan pairings, and I therefore adopted the more complex model of 3 fault segments for the inversions for those later pairings (2017–2019 and 2016–2019), but not for the 2016–2017 pairing as the results did not show any apparent movement consistent with such fault geometry.

The surface fault geometry (including the top segment), compared to the fault traces drawn in ArcGIS is shown in **Figure 105**.

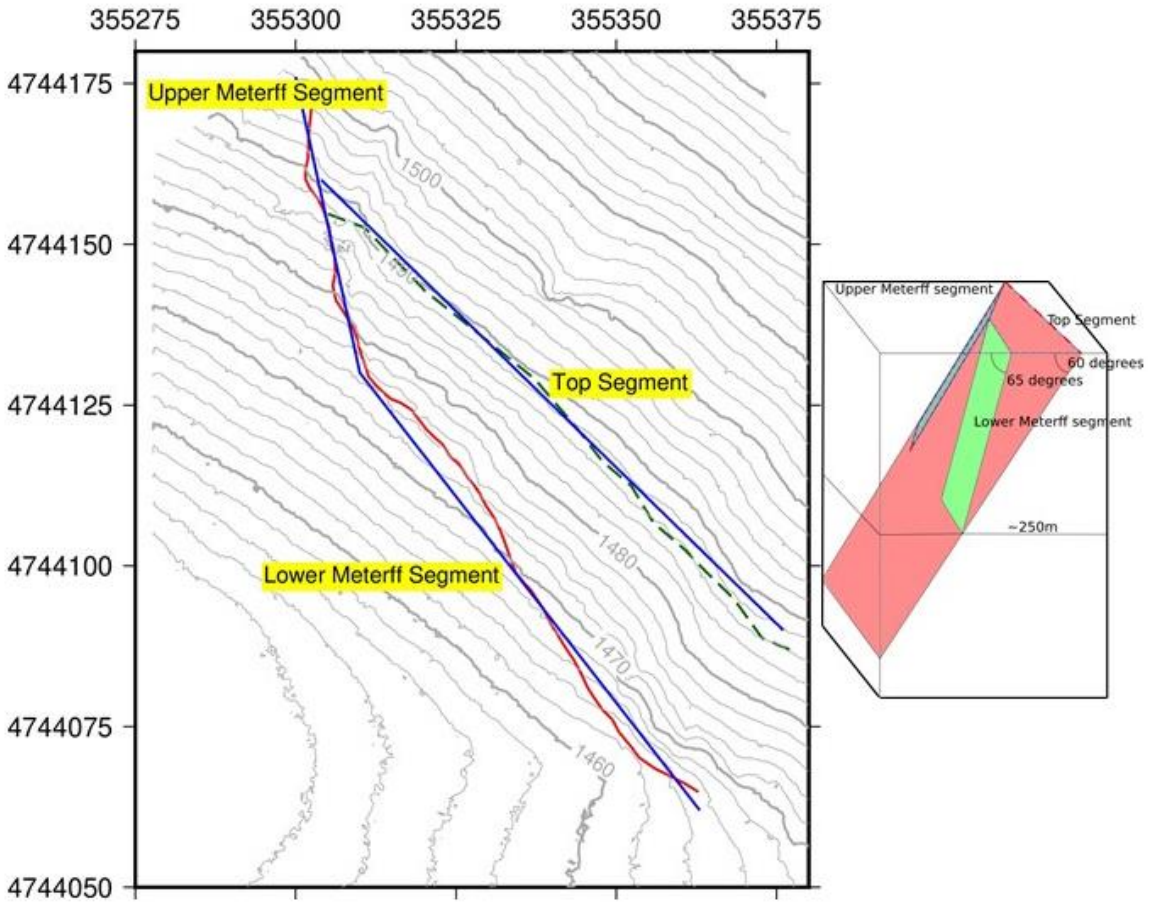

Figure 105: *Surface location of modelled fault segments (in blue) shown against mapped traces of Meterff fault scarp (red) and slope-parallel structure (dashed green). Block diagram is sketch 3D cross-section of the 3-segment geometry.*

I set the dip of the upper Meterff segment at 70^{o} from horizontal and the dip of the lower Meterff segment at 65^{o} (matching the recorded co-seismic dip), on the assumption that it coincides at depth with the top segment (dip set at 60^{0}). For the 3-

segment model, as those would typically be secondary structures I have assumed post-seismic slip is at shallow depth. At those dip settings, the Meterff segments coincide with the top segment at ~250 m depth. I have therefore limited their depth to 250 m in the 3-segment model (but 500 m in the 2-segment model). The top segment is modelled to 500 m depth.

I used variable rake settings for each segment at 90^{o} apart which (with adjustments for the differences in strike) match the typical co-seismic plunge for the Monte Vettore fault segments towards ~203^{o} noted in Galderisi and Galli (2020) (who also noted plunge towards 196^{o} and rake of 68^{o} for the synthetic Colli Alli fault, of which the Meterff fault scarp appears either to be part or a relay structure).

The fault segments were discretised into patches of ~10 m x 10 m. Tables of the fault geometries used are in **Appendix 4**.

4.5.2.2 Inversion settings

As the material is partially unconsolidated, shear modulus for the inversions is set at 2e10 GPa (reflecting the partially unconsolidated nature of the near-surface hanging wall carbonate material) and the Poisson ratio at 0.25. I applied a non-negative least squares constraint to eliminate retrograde motion on the fault patches. Each dataset was weighted equally. The inversions were regularised using a Laplacian smoothing factor of 50. I tried a range of values for smoothing factor, and found that this seemed to strike the right balance between avoiding over-smoothing the data and model, and overfitting the model to the data.

The TLS differencing input data used in each case was reduced in size using a mean filter set at an interval of 3 m x 3 m from the ~ 14,000 points after the application of the final (recursive) filtering stage, which reduced the size of the input files to ~1,550 - 1,630 points.

I experimented with a line-of-sight offset within the inversion process as well as the previous detrending, but found that it largely destroyed the signal. I therefore did not solve for ramps in any of the data on this occasion, as the previous processing stages had already detrended the datasets to take into account any ramps in the data.

4.5.2.3 Inversion results

In general, the shallow slip values observed in the models do not match the apparent slip observed at surface, with slip values of less than 0.5 mm.

(a) 2016–2017

In the 2016–2017 inversion, the overall picture for the lower Meterff segment is of right-lateral slip of up to ~0.2 mm at ~150-250 m depth (and in patches at the surface on the upper Meterff segment). There is also a patch of dip-slip displacement of ~0.1 mm on the lower segment at ~50-100 m depth (**Figure 106**).

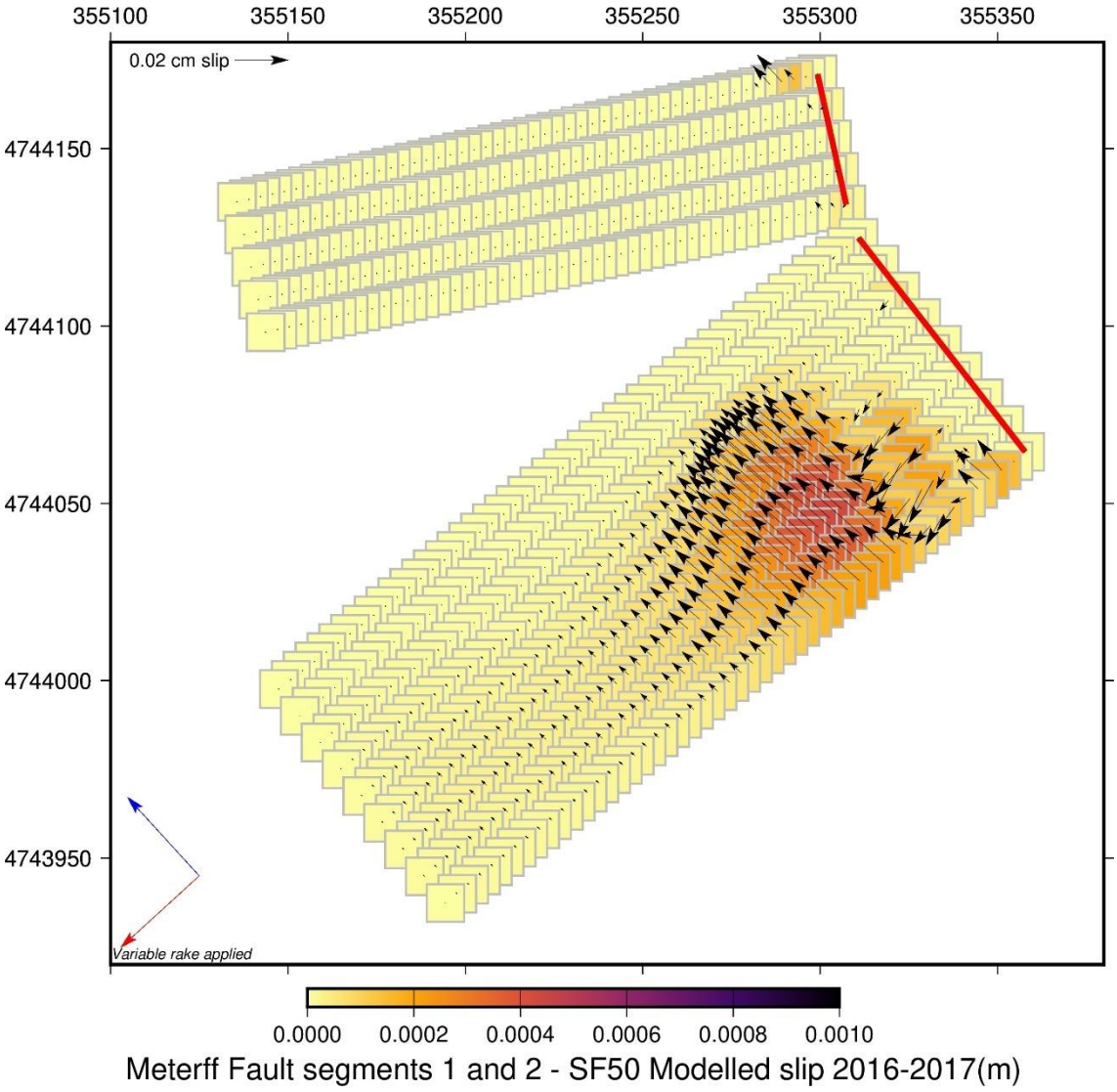

Figure 106: *Inversion results for 2016–2017 showing slip on Meterff upper and lower fault segments.*

The moment release is M_o 5.911^10 Nm (equivalent to ~M_w 1.15).

(b) 2017–2019

In the 2017–2019 slip inversion little slip of any kind is observed on the Meterff upper and lower segments, with such slip as there is being either a patch of dip-slip at ~50-100 m depth on the northwest part of the lower segment or patches of right-lateral displacement within the top 50 m from the surface (upper segment, and southeast part of the lower segment). However, displacement of up to ~0.2-0.3 mm with a small consistent left-lateral element is observed between ~100 m and ~300 m depth on the top segment (**Figure 107**). The moment release is M_o 5.245^10 Nm (equivalent to ~M_w 1.09).

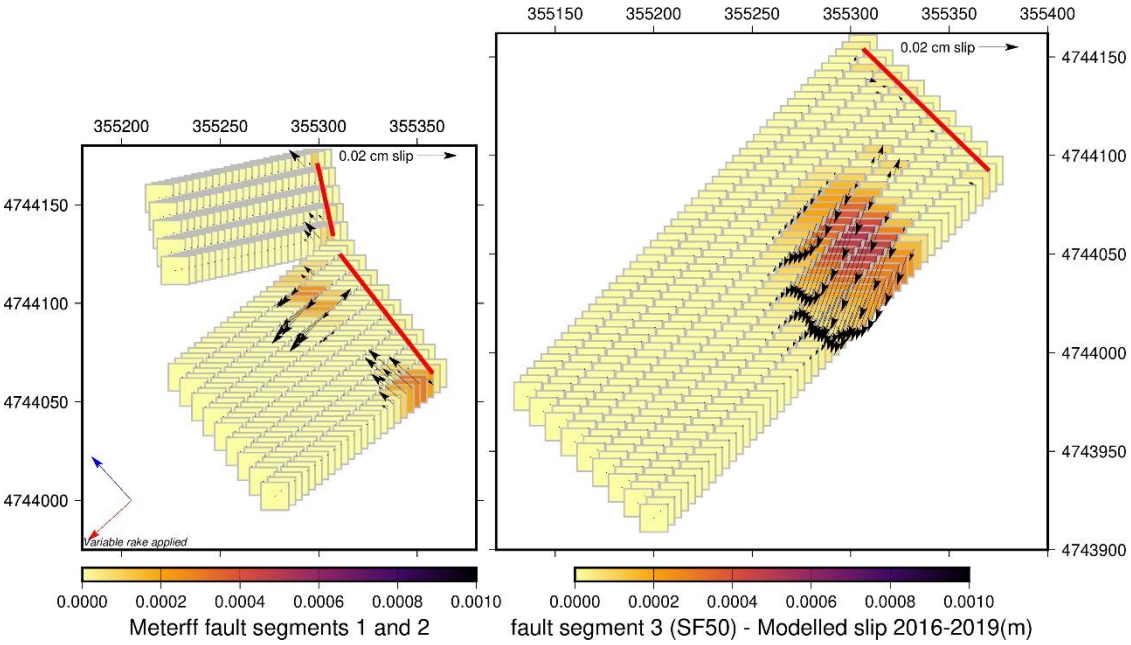

Figure 107: *Inversion results for 2017–2019 showing slip on Meterff upper and lower segments (LH panel) and top fault segment RH panel).*

(c) 2016–2019

In the 2016–2019 inversion, the slip observed is very similar to the 2017–2019 inversion. Observed slip on the top segment is very close to the location, magnitude and direction observed in the 2017–2019 inversion. The principal difference between the respective inversions is a small amount (< 1 mm) of right-lateral slip observed at ~ 50-60 m depth on the northwest portion of the lower Meterff segment, rather than

dip-slip movement. Dip-slip movement of up to ~0.2-0.3 mm with a very small left-lateral element on the top segment is similar in location and scale to the 2017-19 result (**Figure 108**). The moment release is M_o 2.959^10 Nm (equivalent to ~M_w 0.91).

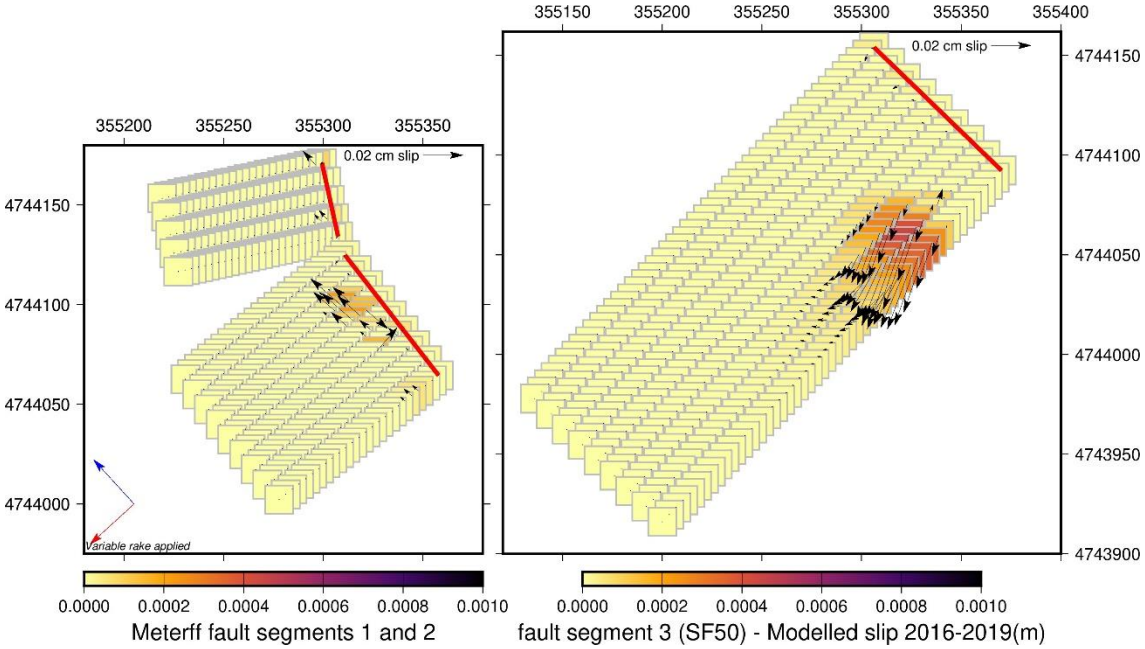

Figure 108: *Inversion results for 2016–2019 showing slip on Meterff upper and lower segments (LH panel) and top fault segment RH panel).*

4.5.2.4 Inversion results – fit to data

Table 4.5 shows the respective standard deviation (std) results for the observed input data for a test area in the footwall of Meterff, and the root mean squares (RMS) misfit for the model.

Table 4.5 TLS fit of model to observed input data

Dataset	test std (m)	RMS misfit (m)
TLS east-west 16–17	0.0143	0.0190
TLS north-south 16–17	0.0151	0.0180
TLS vertical 16–17	0.0148	0.0160
TLS east-west 17–19	0.0171	0.0172
TLS north-south 17–19	0.0190	0.0130
TLS vertical 17–19	0.0095	0.0131
TLS east-west 16–19	0.0153	0.0184
TLS north-south 16–19	0.0190	0.0162
TLS vertical 16–19	0.0178	0.0228

Figures showing the observed data, model, and residuals for each of the dataset pairs are in **Appendix 4**. An example for the 2016–2019 inversion (vertical slip) is at **Figure 109**.

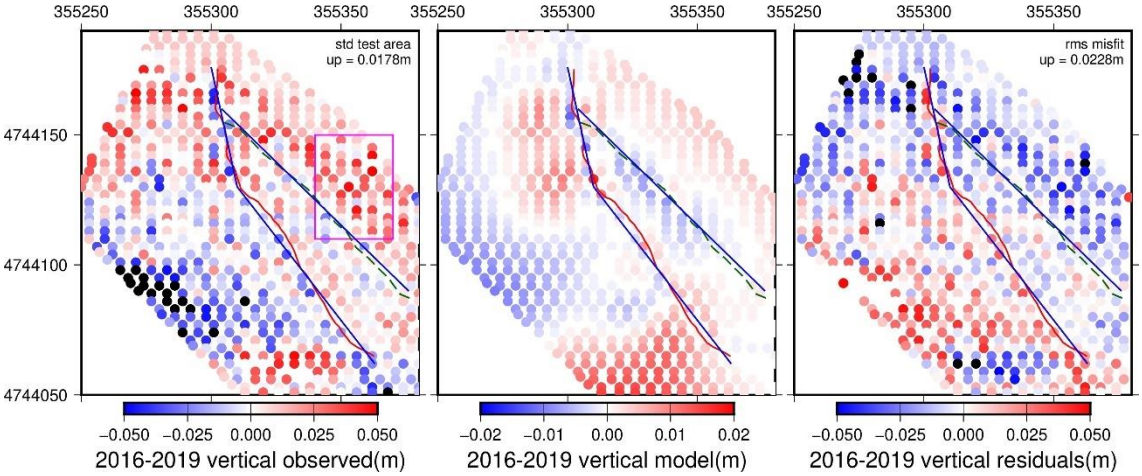

Figure 109: *Example of fit of model to datasets, 2016–2019 vertical data, using 3 fault segment geometry. Magenta box in LH panel (observed) is the area used to calculate standard deviation of input data. Blue lines are fault segments used in model, red line Meterff fault trace and green dashed line top segment trace for comparison with model geometry. Note different scales used in model panel (centre) compared to observed (LH) and residuals (RH).*

4.6 Discussion

4.6.1 The reliability of the Meterff scarp in 2016 as co-seismic evidence to help assess potential future seismic hazard

How reliable was the Meterff scarp even in 2016 as evidence of co-seismic slip distribution and scale? The Meterff fault scarp was apparently not mapped when Pierantoni et al. drew their geological map of the area in 2013. Despite it not appearing on that map, it appears that at least in some places, it had previously ruptured to the surface, although the evidence of previous rupturing may not have been extensive. On my return visit to the site in May 2022 to observe progress visually, it was apparent that much of the scarp was deteriorating rapidly in the lower parts of the slope, away from the more prominent scarp where the greatest co-seismic slip was seen. Photographs of the site in May 2022 appear in **Appendix 4, Part 2**.

The mapped normal (synthetic) Colli Alti fault in this area to the west of the Meterff site had a strike of nearly ~175°. To the east of the area a much longer fault ~north-south trending fault was mapped towards the base of the Monte Vettore ridge. Minor faults between the two north-south trending faults trending at ~150° were mapped to the north of the Meterff site and may function as relays between the two synthetic structures. The Meterff scarp which was displaced by the Norcia earthquake has a strike of ~142° for much of its length and is therefore likely to have been the result of distributed faulting within a relay zone. Both its co-seismic and its post-seismic behaviour are therefore likely to be influenced at least to some degree by displacement on surrounding structures not covered by the TLS data. It is also possible that at least some of the deformation some of the co-seismic deformation was the result of deep-seated landsliding (as in e.g. Huang et al., 2017 in respect of the Amatrice earthquake), which might further complicate the picture.

Although I have attempted to model co-seismic displacement below the surface using a joint inversion of the Pleiades and other geodetic datasets, I have done so using a fault segment with geometry matching the Colli Alti fault, and I have not tried to model the much smaller Meterff fault separately as the resolution of the model in this area makes that unrealistic. That modelling using the expanded (and less reliable) area of Pleiades data does not reveal any particular complexity in respect of the Colli Alti fault segment. The modelled slip at depth is essentially dip-slip, towards 250-260°, on a fault segment with a strike of ~170°. The southern-most end of that segment (nearest to the area where the Meterff scarp is situated) shows less slip than further north, but the slip vectors are consistent throughout.

The co-seismic field results record left-lateral kinematics, and slip vectors trending either towards ~225° (in the locations within the study area – from Villani et al., 2018) or ~196° (the Colli Alti fault – from Galderisi and Galli, 2020). Near-surface left-lateral kinematics trending towards ~200° would be consistent with the detailed results elsewhere from the inversion discussed in Chapter 3, particularly as regards synthetic splays, and also as regards parts of the main Monte Vettore fault, especially when the strike of those segments differs from the overall strike of the fault. The co-seismic field

measurements at the surface taken from the Meterff scarp do not therefore reflect the slip modelled at depth, but may still accurately reflect the near-surface position.

Another aspect of the reliability of the scarp as co-seismic evidence is whether it reflects the distributed nature of faulting even within this relatively small area. In this respect, and as discussed in more detail below, it is possible that the co-seismic results in the form of the Meterff scarp did not reflect the extent to which the Meterff scarp may be associated with another, probably less-steeply dipping, structure further up the slope which may not have ruptured the surface in 2016 to any measurable extent, but which has subsequently seen displacement. If so (and the evidence is not clear-cut), the co-seismic evidence in the form of the Meterff scarp might not have fully represented the extent of distributed faulting.

4.6.2 The extent and nature of afterslip

(a) Differencing results – discussion

Post-seismic displacement on the Meterff scarp is significantly smaller in scale than the co-seismic slip values of up to 1 m. The majority of the post-seismic displacements are of the order of no more than ~1-3 cm (either vertically or horizontally), which has represented a challenge to identify accurately, even using repeat high-resolution TLS. Nevertheless, using a cautious approach of alignment of scans, ICP, detrending and filtering to remove noise, it has been possible to observe patterns of displacement which provide some reliable information on the processes which have operated on the scarp and surrounding area between 2016 and 2019. Those displacement patterns suggest that afterslip, rather than gravitational processes dominated initially, but that afterslip was probably short-lived and that gravitational processes now dominate.

The top of the Meterff hanging wall immediately adjacent to the Meterff fault scarp is an area of relative downwards vertical displacement of ~2-4 cm in the hanging wall seen in the 2016–2017 and 2016–2019 pairings (but not observed in the 2017–2019 results). This appears to reflect downwards post-seismic settlement of the hanging wall in the period shortly after the co-seismic movement of the scarp within the first few metres of the hanging wall.

Further away from the scarp in the lower slope areas, downwards displacement of the hanging wall is still apparent in the 2016-2017 results, although less pronounced and more patchy in spatial coverage (it does not appear to be present in the area of slope immediately below the most prominent scarp). This pattern of greater post-seismic displacement adjacent to the scarp, declining with distance away from the scarp is similar to that observed in Wilkinson et al., 2012 in respect of the L'Aquila earthquake (see **Figure 71**), although smaller in scale. As it is not repeated in the 2017–2019 results these slip elements appear to be a relatively short-lived post-seismic effect in the form of afterslip. That in turn would be consistent with an exponential decay model (e.g. Marone e al., 1991, Zhou et al., 2018). As I only have 2 time differences to test such a model and values of slip vary along strike, I have not attempted a direct comparison with an ideal model. The spatial variation in the extent to which vertical displacement is observed further away from the scarp appears to be inversely connected to the amount of co-seismic slip, which varies along the scarp (greatest at the northwest end, and least at the southeastern end). The probable explanation for this spatial difference is that it reflects a high co-seismic slip gradient, with more accumulated slip deficit at the southeast end arising from relatively little co-seismic slip on that section compared to slip on the section further to the northwest (e.g. Cheloni et al., 2010 and Wilkinson et al., 2012). Much greater co-seismic slip values were recorded at the higher slope levels (up to ~1 m) than in the lower levels (~0-20 cm slip).

In the footwall of the Meterff scarp there is some vertical displacement which is observed in the 2016–2019 and 2017–2019 results (but not in the 2016–2017 results). From a distance, and looking at the results, this could be seen to be connected with a second, contour-paralleling, fault which either terminates at its northeastern end where it abuts the Meterff scarp or possibly continues across it and further round the slope to the northwest. Such a structure does not appear to have featured in the 2016 Open EMERGEO Joint Working Group fieldwork results. There is one possible exception where a single result records combined offset of > 1 m (see **Figure 77(a)**). However, that result's recorded location places it at a few metres to the east of the Meterff fault scarp, and its magnitude suggests that it properly belongs along the line

of the Meterff scarp where the co-seismic displacement observed is at its greatest and is very probably therefore slightly misplaced by a GNSS reading rather than a genuine recording of movement on this second structure.

Whether such a second structure was visible but unrecorded in 2016 is difficult to resolve from the photographs available. The 2016 panoramic photograph (**Figure 81**) does not readily enable the structure to be picked out.

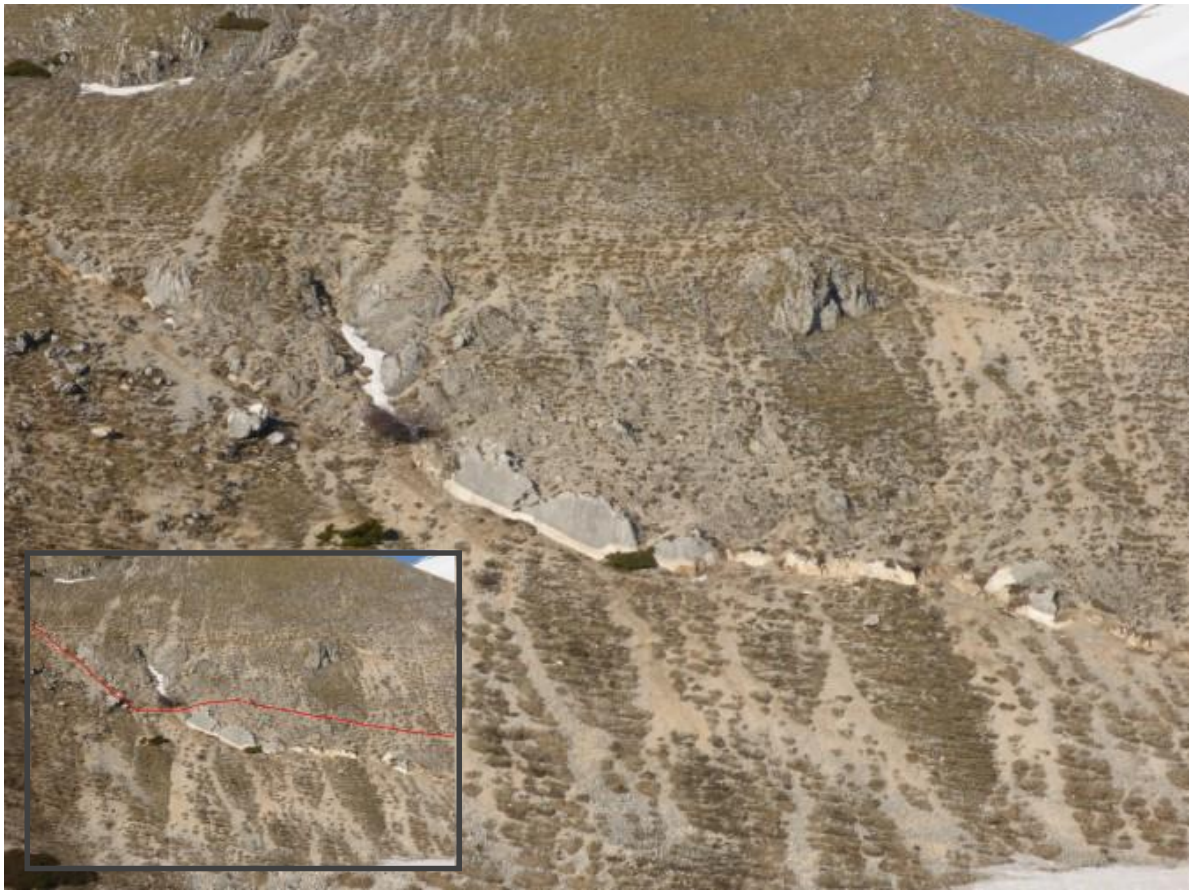

Figure 110: *30 March 2017 photograph of Meterff scarp, looking northeast (photograph taken by Laura Gregory, University of Leeds). Box in lower left (red line) shows smaller scale possible interpretation of continuation of structure across line of Meterff scarp.*

In photographs from March 2017, a possible second structure is more clearly visible in this area (e.g. **Figure 110**), and appears to continue along the hillside towards the ESE. In this view, it could be argued that the structure naturally bends round the hill side

and continues to the northwest as the aspect of the hillside changes, with the Meterff fault scarp crossing its line, and ending in a shorter segment (partially covered by snow in this Figure).

The 2016–2017 results do not suggest any consistent vertical or horizontal movement in this area of the footwall. However, the 2017–2019 and 2016–2019 results suggest both relative vertical displacement of up to ~ 3 cm along the line of this structure, and a small change in relative east-west displacement vectors along the same line. Although this could represent afterslip on a possible second structure that did not apparently experience co-seismic slip which ruptured the surface, I could not find any convincing evidence of this when I revisited in 2022. Photos taken on the footwall side (**Appendix 4, Part 2**) show a complicated picture of exposed and heavily eroded bedrock interspersed with debris from further up the slope in what seem to be largely parallel bedding planes of ~ 40-50 cm to 1m width which dip gently towards the northeast. However, those are far from continuous in the field. Further up the footwall slope there is less bedrock and more scree. The relative vertical movement could well be the result of erosional processes and gravity (possibly deep-seated, e.g. Huang et al., 2017), rather than afterslip. However, the east-west displacement is very difficult to explain using gravitational processes. A possible explanation is that the deformation seen in the footwall after 2017 is a mixture of gravitational (parallel to slope) and afterslip (east-west) processes. However, the results (e.g. **Figures 96 and 99**) suggest that the displacement in both respects is greatest at the same point, which is difficult to square with a dual cause.

A complicating factor in this respect is whether displacement may have been triggered by post-seismic movement on neighbouring principal fault planes, as part of a complex relay zone of which both it and the Meterff scarp are only small parts. However, I do not have the data available from the neighbouring faults which would be necessary to test that possibility.

One further feature which appears only in the later results (2017–2019 and 2016–2019) is the ~2-3 cm ESE/WNW horizontal movement of the Meterff hanging wall and footwall relative to each other. In **Figures 97 and 100** the WNW movement appears

more pronounced in the footwall than the ESE movement in the hanging wall. It is also more pronounced above the possible second structure (especially within the 2016–2019 results). The results show relative (rather than absolute) displacement so characterising this as horizontal displacement of the footwall may be misleading. It is more likely in practice that it is the hanging wall which is slipping towards the ESE relative to the footwall. If so, a possible explanation for this is that at very near-surface level (perhaps within the top ~100 m or so), the degree of co-seismic left-lateral slip on the rupture itself did not fully reflect the near-surface (but deeper) left-lateral slip in the top ~1 km. Therefore, this may be a localised recovery of slip deficit. Again, it is also possible that the displacement is influenced by post-seismic displacement on larger neighbouring structures.

Although fluid diffusion has been shown previously to influence the localisation of post-seismic slip (e.g. Cheloni et al., 2010 and Pousse-Beltran et al., 2020) it has not been possible to determine whether it has played an active role here. It does not appear necessary to allow for such a possibility in this case, in part because the scales involved here are generally too small to gauge whether there is any particular concentration of slip in one area rather than another. As noted above, the vertical post-seismic displacement of the hanging wall of the Meterff scarp relative to the footwall is arguably more pronounced in the lower (southeast) parts of the slope than in the upper (northwest) parts. However, rather than being explained by fluid diffusion this is more likely to be attributable to local high gradients in co-seismic slip (e.g. Cheloni et al., 2010 and Wilkinson et al., 2012).

(b) Modelling results - discussion

The results for modelled slip at depth from the inverse modelling vary considerably between the 2016–2017 results and the later results.

In the 2016–2017 results, the modelled slip on both the Meterff segments is predominantly right-lateral (with an element of dip-slip nearer the surface). The horizontal slip vectors at the surface derived from the TLS results for 2016–2017 show little coherent pattern. The co-seismic slip vectors observed in the field were left-lateral. Therefore, it is difficult to explain the reasons behind the predominantly right-

lateral slip vectors modelled at depth. The fit of the model to data is not strong in this respect, and there is little or no consistent pattern in the 2016–2017 horizontal results. This suggests that the model just may not work particularly well as regards the 2016–2017 horizontal vectors. The model appears to be a marginally better fit to the vertical data for the 2016–2017 pairing, which are more pronounced than the horizontal results.

The modelling for the later results proceeds on the basis that there is a second structure involved. As discussed above, that is undecided. If it is not involved, the modelling would be of data which is largely gravity-driven, and therefore inappropriate.

The later modelling results (2017–2019 and 2016–2019) largely show slip kinematics at depth on the top fault segment which are ~90^{o} anticlockwise from the 2016–17 results for the meterff fault segments. They show predominantly dip-slip displacement at depth combined with a small component of left-lateral slip, with slip trending overall towards ~200^{o} concentrated on the top segment. However, there is some consistency in the results for the meterff segments, as the results show right-lateral slip on the Meterff lower segment (as well as some dip-slip movement in the 2017-2019 results). As with the 2016–2017 results, the modelled amount of slip at depth is very small (the largest slip values are no more than ~0.2 mm, and on the Meterff). The comparable post-seismic TLS results show relative vertical displacement of in the order of 2-4 cm, and similar maximum values for horizontal displacement. If the top segment does represent a second structure, the post-2017 displacement appears to be a post-seismic adjustment by way of afterslip (e.g. Freed et al., 2007) where co-seismic slip at depth has not been reflected by slip at or near the surface on that segment. Although this led to displacement on the Meterff scarp, this may have left unrecovered slip on the top segment. Again, it should be noted that post-seismic displacement on larger neighbouring faults may be a contributing factor to this post-seismic displacement.

Overall, though, modelling the results for a small area on its own when it is part of a much larger overall complicated picture (and when at least some of the deformation is gravitational rather than seismic) is unlikely to produce reliable results, and I am not

confident that the inversions have produced a reliable model of sub-surface slip. I do not feel that modelling here has significantly contributed to understanding slip at depth in this instance.

4.6.3 The effect of geomorphological processes such as weathering or gravitational erosion.

The Meterff site is steep, exposed and at relatively high elevation and therefore potentially prone to gravitational erosion (e.g. Kokkalas and Koukouvelas, 2005 and Wallace, 1977). In common with much of the surrounding area there are extensive slope deposits in the form of scree. Field photographs from 2016 and 2019 (**Figures 81 and 73**) show a consistent pattern of apparently erosional material in the hanging wall following defined channels orthogonal to the slope contours which appear often to emanate from gaps in the Meterff scarp where there is little exposure of bedrock. Similar, but less well-defined channels also appear in the footwall above the Meterff scarp. Small piles of scree appear in several places where the slope meets the alluvial channel at its foot. There is also an intermittent but largely continuous band of erosional material in the hanging wall immediately below the fault scarp, of ~50 cm – 1 m width. A comparison of the respective photographs from 2016 and 2019 suggest that there has been little change in any of these patterns since 2016. However, the photographs I took when revisiting the site in May 2022 (**Appendix 4, part 2**) show what appears to be an increased accumulation of larger scree towards the foot of the slope, and a large (20 m+) patch of scree within the bed of the alluvial channel.

Photographs of the same site taken in March 2017 on a separate scanning expedition show loose debris on the floor further up the alluvial channel (e.g. **Figure 111**). Photographs taken on my May 2022 visit also show such debris (**Appendix 4, part 2**).

This, and the location of the alluvial channel at the foot of a steep and extensive area of mountainside to the east of the Meterff site, suggest that the alluvial channel itself is likely to be significantly affected by seasonal factors such as rainfall run-off and possibly avalanches.

Figure 111: *Field photograph of Meterff site from 30th March 2017 looking northeast (photograph taken by Laura Gregory, University of Leeds).*

There is, therefore, significant potential for the geomorphology to change even over the period of a few years. With the exception of possible changes to the alluvial channel, there is little in the results from the pairings of the scans to suggest that erosional and gravitational factors played a measurable part in the deterioration of the Meterff scarp over the 3 years of this study. I have not been able to discern any recognisable pattern in the differencing results which equates to the slope-parallel erosional channels in both hanging wall and footwall (although, at the scales involved, the erosion could be contributing to the noise in the differencing results). Nor, with the possible exception of the relative downwards displacement of the Meterff hanging wall in the lower parts of the slope, is there a general overall displacement towards the southwest which might be expected if gravitational factors were predominant throughout. Such erosional and gravitational deposits as there are seems to be concentrated into the slope-parallel channels which did not appear to have changed

significantly in the intervening 3 years. However, on my visit in May 2022 the extent of the deterioration of the lower slope parts of the scarp seems to have increased significantly in the intervening period (see photographs in **Appendix 4, part 2**).

The results from the alluvial channel area are among the noisiest, suggesting the greatest amount of displacement in the first 3 year period up to August 2019. Each of the respective pairings apparently produces a possible relative accumulation of material at the foot of the slope compared to the lower levels of the slope of in the order of a few cms. Although this might make sense if there had been extensive erosion of the Meterff scarp slope over the intervening period, that possible conclusion needs to be treated with caution in terms of evidence of deterioration of the Meterff site because (1) it is impossible to disentangle the results from deterioration of the Meterff scarp slope from the seasonal effects of rainfall and avalanches from further away; and (2) the results from scan returns from ground surfaces which are largely parallel to the direction of the scans are likely to be less reliable than those from more vertical surfaces such as the hillside. Nevertheless, photographs taken in May 2022 now show a clear accumulation of material at the foot of the Meterff slope consistent with erosion of the hanging wall and footwall (**Appendix 4, part 2**), which suggests that it has been an ongoing process throughout the period.

4.7 Conclusion

Although TLS has been used successfully on a number of occasions to measure post-seismic deformation in a relatively controlled area over a period of up to a few months following an earthquake (e.g. Wilkinson et al., 2010, Wilkinson et al., 2012, DeLong et al., 2015), this study may be the first time anyone has attempted to use differential post-seismic TLS on a non-smooth surface over an extended time period at multiple sites with differing topography.

The Meterff site presents considerable difficulties in characterising post-seismic displacement both because of its small scale, and because of the fact that this scarp and its surrounding area are part of what appears to be a relay zone, and therefore difficult to analyse in isolation. However, the processing of the detailed TLS scans with

careful use of filters and detrending has produced results which allow some conclusions to be drawn as to the nature of post-seismic displacement at or adjacent to the Meterff scarp.

The near-scarp vertical slip in the hanging wall of the Meterff scarp and the wider scale vertical displacement of the hanging wall relative to the footwall over time is likely to be due to afterslip by way of co-seismic slip deficit recovery on that structure. The profile of that slip with the greatest amount of slip observed immediately next to the scarp (likely controlled by changes in competency due to the earthquake) reducing with distance from the scarp matches similar profiles seen elsewhere (e.g. Wilkinson et al., 2012). That slip appears to reduce over time, consistent with the expected exponential decay curve (ibid, Marone et al., 1991, and Zhou et al. 2018). Spatial variations in the amount of slip along strike may be explained by localised high co-seismic slip gradients.

Afterslip may also be the cause of the deformation seen within the footwall of the Meterff scarp, in relation to the possible second structure. If so, that structure does not appear to have ruptured to the surface co-seismically. The post-seismic displacement after 2017 shows a mixture of vertical and left-lateral slip at the surface, and would be consistent with the modelling of the slip on that structure at depth. This slip would also be consistent with the likely near-surface co-seismic slip vectors, and reflect recovery of co-seismic slip deficit on that structure.

The overall ESE/WSW horizontal displacement recorded at the surface between the Meterff hanging wall and footwall may also reflect similar slip deficit recovery.

Afterslip on the Meterff fault appears largely to have ceased by 2019. This probably reflects the limited amount of unrecovered co-seismic slip deficit on a structure which is very unlikely to extend significantly below ground beyond ~ 250 m if, as modelled, it coincides with the second structure at that depth.

It has not been necessary in this case to imply significant erosional/gravitational effects over a short time period (3 years) even in an area subject to extremes of climate/steep topography. However, over time those factors are likely to become

more relevant as the photographs taken in May 2022 illustrate. The deterioration of the scarp within that longer time period due to a lack of stability suggests that relatively little of the scarp will be available for study in the future.

The possible presence of the second structure suggests that faulting in the area may have been more distributed than implicit from the evidence of the Meterff scarp itself (perhaps not surprising in an area which appears to function at least in part as a relay zone). Therefore, even in 2016 before any post-seismic displacement the Meterff scarp may not have provided an accurate guide to potential future seismic hazard. It is possible in a relay zone that the structures are even more complex than is apparent from this study.

CHAPTER 5. Comparative study of the differing causes and effects of post-seismic displacement on fault scarps at six sites using differential Terrestrial Laser Scans

5.1 Introduction

As described in the introduction to Chapter 4, fault scarps are a potentially important source of evidence as to the previous history of earthquakes and long-term slip rates on faults in areas of active tectonics, which can in turn be used in constructing seismic hazard models and understanding fault behaviour. However, their reliability as evidence needs to be tested by an assessment of three factors:

- the distribution of co-seismic slip between on-fault and near-fault deformation;
- the extent and nature of afterslip; and
- the effect of geomorphological processes such as weathering or gravitational erosion.

I have described in detail in Chapter 4 how the post-seismic processes have operated in the context of one scarp, the Meterff site, and their relationship to co-seismic slip distribution. It is to be expected, however, that the extent and nature of post-seismic slip will differ between sites as a result of differences in how those 3 factors operate. For instance, differences in the extent of co-seismic slip and the extent to which there is a remaining slip deficit after an earthquake may well affect the extent and nature of afterslip (e.g. Cheloni et al., 2010, Wilkinson et al., 2010). The extent of weathering or gravitational erosion will depend on factors such as local topography (e.g. Kokkalas and Koukouvelas, 2005) and competence of the local rock units (e.g. Bucknam and Anderson, 1979 and Wallace, 1980).

In this Chapter, in order to assess how differences in those 3 factors result in differing outcomes over time, I compare the Meterff scarp post-seismic displacement results using differential TLS scans against the results from 5 other sites which are in the same region as the Meterff scarp, and where co-seismic slip at the surface was observed as a

consequence of the Norcia 30th October 2016 M_w 6.6 earthquake. Those sites vary considerably in terms of both co-seismic displacement and topography.

In each case, the TLS data processing steps are essentially the same as in the previous Chapter, and I will not therefore repeat them here. Where there are relevant differences, however, I will explain those.

5.2 Description of sites and data collection

5.2.1 Choice of sites, location and description.

In late October 2016, a team of geoscientists from the University of Leeds was already in the Castelluccio di Norcia area, with a tri-pod-mounted laser scanner, with a view to conducting research funded by a NERC Urgency grant. Their field campaign aimed to scan several sites associated with the 24th August 2016 Amatrice and 26th October 2016 Visso earthquakes where surface ruptures were visible. As part of this campaign, a TLS scan was taken on 29th October 2016 at a site below a ski station which is part of the Frontignano ski resort (Bove Road). The Visso earthquake of 26th October 2016 had left a visible rupture across a gravel road leading up to the ski station. Once travel was again permitted in the area for geological fieldwork after the devastation caused by the Norcia earthquake on 30th October 2016, the team returned to scan a number of sites where new surface ruptures had appeared, including the Bove Road site on 5th November 2016. The size and extent of the rupture had increased by that stage.

The majority of the new sites scanned are further to the south of the Bove Road site, adjacent to the main Monte Vettore ridge, where the greatest co-seismic displacement was visible. Some of those sites were scanned at least twice in the period of the next few days following the Norcia earthquake. Those and other sites were scanned again in autumn 2017 by a team from Leeds and Durham Universities, and in August 2019 by a University of Durham team including myself. Although relatively removed from the main area of displacement associated with the Norcia earthquake, the Bove Road site was scanned again in both 2017 and 2019 as it enabled a comparison at that site between co-seismic and post-seismic displacements.

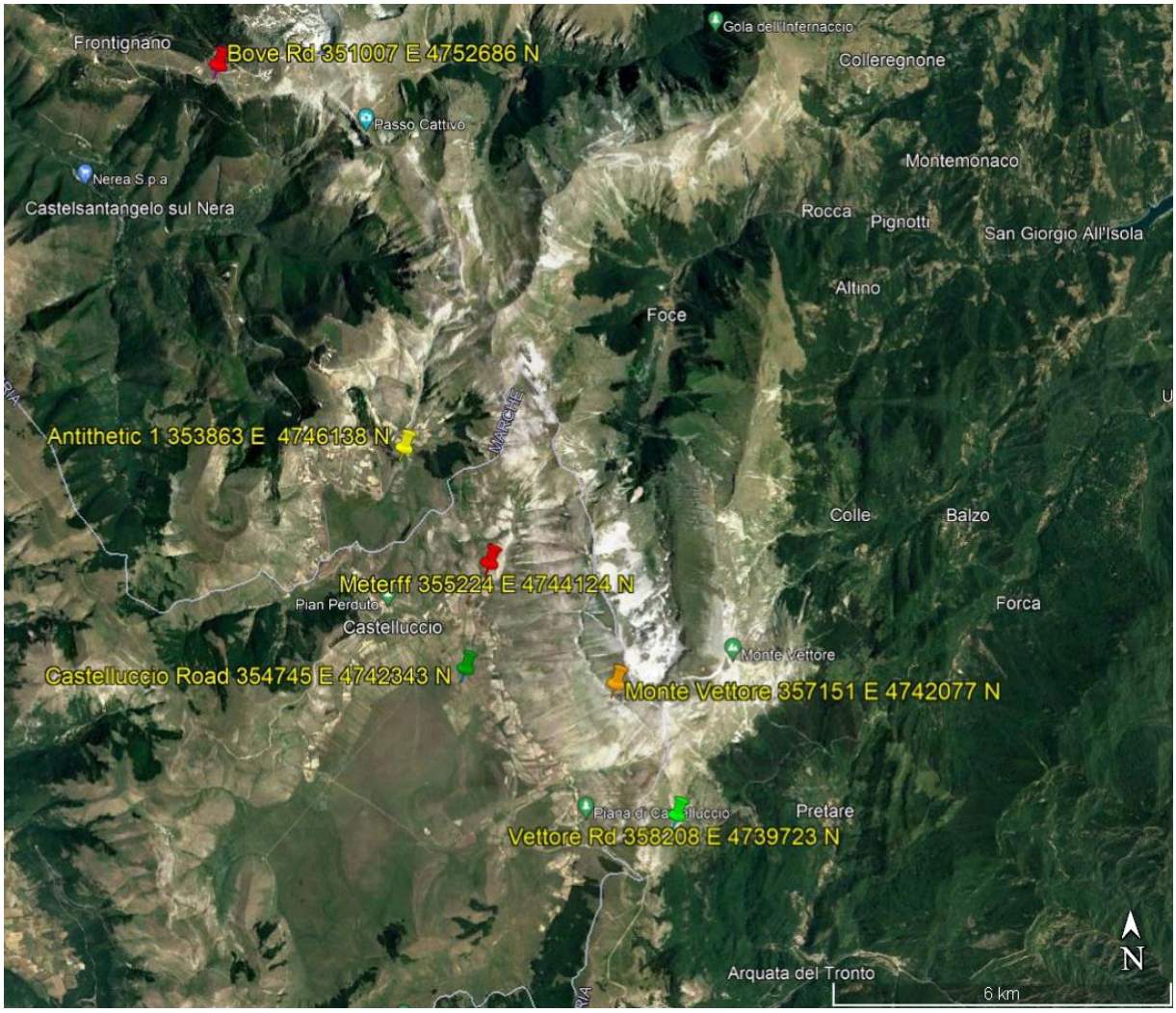

Figure 112: *Google Earth image showing locations of the six TLS sites discussed in this Chapter.*

The location of the 6 sites used here are shown in the Google Earth image, **Figure 112**. From north to south those are:

- Bove Road (at 351007, 4752687 UTM 33T);
- an antithetic site on a hillside at Colle Vinto (Vettore Antithetic 1, at 353863, 4746138 UTM 33T);
- the Meterff site adjacent to Colli Alti e Bassi covered in Chapter 4 (at 355224, 4744124 UTM 33T);
- a relatively level site straddling Castelluccio Road on the plain to the southeast of Castelluccio (Pian Grande) (the Castelluccio Road site, at 354745, 4742343 UTM 33T);

- a steep, elevated site below the main Monte Vettore ridge under the Scoglio dell'Aquila outcrop (the Monte Vettore site, at 357151, 4742078 UTM 33T); and
- another site straddling a road, at the Southern end of Monte Vettoretto, where the road is set into a hillside (the Vettore Road site, at 358208, 4739723 UTM 33T).

In May 2022 I revisited all of the sites without a scanner (with the exception of the Monte Vettore site, which was inaccessible during my visit due to bad weather).

5.2.2 Data Collection methods

The individual scan positions and settings used are described in more detail under the sections below dealing with the individual sites. As with the Meterff site, the principle followed has been broadly to duplicate the scan positions used in each case on separate occasions, enabling repeat scans of the individual fault scarps and surrounding areas. I then used those scans to create DEMs, and then differenced the DEMs, using the Iterative Closest Point ("ICP") algorithm to derive displacement in 3 dimensions before detrending to remove biases from any ramps in the ICP results (likely to be the result of slight levelling differences in the scanner set-ups).

5.2.3 Overall geological setting.

Figure 113 shows the geological setting of the 5 southern-most sites, drawn onto a 2013 geological map of the area (from Pierantoni et al., 2013).

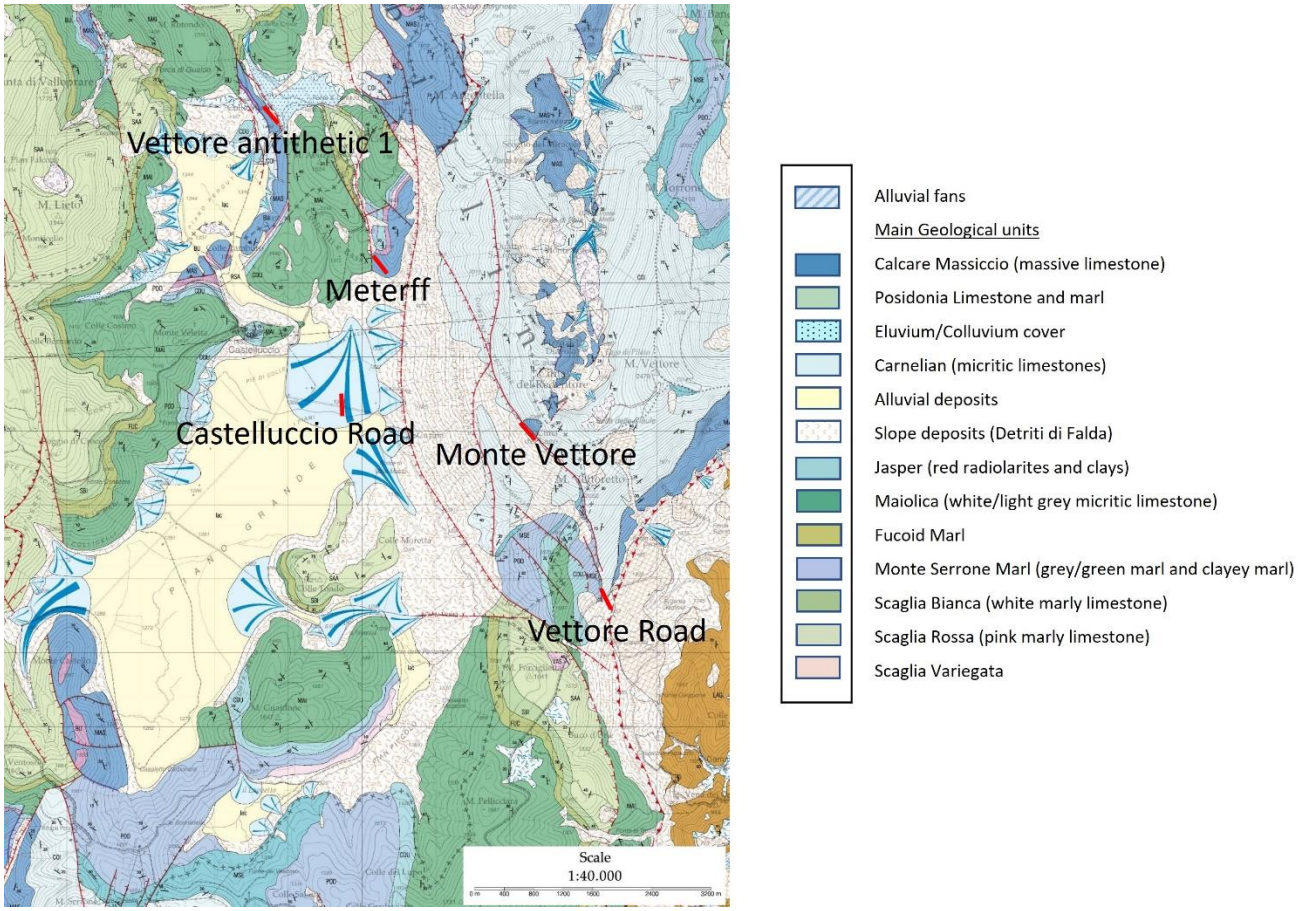

Figure 113: *Setting of 5 TLS sites (approximate positions of the scanned scarps added in bold red) against geological map, adapted from [Pierantoni et al., 2013]*

5.2.4 Description of individual sites.

5.2.4.1 Vettore Antithetic 1 site

This is a hillside site on a NNE-facing slope, with co-seismic antithetic slip towards the northeast. Scans were taken of this site on 2 November 2016, 6th October 2017 and 27th August 2019. **Figure 114** is a photograph of the site in August 2019, with a zoomed- in section showing detail of the scarp.

Figure 114: *Vettore Antithetic 1 site taken on 29th August 2019, looking southwest (upper figure) and detail (lower figure). Scale is ~300 m across (upper), ~150 m (lower).*

The scanner position used was on the raised ground to the far right of this figure. The site features a NNE-facing slope of limestone bedrock with some scree, facing two lower raised areas across a drainage channel. The Pierantoni et al., 2013 geological map describes the units as respectively Calcare Massiccio (massive limestone) (the hillside) and Eluvium/Colluvium cover (the other units). Previous faulting appears to have been mapped in the Pierantoni map as an antithetic fault following the line of the foot of the main slope, part of wider antithetic faulting trending ~335° referred to elsewhere (e.g. in Galderisi and Galli, 2020) as the San Lorenzo Fault.

In this segment of the fault scarp, its trend is predominantly southeast-northwest. One prominent feature of this section of the scarp is the sub-vertical ~4 m high outcrop at ~50 m from the left-hand edge of this figure (below a small tree) The hanging wall area to the east of this outcrop contains a number of larger individual rock fragments of > 20 cm x 20 cm which appear to have been detached from the footwall bedrock (with new additions observed in May 2022 - see photographs in **Appendix 5**). Elsewhere further north along the hanging wall the debris consists of much smaller scale rock fragments, as light scree.

The co-seismic measurements recorded by the Open EMERGEO Joint Working Party (Villani et al., 2018) recorded combined offset of ~30 cm – 1 m along this section of scarp. The higher values are concentrated at the far northwest end of the scarp (as it bends around towards the WNW), and around the area of the sub-vertical outcrop. **Figure 115** shows the location and size of the co-seismic combined offset (either recorded as such, or a combination of recorded throw and opening), together with the recorded rock type (with “debris” recorded as the rock type more consistently around the area of the sub-vertical outcrop).

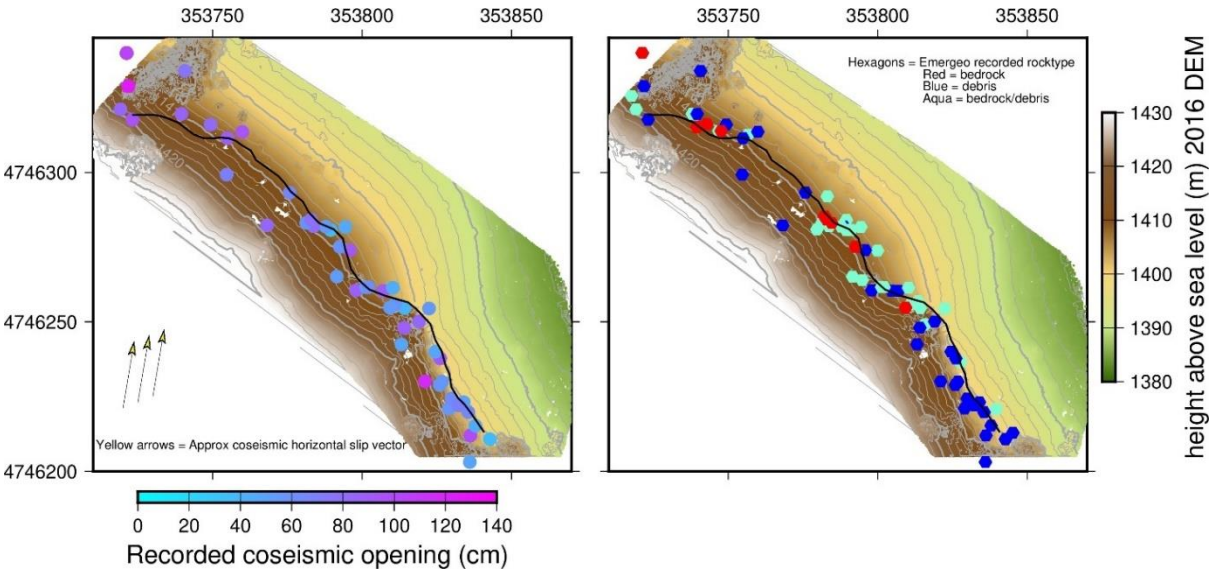

Figure 115: *Vettore Antithetic 1 co-seismic measurements recorded by the Open EMERGEO Joint Working Party (Villani et al., 2018). LH panel shows recorded offset, or combined throw and opening. Yellow arrows show approximate direction of co-seismic slip measured on the fault. RH panel shows recorded rock type (bedrock red, debris blue, bedrock/debris aquamarine). Background is DEM from 2016 scan, with contours at 2 m intervals.*

5.2.4.2 Castelluccio Road site

At this site the geology is unconsolidated alluvial fan material from the steep slopes further to the north and east, and the topography is essentially flat. The co-seismic rupture at this site was visible co-seismically due to offsets across Castelluccio Road, which at this point runs roughly ENE-WSW across the Pian Grande. As well as rupturing the road surface in two places, a small offset was also visible in the neighbouring fields (then largely devoid of seasonal vegetation). The site was scanned several times in 2016, including once on 30 October 2016, when the photograph at **Figure 116** was taken, and again on 8th November 2016, by which time the ruptures across the road had been temporarily repaired. By the time of a follow-up visit in July 2017 the road had been fully repaired. Further scans were taken on 2nd October 2017 and (by myself with a colleague) on 30th August 2019.

Figure 116: *Castelluccio Road site photograph taken on 30th October 2016, looking east (photograph taken by Laura Gregory, University of Leeds).*

My sketch of the location as it appeared in 2019 is at **Figure 117**. As I note on that sketch, although any offset in the fields to the north of the road was indistinct due to the vegetation, there still appeared to be an offset to the south of the road. A Google Earth image of the site in 2020 (**Figure 118**) still shows a division in vegetation cover along the lines of the scarp observed in 2016, with ploughing traces evident. By May 2022 the surrounding fields had been thoroughly ploughed, with the previous offset only visible as a gradual downwards change in levels from east to west on both sides of the road (see photographs in **Appendix 5**).

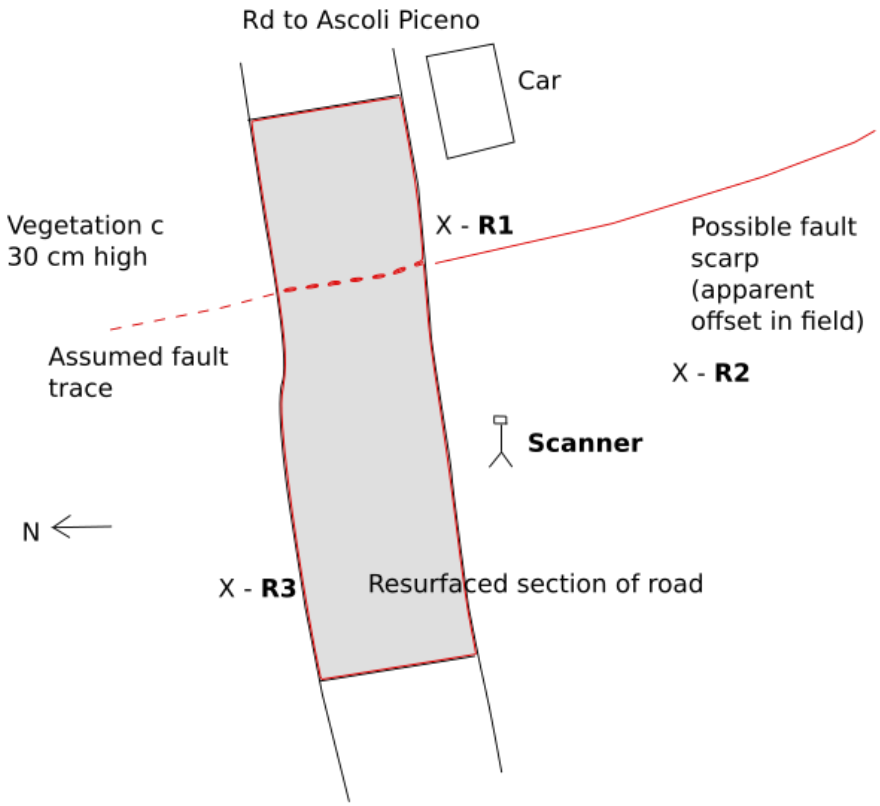

Figure 117: *Field sketch of Castelluccio Road site on 30th August 2019 showing scanner and reflector positions.*

Figure 118: *Google Earth image of Castelluccio Road site (from image dated 29 June 2020), showing locations of reflectors used in 30th August 2019 scan.*

Co-seismic measurements by the Open EMERGEO Joint Working Party (Villani et al. 2018) recorded offsets of ~10 cm or less, with dip directions of ~270° along a largely north-south trending structure. No slip vectors were recorded, presumably due to the unconsolidated nature of the material.

5.2.4.3 Monte Vettore site

This site saw co-seismic movement of up to in excess of ~1-2 m in the Norcia earthquake, and had also experienced movement in the earlier 29th August 2016 Amatrice earthquake. In an elevated (at ~2170 m a.s.l.), steep and exposed position, the footwall consists of Calcare Massiccio (massive limestone) bedrock, in the form of the large Scoglio dell'Aquila outcrop (> ~100 m in height), set against a hanging wall of various slope deposits of scree and larger boulders (**Figure 119).**

Figure 119: *Monte Vettore site, photograph taken in October 2017, looking north along Monte Vettore fault scarp, with the Scoglio dell'Aquila outcrop in upper centre and upper RH part of the figure (photograph taken by Laura Gregory, University of Leeds).*

On 1 November 2016 this site was scanned by the University of Leeds team (along with other sites on the main Monte Vettore scarp). Although the site was scanned again in October 2017, due to difficulties in co-locating the other pairs of scans in this study I have only used the 1 November 2016 scan of the site under the Scoglio dell'Aquila outcrop and equivalent multiple scans which we took on 28th August 2019.

Figure 120 (my field sketch) shows the scanner set-up used in 2019.

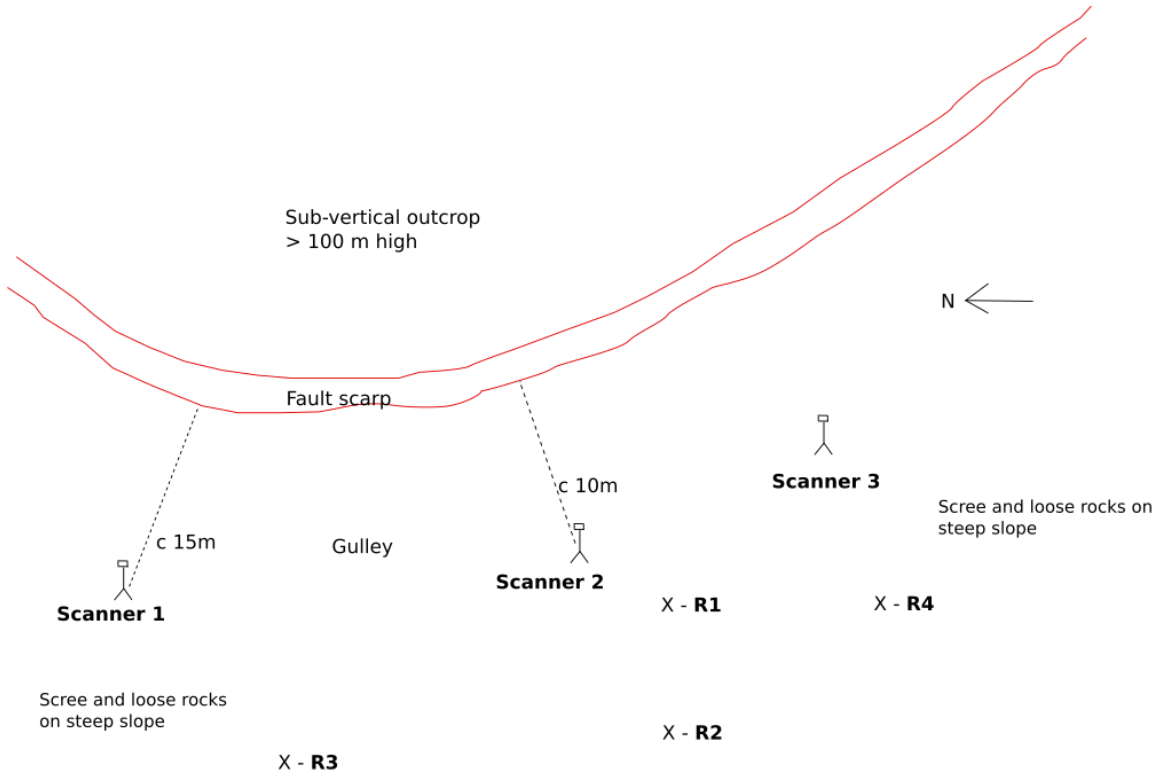

Figure 120: *Field sketch of Monte Vettore site from 28th August 2019 showing scanner and reflector positions.*

The co-seismic measurements by the Open EMERGEO Joint Working Group (Villani et al. 2018) recorded offsets of up to ~2 m with largely normal kinematics on a plane with a 141° strike, dipping at ~71°, and with slickenlines plunging at 69° towards 203° (see summary in Galderisi and Galli, 2020).

5.2.4.4 Vettore Road site

This site also features an initial rupture of the road surface which has subsequently been repaired. It is at the southern-most end of two units of respectively Calcare Massiccio and Carnelian micritic limestone which are upslope from the site, where the exposed geology is largely bedrock covered by some light scree in places. It is at the end of the main area of co-seismic deformation along the Monte Vettore fault, close to the line of the OAST (the Olevano-Antrodoco-Sibellini Mountains Thrust), which runs ~south-north at this point, just to the east of the site. To its immediate south where the slope falls away below the road the bedrock is covered by various slope deposits (largely man-made) near to the road. The scarp trends almost due north-south.

Figure 121: *Vettore Road site photograph taken on 27th August 2019, looking WSW, repaired road section to right of snow pole.*

At this point the road (Vettore Road) trends WSW – ENE. The scarp follows the line of previous normal faulting extending south from the main Monte Vettore fault scarp (see **Figure 113**). **Figure 121** shows the repaired road section in 2019.

As this figure shows, the line followed by the road has been enhanced by man-made levelling, cutting into the slope to the north, and adding material to the slope to the south. In May 2022 the road had been fully levelled, and the banking in the roadside to the NNE had protective mesh on it to stop rock falls. The slope below the road had cracks of ~ 5 cm in the unconsolidated ballast, indicating continuing movement of material (see photographs in **Appendix 5**).

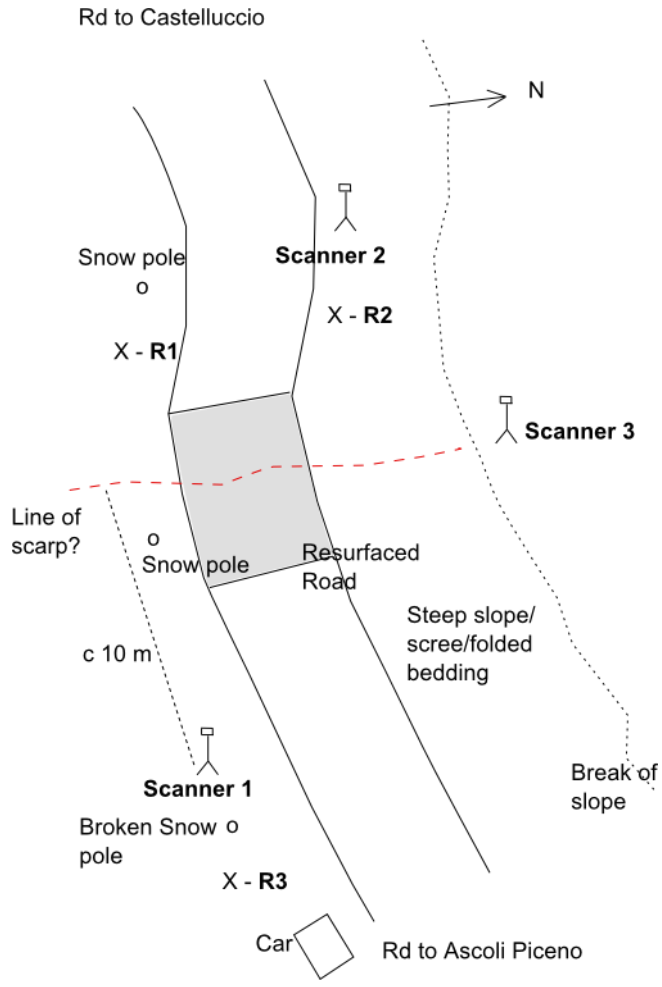

Figure 122: *Field sketch of scanning positions used on 27th August 2019, showing approximate scarp line in relation to repaired road section, scanner and reflector positions.*

This site ruptured initially during the Amatrice earthquake, displaying subsequent signs of afterslip. After the Norcia earthquake the site was scanned several times in 2016, including on 30th October 2016 and 6th November 2016. It was scanned again on 3rd October 2017. We scanned it using 3 scan positions on 27th August 2019, two by the roadside, and one from looking down on the road from a break in the slope above to the north of the road (see my field sketch, **Figure 122**).

There are relatively few co-seismic measurements for this site by the Open EMERGEO Joint Working Party (Villani et al. 2018) (only 8 in all). Those show combined offset of between 13 and 18 cm, almost all measured on the tarmac area, with one recorded slip vector towards 220^{o}.

5.2.4.5 Bove Road site

The Bove Road site, to the south of the ski resort town of Frontignano and part of the wider ski resort, is another elevated site at ~1700 m a.s.l.. It is somewhat removed from the other sites described above, being over 7 km to the NNW of the Vettore Antithetic 1 site. The geology of the area is shown in the extract from the Regione Marche Carta Geologica Regionale (https://www.regione.marche.it) (**Figure 123**).

The fault giving rise to the scarp here forms part of a fault system where over time the newer rocks in the hanging wall (Fucoid Marl) have become exposed through erosion following repeated downthrow compared to the Maiolica unit of the footwall along a line trending ~NNW-SSE.

The scarp crosses a ~north-south gravel access road (strada bianca) leading to a ski lift station which is at the top of a chair lift from the bottom of the ski slopes. The scarp has a bearing of ~southeast-northwest, descending from a relatively gentle slope to the southeast, across the road, then more steeply downhill to the northwest. By 2017, the gravel road section had been repaired. The site is crossed by a couple of footpaths and, in the ski-ing season, by an exit from the ski lift station leading to blue ski runs on the lower slopes, as well as being part of a return route from the upper black ski runs which start at the lower elevations of Monte Bove Sud at ~ 1900/2000 m.

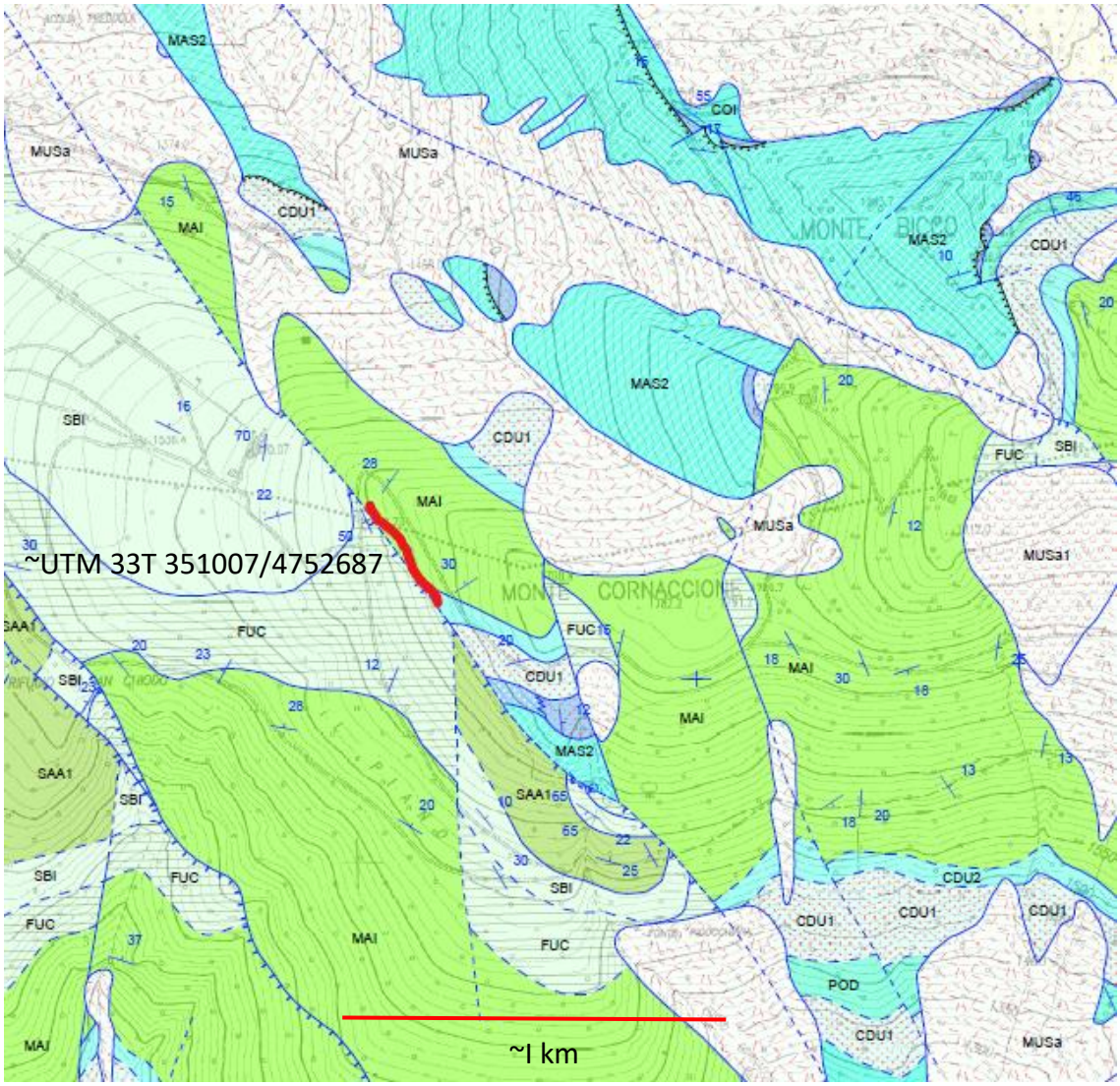

***Figure 123**: Adapted extract from [Regione Marche Giunta Regionale, Carta Geologica Regionale 1:10,000](), Sezione 325070 Monte Bove accessed on 3rd March 2022 at https://www.regione.marche.it. Approximate Bove Road site marked in bold red. This extract shows an area of ~2.5 km x 2.5 km. Main units shown in order of newer to older units are: (Oligocene) Slope deposits (dashed pink lines against white background, MUSa/MUSa1); (Cretaceous-Miocene) Scaglia Rossa (khaki green, SAA1-3), Scaglia Bianca (pale green, SBI), Fucoid Marl (pale green with stripes, FUC), Maiolica (bright light green, MAI); (Jurassic) Calcari Diasprini Umbro-Marchigiani (CDU1-2, turquoise and light green with red dots), Gruppo del Bulgarone (blue with red dots, BUG1), and Calcare Massiccio (Massive limestone) del M Nerone (turquoise with white stripes, MAS2).*

Figure 124: *Rupture from Norcia earthquake across gravel access track looking north to Bove Rd ski lift, taken on 5th November 2016 at ~UTM 33T 351007/4752687 (photograph by Luke Wedmore, then University of Leeds, now University of Bristol).*

As described above, this site was scanned on 29th October 2016, at a time when a small amount of displacement (< ~5 cm) could be measured across the track, with cracks near the ski station, but displacement was not clearly visible elsewhere on the hillside to the southeast. On the return visit on 5th November 2016, displacement was visible across the track (**Figure 124**), with further surface cracks near the ski station, and displacement elsewhere in the scarp to the southeast of the track. Subsequently the site was rescanned on 2nd October 2017, and (by us) on 29th August 2019 from essentially the same scan positions. By May 2022 the scarp had deteriorated significantly through erosion (see photographs in **Appendix 5**).

Co-seismic offset was measured by the Open EMERGEO Joint Working Party (Villani et al., 2018) as being between ~5 cm on the road and up to ~30 cm further up the slope to the southeast. No slip vectors were recorded.

5.2.5 Co-seismic results using shallow slip distribution models.

The Bove Road site falls outside the area covered by the Pleiades data used in this study. The near-surface slip vectors for the Bove Road area which I modelled in the joint inversion described in Chapter 3 therefore rely mainly upon far-field data (InSAR and regional GNSS) and lack near-surface detail. The modelled results for slip on Faults 1 and 2 which cover the Bove Road area show relatively near-surface slip (within 1 km of the surface) of ~ 20 cm towards vectors ranging from ~260^{o} to ~280^{o}, with patches of larger amounts of slip at greater depths generally towards ~205^{o}.

The other TLS sites are within the area covered by the Pleiades data, and I have therefore been able to model slip at depth at those sites in more detail. **Figure 125** shows the location of the other sites in the context of the down-sampled slip vectors in the central area.

More detail of the near-surface slip in the central area, without downsampling, can be seen from **Figure 126**. Note that this figure does not extend quite as far northwest as the Vettore Antithetic 1 site.

The predominant modelled co-seismic slip vectors at depth for the Monte Vettore and Vettore Road sites are dip-slip displacement towards ~250/260^{o}. In the cases of the Meterff and Castelluccio Road sites the model does not expressly allow for structures in those locations, as the structures are minor synthetic structures in the hanging wall of the main Monte Vettore fault, or other more significant synthetic structures. Slip in the hanging wall of the more major structures is also towards the same vectors. In the case of the Vettore Antithetic 1 site, the modelled near-surface slip is predominantly right lateral (towards ~150^{o}).

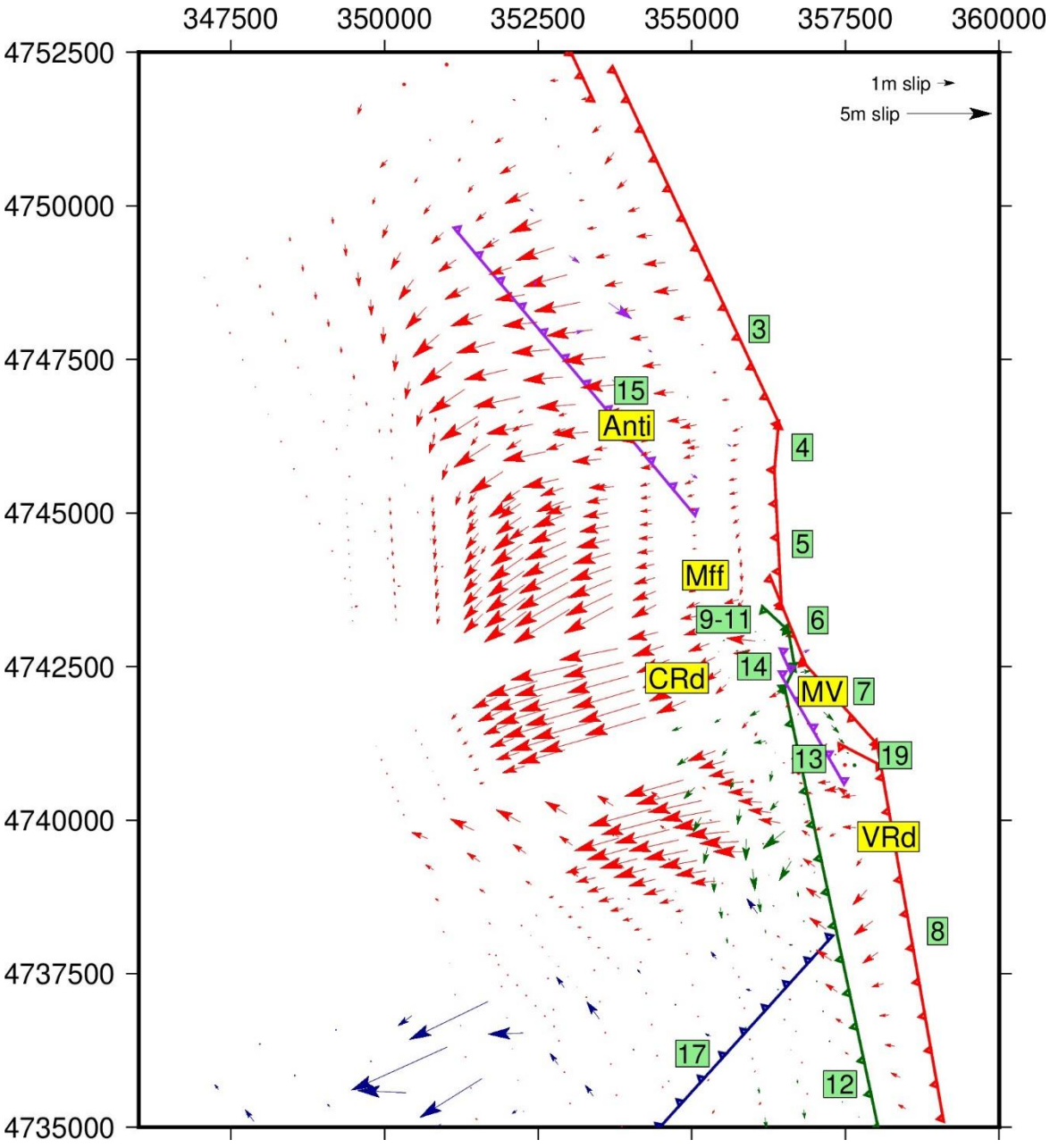

Figure 125: *Orientation and magnitude of slip vectors resulting from joint inversion in central part of area modelled in Chapter 3 showing detail of slip at depth, projected in 2D onto surface, down-sampled to ~0.5 km x 0.5 km patches. Colours of vectors shown match faults shown at surface. Approximate location of TLS sites shown in yellow boxes (Anti = Vettore Antithetic 1, Mff = Meterff, CRd = Castelluccio Road, MV = Monte Vettore, VRd = Vettore Road).*

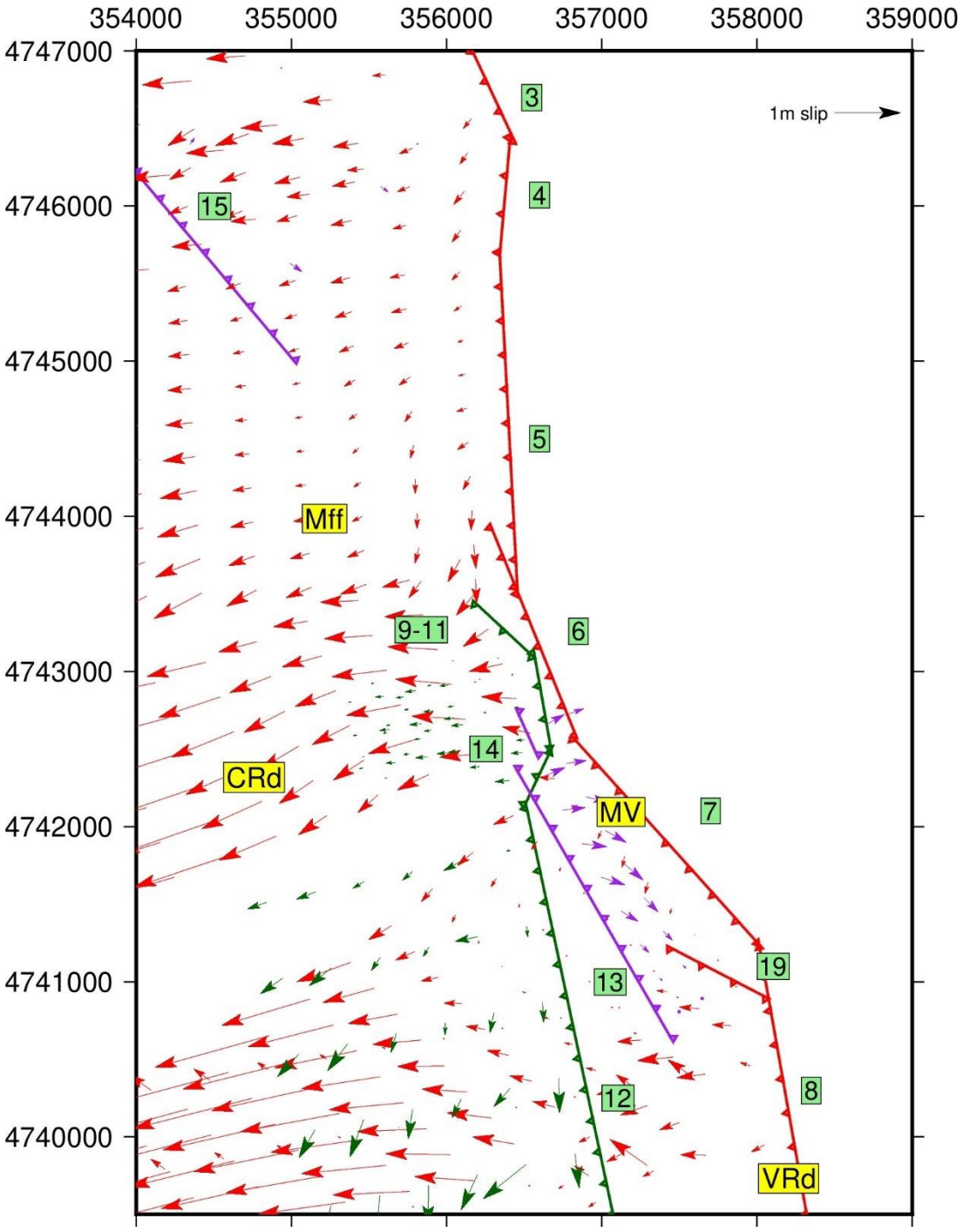

Figure 126: *Orientation and magnitude of slip vectors resulting from joint inversion in central area showing detail of slip in near-surface area projected in 2D onto surface, without down-sampling. Colours of vectors shown match faults shown at surface. Approximate location of TLS sites shown in yellow boxes (Mff = Meterff, CRd = Castelluccio Road, MV = Monte Vettore, VRd = Vettore Road).*

5.3 Data processing

5.3.1 Summary of methods applied

In summary, the methods used in each case are those described in detail in Chapter 4, to which reference should be made for a fuller explanation.

Pairs of scans from separate occasions are aligned using bulk shifts followed by rough alignment through point-pair picking, and then fine alignment using the open source CloudCompare software. The DEMs created from those aligned scans are then differenced using the Matlab ICP algorithm (Bouaziz et al., 2013, Chen and Medioni, 1992, Nissen et al., 2017), to derive separate component results for east-west, north-south and vertical displacement. Each of those displacements is then detrended by applying a best fit plane correction deducting any ramps in those results, using results which are selected on the basis of proximity to the input datasets used in the Matlab ICP process (to avoid obviously spurious results where one or other of the input datasets does not have any data), plus a threshold of a maximum value which excludes improbable values.

5.3.2 Variations in methods applied

It has proved difficult to maintain a common approach to fine registration of the point clouds using the ICP registration tool within the CloudCompare software because of differences between the sites. Ideally, fine registration should be done by identifying a patch common to both point clouds which has not moved between the dates the scans were taken and using the results from that area to apply a transformation to the whole later cloud. In a co-seismic situation this would generally be done by identifying a patch of the footwall, deriving the rigid transformation necessary to register that part of the later cloud to the earlier cloud equivalent, and then applying the same transformation to the whole of the later cloud (which I have done successfully in relation to the only co-seismic pairing here, at the Bove Road site). As noted above in connection with the Meterff site, in a post-seismic situation with ongoing erosional process over time gaps of at least 12 months in each case, I was not able to identify suitable patches within the footwall in that case, and therefore used the whole clouds in the registration process. I used the same process for:

- the Monte Vettore site (where the footwall is near-vertical),
- the Castelluccio Road site (where the footwall is either resurfaced road or agricultural land) (with the exception of the scan pairing which covers 9 days immediately following the earthquake),
- the majority of the Vettore Road site pairings (where the footwall consists largely of road, which has been resurfaced, or the road bed which is unstable), and
- the post-seismic Bove Road data where there is widespread erosion across the slope.

The user guide to the CloudCompare software (https://www.cloudcompare.org/doc/wiki/index.php/Align) also suggests that the ICP registration tool may not work when the clouds have significant differences between them, and in that case fine alignment might not be appropriate. At the Vettore Road site, the fine alignment produced unrealistic values for the scan pairing covering 2017 and 2019, and I have used only the roughly aligned data and did not use the fine alignment tool. The patch-based approach worked best at the Vettore Antithetic 1 site, where part of the footwall has not changed significantly over time.

In the case of the Meterff site results, as described in more detail in Chapter 4 I applied a further filtering stage to remove outliers using a recursive filter which replaces values which exceed a threshold compared to median values within set widow sizes which increase with successive iterations. This retains detail in areas of high point density, and replaces values in outlying areas of low data density. In the case of the Meterff site, the noise in the data away from the fault scarp itself compared to the more consistent results closer to the fault scarp suggested that this filter would assist in removing excessive noise in the signal. I used the same recursive filter for the results obtained from differencing the 2016 and 2019 scans on the Vettore Antithetic 1 site (2016–2019 and 2017–2019 pairings) as the noise in those results appeared to be obscuring the underlying signal. However, the data in the other locations have not fitted that pattern, and the filter has not been applied in the other locations to avoid unnecessarily degrading the signal.

At the Monte Vettore site, vegetation in the form of large tufts of coarse grass appeared potentially to bias the results. In that location I have applied a lowest points filter to each of the aligned datasets before using the ICP algorithm. The filter uses decreasing area window sizes containing increasing point densities to select the lowest points within each window, removing points above the lowest point elevation (retaining the ground surface detail in areas of high point density). However, although I experimented with using this filter for other locations, this technique has the effect of significantly reducing the point density within the point clouds and the vegetation in other sites was not obviously a distorting factor. Therefore, I only used the lowest points filter in the Monte Vettore location in processing the results set out below.

Although I attempted to model slip at depth on some of the sites in addition to the Meterff site, it was apparent that the results were heavily influenced by local variations in displacement at the surface due to erosion (rather than afterslip), and I did not feel that anything useful could be derived from the results.

5.4 Results

5.4.1 Vettore Antithetic 1 site

2016–2017

The scans here are both post-seismic and date respectively from 2nd November 2016 and 6th October 2017. The results for the 2016–2017 displacement show a consistent pattern of relative displacement of the footwall, although with noisier results in the hanging wall. Vertical displacement of the hanging wall relative to the footwall is in the order of ~3 cm downwards, with horizontal movement of ~2-4 cm towards WSW (**Figure 127**).

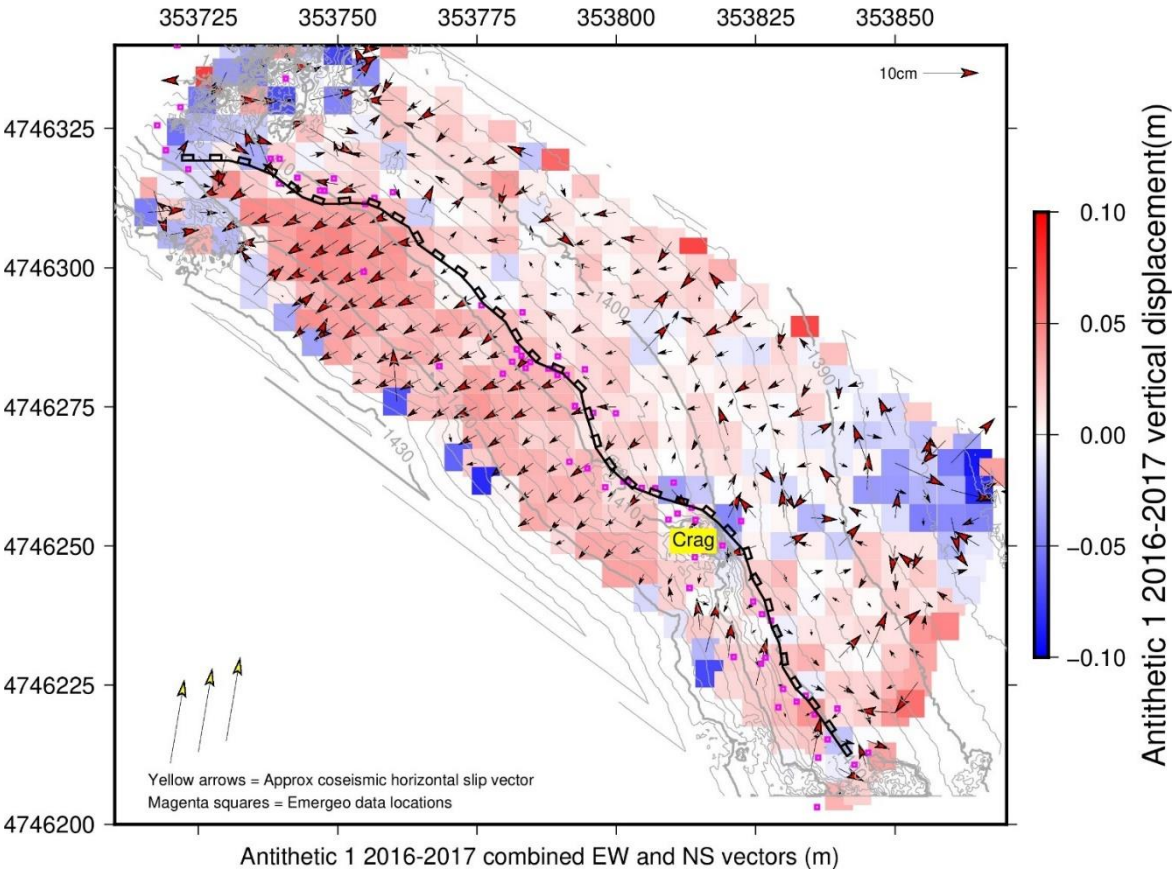

Figure 127: *Vettore Antithetic 1 2016–2017, median displacement gridded at 5 m x 5 m showing horizontal displacement vectors (arrows) against vertical displacement (background). Contours at intervals of 2 m, from DEM derived from 2nd November 2016 scan. Values at the edge of the data are masked by limiting to movement of +/- 10 cm, to exclude clearly erroneous values from an edge effect. The "Crag" label shows the approximate location of the sub-vertical crag referred to in the text.*

There is little or no displacement seen in the footwall area of the sub-vertical crag. In the hanging wall below the crag such horizontal movement as there is trends largely towards northeast. There is downwards displacement (of 2-3 cm) in the area immediately below the crag, and over an area extending towards the ENE.

The individual components of slip before median filtering are shown in **Appendix 5.**

2017–2019

I used a recursive filter to remove excessive noise from the ICP displacement results from differencing the scans from 6th October 2017 and 26th August 2019 (**Figure 128)**.

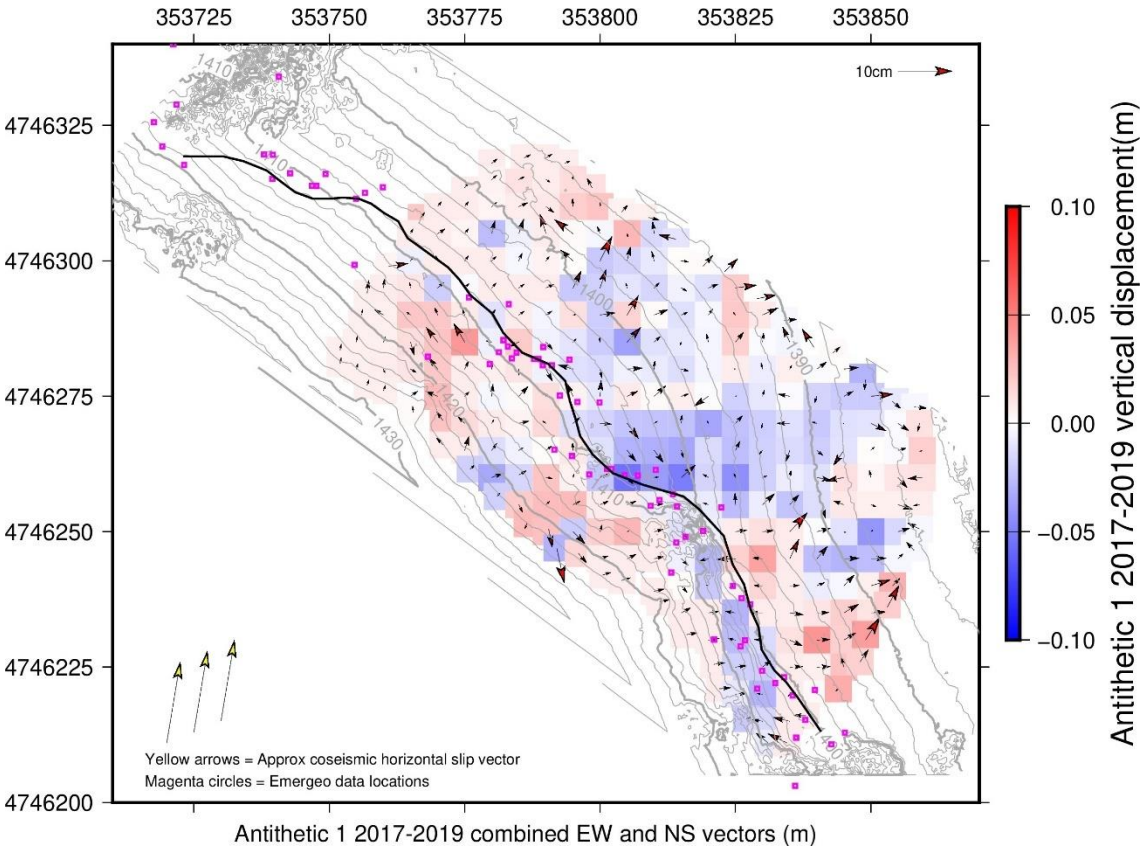

Figure 128: *Vettore Antithetic 1 2017–2019, median displacement gridded at 5 m x 5 m showing horizontal displacement vectors (arrows) against vertical displacement (background). Contours at intervals of 2 m, from DEM derived from 2nd November 2016 scan. Values at the edge of the data are masked by limiting to movement of +/- 10 cm, to exclude clearly erroneous values from an edge effect.*

Vertical movement between footwall and hanging wall in areas away from the crag is concentrated in the central part of the scarp, where there is relative downwards displacement of ~2-4 cm near the scarp, with lower values further away from the scarp. There is relative upwards displacement of ~ 2-3 cm below the crag to the east in the hanging wall, and possibly some degradation in the footwall of the crag and the footwall area to its southeast. There is also relative horizontal displacement of ~ 1-2 cm towards the ENE in the same area of the hanging wall. The separate slip components before recursive filtering are shown **Appendix 5**, and show a high level of noise.

2016–2019

I also used a recursive filter to remove excessive noise from the ICP displacement results from differencing the scans from 2nd November 2016 and 29th August 2019 (**Figure 129)**.

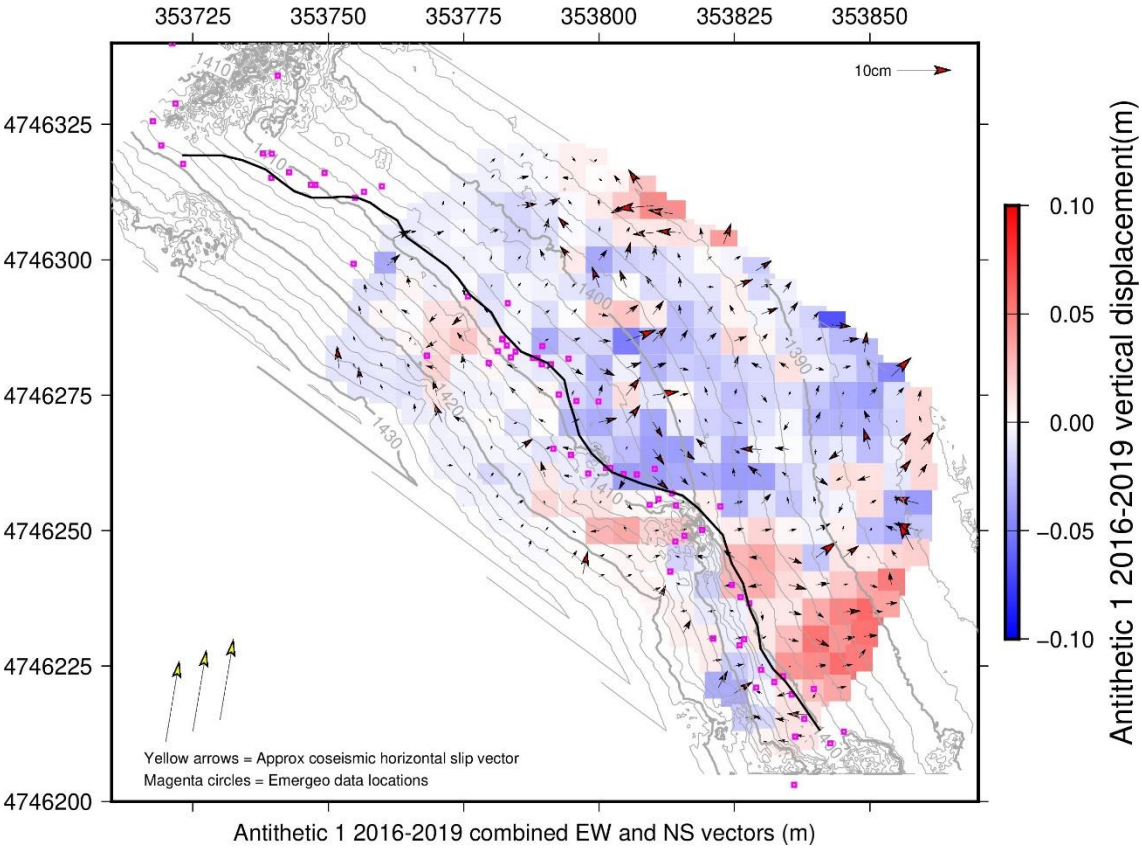

Figure 129: *Vettore Antithetic 1 2016–2019, median displacement gridded at 5 m x 5 m showing horizontal displacement vectors (arrows) against vertical displacement (background). Contours at intervals of 2 m, from DEM derived from 2nd November 2016 scan.*

The relative vertical displacement between scans is similar in pattern to that seen in 2017–2019, although spread over a larger area (which reflects the wider distribution of slip seen in the 2016–2017 results). The hanging wall is, generally, displaced downwards compared to the footwall by ~2-5 cm. The exception to this is at the far southeast, where displacement is upwards by ~2-3 cm. Horizontal slip vectors are inconsistent (ignoring values seen at the edges of the figure), but in the southeast show some general movement towards the ENE in the hanging wall. The separate slip

components before recursive filtering are shown **Appendix 5**, and show a high level of noise.

5.4.2 Castelluccio Road site

October–November 2016

I have used 2 of the scans taken in quick succession after the Norcia earthquake, on 30th October 2016 and 8th November 2016. Recorded co-seismic slip was less than 10 cm. However, even within this 9 day period, there is some vertical displacement.

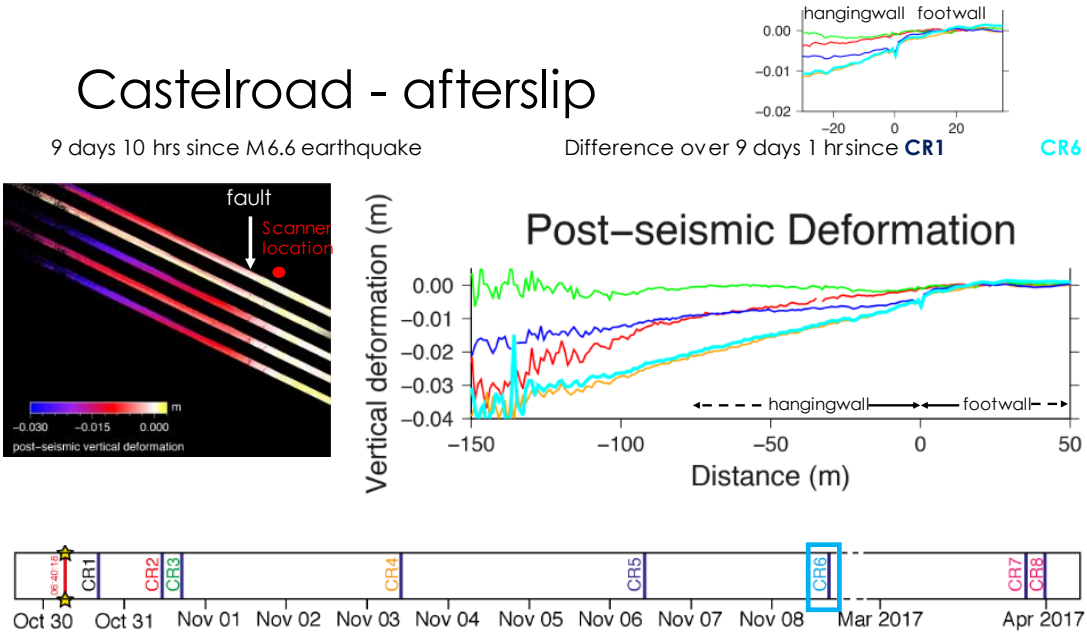

Figure 130: *Cumulative post-seismic deformation over 9 days after the Norcia earthquake recorded on the road section, from Wedmore et al., 2017. The numbering e.g. "CR1" and "CR2" refers respectively to the first and second scans after the earthquake.*

Using differential TLS, Wedmore et al., 2017 found post-seismic slip in the hanging wall of the road section of up to ~ 4 cm by 8th November 2016 (although they recorded slightly lower slip of up to ~2 cm at 150 m away from the scarp in the previous scan). **Figure 130** shows their results from the first 9 days after the Norcia earthquake.

The majority of slip recorded by Wedmore et al., 2017 occurred within the first 24 hours after the earthquake (shown by the red line on the main panel in their figure). **Figure 131** shows my results from two profiles taken from either side of the road

across the line of the scarp, together with the vertical results across the road and surrounding area.

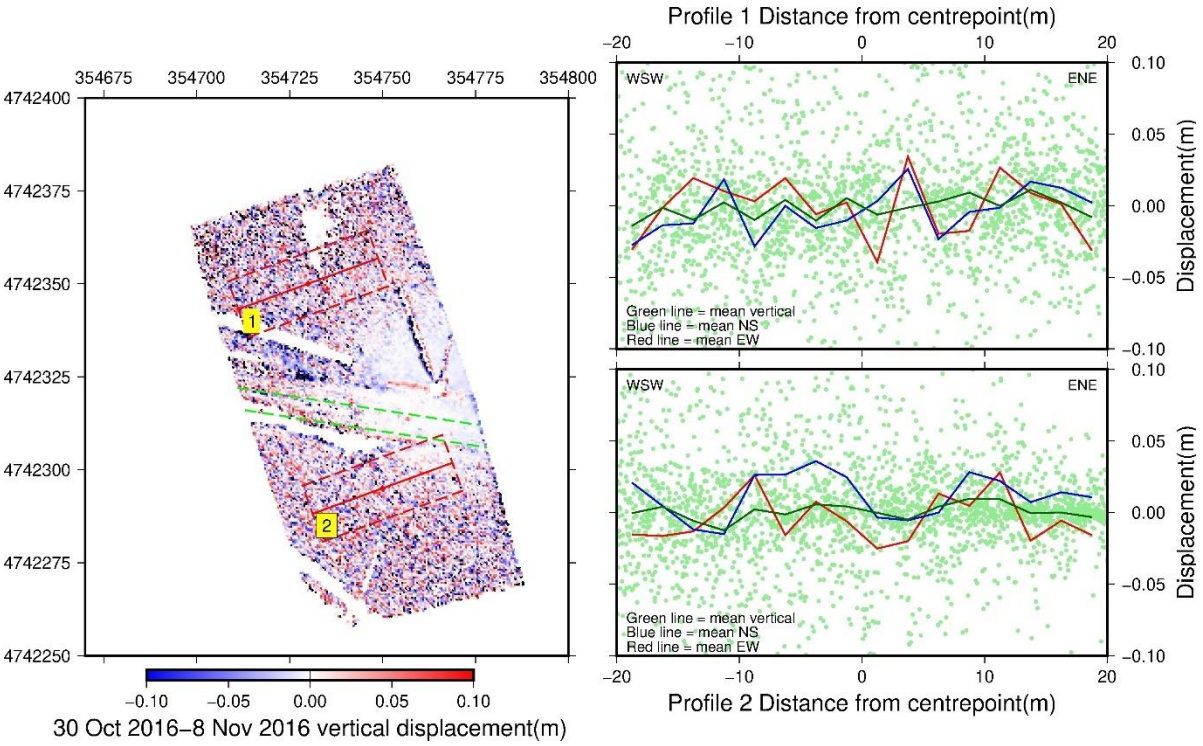

Figure 131: *Castelluccio Road site, 30th October 2016–8th November 2016 vertical displacement (LH panel) and profile across scarp, to north and south of road (upper and lower RH panels). Green dashed lines in LH panel are approx. road extent. In the RH panels mean values for datapoints within the dashed red box in the LH panel are shown for east-west (red line), north-south (blue line) and vertical (green line). Green dots in RH panels are vertical datapoints.*

Unlike Wedmore et al., 2017, I have not used the road itself as an area for detailed study, as it has been resurfaced since on several occasions. I have also used a relatively short (east-west) sub-section of the data (~50 m compared to Wedmore et al., 2017's ~200 m), to ensure overlap between each of the scans.

The horizontal results show little clear pattern, except possibly a small degree of movement (~2 cm) towards the west in the hanging wall immediately next to the scarp. The vertical results show only a small amount of relative movement (~1 cm downwards) in the hanging wall, compared to the footwall (which is consistent with the Wedmore et al., 2017 results from the road section over the 20 m from the scarp).

2016–2017

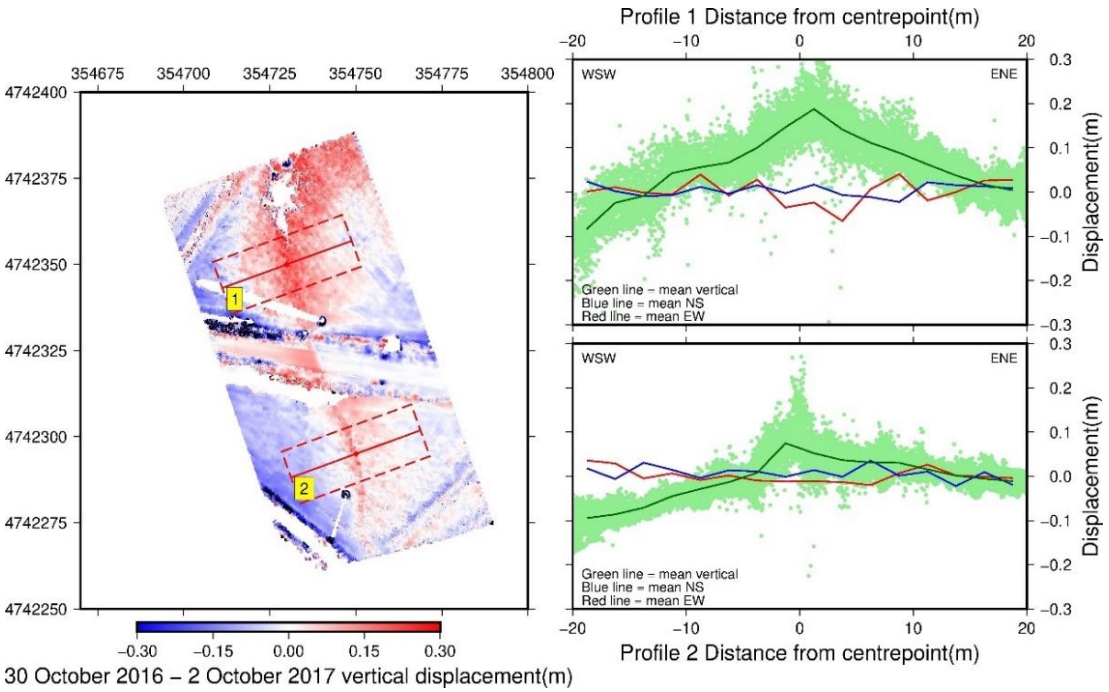

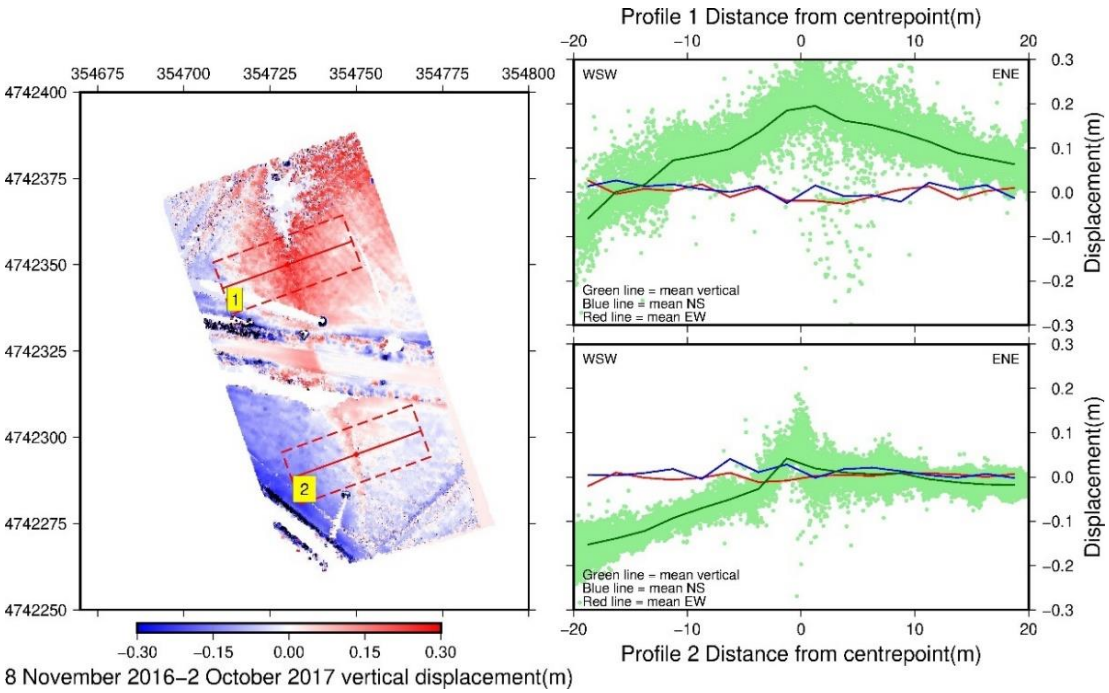

Figure 132: *Castelluccio Road site, 30th October 2016–2nd October 2017 (upper figure) and 8th November 2016–2nd October 2017 (lower figure): vertical displacement (LH panel) and profile across scarp, to north and south of road (upper and lower RH panels). RH panels description as in* ***Figure 131****.*

The next scan I have used was taken on 2nd October 2017. The horizontal displacements between either of the 2016 scans and the 2017 scan show no clear pattern. However, away from the road itself, the patterns shown in the vertical displacements are very similar to each other, with a band of relative vertical displacement along the lines of the scarp (hanging wall moving downwards overall relative to the footwall by ~10 cm, but with an upwards spike along the line of the scarp).

The displacement between the 30th October 2016 scan and the 2017 scan is shown in **Figure 132** (upper figures**)**, again by reference to profiles either side of the road. Given the length of the intervening period (which covers a full growing season), it seems very likely that the upward spike reflects levelling of the ground across the scarp to enable crop planting and harvesting. The equivalent profiles for the period 8 November 2016 to 2nd October 2017 are in **Figure 132** (lower figures)**.**

2017–2019

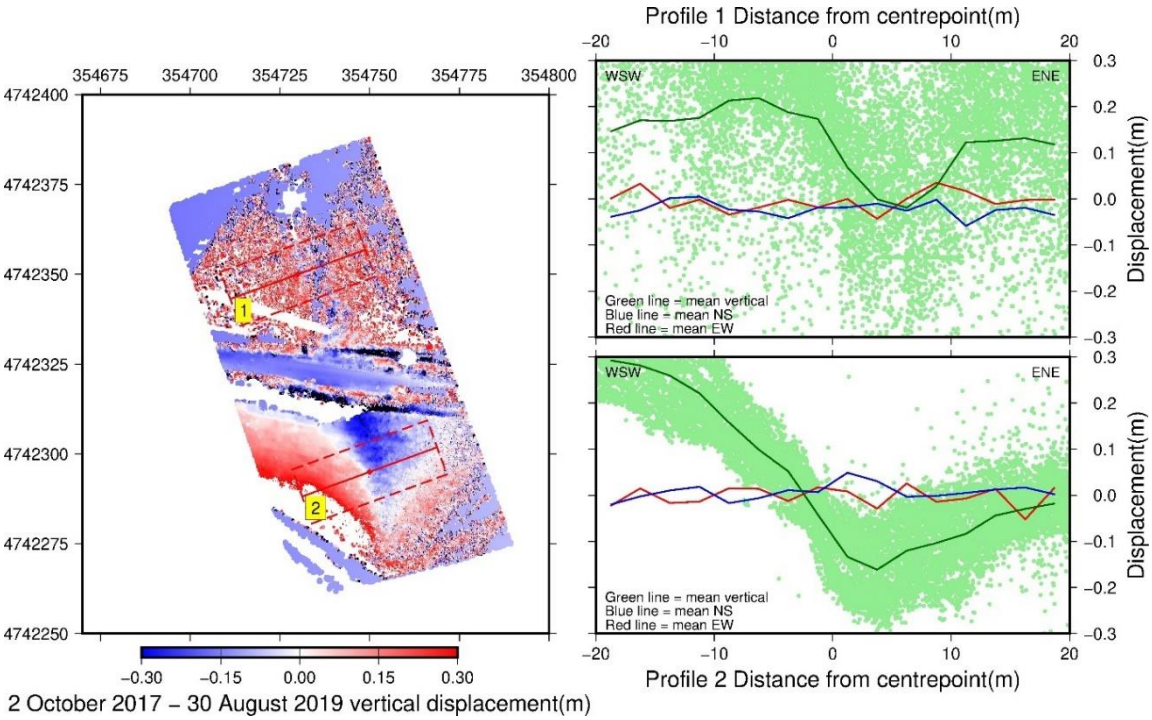

Figure 133: *Castelluccio Road site, 2nd October 2017–30th August 2019 vertical displacement (LH panel) and profile across scarp, to north and south of road (upper and lower RH panels). RH panels description as in* ***Figure 131****.*

The vertical displacements between 2017 and 2019 also appear to be heavily influenced by extraneous factors, probably the result of ploughing in the crop fields either side of the road to try to level the ground.

Horizontal displacements again show no clear pattern, but the vertical displacements show apparent relative uplift of ~20-30 cm in the hanging wall compared to the footwall, with a noticeable dip ~5 m to the east of the scarp in the footwall. **Figure 133** shows the results for the same profiles as above, for displacement between 2nd October 2017 and 30th August 2019.

5.4.3 Monte Vettore site

As explained above, the results for this site are limited here to a comparison between scans taken on 1st November 2016 and scans on 28th August 2019. Due to the presence of large tufts of coarse grass in many locations, both sets of data were filtered using a lowest points filter, before using the ICP algorithm.

Figure 134 shows the respective vertical and horizontal displacements between 2016 and 2019 as mean values over 5 m x 5 m squares. Note that there is a gap of a ~50 m x 15 m patch in the data in the hanging wall, broadly either side of latitude 4742000. This is due to the 2016 scans having been taken from an elevation which did not succeed fully in capturing the hanging wall.

The majority of the vertical displacement in the hanging wall is downwards (generally by ~2-10 cm). The largest of those values appears either under the part of the scarp where historically there seems to have been the largest offset (between scanner positions 1 and 2 in my field sketch, **Figure 120**), or in one location immediately adjacent to the scarp at the east end of the scarp section shown. There are, however, patches of upwards displacement in the hanging wall at the far northwest, immediately below the outcrop in the centre of the figure, and in the area further to the southeast. Those also coincide with horizontal displacement towards the southwest. At this scale, displacement shown on the near-vertical footwall is unlikely to be reliable. **Figure 135** shows the individual components of displacement, this time using median values over a 1 m x 1m grid.

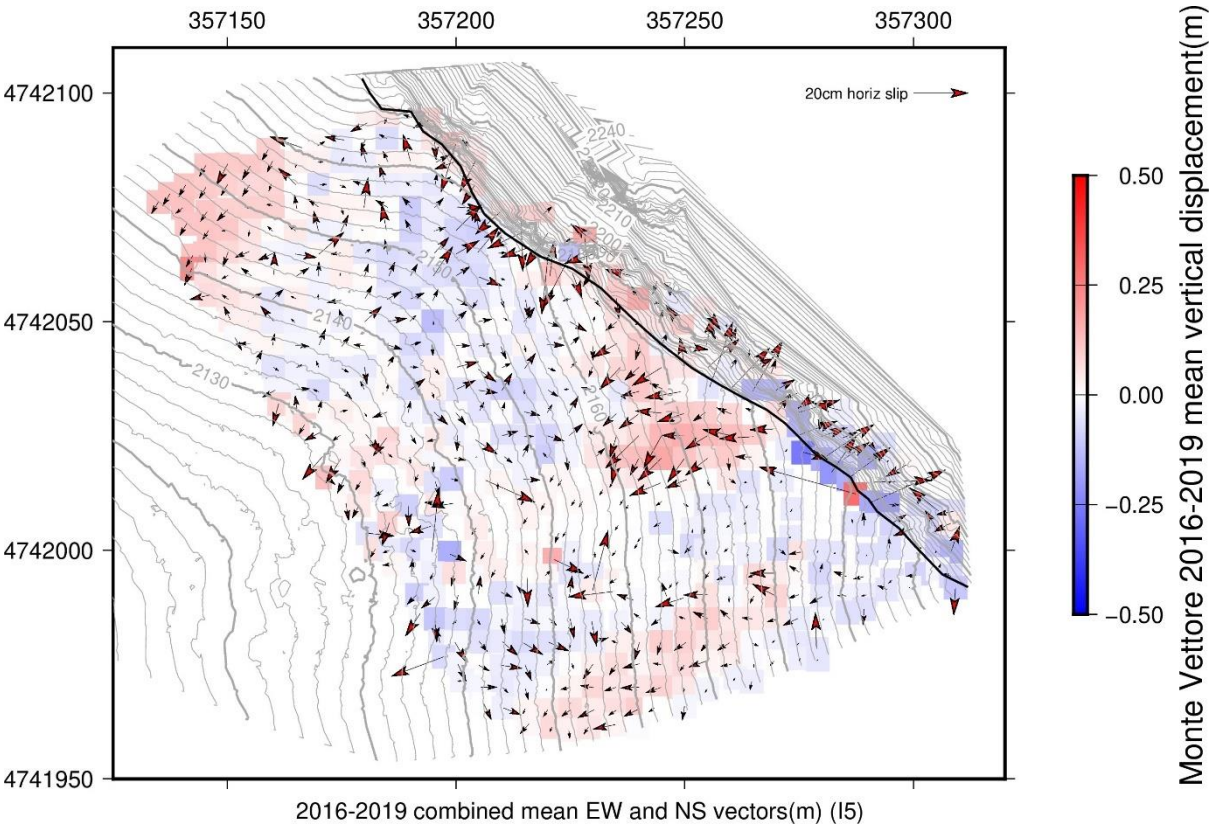

Figure 134: *Monte Vettore 2016–2019 combined mean horizontal displacements (arrows) set against a background of mean vertical displacement underlain by contours from by a DEM derived from the 2019 scans. Black line = estimated fault scarp line drawn in ArcGIS.*

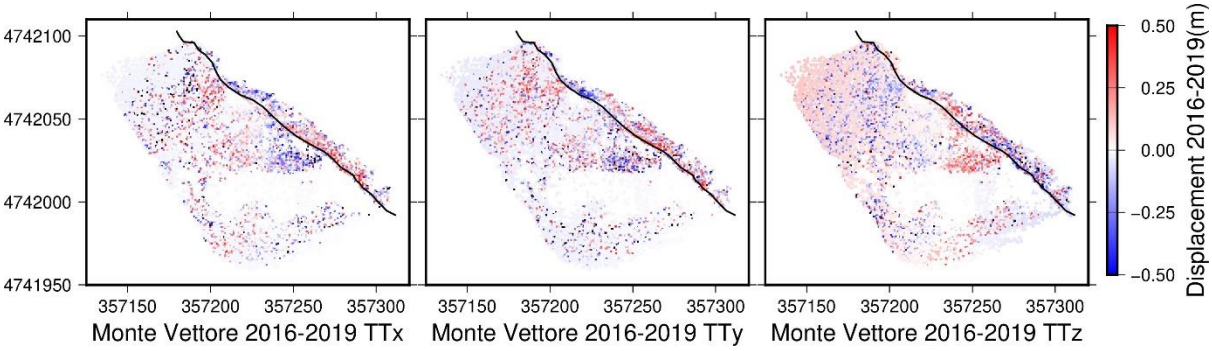

Figure 135: *Monte Vettore 2016–2019 post-seismic displacements in east-west (LH), north-south (centre) and vertical (RH) components, each median values on a 1 m x 1 m grid. Negative values for the LH and centre panels are west and south movement respectively.*

Figure 136 shows the vertical results from this Figure overlain on a plan view Google Earth image of the area. The upwards vertical patches in the hanging wall appear to coincide with areas of deposition of material from the footwall in the form of relatively light scree at either end of the figure, and more sizeable debris immediately below the outcrop in the centre of the figure.

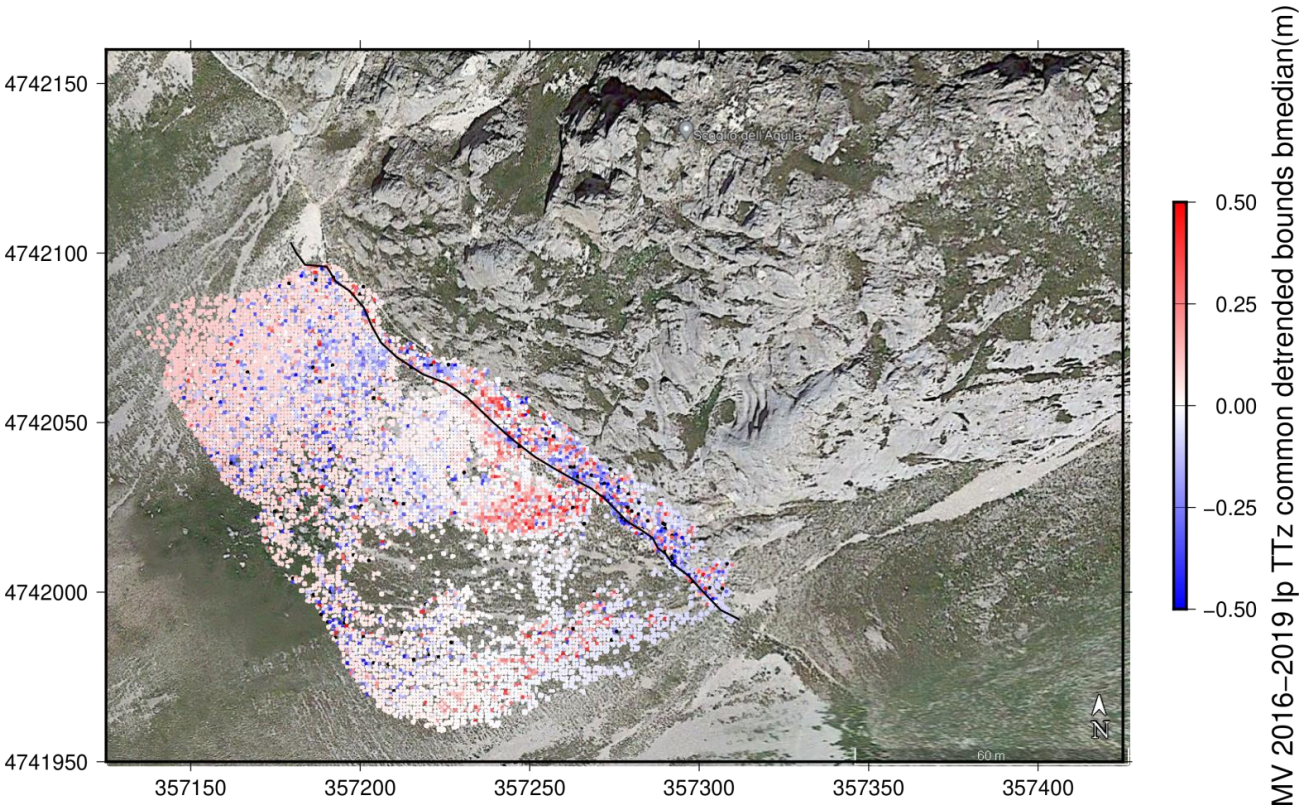

Figure 136: *Monte Vettore 2016–2019 vertical displacement results overlain on Google Earth image from 30 June 2020 of the Scoglio dell'Aquila outcrop and surrounding area.*

5.4.4 Vettore Road site

The majority of the topography of Vettore Road site has been influenced by man-made intervention. The road is tarmacked, and the down-slope side on the south has been built up to level the ground for the road foundations. The up-slope side is bedrock with some light scree, but has been excavated in the past to accommodate the width of the road. The results for the Vettore Road site differ depending upon whether they relate to the tarmacked road itself, or to its surroundings.

Oct 2016–Nov 2016

The observed displacement in the 7 days between the first 2 scans I have used from 2016 (30th October and 6th November) is largely vertical. This matches the more detailed findings by the University of Leeds team (Wedmore et al., 2017) who had also taken three scans in the intervening period. **Figure 137** shows a cross-section of their results from the road up to 6th November 2016.

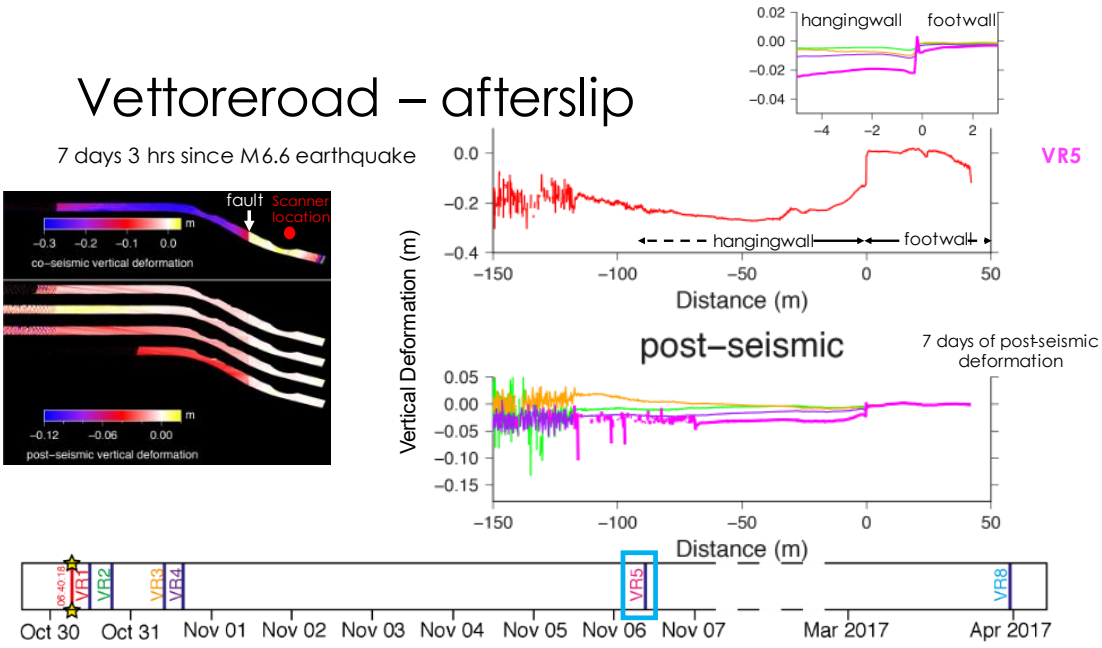

Figure 137: *Cumulative afterslip up to 6th November 2016 on the road section of the Vettore Road site, from Wedmore et al., 2017. The numbering e.g. "VR1" and "VR2" refers respectively to the first and second scans after the earthquake.*

In my results, the hanging wall side is displaced downwards relative to the footwall, but the displacement is greater (at ~6 cm) away from the road itself, and only ~ 1-2 cm on the road. On the road this vertical displacement is accompanied by a small degree of horizontal slip (~ 1-2 cm) towards ~270°. Away from the road on its south side where the ground is relatively flat the vertical slip is greater (~5 cm), and initially towards ~210°. Further away from the road at about the break in slope, slip is shown as being towards ~75°. **Figure 138** shows the various vectors in one figure, with median values over a 1 m x 1 m grid.

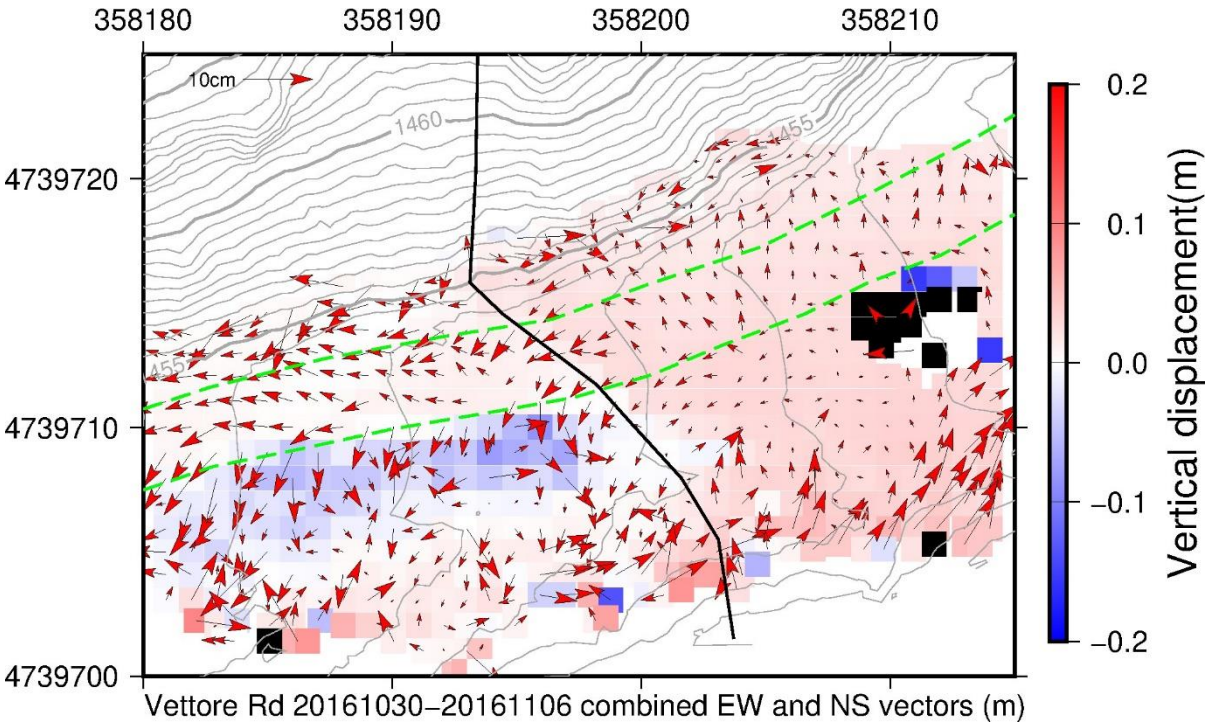

Figure 138: *Vettore Road 30th October 2016–6th November 2016 median displacement values in 1 m x 1 m grid, combined east-west and north-south vectors (arrows) set against background of vertical displacement and contours at 50 cm intervals from DEM derived from 2019 scans. Green dashed lines = approximate edges of road surface. Black line = estimated fault scarp line drawn in ArcGIS.*

The individual components of slip (without median filter) are shown in **Appendix 5**.

The anomalous values at far east of the figures are due to parked cars in the earlier scan.

2016–2017

The road was re-surfaced between 2016 and the scans on 3rd October 2017. This is reflected in the results for displacement between the two 2016 scans and the 2017 scan (**Figures 139** upper and lower panels respectively) with a small vertical increase of ~ 2 cm along the line of the scarp. However, in the unpaved area to the south of the road, the downwards movement of the hanging wall relative to the footwall continues with a further ~ 5 cm displacement, and horizontal movement of the hanging wall towards ~260/270°, particularly evident in the displacement relative to the later 2016 scan.

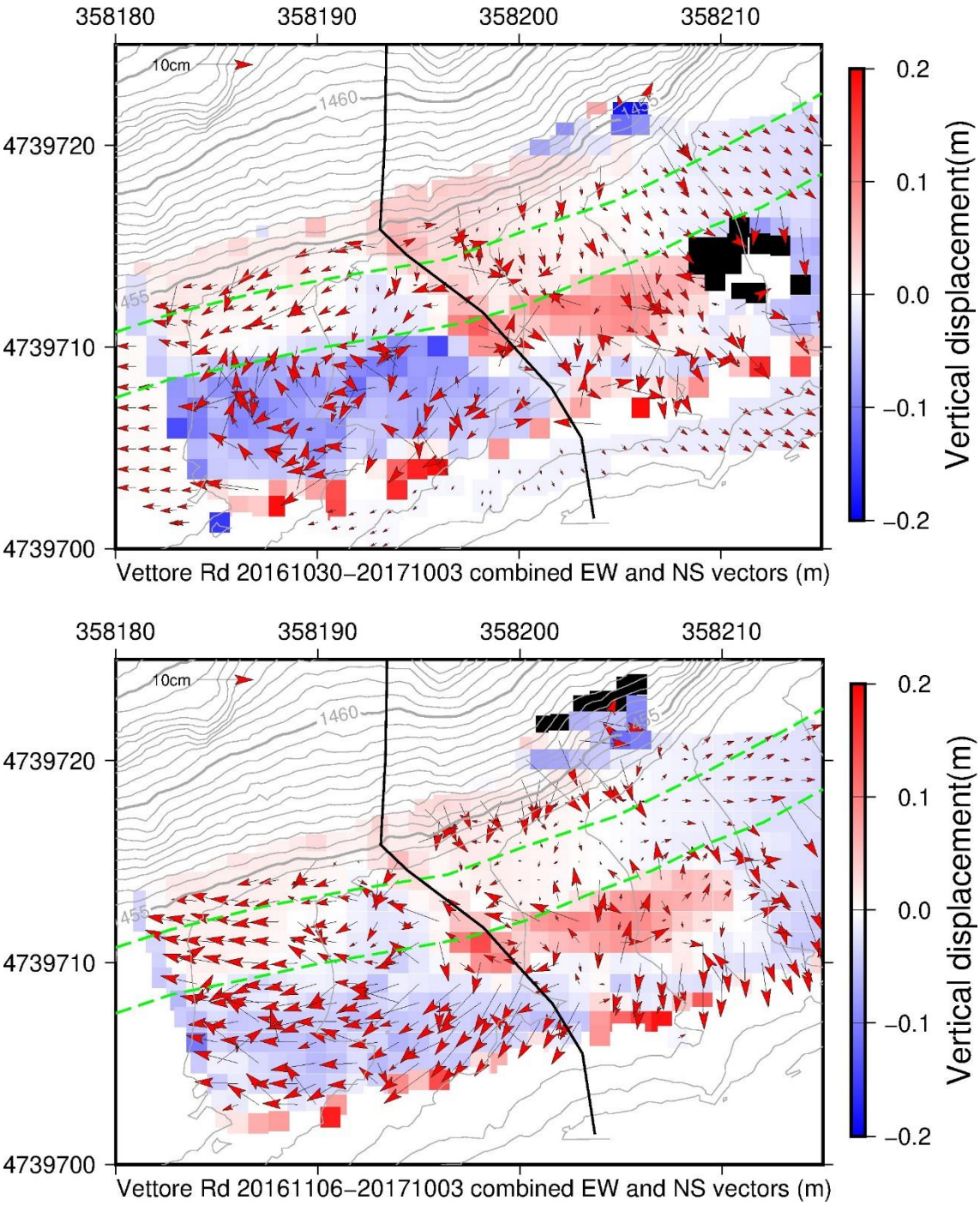

Figure 139: *Vettore Road 30th October 2016 (upper panel) and 6th November 2016 (lower panel)–3rd October 2017 median displacement values in 1 m x 1 m grid, combined east-west and north-south vectors (arrows) set against background of vertical displacement and contours at 50 cm intervals from DEM derived from 2019 scans. Green dashed lines = approximate edges of road surface. Black line = estimated fault scarp line drawn in ArcGIS.*

There may also be an accumulation of material where the land begins to fall away after the break in slope, although this may be an anomaly from processing scans which do not completely overlap.

2017–2019

The results for displacement between 2017 and the scans on 27th August 2019 (**Figure 140**) also show what appears to be further re-surfacing of the road (on our visit in 2019, it looked as though the road had been repatched twice, with further minor repairs since). As noted above, the results here are based on alignment of the scans within CloudCompare without the final, fine alignment step used elsewhere.

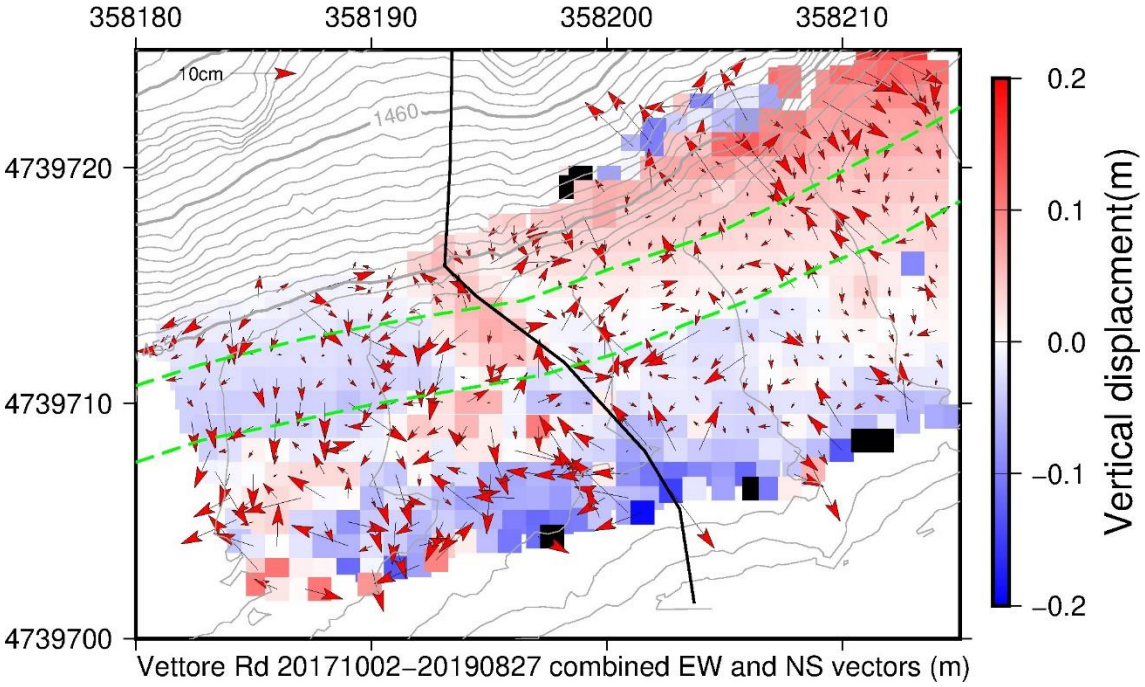

Figure 140: *Vettore Road 3rd October 2017–27th August 2019 median displacement values in 1 m x 1 m grid, combined east-west and north-south vectors (arrows) set against background of vertical displacement and contours at 50 cm intervals from DEM derived from 2019 scans. Green dashed lines = approximate edges of road surface. Black line = estimated fault scarp line drawn in ArcGIS.*

There appears to be a clear distinction on the road itself between the hanging wall and footwall side, with the hanging wall away from the repatching showing relative downward displacement of ~ 3-4 cm compared to the footwall side. Away from the

road itself, however, there does not appear to be the same distinction, with most of the hanging wall and footwall showing a small amount (< 5-10 cm) of downward displacement (although a small strip along the side of the road on the hanging wall side shows upwards vertical movement of ~ 2-3 cm). However, the area to the south of the road appears unstable. Even after the remedial works which had been carried out prior to my visit in May 2022, cracks were evident in this area and strengthening works had been carried out on this slope further west (see photographs in **Appendix 5**).

5.4.5 Bove Road site

Co-seismic deformation

The co-seismic displacements at the Bove Road site derived from scans immediately before and after the Norcia earthquake have been addressed in Wedmore et al., 2019. That study found across-fault vertical displacement of ~6 cm, and horizontal displacement of ~3-4 cm on a southwest-northeast axis.

My results for co-seismic displacement (using a smaller subset of the same scans) are essentially the same (**Figure 139**), although with slight discrepancies which are likely to be due to slightly differing alignment of the scans using CloudCompare.

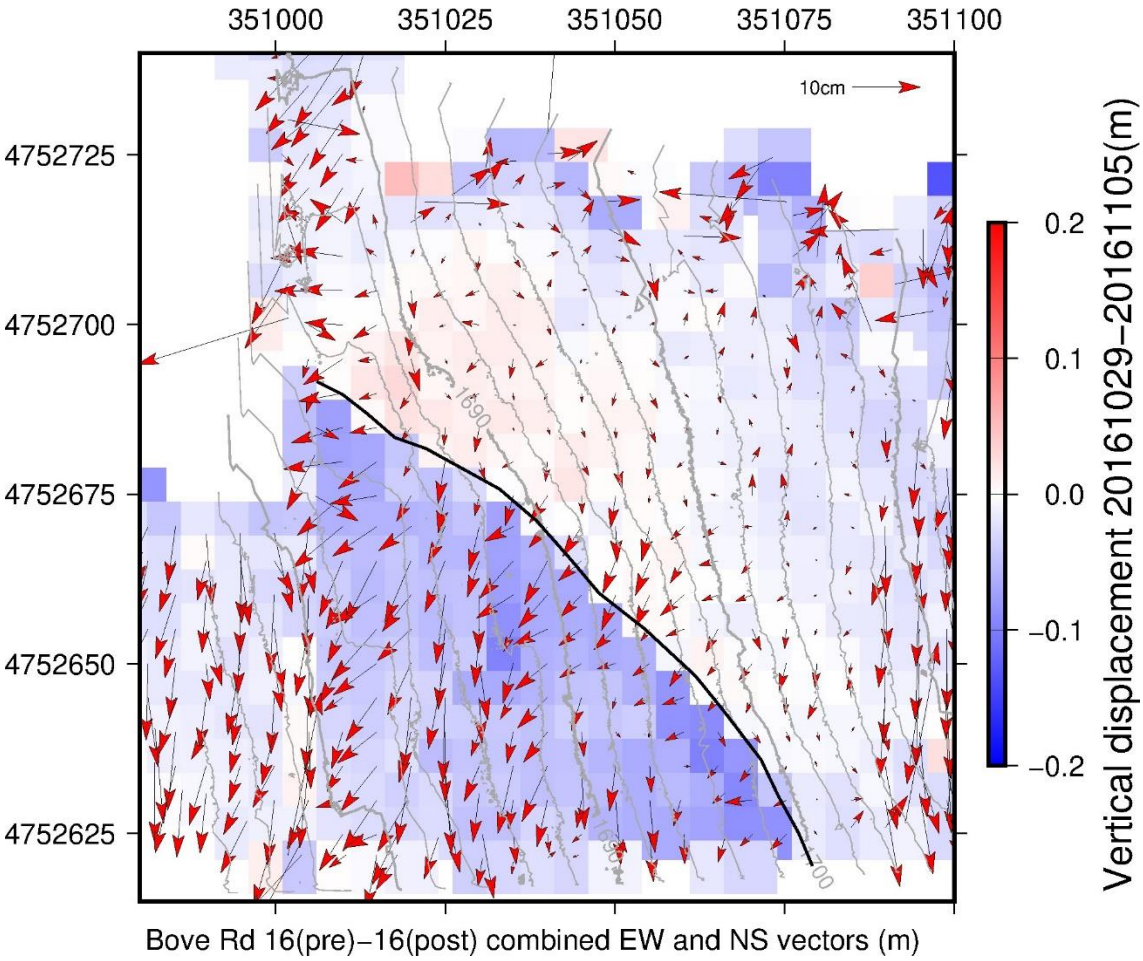

Figure 141: *Bove Road 29th October–5th November 2016 median co-seismic displacement values in 5 m x 5 m grid, combined east-west and north-south vectors (arrows) set against background of vertical displacement and contours at 2 m intervals from DEM derived from 2019 scans. Black line = estimated fault scarp line drawn in ArcGIS.*

2016–2017

The post-seismic displacement between 5th November 2016 and 2nd October 2017 shows little clear pattern (**Figure 142**). Aside from downwards vertical displacement of ~3-4 cm along some parts around the line of the scarp (including on the footwall side), there is an apparently linear patch of upwards vertical displacement of ~5-10 cm in the hanging wall at ~351030/4752630 UTM 33T. Horizontal displacement vectors show little consistency, and are in any event negligible.

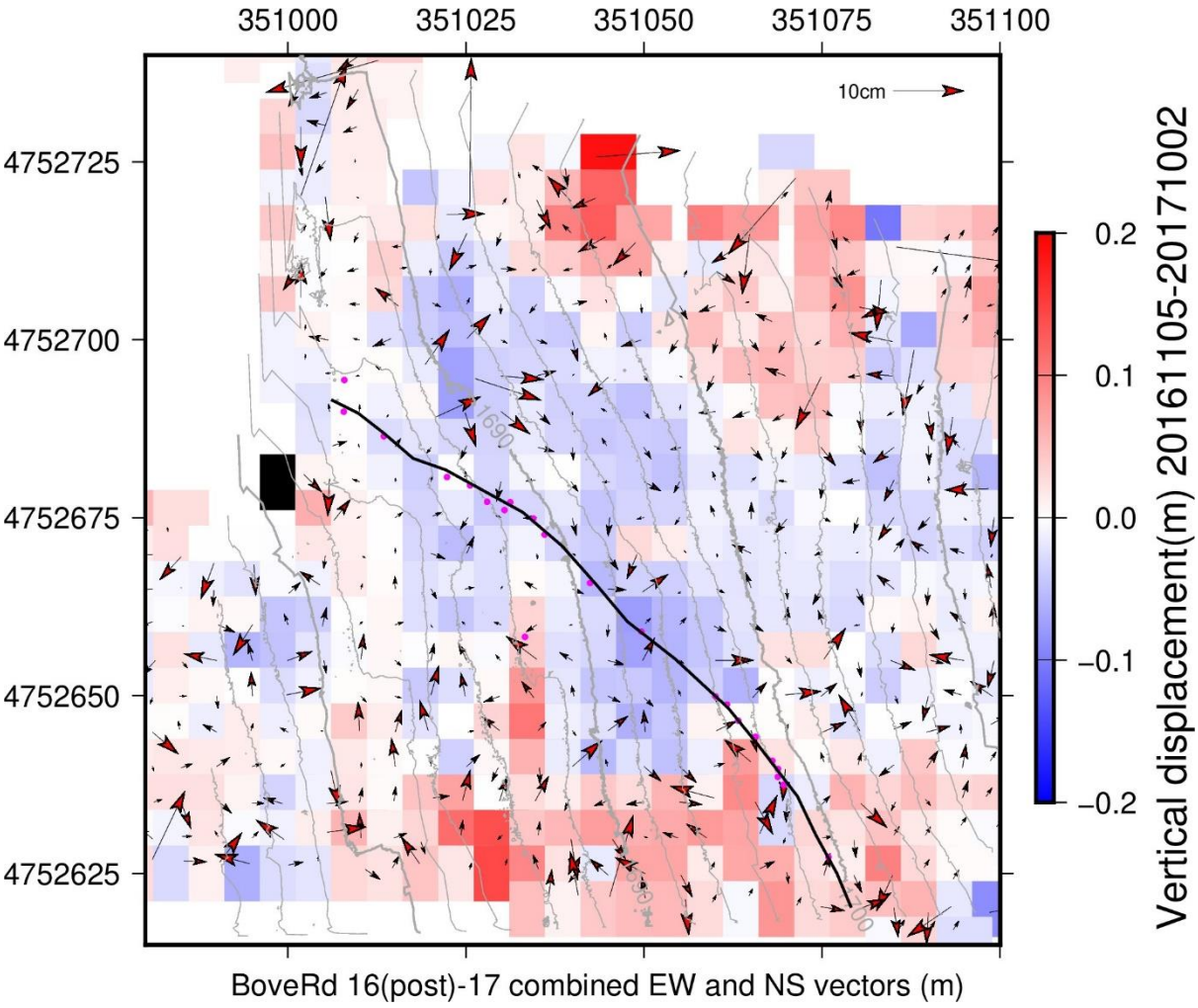

Figure 142: *Bove Road 5th November 2016–2nd October 2017 median displacement values in 5 m x 5 m grid, combined east-west and north-south vectors (arrows) set against background of vertical displacement and contours at 2 m intervals from DEM derived from 2019 scans. Black line = estimated fault scarp line drawn in ArcGIS.*

2017–2019

The results for displacement between 2nd October 2017 and 29th August 2019 show a upwards displacement in the hanging wall between the scarp and the road which is consistent with the 2016–2017 results for the same area (**Figure 143)**. There is also some relative downward displacement of ~ a few cm is seen along parts (but not all) of the line of the scarp.

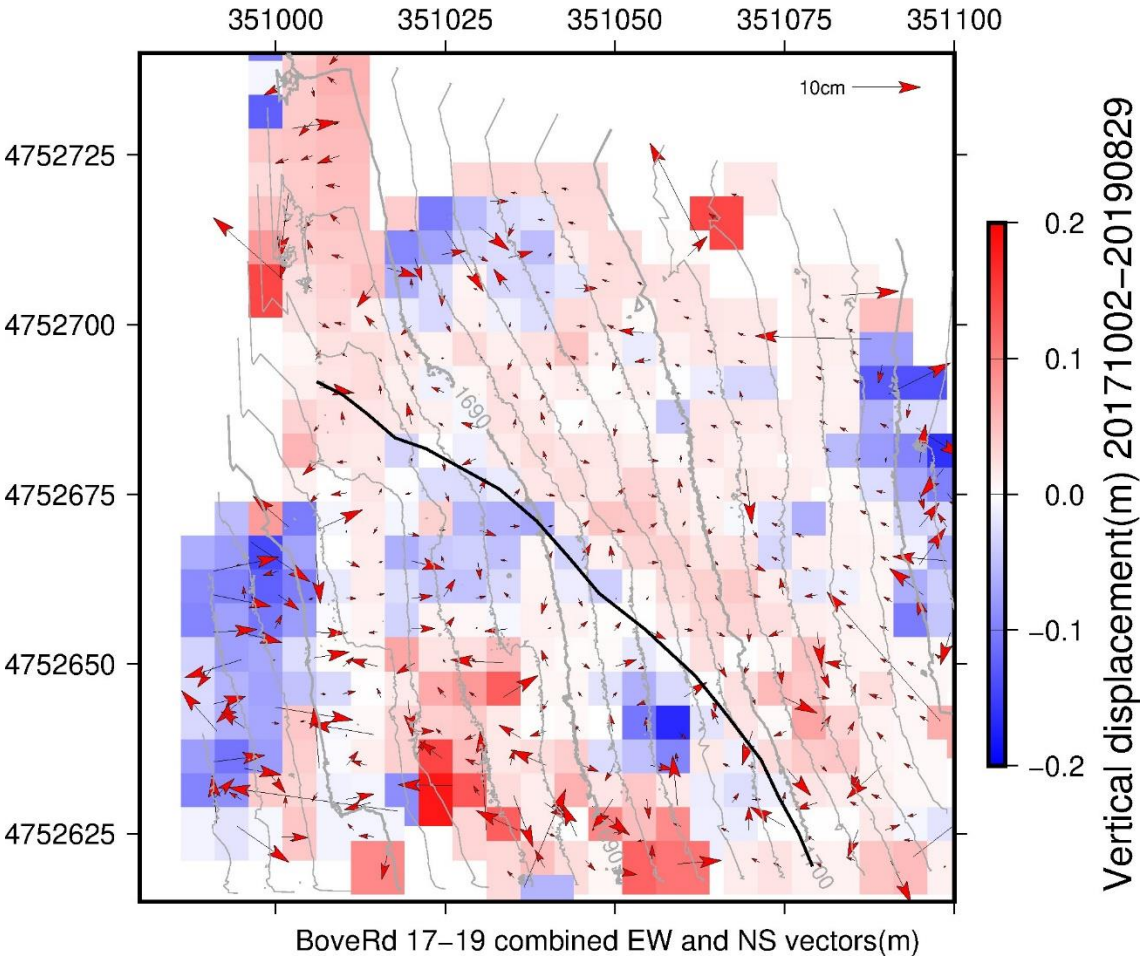

Figure 143: *Bove Road 2nd October 2017–29th August 2019 median displacement values in 5 m x 5 m grid, combined east-west and north-south vectors (arrows) set against background of vertical displacement and contours at 2 m intervals from DEM derived from 2019 scans. Black line = estimated fault scarp line drawn in ArcGIS.*

5.5 Discussion

5.5.1 Introduction

The possible causes of post-seismic deformation can be grouped broadly into two main parts: those related to the after-effects of the earthquake itself, and those which are external to the earthquake, such as erosion and gravity.

In the limited studies to date of post-seismic deformation associated with the Norcia earthquake (Pousse-Beltran et al., 2020 and Mandler et al., 2021), the effects of erosion and gravity were largely discounted as there was no clear link between the topography of the individual locations studied and the deformation observed for

gravity to be a significant factor (Pousse-Beltran et al., 2020). The timescales involved in the Pousse-Beltran et al., 2020 study (10 weeks after the Norcia earthquake) were also unlikely to be sufficient for erosion to be a significant factor on its own. In relation to post-tectonic seismic-related deformation, although poro-elastic effects were thought possibly to have played a part in triggering later shocks after the L'Aquila earthquake (Cheloni et al., 2010), poro-elastic rebound following the Norcia earthquake was also largely discounted (Pousse-Beltran et al., 2020 and Mandler et al., 2021). Afterslip was thought to be the predominant cause of post-seismic slip of some ~4-5 cm in two areas slightly to the southwest of the Vettore Road site and bounded by the OAST, and towards the west side of Pian Grande. That slip largely follows the predicted pattern of logarithmic decay over time (Pousse-Beltran et al., 2020, citing the models of Marone et al., 1991 and Zhou et al., 2018). Although generally thought to produce noticeable effects over a longer time scale and larger area, viscoelastic relaxation of the lower crust was not ruled out as a possible contributory mechanism (Mandler et al., 2021). In the case of the area bounded by the OAST, afterslip might have been triggered in response to heterogeneities in pore fluid pressure arising from the juxtaposition of differing rock units following the thrust event (Pousse-Beltran et al., 2020).

As noted in Chapter 4, the vertical and horizontal displacement seen at the Meterff site is largely consistent with initial afterslip and recovery of slip deficit on the Meterff scarp itself and possibly later displacement for the same reason on a possible associated structure to the northeast of the scarp. The extent of displacement decays with distance from the fault and over time. Modelling which incorporates a possible second structure suggests that most of the later post-seismic slip has been concentrated on the associated structure (rather than the Meterff fault itself), with slip vectors very similar to co-seismic slip vectors modelled for the same area. Slip had almost ceased by 2019 (although erosion continues to play a significant part in degradation of parts of the scarp site). Variations in vertical movement in the hanging wall may be spatially controlled by high gradients in co-seismic slip along the Meterff fault. Co-seismic deformation observed may not have been fully representative of the

true nature of the distributed faulting in the area, insofar as it did not reveal the presence of a possible neighbouring associated structure.

The Meterff site is, however, different in a number of respects from the other sites covered here:

- Overall tectonic setting. Meterff seems to be part of a relay structure, whereas the other sites are more directly either on the main Monte Vettore fault line (Monte Vettore and Vettore Road), or on synthetic (Castelluccio Road and Bove Road) or antithetic (Vettore Antithetic 1) structures in the hanging wall. The Vettore Road site has the additional possible complication of the neighbouring underlying OAST structure.
- Underlying geology. Meterff's underlying geology (Massive limestone), although similar to the Vettore Antithetic 1, Monte Vettore and Vettore Road sites, differs from the sites at Bove Road (Maiolica, more thinly bedded mictric limestone) and Castelluccio Road (unconsolidated fan deposits).
- Topography. Meterff's exposed hillside location has similarities to the Vettore Antithetic 1 site, and to a lesser extent the more elevated Monte Vettore and Bove Road sites but differs considerably from the relatively flat Castelluccio and Vettore Road sites.
- Co-seismic slip patterns. There are also significant differences between the sites in the extent and spatial heterogeneity of co-seismic slip.

How significant are these various differences between the sites in terms of the pattern, nature and extent of post-seismic slip?

5.5.2 Seismic-related slip

In the Meterff, Vettore Antithetic 1, Castelluccio Road and Vettore Road sites, at least some of the post-seismic slip appears to follow the expected after-slip pattern of continuing downwards movement of the hanging wall side relative to the footwall, which reduces in size over time and with distance from the fault. The models suggest that the decay in the rate of slip should be exponential over time (e.g. Marone et al., 1991, and Zhou et al., 2018). Other observations at this scale also show decay in the extent of slip with distance from the fault (e.g. Wilkinson et al., 2010 and 2012).

As noted in Chapter 4, the afterslip on the main Meterff fault scarp is consistent with exponential decay by way of afterslip, and reduces with distance in the hanging wall away from the scarp. In that site there is also a noticeable pattern of off-fault post-seismic deformation in the footwall to the scarp structure itself, but this seems to be an anomaly possibly due to its role as a relay site in the overall tectonic setting and/or due to a possible associated structure which may not have displaced co-seismically. Neither of those factors is seen elsewhere in these sites.

In the Vettore Antithetic 1 site, away from the far southeast end of the site where the deformation pattern seems to be heavily influenced by gravitational erosion, the relative vertical displacement between the 2016 and 2017 scans is ~ 3 cm either side of the scarp itself, and ~1-2 cm downwards further away in the hanging wall. The slip is greatest in the central portion of the scarp, with less slip seen towards the northwest (where co-seismic slip values recorded in the field were highest). A median profile across the central part of the scarp away from the crag shows that this vertical movement is accompanied by relative northeast-southwest horizontal displacement of ~ 2-3 cm within 2-3 m of the scarp (in other words, movement orthogonal to the scarp) (**Figure 144**).

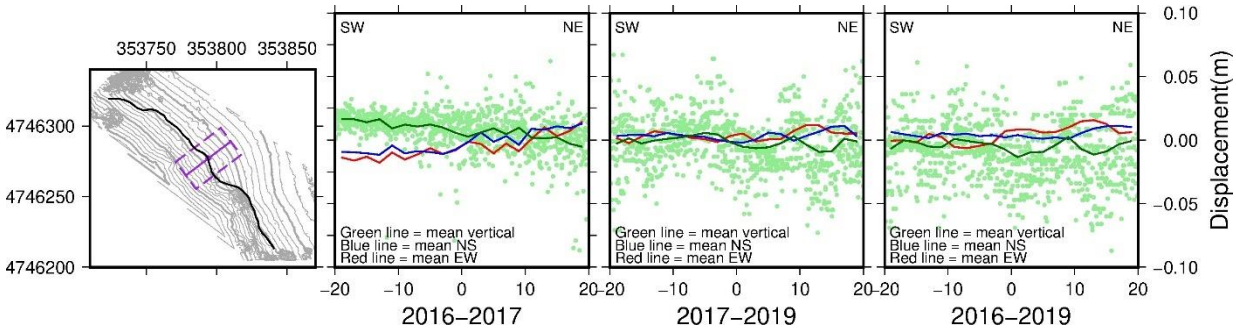

Figure 144: *Vettore Antithetic 1 site results showing displacement within 24 m wide 40 m long profile centred on fault scarp (purple box in LH panel), 2016–2017 (median), filtered 2017–2019 (median), and (for comparison) filtered 2016–2019 (median) results. The results panels show mean values for datapoints for east-west (red line), north-south (blue line) and vertical (green line). Green dots are vertical datapoints.*

Between 2017 and 2019, although the horizontal displacement pattern is repeated, there is little vertical movement. The recorded co-seismic slip at this part of the fault

scarp was ~50 cm. The differences suggest a high co-seismic slip gradient, with greater co-seismic slip deficit at the centre of the scarp than at the northwest end. The pattern of declining rates of post-seismic slip over time is consistent with an exponential decay curve. Afterslip appears largely to have stopped by 2019, which is probably a reflection of the relatively shallow depth of the antithetic structure, which is unlikely to have accumulated a significant amount of co-seismic slip deficit.

At the Monte Vettore site, although some of the displacement observed is apparently gravitational or erosional, there is also some post-seismic downward vertical displacement of the hanging wall of in the order of ~2-10 cm (against co-seismic deformation of up to ~> 2 m). As my results only contain one set of displacement values, it is not possible to say whether the post-seismic afterslip follows an exponential decay curve. The data suggest that slip is smaller with distance away from the fault in the area where there appears to be least gravitational effect (slip is ~ 8-9 cm within the first 2-3 m next to the scarp, and reduces to near-zero within 20 m). This relatively small amount of post-seismic slip on a major structure might reflect the lack of accumulated slip deficit on a structure which was activated at least twice in the CIES (although there was ~ 2 months between the earthquakes, this is unlikely to be long enough for there to have been a significant degree of healing – Marone et al., 1998a).

At the Castelluccio Road site, there appears to have been a combination of post-seismic slip and anthropogenic influence (probably in the form of seasonal ploughing) either side of the main road, with repeated wholescale re-surfacing making the road itself unsuitable to gauge displacement over the timescales of this study. The displacement observed away from the road appears different in pattern from the displacement seen on the other sites with an upwards spike along the line of the scarp in the 12 months following the earthquake, but that difference is probably explicable by agricultural processes. Away from those areas the respective footwall and hanging wall initially show little deviation. However, over time initial downwards vertical displacement of the hanging wall relative to the footwall of ~1 cm increased to up to ~10 cm 20 m away from the scarp, particularly south of the road. This seems consistent with afterslip from co-seismic slip deficit. By 2019 the signal was obscured, with the area west of the scarp being significantly uplifted, particularly north of the

road. It seems very likely that this displacement is anthropogenic in origin (probably by ploughing to level the fields).

At the Vettore Road site, the position is complicated by the different behaviour of the road and non-road surfaces, and the relatively unconsolidated nature of the road bed. Initial downwards movement of the hanging wall in a relatively small strip along the side of the road in the space of 7 days is followed by downthrow over the following year, over a wider area. Between 2017 and 2019 there is less movement, but the pattern seen in the first 7 days after the earthquake is effectively reversed, with upward movement in the hanging wall next to the road, and downwards movement further away. These changes are also accompanied by changes in the horizontal slip vectors. Horizontal movement in the footwall is mainly, but not exclusively, down slope.

I have analysed the stages of displacement on the road itself, using a short profile orthogonal to the fault scarp, and avoiding as far as possible the roadside surface (**Figure 145**).

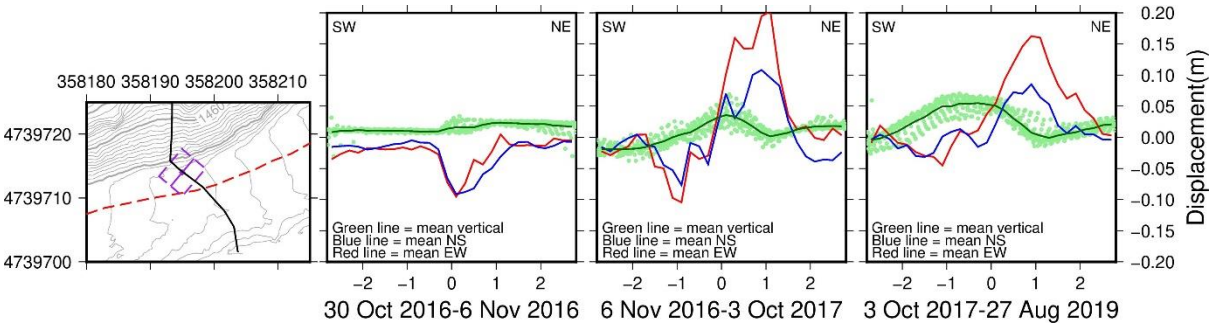

Figure 145: *Vettore Road displacement over time along a profile perpendicular to the fault scarp, over an area of 5.6 m x 4.8 m (location shown in RH panel (purple) against contours and road edge (dashed red line)). Results from left to right are 7 day period in 2016, 2016–2017 and 2017–2019. Green dots in main panels are vertical displacement data points, green line is mean of vertical displacement, red line mean of east-west displacement, blue line mean of north-south displacement.*

These results are heavily influenced by the re-surfacing work which has been carried out. However, away from the resurfacing (~> 2 m from the scarp), relative downwards vertical hanging wall displacement of ~ 1-2 cm over 7 days observed in 2016 is

followed by a further ~ 5 cm displacement between 2016 and 2017, and less than ~ 2 cm between 2017 and 2019. That pattern, at least, is consistent with the expected exponential decay curve. The roadside results may also seem to be reasonably consistent with exponential decay, but are likely to be complicated by a number of other factors, such as the effect of parked vehicles over at least part of the area, run-off of debris from the road, and some gravitational or erosional effects in unconsolidated ground.

5.5.3 The effect of factors external to seismicity

Although weathering and gravitational erosion is likely to play a role in the long term in relation to the geomorphology of the Meterff site, up to 2019 it did not appear to have played a significant part in the pattern of post-seismic surface deformation, except possibly in the run-off at the foot of the slope. There was some limited erosion in places along the line of the scarp, which can perhaps be explained by the disruption caused by the earthquake, and exposure of new surfaces which may then be more prone to erosion. However, on my return visit in May 2022 it was apparent that erosion had become a significant factor in degradation of the scarp in many areas. It is possible that this may in turn have reflected some deeper-seated mass wasting, as in Huang et al., 2017 although as the effects to seem to have been relatively localised this explanation may be unlikely, and surface erosion through weathering and gravity appears the more likely reason.

In the other sites erosional factors appear to have played a significant part from the outset.

In the Vettore Antithetic 1 site, the footwall of the southern-most section of the scarp appears to be relatively unstable compared to the rest of the footwall due to its steepness. Co-seismic measurements almost exclusively describe the terrain as “debris”. Over even a relatively short period of time, the consequence of this instability seems to have been the accumulation of large-scale scree or detached rocks which (in differential TLS results shown as mean values over 5 m x 5 m areas) together create a misleading impression of upwards vertical movement of the hanging wall relative to the footwall, particularly since 2017. A comparison of the area involved, using Google

Earth images from May 2016 and June 2020 suggests that at least some of the debris in this area pre-dated the CIES (**Figure 146**).

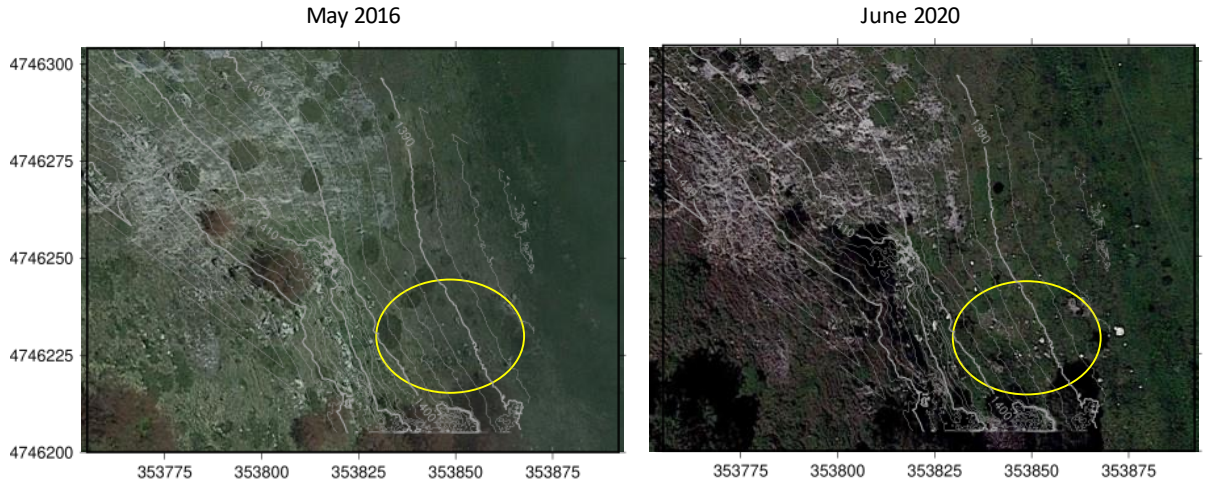

Figure 146: *Google Earth images from May 2016 (LH) and June 2020 (RH) showing in yellow circles area apparent area of larger debris deposition, with contours overlaid from 2nd November 2016 TLS-derived DEM.*

On my visit to the site in May 2021 it was apparent that large segments of rock > 20 cm x 20 cm and up to at least ~50 cm x 50 cm had recently become detached from the outcrop and the footwall immediately next to it (see photographs in **Appendix 5**).

The amount of material deposited post-seismically between 2016 and 2017 was very limited (~1- 2cm at a couple of areas between 6 and 10 m from the Vettore Antithetic 1 scarp). Presumably most loose material had been dislodged co-seismically. Between 2017 and 2019 debris was accumulated over a wider area (up to ~ 20 m from the scarp), with up to 3 cm accumulating in the area ~ 6 m from the scarp (see profile in **Figure 147**). The profile suggests that the footwall is eroding immediately next to the scarp (which is borne out by my field photos from May 2022 – **Appendix 5B**).

Given this apparent increase in the rate of accumulation in this period and the probable presence of similar debris before the CIES it is unlikely that the process is one associated with afterslip. The cause of the increase appears to be larger scree or debris becoming detached from the steep footwall and adding to the material already present.

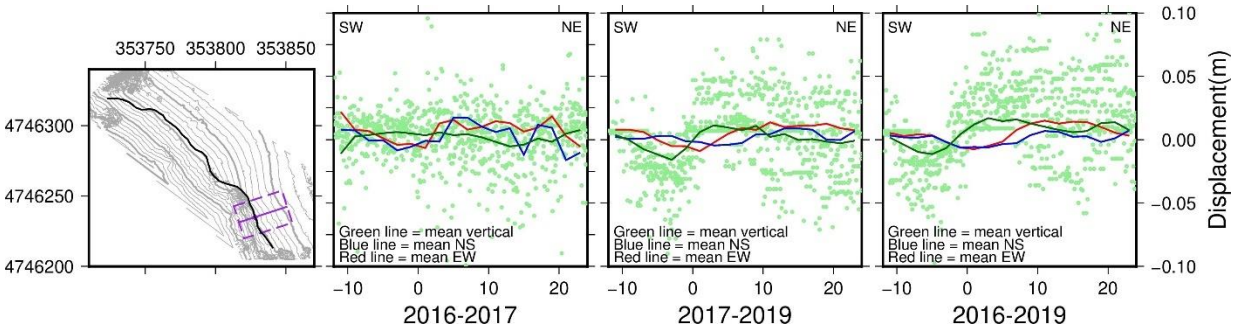

Figure 147: *Vettore Antithetic 1 site results showing displacement within 24 m wide 36 m long profile centred on fault scarp below outcrop (purple box in LH panel), 2016–2017 (median), 2017–2019 (median), and (for comparison) filtered 2016–2019 (median) results. In the results panels mean values for datapoints for east-west (red line), north-south (blue line) and vertical (green line). Green dots are vertical datapoints.*

Away from the outcrop, other areas of the scarp are now showing signs of rapid degeneration through erosion (see photographs in **Appendix 5B**).

The combined processes of weathering and gravitational erosion also seem to be significantly affecting the Monte Vettore site, with material eroded from the very steep footwall side, depositing large-scale scree and boulders on the hanging wall side in three distinct areas. Given the very steep, elevated and exposed position of the main Scoglio dell'Aquila outcrop, such erosion would be expected even without the after-effects of the Norcia earthquake. Two of the depositional sites (at the far north and south of the area studied) involve smaller scale scree deposited over distances of at least 50-60 m from the scarp, with channels eroded well into the footwall either side of the main Scoglio dell'Aquila outcrop. In the third area, immediately below the Scoglio dell'Aquila outcrop the debris is larger in size, but does not appear to extend out from the scarp to the same extent (perhaps because it is less easily moved from its initial resting place due to its mass). Although it is difficult to disentangle the ongoing erosional processes from the tectonic effects of the Norcia earthquake, there does not appear to be any obvious reason to attribute the build-up of smaller scree to degradation of the scarp. The scree seems to come from further up the footwall. It is

probable, though, that at least some of the larger material immediately below the main Scoglio dell'Aquila outcrop in the centre of the site was dislodged co-seismically by the disturbance created by the earthquake (although, of course, this would not show up in the post-seismic results).

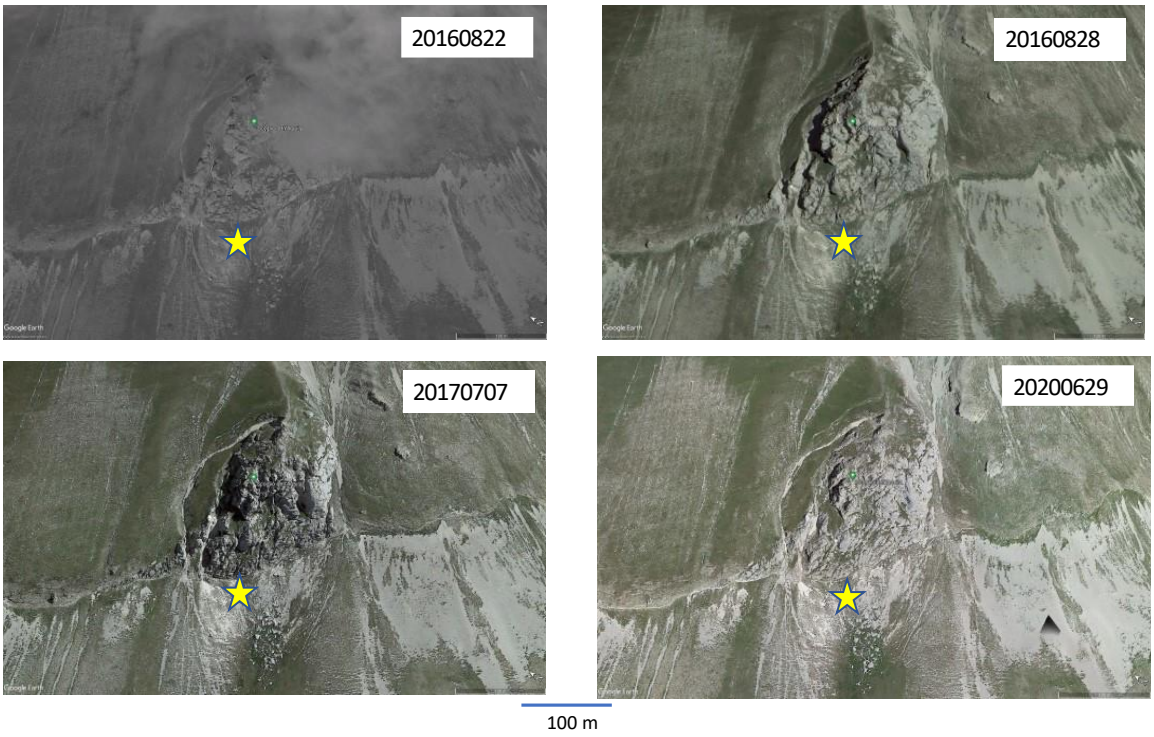

Figure 148: *Google Earth historical images of Scoglio dell'Aquila, taken ~vertically, looking northeast, images from 22nd August 2016 (TL), 28th August 2016 (TR), 7th July 2017 (LL) and 29th June 2020 (LR). Location of yellow star is ~UTM 33T 357151/4742078.*

A visual comparison of historical Google Earth images over time (**Figure 148**) suggests that the pattern of deposition observed in 2019 was already established before the Amatrice earthquake on 24th August 2016, and has not changed significantly over time (although the pre-Amatrice earthquake image is partially obscured by cloud). Therefore, if there is any contribution to erosion due to the effects of the Norcia earthquake, it is likely to be secondary to ongoing processes outside the tectonic cycle.

A similar visual comparison between higher resolution (50 cm) Pleiades optical satellite images from either side of the Norcia earthquake (**Figure 149**) also suggests little co-seismic change in the overall location and extent of debris on the hanging wall

(although local movement would undoubtedly have occurred, give the scale of co-seismic displacement in this area).

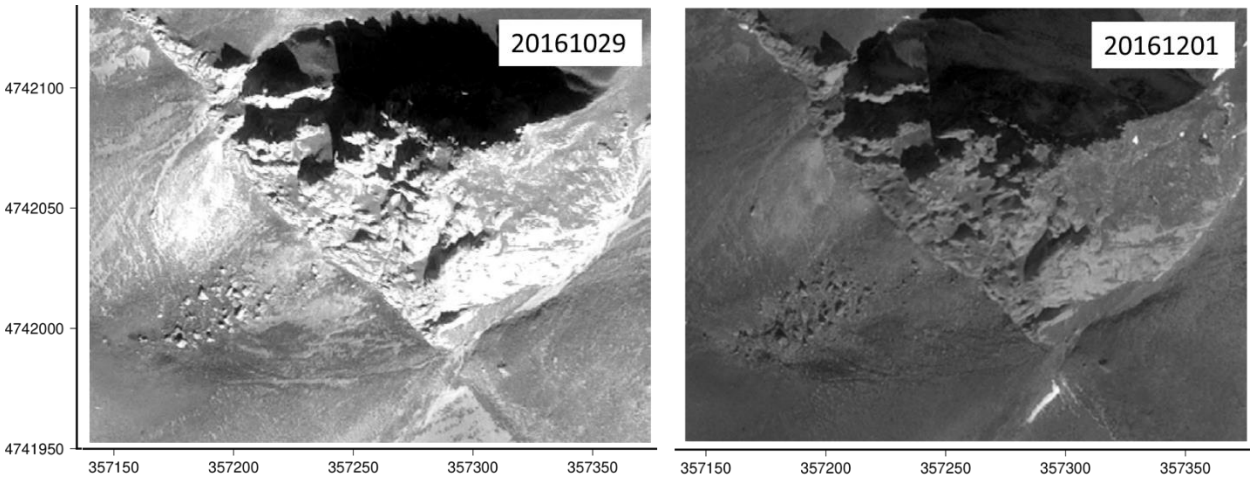

Figure 149: *Monte Vettore site - Pleiades optical satellite images from 29th October 2016 and 1st December 2016 respectively.*

A third site where erosion appears to have played a significant role in post-seismic deformation is the Bove Road site. The co-seismic slip appears to follow a regular pattern, with downwards and southwest relative displacement of the hanging wall largely uniform along the scarp. However, rather than an afterslip pattern of downward displacement on the hanging wall side, there is instead general and patchy degradation along the line of the scarp, and an apparent accumulation of material in a hollow between the scarp and the gravel track. Given that the site also ruptured during the Visso earthquake, it is unlikely that there was a significant element of co-seismic slip deficit, and this degradation appears to be erosional in origin.

Figure 150 shows the post-seismic vertical displacement over time either side of the fault scarp using median values, with displacement spread over ~2-3 m either side of the scarp. In this case, much of the displacement near to the scarp itself takes place in the first 12 months after the earthquake. More recently erosion has taken place ~10 m away from the scarp in the hanging wall, with an accumulation of up to ~5 cm of material at ~20 m to the southwest of the scarp.

By the time of my visit in May 2022, the scarp itself was becoming indistinct, and much of the accumulation of material on the hanging side of the scarp appeared to be

derived from erosion of bedrock (presumably the newer Fucoid Marl unit, rather than the footwall Maiolica unit) in blockier fragments within the hanging wall itself at ~10 m from the scarp line (see photographs in **Appendix 5**).

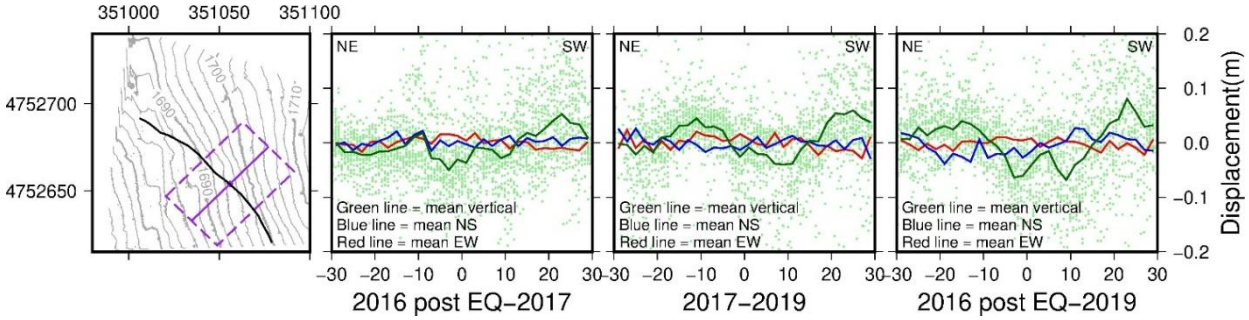

Figure 150: *Bove Road site results showing post-seismic displacement within 40 m wide 60 m long profile centred on fault scarp (purple box in LH panel), 2016–2017, 2017–2019 and (for comparison) 2016–2019 median results. In the results panels mean values for datapoints for east-west (red line), north-south (blue line) and vertical (green line). Green dots are vertical datapoints.*

Whilst erosion due to weathering and gravitational effects may be a natural result of an elevated and exposed site on a steep hillside (e.g. Kokkalas and Koukouvelas, 2005), perhaps exacerbated by freeze-thaw (e.g. Wallace, 1977), there are two other potential factors which may be at play. One is that the underlying bedrock geology (Maiolica, micritic limestone in thin-medium beds) is different to the geology in the other sites (principally Massive Limestone), and perhaps more susceptible to weathering erosion due to the increased percentage of rock area exposed to the elements. The other is that the area is part of a ski resort, and at least part of the scarp area is within an area which will be traversed in winter by skiers descending to lower slopes, which may add to erosion, particularly where there is a new, small step in the slope in the form of a scarp.

There is also some evidence of possible gravitational effect in the case of the Vettore Road site, where there appears to be an element of deposition of material down slope from the road verge. This needs to be treated with caution as it is at the edge of the area covered by the scans, and although apparent in most of the results up to 2017, it does not appear in the 2017–2019 results. Nevertheless, as the slope immediately

adjacent to the road is made up of unconsolidated material built up in support of the road foundations, some gravitational displacement would be expected over time (and was clearly apparent by 2022 – see photographs in **Appendix 5**).

5.5.4 The balance of factors across the sites

It is unsurprising in an elevated mountainous area with pronounced steep topography that gravitational and weathering erosion plays a significant role in scarp degradation (Wallace 1977). Although not necessarily evident from the scans themselves in the ~3 year period since the Norcia earthquake, the rate at which scarps visibly appear to be eroding at the Meterff, Vettore Antithetic 1 and Bove Road sites in particular by the time of my visit in May 2022 suggests that there will be little coherent evidence left of the Norcia earthquake at those sites within ~10-20 years (the lower end of the time frame suggested in Quigley et al. 2011). As that study observes, this is one of the consequences of the wide distribution of slip at shallow depths (as is expected to be the case in relatively immature continental earthquake zones, e.g. Milliner et al., 2016, Teran et al., 2015, Gold et al., 2021). Erosion is already a factor to be taken into account in assessing the reliability of individual scarps as evidence, but will be a significant factor in the future in the overall assessment of co-seismic slip. If the widely distributed nature of co-seismic slip is no longer apparent in the evidence preserved in the landscape, then concentrating solely on the "highlights" which remain visible will result in a very distorted picture of co-seismic slip in the future.

By comparison, the effects of afterslip in these locations are both relatively short-lived and restrained. Where it is apparent, the afterslip seems largely localised within a few metres of the scarp, and at values which represent a small fraction of the co-seismic slip. Even at sites such as Meterff where there seems to have been a steep co-seismic slip gradient between the upper and lower parts of the scarp, the post-seismic slip on the lower part (which saw much less slip (at < ~ 10 cm) than the upper part (up to 1 m)) was no more than a few cms at most, and appears to have stopped by 2019. Meterff did not apparently rupture during the previous CIES earthquakes, and would perhaps be a site where (proportionately) the most post-seismic slip might be expected. The same applies to the Vettore Antithetic 1 site. Despite not previously rupturing, although co-seismic offset was recorded at > 50 cm in places, the post-

seismic slip is no more than up to ~5 cm, and again appears to have stopped by 2019. In both cases fault geometry is likely to play a role in limiting afterslip. Meterff seems to be part of a relay structure, and is unlikely to extend significantly below the surface. Vettore Antithetic 1 is likely to be a steeply dipping splay originating at relatively shallow depth from a less steeply-dipping synthetic hanging wall structure.

Although difficult to compare directly as the timescales and co-seismic displacement are different, the displacements observed at the Meterff and Vettore Antithetic 1 sites seem to be broadly consistent with the relative magnitude of post-seismic slip observed in relation to the 2009 L'Aquila earthquake (Wilkinson et al., 2012). In that case, where there had been no preceding rupture, at the site with the largest displacement (site PAG) co-seismic vertical displacement of ~7.5 cm was followed by post-seismic afterslip of ~1.5 cm over ~124 days. At other L'Aquila sites, co-seismic horizontal displacement of ~0.2-0.5 cm (with no vertical component) was followed by vertical afterslip of ~1.3 cm and 1.1 cm together with observed subsidence of the hanging wall trough (sites SP and EP) (ibid).

The afterslip on the Monte Vettore site of possibly up to ~ 10 cm is slightly greater in overall magnitude than at the other sites, but that itself is a small fraction of the co-seismic offset of up to ~2 m seen in that area. The results at that site are in any event masked to some extent by the extensive erosion. As the site also ruptured during the Amatrice earthquake, it is arguable that it is unlikely that there would be a significant degree of co-seismic slip deficit unless the intervening 2 month period was sufficient for the fault to heal/strengthen. At the Bove Road site, the same explanation about previous slip probably applies. There, the ground was ruptured during the Visso earthquake 4 days prior to the Norcia earthquake. Although slip is seen clearly in the co-seismic results, it is difficult to make out a convincing case for any post-seismic degradation at the Bove Road site being of seismic origin.

Therefore, in these sites, although afterslip plays a limited role in the post-seismic development of deformation in the near-fault area, that is comparatively limited. Within 3 years after the Norcia earthquake erosional factors are already important, and will become increasingly so as time passes.

5.5.5 Repeatability of the processing steps

I had hoped in analysing the data across the various sites to be able to derive a single, repeatable process which could be followed in every case, refining the methods used elsewhere to measure deformation using repeat TLS (e.g. Wilkinson et al., 2012 and Wedmore et al., 2019) to take account of extended time periods and the scale and nature of deformation over time. I anticipated that the relatively straight-forward case of co-seismic or immediate post-seismic deformation would need adaptation to cope with smaller scales, less reliable duplication between data collection, and intervening non-seismic-related factors such as erosion. Ultimately, the differences between the various sites and datasets and the challenges those have posed have meant that I have had to develop what could be described as a suite of possible variations around a core set of guidelines. For example, it has become apparent that the "ideal" method of finely aligning scans using a fixed sample patch in the footwall as a reference point for registration of a whole scan before differencing does not work well when the footwall itself degrades over time (such as over a winter in a steep, exposed mountain setting such as the Meterff site). This is the case even if the scale of the degradation is not large, as small scale changes over a limited area are magnified when applied across a larger scan area. Similarly, the choice of filtering techniques used will vary according to the nature of the sites and the quality of the data. Low point filtering to remove seasonal vegetation can remove much of the underlying data and I have only used it sparingly. My recursive filter provides an effective solution to denoise data which have excessive noise which seems related to the quality of the data coverage, but is not necessary in every case where the data is less noisy. Nevertheless, if the various alternative techniques discussed are used with appropriate caution, I believe that my "suite" of possible variations provides a reliable and repeatable method of deriving cm-scale deformation over time using repeat TLS.

5.6 Conclusion

A comparison of the post-seismic deformation at the 6 sites reviewed in this study shows a variety of post-seismic responses. Each of those seems to be governed primarily by factors specific to that site. Although this means that there are relatively few common factors which will be applicable in every case, it highlights the need to

adopt a holistic approach looking at both co-seismic slip distribution (where possible) and individual site characteristics in assessing the reliability of any individual fault scarp as evidence of previous slip history.

Within the 6 sites, the Meterff site may be unusual in that its post-seismic deformation patterns possibly reveal the presence of a structure which was not apparent from the co-seismic evidence of surface ruptures. In doing so, it might raise the question of whether the co-seismic evidence in the form of surface ruptures is an accurate representation of the extent and nature of co-seismic slip distribution. However, in this particular instance, the evidence is not wholly convincing and the area seems to be part of a relay zone that is likely to involve particularly complex kinematics, suggesting that caution is needed in drawing any wider conclusions.

In other respects, post-seismic deformation on the Meterff scarp is consistent with afterslip decaying over time and distance, with co-seismic slip gradients producing differing results along strike and erosion paying little or no role in the first couple of years. However, erosion is now clearly the dominant factor, with afterslip having apparently ceased by 2019.

Post-seismic deformation on the Vettore Antithetic 1 fault away from the area of the prominent outcrop is also consistent with time-limited exponential afterslip, with modelled vectors of near-surface slip consistent with the recovery of co-seismic slip deficit. However, in the area below and to the east of the outcrop the results show the effect of gravitational/possibly weathering erosion, likely due to differences in competency in the footwall and/or the steepness of the slope, and probably initially pre-dating the Norcia earthquake.

The Monte Vettore fault site also exhibits a mixture of afterslip and gravitational/weathering erosion. The afterslip pattern is difficult to isolate as the erosional effects are more pronounced, but its main effects appear to be limited to one area only, possibly the result of high co-seismic slip gradients influenced by changes in fault geometry. This scarp ruptured in both the Norcia and Amatrice earthquakes. Therefore, accumulated slip deficit is likely to be very limited in scale compared to the size of co-seismic deformation. The afterslip pattern appears to show

greater deformation near the fault (as expected). There is clearer evidence of post-seismic erosion at the Monte Vettore site, but this is consistent with a pattern of erosion which pre-dated either earthquake, suggesting that the effects of the earthquake on erosion are limited in scale.

Disregarding the apparent uplift close to the scarp at the Castelluccio Road site between 2016 and 2017 as deriving from anthropogenic activity, the slip further away in the hanging wall appears a more reliable indicator of afterslip through recovery of co-seismic slip deficit.

Post-seismic deformation at the Vettore Road site is probably consistent with afterslip, with exponential decay (as seen either side of the repaired road section). However, the picture at that site is complicated by its largely man-made nature.

The post-seismic deformation at the Bove Road site is almost exclusively erosional. At this site there are perhaps more complicated reasons for the erosion, including possibly disturbance of relatively incompetent rock due to the earthquake (as displacement has slowed over time), allied to weathering and human factors.

In summary, in using fault scarps as evidence of previous seismic slip history, the results from these sites show firstly a need to select sites carefully to avoid extraneous factors unrelated to natural processes (such as human activity), and secondly a need to assess carefully the mixture of geology, topography, size distribution and nature of co-seismic slip, and other site specific factors in order to better understand the processes which have operated on any fault scarp since previous tectonic activity, and which may affect its reliability as evidence of co-seismic slip. Geology itself can bring a variety of different influences to bear, such as the location and extent of the damage zone and fault gouge, which can in turn result in localised fluid flow patterns. The interrelation of faults to one another and their intersections will also significantly impact both co-seismic and post-seismic deformation patterns.

The results show that fault scarps are potentially unreliable as evidence of previous co-seismic slip history. Although the results suggest that afterslip patterns are consistent with the expected pattern of exponential decay over time, quantifying the extent of

that unreliability over an extended area and extended time period will be a considerable challenge, which is beyond the scope of this thesis (and possibly beyond the limits of the technology used here). The results from these specific sites suggest that afterslip had largely ceased within 3 years after the Norcia earthquake but gravitational and weathering erosional effects continued. In this particular setting, with widely distributed co-seismic slip in an elevated, steep area prone to weathering as well as gravitational factors, erosion will be the most important factor is assessing the reliability as evidence of previous co-seismic slip of both the individual scarps, and the landforms in the area as a whole.

CHAPTER 6. Conclusions and suggestions for further work

6.1 Introduction and thesis aim

The primary aim of this thesis was to explore the reliability of fault scarps as evidence of co-seismic slip by investigating how those scarps develop over time. My hypothesis was that scarps are likely to be highly variable as such evidence due to:

(1) their inability accurately to present co-seismic evidence of near-surface fault slip distribution; and/or

(2) the subsequent effects of ongoing degradation from either short-term processes such as tectonic-related after-slip, or longer-term processes such as gravitational or weathering erosion.

The research described in this thesis has been made possible by the availability of two remote sensing datasets that would not always be readily available to researchers: the Pleiades optical satellite data (not normally available otherwise than on commercial terms, but made freely available on this occasion through the CEOS (Committee on Earth Observation Satellites) seismic hazards project); and repeat Terrestrial Laser Scans, including scans taken immediately after the Norcia earthquake. This has provided a unique opportunity to study both co-seismic regional scale deformation and post-seismic deformation at fault scarp scale. Both areas of investigation have highlighted the need for any assessment of future seismic hazard to take into account a variety of localised factors that will have a bearing on the reliability of fault scarps as evidence of co-seismic slip.

The conclusions of the preceding chapters are dealt with separately in each of those chapters, summarised below, as well as suggestions for future research.

6.2 Discussion

(a) My modelling results from a joint inversion using optical satellite data in addition to far-field datasets show that near-surface co-seismic slip associated with the 30th October 2016 Norcia earthquake was distributed widely by transfer onto minor structures in the hanging wall of the main Monte Vettore fault in the area of greatest co-seismic deformation. Near-surface slip on those minor structures and on the main Monte Vettore fault varied in both magnitude and vectors from slip at depth as a consequence of that slip distribution.

At regional scale, co-seismic slip seen at the surface on a main fault plane may not reflect either the magnitude of slip at depth or the underlying slip vectors. This issue is of importance as inverse models of co-seismic slip at depth that fail to take into account the distributed nature of near-fault deformation in relatively immature fault zones risk omitting a crucial part of the data as to surface movement. Without that data, any models are inherently unlikely to be reliable. My research describes a method for processing optical satellite data which removes noise and artefacts to the extent that the results can be used with confidence in such detailed modelling. The results of the modelling are also I believe reliable, in terms of the fit of the model to data. The model was the result of numerous iterations involving many small variations in parameters such as smoothing factor, respective dataset weightings and individual fault geometry, dip, rake, and depth. The far-field geometries and model set-up had previously been subjected to an uncertainty analysis (in Walters et al., 2018), using a Monte Carlo approach. These results could have perhaps been verified by a statistical evaluation of uncertainties using a similar analysis (which would be recommended in any future similar exercise), if time had permitted. However, the absence of such an analysis should not detract from the good fit of the model to the data.

In the case of the Monte Vettore fault, the distributed nature of the faulting in the hanging wall in the west-facing slope below the Scoglio del'Aquila outcrop is apparent from the geomorphology, and from contemporaneous field records made after the Norcia earthquake (Villani et al., 2018). It is also the area where co-seismic

displacement was at its greatest on the main Monte Vettore fault (ibid). It has been suggested (Iezzi et al., 2018) that the peaks of co-seismic displacement recorded during the Norcia earthquake resulted from bends in the Monte Vettore fault, where the strike of the fault deviates from its overall strike, dip of the fault plane is at its steepest, and long-term displacement is also at its maximum. Previous research (e.g. Faure Walker et al., 2010, Wilkinson et al., 2015) had made similar observations based upon changes in fault geometry drawing on other examples in the central Apennines (e.g. the Parasano and Campo Felice faults). It has also been suggested that the bend in the fault at this point might have acted as a stress barrier to rupture propagation in connection with the Amatrice earthquake (Mildon et al., 2017).

It was clear, therefore, that the near-surface co-seismic slip patterns in this area would be unlikely to be straightforward. Any model would need both additional surface detail, and more complicated geometry to characterise that level of complexity. My use of the Pleiades datasets has helped to shed light on this complex picture by adding the previously missing detail of near-fault co-seismic surface deformation to the far-field data used in previous inversions and adopting a more detailed fault model geometry. The results show that co-seismic slip was distributed widely by transfer onto minor hanging wall structures, and that near-surface slip on those minor structures and on the main Monte Vettore fault varied in both magnitude and vectors as a consequence of that slip distribution.

However, in doing so, the model leaves area of uncertainty. The primary controlling influence on that near-surface distribution of slip appears to be the near-surface geometry of the main Monte Vettore fault. However, the minor structures all have strikes that differ from each other and from the main Monte Vettore fault (assuming the surface ruptures accurately represent those structures as they continue below the surface). At what depth and how do the minor structures interact with each other, and with the main fault plane? With differing strikes, it is inevitable that they will not interact at the same depth along their lengths. For example, the antithetic fault (fault 13) could be expected to interact with the main Monte Vettore fault (fault 7) at a shallower depth towards its NNW end than at the SSE end (see **Figure 43** for the respective locations of the fault segments). At the SSE end, how does the antithetic

fault interact with the spur from the main Monte Vettore fault (fault 19)? Does the steeper dip and altered strike of the main Monte Vettore fault plane continue with depth, or is it limited only to the near-surface region where the various structures interact?

The modelling results suggest that more than 50% of the slip on the main Monte Vettore fault in this central area is transferred onto minor structures, of which the majority is transferred onto the antithetic fault (with a relatively small proportion transferred onto the synthetic fault (fault 12)). However, in both cases the majority is partitioned into oblique, near-strike slip. This may be a reflection of their respective geometries. In both cases, the strikes of the minor structures are nearer to the overall strike of the Monte Vettore fault than the strike of fault 7, and this oblique movement may be a corrective mechanism to try to accommodate regional strain patterns. However, with the other uncertainties involved, including matching the differing slip vectors at depth, modelling all of the various interactions and geometries successfully is a very considerable challenge, and beyond the scope of this thesis.

Models of sub-surface slip that use relatively simplistic fault geometry are unlikely to be able to account for any near-surface complexity by way of slip distribution. In this research it has only been possible to characterise that near-fault complexity by utilising datasets additional to the far-field data provided by InSAR and regional GNSS. The use of such data has enabled me to add near-fault detail, and to justify and inform the use of a more detailed fault geometry in inverse modelling. In turn, this has enabled me to fill gaps in the near-surface distribution of slip that other models had not been able to fill in a way that provides insights into the processes involved. This suggests that, where freely available, high-resolution optical satellite data are essential resources, particularly in considering relatively immature fault systems such as the Apennines where near-surface fault complexity is readily apparent from the surface traces. Freely available high resolution data may not be forthcoming in every case, but perhaps should be made available as a scientific research resource where major earthquakes are involved in active tectonic regions.

(b) The repeatable work-flow I developed for the Pleiades data overcomes difficulties in processing differential optical satellite data to effectively denoise the signals and remove artefacts, resulting in a reliable detailed dataset which can be used in inverse modelling.

In addition to the issue of whether high-resolution optical satellite imagery is freely available for research, there are inherent issues with using passive sensing techniques that rely upon good visibility of the Earth's surface and where images will need fine alignment to recover detail of deformation over a wide area at scales that are less than or equivalent to the resolution of the data. The claimed image 2D location accuracy at nadir for Pleiades imagery is 6.5 m (CE90) (Circular (horizontal) error at 90th percentile) (October 2017 figure) (Pleiades Imagery User Guide, 2012). The Pleiades datasets I used lacked detail particularly in areas away from the main fault scarp. They were also clearly misplaced relative to each others' horizontal and vertical coordinates, which required correction of the later image's coordinates. After that initial correction (a process that will be different in each case), the process of correlation using the COSI-Corr tool succeeded in deriving noisy, but realistic results for the horizontal shifts during the earthquake, which matched well with field observations. The main improvement of the quality of those results came from the application and adjustment through experimentation of an iterative median-based filter that kept detail in the areas wanted (near the main area of displacement), but replaced outliers in areas of poorer data coverage. Once that had been achieved, adjustment of the post-earthquake data to allow for the correlation results enabled vertical differencing that was largely reliable (and without some biases in the data seen elsewhere, notably in Delorme et al., 2020).

An outline of the workflow involved is at **Figure 151.**

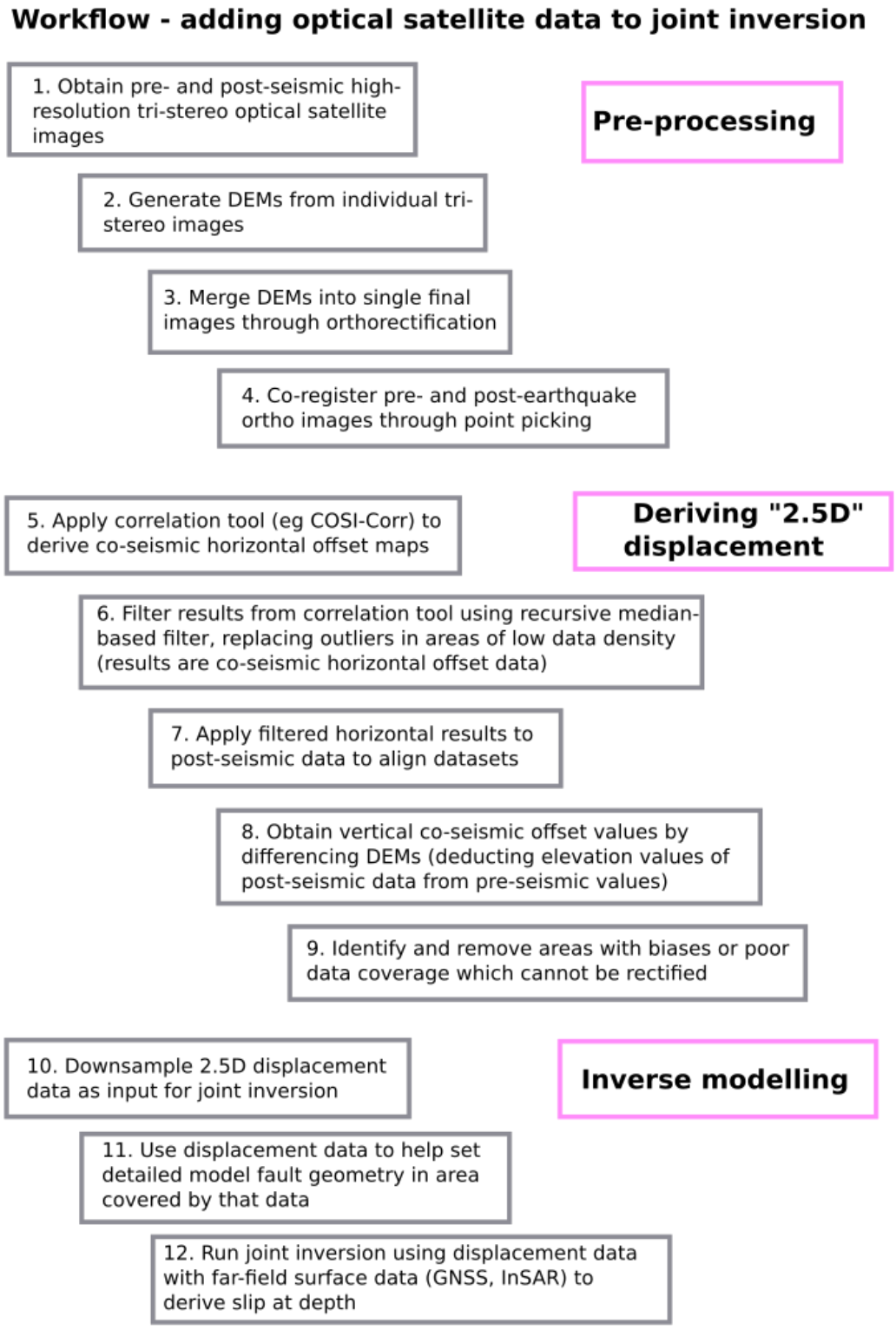

Figure 151: *Outline of Optical Satellite data processing workflow.*

There remained a long-wavelength sinusoidal effect in the data towards the west of the study area (also seen in Delorme et al., 2020's results). I was not able to eliminate that entirely by trying to identify the scale of that effect over a wide profile (in part through masking areas most affected by co-seismic displacement), and subtracting that effect from the data in that area. In the end, for the majority of the inverse modelling, this did not unduly matter – I restricted the areas used to data within 1 km of the fault scarps, and excluded the sinusoidal area entirely. This gave me the data in the area I needed for the inversion in this case. In answer to my request for information CNES (the French National Space Agency) have confirmed that the sinusoidal effect was known about, and related specifically to the on board set-up of the Pleiades 1B satellite (the source of both of the orthoimages I used). The distortion which is introduced in the orthorectification process apparently arises from the use of what CNES describe as "some on board measures that are noisy". CNES say that an on board reconfiguration has "mitigated this artefact" with effect from the end of 2021, so this problem should not arise in any future use of Pleiades data.

(c) The repeatable work-flow I developed for the TLS data also overcomes difficulties in processing differential TLS data to effectively denoise the signals and derive post-seismic deformation at cm scales over areas of up to ~5000 m^2 and time periods of ~3 years.

The workflow I derived for processing the TLS data is also repeatable, but needs more specific tailoring in each case to match the attributes of the sites and scans. Previous use of repeat TLS to derive deformation at these sorts of scales has looked at either less diverse sites (such as roads and relatively flat adjacent areas) over much shorter time periods (e.g. Wilkinson et al., 2010 and 2012), or co-seismic deformation which is an order of magnitude greater than the post-seismic displacement (e.g. Wedmore et al., 2019). Those sites inherently have relatively little gravity-associated deformation to complicate the picture. I believe my study is the first time these techniques have been tested on more complex sites with more challenging topography and over an extended timescale.

Some of the workflow is an adaptation of the workflow used elsewhere (e.g. in Wedmore et al., 2019) (such as the use of the scan alignment tools within CloudCompare and use of the Nissen et al., 2017 modified Iterative Closest Point algorithm). In co-registering scan pairs, the fine alignment process using the CloudCompare tools may need adaptation according to whether it is possible to identify an area which has not altered significantly between scans. The later additions to the workflow here are effectively all noise-reducing and reflect the difficulties in extracting a clear signal at these sorts of tolerances and scales from data which are far from perfect. TLS relies upon returns from objects which may not produce a uniform response depending upon their orientation, and will produce lower returns with distance from the scanner. Scanner set-up is important, as a very small difference in "levelling" the scanners at the outset will produce results which mask the signal. A difference of ~0.01^{o} in levelling between scanners will introduce a false vertical difference between the scans of ~1.5 - 2 cm over a distance of 100 m.

Some of these noise issues can be addressed in the field by taking scans from multiple points and tying them together to avoid some occlusion (e.g. as in Wilkinson et al., 2015). However, the datasets here were undoubtedly noisy. In one case (Monte Vettore) I used a lowest point filter in areas where seasonal vegetation distorted the data. In other cases, using a similar filter on smaller-scale vegetation would have meant much of the underlying signal was lost, and the filter was not appropriate. Where the data quality clearly varied significantly with distance away from the fault scarp (e.g. at the Meterff site) I used my iterative median-based filter to replace outliers away from the main area, keeping the detail near the fault scarp. In all cases I found that identifying and removing ramps from the ICP results restored, rather than destroyed, signals. I was aware that, with signals which were sometimes of the order of only ~2 cm, over-processing the data would have left me with little usable result.

In this particular case, my workflow (**Figure 152**) (with its variations) has succeeded in extracting what I believe are genuine signals at cm scale from the data, rather than artefacts. A possible concern is that the workflow is not "fixed" because of its variations. However, this was essential in this case because all the sites were different,

and the scan pairings represented different challenges for which a “one size fits all” approach would not have been appropriate.

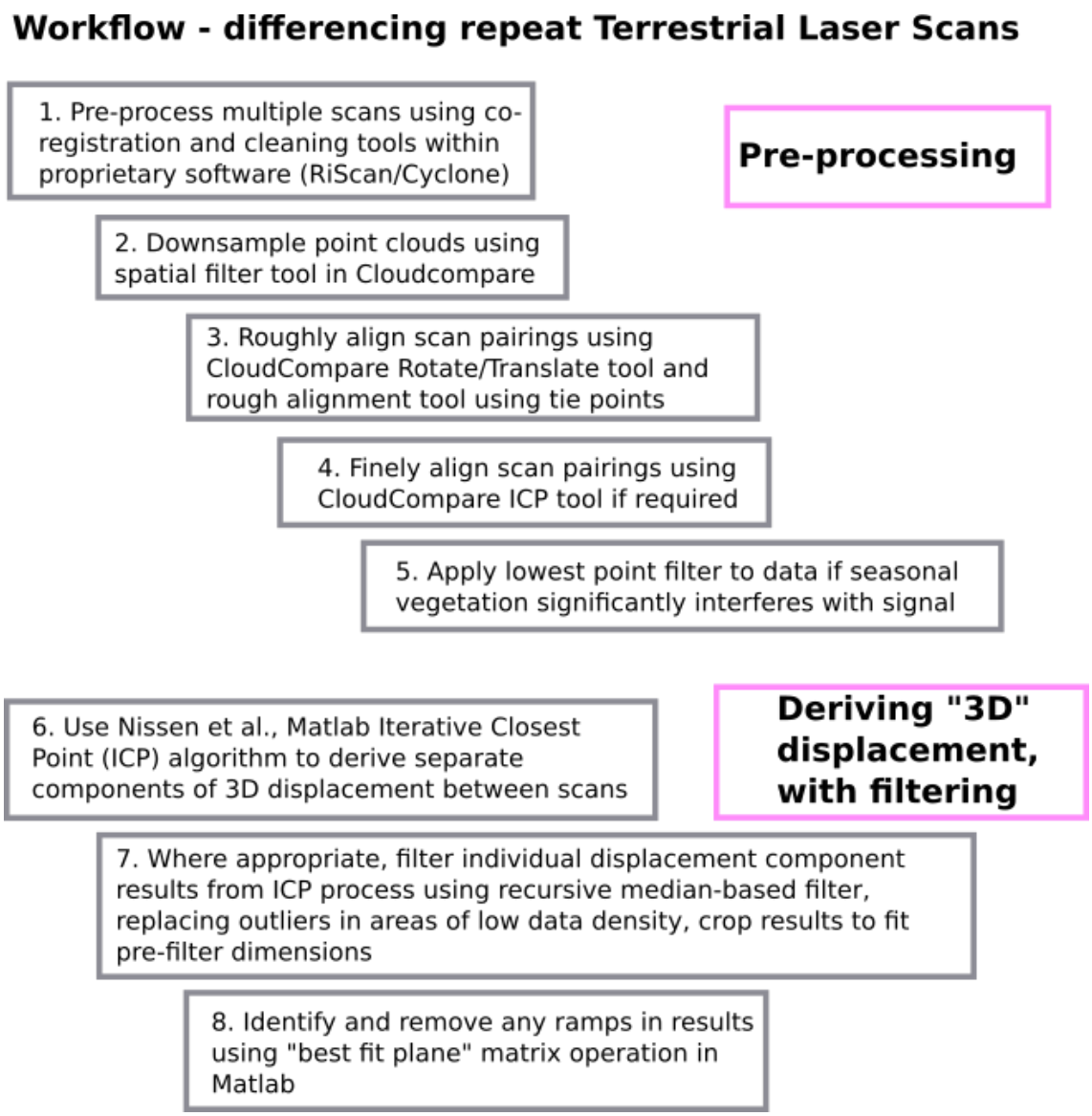

Figure 152: *Outline of TLS processing workflow*

(d) The results from the TLS data demonstrate that a variety of factors need to be considered when assessing the reliability of any fault scarp as evidence of co-seismic slip. Among these is the pattern of co-seismic slip, and its relationship to subsequent deformation.

A potential link between the two main areas of my study is where the pattern of post-seismic afterslip might bear a relationship to the co-seismic distribution of slip. Complex patterns of co-seismic slip are likely to lead to localised high slip gradients, and afterslip in the form of recovery of slip deficit is itself likely to be heavily influenced by the co-seismic partitioning of slip.

One difficulty in interpreting many of the post-seismic results is disentangling afterslip from erosion. It is also worth noting that I have assumed that post-seismic tectonic-related displacement has been confined solely to afterslip, rather than either poroelastic relaxation or any bulk viscoelastic rebound as the temporal and spatial scales have not enabled me to assess any potential contribution from those elements. The Meterff site is one where it is possible to discern variations in the nature of afterslip along the scarp itself that apparently bear an inverse relationship to co-seismic slip (the latter derived from field results, from Villani et al., 2018). This suggests that areas of lesser co-seismic slip have more accumulated slip deficit and are therefore more prone to post-seismic slip. A similar pattern can also be discerned in the Vettore Antithetic 1 site, disregarding the southeast end of the scarp where the scarp appears primarily to be affected by erosion. It is also possible that the Meterff site may contain a second structure which did not rupture co-seismically, but has since undergone displacement as slip deficit is recovered. The afterslip at the Monte Vettore site is arguably restricted to just one main area which might suggest high slip co-seismic gradients apply along the scarp, possibly as a result of changes in fault geometry (although the signal is obscured by gravitational movement elsewhere).

All of these observations are consistent with widely distributed co-seismic near-surface distribution of slip (shown by my modelling results). However, the scales involved make it impossible to match specifically any localised high co-seismic slip gradients to the detail of the modelling. Even at its smallest scale, my discretisation of the slip is on

patches of 250 m x 250 m that in most cases exceed the areas of each of the scarps under consideration.

I had also hoped to model post-seismic slip at shallow depth using inverse modelling from surface deformation slip for the individual TLS sites, and to compare that to my co-seismic slip model. Although I attempted modelling at several of the sites, the results were disappointing because the results are heavily influenced by factors that are erosional. The scales are also too small to produce realistic results, involving only small segments of larger structures. Therefore, I have not been able to make the comparison I had hoped to make.

(e) Other factors identified from the TLS data results that potentially impact the extent to which fault scarps degrade over time include the underlying geology, the local topography, and the extent and nature of human activity.

This research also shows that the extent and nature of co-seismic slip distribution and partitioning is only one of a number of factors that have to be considered in assessing the reliability of a fault scarp as evidence of previous slip history as the scarp has degraded over time. The principal other factors identified from this research include the underlying geology, the local topography, and the extent and nature of human activity. Those are all highly site-specific, with each site having to be considered both within the wider regional context, and more specifically with regard to its individual characteristics. In the 6 sites covered here, each exhibited different degrees and natures of post-seismic deformation, and none of the sites behaved exactly as the other sites did. There were some expected common features, such as near-fault post-seismic relaxation being greatest in the immediate near-fault region, and after-slip decaying over time and distance (both mirroring the findings in e.g. Wilkinson et al., 2010 and 2012). Those common features are likely to feature in other locations, but should not be assessed in isolation. A study of this size and scale is useful as a start to the process of assembling evidence of how scarps degrade over time, giving general guidance as to the sorts of factors that might arise and need to be taken into account. Any guide to their likely relative importance in every case or quantification of the extent of the degradation over time would require a considerably larger database.

(f) In an elevated and steep area of the Apennines, the processes of erosion are rapidly removing much of the evidence of co-seismic slip, in particular on the secondary structures.

Although some erosion was already apparent by August 2019, my return visit to the sites in May 2022 showed that the scarps that relate to the secondary structures (in particular Meterff, Vettore Antithetic 1 and Bove Road) were beginning to deteriorate rapidly due to weathering and gravitational erosion. This is to be expected in mountainous regions with steep topography (e.g. Kokkalas and Koukouvelas, 2005) subject to freeze-thaw conditions over winter (Wallace, 1977), where the bedrock seems to be susceptible to extensive fracturing. Such erosion would be expected to be most significant in the early period after the scarp formation (Hanks et al., 1984). It would be helpful to revisit these sites again over a longer time period to verify the extent to which evidence continues to be degraded. One consequence of the longer-term degradation of the scarps is that in maybe as little as 20 years time, with the exception of possibly the main structures such as the main Monte Vettore fault, unless there is an intervening tectonic event, there will be little surface evidence left of the distributed faulting on minor structures. As noted above, this means that possibly less than 50% of extent of the co-seismic slip will be recorded in any visible way in the landscape (and the scarps for that element will themselves have deteriorated). The warnings of the challenges facing future seismic-hazard assessment in connection with the widely distributed faulting during the Darfield (Canterbury) earthquake (2010) (Quigley et al., 2011) apply equally here. In that case natural and/or anthropogenic surface processes were expected to reduce or obscure the geomorphic evidence of past surface-rupturing earthquakes (and the scarp heights were lower than many of the surrounding geomorphological features) (ibid).

(g) Fault scarps in a relatively immature fault zone with widely distributed co-seismic slip are likely to be unreliable as evidence of previous co-seismic slip as they are also likely to be an inadequate record of co-seismic slip as well as subject to ongoing processes of post-seismic degradation.

The clear conclusion from the combined effects of afterslip and erosion in this mountainous area is that post-seismic processes severely compromise the value of fault scarps as evidence of previous co-seismic slip. However, the ability of fault scarps to represent the size and distribution of co-seismic slip in a relatively immature fault zone is also highly questionable. In this case, I have used detail of the surface ruptures to model a relatively complicated picture of near-surface near-fault slip. However, I have assumed that slip on all the structures has ruptured to the surface. It could reasonably be expected that slip at depth is much more complicated than modelled, and that slip on other minor structures may not rupture to the surface in the same way. This may be behind the possible presence of a second structure at the Meterff site. Relatively major structures in this area which are identified using records of aftershocks include the Norcia Antithetic fault and Pian Piccolo fault which did not rupture to the surface. Therefore, it seems probable that more minor, unidentified blind structures will also play a part in the partitioning of slip away from the main Monte Vettore fault, further reducing the evidential value of fault scarps as records of co-seismic slip.

6.3 Suggestions for further work

The noise in the TLS data (compared to the resolution required to detect post-seismic slip on minor structures) meant that a variety of filtering and de-noising methods had to be considered. This in turn means that the workflow for the TLS data, although repeatable, is not fully standardised. The scans here were taken in different conditions, using different scanners and resolutions, and from not identical locations. Some of the scans taken in 2016 in the few days immediately following the Norcia earthquake were understandably swiftly arranged, and lacked full prior planning. It might be possible to reduce the level of noise in the results in any future work by ensuring greater consistency between the repeat scans. For example, minor changes in the placement

of scanners could lead to areas of occluded data in some but not all of the scans. In some cases there was less than a 100% overlap between the scan results which is likely to affect both the alignment process using CloudCompare and possibly the use of the ICP algorithm in differencing. Differing scan resolutions might also introduce areas of difference between the datasets (although this should be alleviated by common spatial downsampling). By comparison, the nearest comparable research using differential TLS (Wilkinson et al., 2010 and 2012), used the same scanner from the same positions, with semi-permanent reflector positions.

As noted above, the circumstances which resulted in the datasets being available for this study are not necessarily replicable in other locations. I was fortunate that optical satellite data was made freely available here, and given its potential use commercial organisations should be encouraged to make it freely available for research purposes when new tectonic events occur in active and populated tectonic regions.

In this case, repeat TLS was possible due to the coincidence that a team with a scanner was already in situ before the Norcia earthquake, and the areas of greatest co-seismic offset were in locations which were readily accessible. This also meant that repeat visits to scan the same locations on subsequent occasions were not prohibitively expensive. It is unfortunate that Covid-19 prevented a further visit to the sites in 2021, which would have enabled a longer period of study, and possibly the acquisition of sufficient data points to test whether decay was exponential at some of the sites (although it appears that afterslip had largely stopped at each of the sites by 2019).

In the case of any future continental earthquake in an active tectonic region, it may not be as relatively straight-forward as it was here to obtain the same detailed level of post-seismic data. However, there is clearly potential for the same approach to be followed at other locations in the future. Advances in the use of airborne drones (UAVs – Unmanned Aerial Vehicles) and Structure from Motion (SfM) photogrammetry techniques (e.g. Westoby et al., 2012, Hugenholtz et al. 2013) mean that those might represent a realistic alternative to the use of repeat laser scans. Using point clouds from photogrammetry to construct Digital Elevation Models which can then be used with differencing techniques could potentially measure centimetre-scale displacement

over time, and over extended areas when TLS might be unrealistic. As a recent example, the results from a comparison of the use of TLS and UAV-SfM photogrammetry in monitoring post-fire sliding phenomena on slopes at centimetre scale show little qualitative difference in results (with the UAV-SfM results representing an improvement in some cases, where vegetation obscures the TLS line-of-sight) (Deligiannakis et al., 2021). Studies involving the comparative use of the techniques in connection with mapping outcrops suggest that, although processing the SfM data can be more complex than the TLS data (Wilkinson et el., 2016), over an extended outcrop where there might be difficulties with occlusion in respect of TLS, SfM might produce a better overall geological model, although less accurate surface reconstructions (Cawood et al., 2017). Improvements could be made with better SfM survey design (Wilkinson et al., 2016 and Cawood et al., 2017). UAVs would certainly be cheaper, and more easily portable and deployable technology than TLS.

The fault scarp sites under consideration here are varied in many respects (such as topography, exposure to elements, and whether they relate to the main Monte Vettore fault or to minor structures with varying orientations within the hanging wall). However, they are all situated within the same normal fault system, and with underlying geology which is predominantly composed of carbonates.

Future studies should aim to measure scarp degradation over a greater period of time, and in areas with a different mix of geology, systems of differing maturity, or reverse/strike-slip faulting. Such future work should where possible (which might not be realistic in all cases) avoid sites where human activity is likely to play a significant part in post-seismic deformation as such activity introduces uncertainty in separating the true post-seismic signal from afterslip or natural erosion. Such research would contribute to a fuller understanding of what factors apply in different geological settings, and how those compare to the factors seen here, helping to build a more comprehensive database of how scarps degrade over time.

Without further work, one of the remaining problems in this area of research is that it is difficult to quantify the combined effect of those factors on the scarp that would be needed in order to better understand the possible error margins involved in using fault

scarps as evidence of historic slip. Although that should be an overall aim, the database required to do that will have to be substantially more extensive than the 6 sites studied here. Even so, this study already shows that there are many potential factors which could impact on the reliability of a fault scarp as evidence of a fault's previous slip history.

Appendices (see separate document)

References

AIRBUS DEFENCE AND SPACE INTELLIGENCE 2012. Pleiades Imagery User Guide v 2.0, accessed February 2022. https://www.intelligence-airbusds.com/files/pmedia/public/r51130_9_leaflet-pleiadesneov2.pdf

AMBRASEYS, N. N. 1971. Value of Historical Records of Earthquakes. Nature, 232, 375-379. doi: https://doi.org/10.1038/232375a0

AYOUB, F., LEPRINCE, S., BINET, R., LEWIS, K. W., AHARONSON, O. & AVOUAC, J. P. Influence of camera distortions on satellite image registration and change detection applications. 2008. IEEE, II-1072-II-1075. doi: https://doi.org/10.1109/IGARSS.2008.4779184

BAGNARDI, M., GONZÁLEZ, P. J. & HOOPER, A. 2016. High-resolution digital elevation model from tri-stereo Pleiades-1 satellite imagery for lava flow volume estimates at Fogo Volcano: Tri-Stereo Pleiades DEM of Fogo Volcano. Geophysical Research Letters, 43, 6267-6275. doi: https://doi.org/10.1002/2016GL069457

BERTHIER, E., VINCENT, C., MAGNÚSSON, E., GUNNLAUGSSON, Á. Þ., PITTE, P., LE MEUR, E., MASIOKAS, M., RUIZ, L., PÁLSSON, F., BELART, J. M. C. & WAGNON, P. 2014. Glacier topography and elevation changes derived from Pléiades sub-meter stereo images. The Cryosphere, 8, 2275-2291. doi: https://doi.org/10.5194/tc-8-2275-2014

BOUAZIZ, S., TAGLIASACCHI, A. & PAULY, M. 2013. Sparse iterative closest point. Computer Graphics Forum, 113-123. doi: https://doi.org/10.1145/2988458.2988490

BOWMAN, D., KING, G. & TAPPONNIER, P. 2003. Slip Partitioning by Elastoplastic Propagation of Oblique Slip at Depth. Science, 300, 1121-1123. doi: https://doi.org/10.1126/science.1082180

BUBECK, A., WILKINSON, M., ROBERTS, G. P., COWIE, P. A., MCCAFFREY, K. J. west., PHILLIPS, R. & SAMMONDS, P. 2015. The tectonic geomorphology of bedrock scarps on active normal faults in the Italian Apennines mapped using combined ground penetrating radar and terrestrial laser scanning. Geomorphology, 237, 38-51. doi: https://doi.org/10.1016/j.geomorph.2014.03.011

BUCKLEY, S. J., HOWELL, J. A., ENGE, H. D. & KURZ, T. H. 2008. Terrestrial laser scanning in geology data acquisition, processing and accuracy considerations. Journal of the Geological Society, 165, 625-638. doi: https://doi.org/10.1144/0016-76492007-100

BUCKNAM, R. C. & ANDERSON, R. E. 1979. Estimation of fault-scarp ages from a scarp-height-slope-angle relationship. Geology, 7, 11-14. doi: https://doi.org/10.1130/0091-7613(1979)7<11:EOFAFA>2.0.CO2

BURBANK, D. W. & ANDERSON, R. S. 2012. Tectonic Geomorphology, 2nd Edition Hoboken, Wiley.

CARTWRIGHT, J. A., TRUDGILL, B. D. & MANSFIELD, C. S. 1995. Fault growth by segment linkage: an explanation for scatter in maximum displacement and trace length

data from the Canyonlands Grabens of SE Utah. Journal of Structural Geology, 17, 1319-1326. doi: https://doi.org/ 10.1016/0191-8141(95)00033-A

CAVINATO, G. P. & DE CELLES, P. G. 1999. Extensional basins in the tectonically bimodal central Apennines fold-thrust belt, Italy: response to corner flow above a subducting slab in retrograde motion. Geology, 27, 955-958. doi: https://doi.org/0.1130/0091-7613(1999)027<0955:EBITTB>2.3.CO2

CAWOOD, A. J., BOND, C. E., HOWELL, J. A., BUTLER, R. W. H. & TOTAKE, Y. 2017. LiDAR, UAV or compass-clinometer? Accuracy, coverage and the effects on structural models. Journal of Structural Geology, 98, 67-82. doi: https://doi.org/10.1016/j.jsg.2017.04.004

CHELONI, D., DE NOVELLIS, V., ALBANO, M., ANTONIOLI, A., ANZIDEI, M., ATZORI, S., AVALLONE, A., BIGNAMI, C., BONANO, M., CALCATERRA, S., CASTALDO, R., CASU, F., CECERE, G., DE LUCA, C., DEVOTI, R., DI BUCCI, D., ESPOSITO, A., GALVANI, A., GAMBINO, P., GIULIANI, R., LANARI, R., MANUNTA, M., MANZO, M., MATTONE, M., MONTUORI, A., PEPE, A., PEPE, S., PEZZO, G., PIETRANTONIO, G., POLCARI, M., RIGUZZI, F., SALVI, S., SEPE, V., SERPELLONI, E., SOLARO, G., STRAMONDO, S., TIZZANI, P., TOLOMEI, C., TRASATTI, E., VALERIO, E., ZINNO, I. & DOGLIONI, C. 2017. Geodetic model of the 2016 Central Italy earthquake sequence inferred from InSAR and GPS data. Geophysical Research Letters, 44, 6778-6787. doi: https://doi.org/10.1002/2017GL073580

CHELONI, D., D'AGOSTINO, N., D'ANASTASIO, E., AVALLONE, A., MANTENUTO, S., GIULIANI, R., MATTONE, M., CALCATERRA, S., GAMBINO, P., DOMINICI, D., RADICIONI, F. & FASTELLINI, G. 2010. Co-seismic and initial post-seismic slip of the 2009 M_w 6.3 L'Aquila earthquake, Italy, from GPS measurements. Geophysical Journal International. doi: https://doi.org/10.1111/j.1365-246X.2010.04584.x

CHELONI, D., FALCUCCI, E. & GORI, S. 2019. Half-Graben Rupture Geometry of the 30 October 2016 M_w 6.6 Mt. Vettore-Mt. Bove Earthquake, Central Italy. Journal of Geophysical Research: Solid Earth, 124, 4091-4118. doi: https://doi.org/10.1029/2018JB015851

CHEN, Y. & MEDIONI, G. 1992. Object modelling by registration of multiple range images. Image and Vision Computing, 10, 145-155. doi: https://doi.org/10.1016/0262-8856(92)90066-C

CHIARABBA, C., AMATO, A., ANSELMI, M., BACCHESCHI, P., BIANCHI, I., CATTANEO, M., CECERE, G., CHIARALUCE, L., CIACCIO, M. G., DE GORI, P., DE LUCA, G., DI BONA, M., DI STEFANO, R., FAENZA, L., GOVONI, A., IMPROTA, L., LUCENTE, F. P., MARCHETTI, A., MARGHERITI, L., MELE, F., MICHELINI, A., MONACHESI, G., MORETTI, M., PASTORI, M., PIANA AGOSTINETTI, N., PICCININI, D., ROSELLI, P., SECCIA, D. & VALOROSO, L. 2009. The 2009 L'Aquila (central Italy) M_W6.3 earthquake: Main shock and aftershocks. Geophysical Research Letters, 36, 18. doi: https://doi.org/10.1029/2009GL039627

CHIARALUCE, L., BARCHI, M., COLLETTINI, C., MIRABELLA, F. & PUCCI, S. 2005. Connecting seismically active normal faults with Quaternary geological structures in a complex extensional environment: The Colfiorito 1997 case history (northern

Apennines, Italy): Geological versus seismological faults. Tectonics, 24 (1). doi: https://doi.org/10.1029/2004TC001627

CHIARALUCE, L., DI STEFANO, R., TINTI, E., SCOGNAMIGLIO, M., MICHELE, M., CASAROTTI, E., CATTANEO, M., DE GORI, P., CHIARABBA, C., MONACHESI, G., LOMBARDI, A., VALAROSO, L., LATORRE, D. & MARZORATI, S. 2017. The 2016 Central Italy Seismic Sequence: A First Look at the Mainshocks, Aftershocks, and Source models. Seismological Research Letters, 88, 757-771. doi: https://doi.org/10.1785/0220160221

CIVICO, R., PUCCI, S., VILLANI, F., PIZZIMENTI, L., DE MARTINI, P. M. & NAPPI, R. 2018. Surface ruptures following the 30 October 2016 M_w 6.5 Norcia earthquake, central Italy. Journal of Maps, 14, 151-160. doi: https://doi.org/10.1080/17445647.2018.1441756

CLOUDCOMPARE online user guide https://www.cloudcompare.org/doc/wiki/index.php/Main_Page [Accessed on multiple occasions]

COLTORTI, M. & FARABOLLINI, P. 1995. Quaternary evolution of the Castelluccio di Norcia Basin. Il Quaternario, 8, 149-166.

COPLEY, A. 2014. Postseismic afterslip 30 years after the 1978 Tabas-e-Golshan (Iran) earthquake: observations and implications for the geological evolution of thrust belts. Geophysical Journal International, 197, 665-679. doi: https://doi.org/10.1093/gji/ggu023

D'AGOSTINO, N., JACKSON, J. A., DRAMIS, F. & FUNICIELLO, R. 2001a. Interactions between mantle upwelling, drainage evolution and active normal faulting: an example from the central Apennines (Italy). Geophysical Journal International, 147, 475-497. doi: https://doi.org/10.1046/j.1365-246X.2001.00539.x

D'AGOSTINO, N., GIULIANI, R., MATTONE, M. & BONCI, L. 2001b. Active crustal extension in the Central Apennines (Italy) inferred from GPS measurements in the interval 1994-1999. Geophysical Research Letters, 28, 2121-2124. doi: https://doi.org/10.1029/2000GL012462

DE GUIDI, G., VECCHIO, A., BRIGHENTI, F., CAPUTO, R., CARNEMOLLA, F., DI PIETRO, A., LUPO, M., MAGGINI, M., MARCHESE, S., MESSINA, D., MONACO, C. & NASO, S. 2017. Brief communication: Co-seismic displacement on 26 and 30 October 2016 (M_w = 5.9 and 6.5) – earthquakes in central Italy from the analysis of a local GNSS network. Natural Hazards and Earth System Sciences, 17, 1885-1892. doi: https://doi.org/10.5194/nhess-17-1885-2017

DELIGIANNAKIS, G., PALLIKARAKIS, A., PAPANIKOLAOU, I., ALEXIOU, S. & REICHERTER, K. 2021. Detecting and Monitoring Early Post-Fire Sliding Phenomena Using UAV–SfM Photogrammetry and t-LiDAR-Derived Point Clouds. Fire, 4, 87. doi: https://doi.org/10.3390/fire4040087

DELONG, S. B., LIENKAEMPER, J. J., PICKERING, A. J. & AVDIEVITCH, N. N. 2015. Rates and patterns of surface deformation from laser scanning following the South Napa

earthquake, California. Geosphere, 11, 2015-2030. doi: https://doi.org/10.1130/GES01189.1

DELORME, A., GRANDIN, R., KLINGER, Y., PIERROT-DESEILLIGNY, M., FEUILLET, N., JACQUES, E., RUPNIK, E. & MORISHITA, Y. 2020. Complex Deformation at Shallow Depth During the 30 October 2016 M_w6.5 Norcia Earthquake: Interference Between Tectonic and Gravity Processes? Tectonics, 39 (2). doi: https://doi.org/10.1029/2019TC005596

DIETERICH, J. H. 1979. Modeling of rock friction: 1. Experimental results and constitutive equations. Journal of Geophysical Research, 84, 2161-2168. doi: https://doi.org/10.1029/JB084iB05p02161

DI STEFANO, R., KISSLING, E., CHIARABBA, C., AMATO, A. & GIARDINI, D. 2009. Shallow subduction beneath Italy: Three-dimensional images of the Adriatic-European-Tyrrhenian lithosphere system based on high-quality P wave arrival times. Journal of Geophysical Research, 114, B05305. doi: https://doi.org/ 10.1029/2008JB005641

DOLAN, J. F. & HARAVITCH, B. D. 2014. How well do surface slip measurements track slip at depth in large strike-slip earthquakes? The importance of fault structural maturity in controlling on-fault slip versus off-fault surface deformation. Earth and Planetary Science Letters, 388, 38-47. doi: https://doi.org/10.1016/j.epsl.2013.11.043

ELLIOTT, J. R., NISSEN, E. K., ENGLAND, P. C., JACKSON, J. A., LAMB, S., LI, Z., OEHLERS, M. & PARSONS, B. 2012. Slip in the 2010-2011 Canterbury earthquakes, New Zealand. Journal of Geophysical Research, 117 (B3). doi: https://doi.org/10.1029/2011JB008868

ELLIOTT, J. R., WALTERS, R. J. & WRIGHT, T. J. 2016. The role of space-based observation in understanding and responding to active tectonics and earthquakes. Nature Communications 7(1), 1-16. doi: https://doi.org/10.1038/ncomms13844

ESA EOPORTAL DIRECTORY 2021. KOMPSAT-3 [Online]. Available: https://directory.eoportal.org/web/eoportal/satellite-missions/k/kompsat-3 [Accessed November 2021].

ESA EOPORTAL DIRECTORY. 2021a. Pleiades [Online]. Available: https://directory.eoportal.org/web/eoportal/satellite-missions/p/pleiades [Accessed November 2021].

ESA EOPORTAL DIRECTORY. 2021b. SPOT-6 and SPOT-7 [Online]. Available: https://directory.eoportal.org/web/eoportal/satellite-missions/s/spot-6-7 [Accessed November 2021].

ESA EOPORTAL DIRECTORY. 2021c. Pleiades Neo [Online]. Available: https://www.eoportal.org/satellite-missions/pleiades-neo#pl%C3%A9iades-neo-constellation-of-airbus-ds {Accessed October 2022]

FALCUCCI, E., GORI, S., GALLADINI, F., G., FUBELLI, G., MORO, M. & SAROLI, M. 2016. Active faults in the epicentral and mesoseismal Ml 6.0 24, 2016 Amatrice earthquake region, central Italy. Methodological and seismotectonic issues. Annals of Geophysics, 59. doi: https://doi.org/10.4401/ag-7266

References

FAURE WALKER, J. P., ROBERTS, G. P., COWIE, P. A., PAPANIKOLAOU, I., MICHETTI, A. M., SAMMONDS, P., WILKINSON, M., MCCAFFREY, K. J. W. & PHILLIPS, R. J. 2012. Relationship between topography, rates of extension and mantle dynamics in the actively-extending Italian Apennines. Earth and Planetary Science Letters, 325-326, 76-84. doi: https://doi.org/10.1016/j.epsl.2012.01.028

FAURE WALKER, J. P., ROBERTS, G. P., COWIE, P. A., PAPANIKOLAOU, I. D., SAMMONDS, P. R., MICHETTI, A. M. & PHILLIPS, R. J. 2009. Horizontal strain-rates and throw-rates across breached relay zones, central Italy: Implications for the preservation of throw deficits at points of normal fault linkage. Journal of Structural Geology, 31, 1145-1160. doi: https://doi.org/10.1016/j.jsg.2009.06.011

FAURE WALKER, J. P., ROBERTS, G. P., SAMMONDS, P. R. & COWIE, P. 2010. Comparison of earthquake strains over 102 and 104 year timescales: Insights into variability in the seismic cycle in the central Apennines, Italy. Journal of Geophysical Research, 115, (B10). doi: https://doi.org/10.1029/2009JB006462

FERRARIO, M. F. & LIVIO, F. 2018. Characterizing the Distributed Faulting During the 30 October 2016, Central Italy Earthquake: A Reference for Fault Displacement Hazard Assessment. Tectonics, 37, 1256-1273. doi: https://doi.org/10.1029/2017TC004935

FIELDING, E. J., LUNDGREN, P. R., BÜRGMANN, R. & FUNNING, G. J. 2009. Shallow fault-zone dilatancy recovery after the 2003 Bam earthquake in Iran. Nature, 458, 64-68. doi: https://doi.org/ 10.1038/nature07817

FLOYD, M. A., WALTERS, R. J., ELLIOTT, J. R., FUNNING, G. J., SVARC, J. L., MURRAY, J. R., HOOPER, A. J., LARSEN, Y., MARINKOVIC, P., BÜRGMANN, R., JOHANSON, I. A. & WRIGHT, T. J. 2016. Spatial variations in fault friction related to lithology from rupture and afterslip of the 2014 South Napa, California, earthquake. Geophysical Research Letters, 43, 6808-6816. doi: https://doi.org/10.1002/2016GL069428

FREED, A. M. 2007a. Afterslip (and only afterslip) following the 2004 Parkfield, California, earthquake. Geophysical Research Letters, 34(6). doi: https://doi.org/10.1029/2006GL029155

FREED, A. M., BÜRGMANN, R. & HERRING, T. 2007b. Far-reaching transient motions after Mojave earthquakes require broad mantle flow beneath a strong crust. Geophysical Research Letters, 34, L19302. doi: https://doi.org/10.1029/2007GL030959

FREED, A. M., BÜRGMANN, R., CALAIS, E., FREYMUELLER, J. & HREINSDÓTTIR, S. 2006. Implications of deformation following the 2002 Denali, Alaska, earthquake for postseismic relaxation processes and lithospheric rheology. Journal of Geophysical Research, 111, B1. doi: https://doi.org/10.1029/2005JB003894

FUNNING, G. J., PARSONS, B., WRIGHT, T. J., JACKSON, J. A. & FIELDING, E. J. 2005. Surface displacements and source parameters of the 2003 Bam (Iran) earthquake from Envisat advanced synthetic aperture radar imagery. Journal of Geophysical Research, 110, (B9). doi: https://doi.org/10.1029/2004JB003338

GALADINI, F. & GALLI, P. 2000. Active Tectonics in the Central Apennines (Italy) – Input Data for Seismic Hazard Assessment. Natural Hazards, 22, 225-268. doi: https://doi.org/10.1023/A:1008149531980

GALADINI, F. & GALLI, P. 2003. Paleoseismology of silent faults in the Central Apennines (Italy): the Mt. Vettore and Laga Mts. Faults. Annals of Geophysics, 46. doi: https://doi.org/10.4401/ag-3457

GALDERISI, A. & GALLI, P. 2020. Offset components and fault-block motion during the 2016 central Italy earthquake (Mw 6.6, Monte Vettore fault system). Journal of Structural Geology, 134, 104014. doi: https://doi.org/10.1016/j.jsg.2020.104014

GALLI, P., GALADINI, F. & CALZONI, F. 2005. Surface faulting in Norcia (central Italy): a "paleoseismological perspective". Tectonophysics, 403, 117-130. doi: https://doi.org/10.1016/j.tecto.2005.04.003

GALLI, P., GALDERISI, A., ILARDO, I., PISCITELLI, S., SCIONTI, V., BELLANOVA, J. & CALZONI, F. 2018. Holocene paleoseismology of the Norcia fault system (Central Italy). Tectonophysics, 745, 154-169. doi: https://doi.org/10.1016/j.tecto.2018.08.008

GALLI, P., GALDERISI, A., PERONACE, E., GIACCIO, B., HAJDAS, I., MESSINA, P., PILEGGI, D. & POLPETTA, F. 2019. The Awakening of the Dormant Mount Vettore Fault (2016 Central Italy Earthquake, M_w 6.6): Paleoseismic Clues on Its Millennial Silences. Tectonics, 38, 687-705. doi: https://doi.org/10.1029/2018TC005326

GAWTHORPE, R. L. & HURST, J. M. 1993. Transfer zones in extensional basins; their structural style and influence on drainage development and stratigraphy. Journal of the Geological Society, 150, 1137-1152. doi: https://doi.org/ 10.1144/gsjgs.150.6.1137

GIRAUDI, C. & FREZZOTTI, M. 1997. Late Pleistocene Glacial Events in the Central Apennines, Italy. Quaternary Research, 48, 280-290. doi: https://doi.org/10.1006/qres.1997.1928

GLEYZES, M. A., PERRET, L. & KUBIK, P. 2012. Pleiades System Architecture and Main Performances. International Archives of the Photogrammetry, Remote Sensing, and Information Sciences, XXXIX-B1, 537-542. doi: https://doi.org/ 10.5194/isprsarchives-XXXIX-B1-537-2012

GOLD, R. D., DUROSS, C. B. & BARNHART, W. D. 2021. Co-seismic Surface Displacement in the 2019 Ridgecrest Earthquakes: Comparison of Field Measurements and Optical Image Correlation Results. Geochemistry, Geophysics, Geosystems: *22*(3), p.e2020GC009326. doi: https://doi.org/10.1029/2020GC009326

GOLD, P. O., OSKIN, M. E., ELLIOTT, A. J., HINOJOSA-CORONA, A., TAYLOR, M. H., KREYLOS, O. & COWGILL, E. 2013. Co-seismic slip variation assessed from terrestrial lidar scans of the El Mayor–Cucapah surface rupture. Earth and Planetary Science Letters, 366, 151-162. doi: https://doi.org/10.1016/j.epsl.2013.01.040

HADDAD, D. E., AKCIZ, S. O., ARROWSMITH, J. R., RHODES, D. D., OLDOW, J. S., ZIELKE, O., TOKE, N. A., HADDAD, A. G., MAUER, J. & SHILPAKAR, P. 2012. Applications of airborne and terrestrial laser scanning to paleoseismology. Geosphere, 8, 771-786. doi: https://doi.org/10.1130/GES00701.1

HANKS, T. C., BUCKNAM, R. C., LAJOIE, K. R. & WALLACE, R. E. 1984. Modification of wave-cut and faulting-controlled landforms. Journal of Geophysical Research, 89, 5771-5790. doi: https://doi.org/10.1029/JB089iB07p05771

HARRIS, R. A. & SEGALL, P. 1987. Detection of a locked zone at depth on the Parkfield, California, segment of the San Andreas Fault. Journal of Geophysical Research, 92, 7945-7962. doi: https://doi.org/10.1029/JB092iB08p07945

HODGE, M., BIGGS, J., FAGERENG, Å., MDALA, H., WEDMORE, L. N. J. & WILLIAMS, J. N. 2020. Evidence From High-Resolution Topography for Multiple Earthquakes on High Slip-to-Length Fault Scarps: The Bilila-Mtakataka Fault, Malawi. Tectonics, 39(2) e2019TC005933. doi: https://doi.org/10.1029/2019TC005933

HUANG, M. H., FIELDING, E. J., LIANG, C., MILILLO, P., BEKAERT, D., DREGER, D. & SALZER, J. 2017. Co-seismic deformation and triggered landslides of the 2016 M w 6.2 Amatrice earthquake in Italy. Geophysical Research Letters, 44, 1266-1274. doi: https://doi.org/ 10.1002/2016GL071687

HUGENHOLTZ, C. H., WHITEHEAD, K., BROWN, O. W., BARCHYN, T. E., MOORMAN, B. J., LECLAIR, A., RIDDELL, K. & HAMILTON, T. 2013. Geomorphological mapping with a small unmanned aircraft system (sUAS): Feature detection and accuracy assessment of a photogrammetrically-derived digital terrain model. Geomorphology, 194, 16-24. doi: https://doi.org/10.1016/j.geomorph.2013.03.023

HUSSAIN, E., WRIGHT, T. J., WALTERS, R. J., BEKAERT, D., HOOPER, A. & HOUSEMAN, G. A. 2016. Geodetic observations of postseismic creep in the decade after the 1999 Izmit earthquake, Turkey: Implications for a shallow slip deficit: Izmit Creep. Journal of Geophysical Research: Solid Earth, 121, 2980-3001. doi: https://doi.org/10.1002/2015JB012737

IEZZI, F., MILDON, Z., WALKER, J. F., ROBERTS, G., GOODALL, H., WILKINSON, M. & ROBERTSON, J. 2018. Co-seismic throw variation across along-strike bends on active normal faults: implications for displacement versus length scaling of earthquake ruptures. Journal of Geophysical Research: Solid Earth, 123(11), pp.9817-9841. doi: https://doi.org/10.1029/2018JB016732

INGLEBY, T. & WRIGHT, T. J. 2017. Omori-like decay of postseismic velocities following continental earthquakes. Geophysical Research Letters, 44, 3119-3130. doi: https://doi.org/10.1002/2017GL072865

INGV WORKING GROUP, G. G. G. D. A. D. A. C. 2016. Preliminary co-seismic displacements for the October 26 (Mw5.9) and October 30 (M_w6.5) central Italy earthquakes from the analysis of GPS stations: Zenodo. doi: https://doi.org/10.5281/zenodo.167959

JOHNSON, A. M., JOHNSON, N. A., JOHNSON, K. M., WEI, W., FLEMING, R. W., CRUIKSHANK, K. M. & MARTOSUDARMO, S. Y. 1997. Analecta of structures formed during the 28 June 1992 Landers-Big Bear, California earthquake sequence (including maps of shear zones, belts of shear zones, tectonic ridge, duplex en echelon fault, fault elements, and thrusts in restraining steps). (No. USGS-OFR-97-94). Geological Survey, Denver, CO (United States).

JOLIVET, L., FACCENNA, C., GOFFÉ, B., MATTEI, M., ROSSETTI, F., BRUNET, C., STORTI, F., FUNICIELLO, R., CADET, J. P., D'AGOSTINO, N. & PARRA, T. 1998. Midcrustal shear zones in postorogenic extension: Example from the northern Tyrrhenian Sea. Journal of Geophysical Research, 103, 12123-12160. doi: https://doi.org/10.1029/97JB03616

JONES, R. R., MCCAFFREY, K. J. W., CLEGG, P., WILSON, R. W., HOLLIMAN, N. S., HOLDSWORTH, R. E., IMBER, J. & WAGGOTT, S. 2009. Integration of regional to outcrop digital data: 3D visualisation of multi-scale geological models. Computers & Geosciences, 35, 4-18. doi: https://doi.org/10.1016/j.cageo.2007.09.007

KOKKALAS, S. & KOUKOUVELAS, I. K. 2005. Fault-scarp degradation modelling in central Greece: The Kaparelli and Eliki faults (Gulf of Corinth) as a case study. Journal of Geodynamics, 40, 200-215. doi: https://doi.org/10.1016/j.jog.2005.07.006

LAJOIE, L. J., NISSEN, E., JOHNSON, K. L., ARROWSMITH, J. R., GLENNIE, C. L., HINOJOSA-CORONA, A. & OSKIN, M. E. 2019. Extent of Low-Angle Normal Slip in the 2010 El Mayor-Cucapah (Mexico) Earthquake From Differential Lidar. Journal of Geophysical Research: Solid Earth, 124, 943-956. doi: https://doi.org/10.1029/2018JB016828

LANARI, R., BERARDINO, P., BONANO, M., CASU, F., MANCONI, A., MANUNTA, M., MANZO, M., PEPE, A., PEPE, S., SANSOSTI, E., SOLARO, G., TIZZANI, P. & ZENI, G. 2010. Surface displacements associated with the L'Aquila 2009 Mw 6.3 earthquake (central Italy): New evidence from SBAS-DInSAR time series analysis. Geophysical Research Letters, 37(20). doi: https://doi.org/10.1029/2010GL044780

LEPRINCE, S., BARBOT, S., AYOUB, F. & AVOUAC, J. 2007. Automatic and Precise Orthorectification, Coregistration, and Subpixel Correlation of Satellite Images, Application to Ground Deformation Measurements. IEEE Transactions on Geoscience and Remote Sensing, 45, 1529-1558. doi: https://doi.org/10.1109/TGRS.2006.888937

LEPRINCE, S., BERTHIER, E., AYOUB, F., DELACOURT, C. and AVOUAC, J. P. 2008. Monitoring Earth Surface Dynamics With Optical Imagery. Eos (Washington, D.C.), 89, 1-2. doi: https://doi.org/10.1029/2008EO010001

LEPRINCE, S., HUDNUT, K.W., AKCIZ, S.O., HINOJOSA-CORONA, A., and FLETCHER, J.M. (2011), Surface rupture and slip variation induced by the 2010 El Mayor-Cucapah earthquake, Baja California, quantified using COSI-Corr analysis on pre- and post-earthquake LiDAR acquisitions, Abstract EP41A-0596 presented at 2011 Fall Meeting, AGU, San Francisco, Calif., 5–9 Dec.

MACKENZIE, D. & ELLIOTT, A. 2017. Untangling tectonic slip from the potentially misleading effects of landform geometry. Geosphere, 13, 1310-1328. doi: https://doi.org/10.1130/GES01386.1

MANDLER, E., PINTORI, F., GUALANDI, A., ANDERLINI, L., SERPELLONI, E. & BELARDINELLI, M. E. 2021. Post-Seismic Deformation Related to the 2016 Central Italy Seismic Sequence From GPS Displacement Time-Series. Journal of Geophysical Research: Solid Earth, 126 (9), p.e2021JB022200. doi: https://doi.org/10.1029/2021JB022200

MANIGHETTI, I., CAMPILLO, M., BOULEY, S. & COTTON, F. 2007. Earthquake scaling, fault segmentation, and structural maturity. Earth and Planetary Science Letters, 253, 429-438. doi: https://doi.org/10.1016/j.epsl.2006.11.004

MARONE, C. 1998a. The effect of loading rate on static friction and the rate of fault healing during the earthquake cycle. Nature, 391, 69-72. doi: https://doi.org/10.1038/34157

MARONE, C. 1998b. Laboratory-derived Friction Laws and their application to seismic faulting. Annual Review of Earth and Planetary Sciences, 26, 643-696. Doi: https://doi.org/ 10.1146/annurev.earth.26.1.643

MARONE, C. J., SCHOLTZ, C. H. & BILHAM, R. 1991. On the mechanics of earthquake afterslip. Journal of Geophysical Research, 96, 8441-8452. doi: https://doi.org/10.1029/91JB00275

MASON, J., SCHNEIDERWIND, S., PALLIKARAKIS, A., MECHERNICH, S., PAPANIKOLAOU, I. & REICHERTER, K. 2017. Hanging-wall colluvial cementation along active normal faults. Quaternary Research, 88, 39-59. doi: https://doi.org/10.1017/qua.2017.32

MCCAFFREY, K. J. W., JONES, R. R., HOLDSWORTH, R. E., WILSON, R. W., CLEGG, P., IMBER, J., HOLLIMAN, N. & TRINKS, I. 2005. Unlocking the spatial dimension: digital technologies and the future of geoscience fieldwork. Journal of the Geological Society, 162, 927-938. doi: https://doi.org/10.1144/0016-764905-017

MENKE, W. & EILON, Z. 2015. Relationship Between Data Smoothing and the Regularization of Inverse Problems. Pure and Applied Geophysics, 172, 2711-2726. doi: https://doi.org/10.1007/s00024-015-1059-0

MICHETTI, A. M., AUDEMARD M, F. A. & MARCO, S. 2005. Future trends in paleoseismology: Integrated study of the seismic landscape as a vital tool in seismic hazard analyses. Tectonophysics, 408, 3-21. doi: https://doi.org/10.1016/j.tecto.2005.05.035

MILDON, Z. K., ROBERTS, G. P., FAURE WALKER, J. P. & IEZZI, F. 2017. Coulomb stress transfer and fault interaction over millennia on non-planar active normal faults: the M_w 6.5–5.0 seismic sequence of 2016–2017, central Italy. Geophysical Journal International, 210, 1206-1218. doi: https://doi.org/10.1093/gji/ggx213

MILLINER, C. W. D., DOLAN, J. F., HOLLINGSWORTH, J., LEPRINCE, S. & AYOUB, F. 2016. Comparison of co-seismic near-field and off-fault surface deformation patterns of the 1992 M_w 7.3 Landers and 1999 M_w 7.1 Hector Mine earthquakes: Implications for controls on the distribution of surface strain: Deformation of Landers and Hector Mine. Geophysical Research Letters, 43, 10-10,124. doi: https://doi.org/10.1002/2016GL069841

MILLINER, C. W. D., DOLAN, J. F., HOLLINGSWORTH, J., LEPRINCE, S., AYOUB, F. & SAMMIS, C. G. 2015. Quantifying near-field and off-fault deformation patterns of the 1992 M_w 7.3 Landers earthquake. Geochemistry, Geophysics, Geosystems, 16, 1577-1598. doi: https://doi.org/10.1002/2014GC005693

MUIR-WOOD, R. & KING, G. C. P. 1993. Hydrological signatures of earthquake strain. Journal of Geophysical Research, 98, 22035-22068. doi: https://doi.org/10.1029/93JB02219

NASA. 1999. Space Science Data Coordinated Archive Ikonos 2 [Online]. Available: https://nssdc.gsfc.nasa.gov/nmc/spacecraft/display.action?id=1999-051A [Accessed November 2021].

NASA EARTH DATA. 2019. New Version of the ASTER GDEM [Online]. Available: https://www.earthdata.nasa.gov/news/new-aster-gdem [Accessed November 2021].

NISSEN, E., KRISHNAN, A. K., ARROWSMITH, J. R. & SARIPALLI, S. 2012. Three-dimensional surface displacements and rotations from differencing pre- and post-earthquake LiDAR point clouds. Geophysical Research Letters, 39(16). doi: https://doi.org/10.1029/2012GL052460

NISSEN, E., MALIREDDI, S. R., CLARK, K., HAMLING, L., LANGRIDGE, R., RIES, W. & TAGLIASACCHI, A. 2017. Three-dimensional coastal deformation in the M_w 7.8 Kaikoura earthquake from differential airborne lidar. Proceedings of the 8th International INQUA Meeting on Paleoseismology, Active Tectonics and Archaeoseismology (Pata). http://web.uvic.ca/~enissen/papers/nissen-etal-2017-PATA.pdf

NISSEN, E., MARUYAMA, T., RAMON ARROWSMITH, J., ELLIOTT, J. R., KRISHNAN, A. K., OSKIN, M. E. & SARIPALLI, S. 2014. Co-seismic fault zone deformation revealed with differential lidar: Examples from Japanese Mw ~7 intraplate earthquakes. Earth and Planetary Science Letters, 405, 244-256. doi: https://doi.org/10.1016/j.epsl.2014.08.031

O'CALLAGHAN, J. 2019. Trump accidentally revealed the amazing resolution of U.S spy satellites. Forbes. Available: https://www.forbes.com/sites/jonathanocallaghan/2019/09/01/trump-accidentally-revealed-the-amazing-resolution-of-u-s-spy-satellites/?sh=6b391e613d89 [Accessed November 2021]

OKADA, Y. 1985. Surface deformation due to shear and tensile faults in a half-space. Bulletin of the Seismological Society of America, 75, 1135-1154. doi: https://doi.org/10.1785/BSSA0750041135

OSKIN, M. E., ARROWSMITH, R., TERAN, O., HINOJOSA CORONA, A., ELLIOTT, A., FLETCHER, J. M., FIELDING, E. J., GOLD, P. O., GONZALEZ GARCIA, J., HUDNUT, K. W. & JING, L.-Z. 2012. Near-Field Deformation from the El Mayor-Cucapah Earthquake Revealed by Differential LIDAR. Science (American Association for the Advancement of Science), 335, 702-705. doi: https://doi.org/10.1126/science.1213778

PANTOSTI, D., D'ADDEZIO, G. & CINTI, F. R. 1996. Paleoseismicity of the Ovindoli-Pezza fault, central Apennines, Italy: A history including a large, previously unrecorded earthquake in the Middle Ages (860-1300 A.D.). Journal of Geophysical Research, 101, 5937-5959. doi: https://doi.org/10.1029/95JB03213

PAPANIKOLAOU, I. D., ROBERTS, G. P. & MICHETTI, A. M. 2005. Fault scarps and deformation rates in Lazio–Abruzzo, Central Italy: Comparison between geological

fault slip-rate and GPS data. Tectonophysics, 408, 147-176. doi: https://doi.org/10.1016/j.tecto.2005.05.043

PEARSON, R. K., NEUVO, Y., ASTOLA, J. & GABBOUJ, M. 2016. Generalized Hampel Filters. EURASIP journal on advances in signal processing, 2016, 1-18. doi: https://doi.org/10.1186/s13634-016-0383-6

PELTZER, G., ROSEN, P., ROGEZ, F. & HUDNUT, K. 1998. Poroelastic rebound along the Landers 1992 earthquake surface rupture. Journal of Geophysical Research, 103, 30131-30145. doi: https://doi.org/10.1029/98JB02302

PERKO, R., RAGGAM, H. & ROTH, P. M. 2019. Mapping with Pleiades - End-to-End Workflow. Remote Sensing, 11. doi: https://doi.org/10.3390/rs11172052

PERRIN, C., MANIGHETTI, I., AMPUERO, J. P., CAPPA, F. & GAUDEMER, Y. 2016. Location of largest earthquake slip and fast rupture controlled by along-strike change in fault structural maturity due to fault growth. Journal of Geophysical Research: Solid Earth, 121, 3666-3685. doi: https://doi.org/10.1002/2015JB012671

PERROY, R. L., BOOKHAGEN, B., ASNER, G. P. & CHADWICK, O. A. 2010. Comparison of gully erosion estimates using airborne and ground-based LiDAR on Santa Cruz Island, California. Geomorphology, 118, 288-300. doi: https://doi.org/10.1016/j.geomorph.2010.01.009

PIERANTONI, P., DEIANA, G. & GALDENZI, S. 2013. Stratigraphic and structural features of the Sibillini Mountains (Umbria-Marche Apennines, Italy). Italian Journal of Geoscience, 132, 497-520. doi: https://doi.org/10.3301/IJG.2013.08

PIERCE, K. L. & COLMAN, S. M. 1986. Effect of height and orientation (microclimate) on geomorphic degradation rates and processes, late-glacial terrace scarps in central Idaho. Geological Society of America Bulletin, 97, 869-885. doi: https://doi.org/10.1130/0016-7606(1986)97<869:EOHAOM>2.0.CO2

PIZZI, A., DI DOMENICA, A., GALLOVIČ, F., LUZI, L. & PUGLIA, R. 2017. Fault Segmentation as Constraint to the Occurrence of the Main Shocks of the 2016 Central Italy Seismic Sequence. Tectonics, 36, 2370-2387. doi: https://doi.org/10.1002/2017TC004652

PIZZI, A. & GALADINI, F. 2009. Pre-existing cross-structures and active fault segmentation in the northern-central Apennines (Italy). Tectonophysics, 476, 304-319. doi: https://doi.org/10.1016/j.tecto.2009.03.018

PIZZI, A. & SCISCIANI, V. 2000. Methods for determining the Pleistocene–Holocene component of displacement on active faults reactivating pre-Quaternary structures: examples from the Central Apennines (Italy). Journal of Geodynamics, 29, 445-457. doi: https://doi.org/10.1016/S0264-3707(99)00053-8

POLLITZ, F. F., WICKS, C. & THATCHER, W. 2001. Mantle Flow beneath a Continental Strike-Slip Fault: Postseismic Deformation after the 1999 Hector Mine Earthquake. Science, 293, 1814-1818. doi: https://doi.org/10.1126/science.1061361

POUSSE-BELTRAN, L., SOCQUET, A., BENEDETTI, L., DOIN, M. P., RIZZA, M. & D'AGOSTINO, N. 2020. Localized Afterslip at Geometrical Complexities Revealed by InSAR After the 2016 Central Italy Seismic Sequence. Journal of Geophysical Research: Solid Earth, 125 (11), p.e2019JB019065. doi: https://doi.org/10.1029/2019JB019065

QUIGLEY, M., VAN DISSEN, R., LITCHFIELD, N., VILLAMOR, P., DUFFY, B., BARRELL, D., FURLONG, K., STAHL, T., BILDERBACK, E. & NOBLE, D. 2011. Surface rupture during the 2010 Mw 7.1 Darfield (Canterbury) earthquake: implications for fault rupture dynamics and seismic hazard analysis. Geology, 40, 55-58. doi: https://doi.org/10.1130/G32528.1

REGIONE MARCHE, 2017. Carta Geologica di Marche [Online]. Available: https://www.regione.marche.it/Regione-Utile/Paesaggio-Territorio-Urbanistica/Cartografia/Repertorio/Cartageologicaregionale10000. [Accessed 3rd March 2022]

REGIONE UMBRIA, 2014. Carta Geologica dell'Umbria [Online]. Available: https://dati.regione.umbria.it/dataset/carta-geologica-dell-umbria. [Accessed 12th October 2021].

RIVA, R. E. M., BORGHI, A., AOUDIA, A., BARZAGHI, R., SABADINI, R. & PANZA, G. F. 2007. Viscoelastic relaxation and long-lasting after-slip following the 1997 Umbria-Marche (Central Italy) earthquakes. Geophysical Journal International, 169, 534-546. doi: https://doi.org/10.1111/j.1365-246X.2007.03315.x

ROBERTS, G. P. 2008. Visualisation of active normal fault scarps in the Apennines, Italy: a key to assessment of tectonic strain release and earthquake rupture. Journal of the Virtual Explorer, 29, 1-10. doi: https://doi.org/10.3809/jvirtex.2008.00197

ROBERTS, G. P. & MICHETTI, A. M. 2004. Spatial and temporal variations in growth rates along active normal fault systems: an example from The Lazio–Abruzzo Apennines, central Italy. Journal of Structural Geology, 26, 339-376. doi: https://doi.org/10.1016/S0191-8141(03)00103-2

ROSS, Z. E., IDINI, B., JIA, Z., STEPHENSON, O. L., ZHONG, M., WANG, X., ZHAN, Z., SIMONS, M., FIELDING, E. J., YUN, S.-H., HAUKSSON, E., MOORE, A. W., LIU, Z. & JUNG, J. 2019. Hierarchical interlocked orthogonal faulting in the 2019 Ridgecrest earthquake sequence. Science, 366, 346-351. doi: https://doi.org/10.1126/science.aaz0109

RUINA, A. 1983. Slip instability and state variable friction laws. Journal of Geophysical Research: Solid Earth, 88, 10359-10370. doi: https://doi.org/10.1029/JB088iB12p10359

SATELLITE IMAGING CORPORATION. 2021. About Digital Elevation Models [Online]. Available: https://www.satimagingcorp.com/services/dem/ [Accessed November 2021].

SCHOLZ, C. H. 1988. The brittle-plastic transition and the depth of seismic faulting. Geologische Rundshau, 77, 319-328. doi: https://doi.org/10.1007/BF01848693

SCHOLZ, C. H. 2019. The Mechanics of Earthquakes and Faulting, 3rd Edition. Cambridge: Cambridge University Press.

SCHWARTZ, D. P. & COPPERSMITH, K. J. 1984. Fault behavior and characteristic earthquakes: Examples from the Wasatch and San Andreas Fault Zones. Journal of Geophysical Research, 89, 5681-5698. doi: https://doi.org/10.1029/JB089iB07p05681

SCOGNAMIGLIO, L., TINTI, E., CASAROTTI, E., PUCCI, S., VILLANI, F., COCCO, M., MAGNONI, F., MICHELINI, A. & DREGER, D. 2018. Complex Fault Geometry and Rupture Dynamics of the M_w 6.5, 30 October 2016, Central Italy Earthquake. Journal of Geophysical Research: Solid Earth, 123, 2943-2964. doi: https://doi.org/10.1002/2018JB015603

SCOTT, C. P., ARROWSMITH, J. R., NISSEN, E., LAJOIE, L., MARUYAMA, T. & CHIBA, T. 2018. The M 7 2016 Kumamoto, Japan, Earthquake: 3-D Deformation Along the Fault and Within the Damage Zone Constrained From Differential Lidar Topography. Journal of Geophysical Research: Solid Earth, 123, 6138-6155. doi: https://doi.org/10.1029/2018JB015581

SEGALL, P., BÜRGMANN, R. & MATTHEWS, M. 2000. Time-dependent triggered afterslip following the 1989 Loma Prieta earthquake. Journal of Geophysical Research, 105, 5615-5634. doi: https://doi.org/10.1029/1999JB900352

STEWART, I. S. & HANCOCK, P. L. 1990. What is a fault scarp? International Union of Geological Sciences, 13, 256-263. doi: https://doi.org/10.18814/epiiugs/1990/v13i4/005

TERAN, O. J., FLETCHER, J. M., OSKIN, M. E., ROCKWELL, T. K., HUDNUT, K. W., SPELZ, R. M., AKCIZ, S. O., HERNANDEZ-FLORES, A. P. & MORELAN, A. E. 2015. Geologic and structural controls on rupture zone fabric: A field-based study of the 2010 M_w 7.2 El Mayor-Cucupah earthquake surface rupture. Geosphere, 11, 899-920. doi: https://doi.org/10.1130/GES01078.1

TUKEY, J. W. 1974. Nonlinear (nonsuperposable) methods for smoothing data. Proc. Cong. Rec. EASCOM '74, 673-681.

VILLANI, F., CIVICO, R., PUCCI, S., PIZZIMENTI, L., NAPPI, R., DE MARTINI, P. M., AGOSTA, F., ALESSIO, G., ALFONSI, L., AMANTI, M., AMOROSO, S., ARINGOLI, D., AUCIELLO, E., AZZARO, R., BAIZE, S., BELLO, S., BENEDETTI, L., BERTAGNINI, A., BINDA, G., BISSON, M., BLUMETTI, A. M., BONADEO, L., BONCIO, P., BORNEMANN, P., BRANCA, S., BRAUN, T., BROZZETTI, F., BRUNORI, C. A., BURRATO, P., CACIAGLI, M., CAMPOBASSO, C., CARAFA, M., CINTI, F. R., CIRILLO, D., COMERCI, V., CUCCI, L., DE RITIS, R., DEIANA, G., DEL CARLO, P., DEL RIO, L., DELORME, A., DI MANNA, P., DI NACCIO, D., FALCONI, L., FALCUCCI, E., FARABOLLINI, P., FAURE WALKER, J. P., FERRARINI, F., FERRARIO, M. F., FERRY, M., FEUILLET, N., FLEURY, J., FRACASSI, U., FRIGERIO, C., GALLUZZO, F., GAMBILLARA, R., GAUDIOSI, G., GOODALL, H., GORI, S., GREGORY, L. C., GUERRIERI, L., HAILEMIKAEL, S., HOLLINGSWORTH, J., IEZZI, F., INVERNIZZI, C., JABLONSKÁ, D., JACQUES, E., JOMARD, H., KASTELIC, V., KLINGER, Y., LAVECCHIA, G., LECLERC, F., LIBERI, F., LISI, A., LIVIO, F., LO SARDO, L., MALET, J. P., MARIUCCI, M. T., MATERAZZI, M., MAUBANT, L., MAZZARINI, F., MCCAFFREY, K. J. W., MICHETTI, A. M., MILDON, Z. K., MONTONE, P., MORO, M., NAVE, R., ODIN, M., PACE, B., PAGGI, S., PAGLIUCA, N., PAMBIANCHI, G., PANTOSTI, D., PATERA, A., PÉROUSE, E., PEZZO, G., PICCARDI, L., PIERANTONI, P. P., PIGNONE, M., PINZI, S., et al. 2018. A

database of the co-seismic effects following the 30 October 2016 Norcia earthquake in Central Italy. (vol 5, 180049, 2018). Scientific Data, 6. doi: https://doi.org/10.1038/sdata.2018.49

VITTORI, E., DEIANA, G., ESPOSITO, E., FERRELI, L., MARCHEGIANI, L., MASTROLORENZO, G., MICHETTI, A. M., PORFIDO, S., SERVA, L., SIMONELLI, A. L. & TONDI, E. 2000. Ground effects and surface faulting in the September–October 1997 Umbria–Marche (Central Italy) seismic sequence. Journal of Geodynamics, 29, 535-564. doi: https://doi.org/10.1016/S0264-3707(99)00056-3

WALLACE, R. E. 1977. Profiles and ages of young fault scarps, North-central Nevada. Geological Society of America Bulletin, 88, 1267-1281. doi: https://doi.org/10.1130/0016-7606(1977)88<1267:PAAOYF>2.0.CO2

WALLACE, R. E. 1980. Degradation of the Hebgen Lake fault scarps of 1959. Geology, 8, 225-229. doi: https://doi.org/10.1130/0091-7613(1980)8<225:DOTHLF>2.0.CO2

WALSH, J. J., NICOL, A. & CHILDS, C. 2002. An alternative model for the growth of faults. Journal of Structural Geology, 24, 1669-1675. doi: https://doi.org/10.1016/S0191-8141(01)00165-1

WALTERS, R. J., GREGORY, L. C., WEDMORE, L. N. J., CRAIG, T. J., MCCAFFREY, K., WILKINSON, M., CHEN, J., LI, Z., ELLIOTT, J. R., GOODALL, H., IEZZI, F., LIVIO, F., MICHETTI, A. M., ROBERTS, G. & VITTORI, E. 2018. Dual control of fault intersections on stop-start rupture in the 2016 Central Italy seismic sequence. Earth and Planetary Science Letters, 500, 1-14. doi: https://doi.org/10.1016/j.epsl.2018.07.043

WEDMORE, L., GREGORY, L., MCCAFFREY, K., WILKINSON, M., ROBERTS, G., FAURE WALKER, J., FERRARIO, F., FRIAERIO, C., GOODALL, H., IEZZI, F., LIVIO, F., MICHETTI, A., MILDON, Z. & VITTORI, F. Co-seismic and shallow post-seismic slip during the 2016 central Italy earthquake sequence revealed by differential terrestrial laser scanning and photogrammetry. EGU (European Geosciences Union) General Assembly April 2017, Vienna, Austria.

WEDMORE, L. N. J., GREGORY, L. C., MCCAFFREY, K. J. W., GOODALL, H. & WALTERS, R. J. 2019. Partitioned off-fault deformation in the 2016 Norcia earthquake captured by differential terrestrial laser scanning. Geophysical Research Letters, 46(6), pp.3199-3205. doi: https://doi.org/10.1029/2018GL080858

WEI, Z., HE, H., LEI, Q., SUN, W. & LIANG, Z. 2021. Constraining co-seismic earthquake slip using Structure from Motion from fault scarp mapping (East Helanshan Fault, China). Geomorphology, 375, p.107552. doi: https://doi.org/10.1016/j.geomorph.2020.107552

WELLS, D. L. & COPPERSMITH, K. J. 1994. New empirical relationships among magnitude, rupture length, rupture width, rupture area, and surface displacement. Bulletin of the Seismological Society of America, 84, 974-1002. doi: https://doi.org/10.1785/BSSA0840040974

WESNOUSKY, S. G. 1988. Seismological and structural evolution of strike-slip faults. Nature, 335, 340-343. doi: https://doi.org/10.1038/335340a0

WESSEL, P., SMITH, W. H. F., SCHARROO, R., LUIS, J. & WOBBE, F. 2013. Generic Mapping Tools: Improved Version Released. Eos, 94, 409-410. doi: https://doi.org/10.1002/2013EO450001

WESTOBY, M. J., BRASINGTON, J., GLASSER, N. F., HAMBREY, M. J. & REYNOLDS, J. M. 2012. 'Structure-from-Motion' photogrammetry: A low-cost, effective tool for geoscience applications. Geomorphology, 179, 300-314. doi: https://doi.org/10.1016/j.geomorph.2012.08.021

WHITMAN, D., ZHANG, K., LEATHERMAN, S. P. & ROBERTSON, W. 2003. Airborne Laser Topographic Mapping: Applications to Hurricane Storm Surge Hazards. Washington, D. C: American Geophysical Union. Earth Science in the City: A Reader, 56, pp.363-376. doi: https://doi.org/10.1029/SP056p03363

WILKINSON, M., MCCAFFREY, K. J. W., ROBERTS, G., COWIE, P. A., PHILLIPS, R. J., MICHETTI, A. M., VITTORI, E., GUERRIERI, L., BLUMETTI, A. M., BUBECK, A., YATES, A. & SILEO, G. 2010. Partitioned postseismic deformation associated with the 2009 M_w 6.3 L'Aquila earthquake surface rupture measured using a terrestrial laser scanner. Geophysical Research Letters, 37(10). doi: https://doi.org/10.1029/2010GL043099

WILKINSON, M., ROBERTS, G. P., MCCAFFREY, K., COWIE, P. A., FAURE WALKER, J. P., PAPANIKOLAOU, I., PHILLIPS, R. J., MICHETTI, A. M., VITTORI, E., GREGORY, L., WEDMORE, L. & WATSON, Z. K. 2015. Slip distributions on active normal faults measured from LiDAR and field mapping of geomorphic offsets: an example from L'Aquila, Italy, and implications for modelling seismic moment release. Geomorphology, 237, 130-141. doi: https://doi.org/10.1016/j.geomorph.2014.04.026

WILKINSON, M. W., JONES, R. R., WOODS, C. W., GILMENT, S. R., MCCAFFREY, K. J. W., KOKKALAS, S. & LONG, J. J. 2016. A comparison of terrestrial laser scanning and structure-from-motion photogrammetry as methods for digital outcrop acquisition. Geosphere v.12 no. 6, pp 1865-1880. doi: https://doi.org/10.1130/GES01342.1

WILKINSON, M. W., MCCAFFREY, K. J. W., JONES, R. R., ROBERTS, G. P., HOLDSWORTH, R. E., GREGORY, L. C., WALTERS, R. J., WEDMORE, L., GOODALL, H. & IEZZI, F. 2017. Near-field fault slip of the 2016 Vettore M_w 6.6 earthquake (Central Italy) measured using low-cost GNSS. Scientific Reports, 7, 1-7. doi: https://doi.org/10.1038/s41598-017-04917-w

WILKINSON, M. W., MCCAFFREY, K. J. W., ROBERTS, G. P., COWIE, P. A., PHILLIPS, R. J., DEGASPERI, M., VITTORI, E. & MICHETTI, A. M. 2012. Distribution and magnitude of post-seismic deformation of the 2009 L'Aquila 1 earthquake (M6.3) surface rupture measured using repeat terrestrial laser scanning. Geophysical Journal International. doi: https://doi.org/10.1111/j.1365-246X.2012.05418.x

WIMPENNY, S., COPLEY, A. & INGLEBY, T. 2017. Fault mechanics and post-seismic deformation at Bam, SE Iran. Geophysical Journal International., 209, 1018-1035. doi: https://doi.org/10.1093/gji/ggx065

WRIGHT, T. J., ELLIOTT, J. R., WANG, H. & RYDER, I. 2013. Earthquake cycle deformation and the Moho: Implications for the rheology of continental

lithosphere. Tectonophysics, 609, 504-523. doi: https://doi.org/10.1016/j.tecto.2013.07.029

XU, G., XU, C., WEN, Y. & JIANG, G. 2017. Source Parameters of the 2016–2017 Central Italy Earthquake Sequence from the Sentinel-1, ALOS-2, and GPS data. Remote Sensing, 9. doi: https://doi.org/10.3390/rs9111182

XU, Q., CHEN, Q., ZHAO, J., LIU, X., YANG, Y., ZHANG, Y. & LIU, G. 2020. Sequential modelling of the 2016 Central Italy earthquake cluster using multisource satellite observations and quantitative assessment of Coulomb stress change. Geophysical Journal International, 221, 451-466. doi: https://doi.org/10.1093/gji/ggaa036

XU, X., TONG, X., SANDWELL, D. T., MILLINER, C. W. D., DOLAN, J. F., HOLLINGSWORTH, J., LEPRINCE, S. & AYOUB, F. 2016. Refining the shallow slip deficit. Geophysical Journal International, 204, 1843-1862. doi: https://doi.org/10.1093/gji/ggv563

ZHOU, Y., PARSONS, B., ELLIOTT, J. R., BARISIN, I. & WALKER, R. T. 2015. Assessing the ability of Pleiades stereo imagery to determine height changes in earthquakes: A case study for the El Mayor-Cucapah epicentral area. Journal of Geophysical Research. Solid Earth, 120, 8793-8808. doi: https://doi.org/10.1002/2015JB012358

ZHOU, Y., THOMAS, M. Y., PARSONS, B. & WALKER, R. 2018. Time-dependent postseismic slip following the 1978 M 7.3 Tabas-e-Golshan, Iran earthquake revealed by over 20 years of ESA InSAR observations. Earth and Planetary Science Letters, 483, 64-75. doi: https://doi.org/10.1016/j.epsl.2016.07.038

ZHOU, Y., WALKER, R. T., HOLLINGSWORTH, J., TALEBIAN, M., SONG, X. & PARSONS, B. 2016. Co-seismic and postseismic displacements from the 1978 M_w 7.3 Tabas-e-Golshan earthquake in eastern Iran. Earth and Planetary Science Letters, 452, 185. doi: https://doi.org/10.1016/j.epsl.2017.12.005

ZINKE, R., HOLLINGSWORTH, J. & DOLAN, J. F. 2014. Surface slip and off-fault deformation patterns in the 2013 M_w 7.7 Balochistan, Pakistan earthquake: Implications for controls on the distribution of near-surface co-seismic slip. Geochemistry, Geophysics, Geosystems: G3, 15, 5034-5050. doi: https://doi.org/10.1002/2014GC005538